Swansea University
Prifysgol Abertawe

DOCTORAL THESIS

Surface Modified Polymers and Nanoparticles for Enhanced Oil Recovery (EOR) Applications

---

Author:

Wafaa AL-SHATTY

Supervisors:

Prof. Andrew R. BARRON

Dr. Shirin ALEXANDER

A thesis submitted in fulfillment of the requirements for the degree of Doctor of Philosophy

in the

Energy Safety Research Institute

College of Engineering

March 2022

Abstract

The study to improve hydrocarbon recovery has attracted a great deal of research attention in many directions such as using chemical treatment or CO_2 injection, and hydrocarbon fracking. The research trials are based on either studying a new approach to recovery or investigating the effect of injection agent treatments. Nanoparticles are a chemical addition that has promise in changing the reservoir properties through different mechanisms such as: wettability alteration, reduce oil/water mobility, increase viscosity, disjoining pressure and interfacial tension reduction. In this thesis, alumina nanoparticles were modified with carboxylic acids to form different degrees of the hydrophobicity. They were investigated as potential candidates for enhanced oil recovery applications. Surface modification of alumina nanoparticles occurs at a molecular level. Consequently, applying these modifications for use as in the chemical treatment of Enhanced oil recovery (EOR) processes could change surface properties of oil, water, and rock. Thus, these modified alumina particles can act as a surface-active agent. Their increasing level of the hydrophobicity (depending on the type of carboxylic acid attached) and concentration shows a reduction in the interfacial tension (IFT) of hexadecane oil. As a result, the ability to modify the degree of hydrophobicity makes them good candidates for EOR.

Carboxylic acid-functionalized alumina nanoparticles (NPs) were tested as a potential candidate for enhanced oil recovery. The NP's size and shape in aqueous solution were investigated by dynamic light scattering (DLS) and small-angle neutron scattering (SANS) as a function of the substituents: 2-[2-(2-methoxyethoxy)ethoxy]acetic acid (MEEA), and Octanoic acid (OCT). The viscosity and density of injected fluids have been interpreted in terms of the NP's chemical functionality. The influence of NPs hydrophobicity was observed in the size and oil

removed from reservoir rock. The octanoic acid-functionalized alumina NPs is considered herein a good candidate for applications in oil recovery.

The evaluation of the mechanism of nanoparticles/surfactant complex adsorption at the critical oil/water interface was studied with a sophisticated technique (Neutron Reflectometry) to give insight on nanoparticles/oil interactions in oil recovery systems. Here, the adsorption of two modified alumina nanoparticles with different degrees of hydrophobicity (hydrophilic 2-[2-(2-methoxyethoxy) ethoxy] acetic acid (MEEA), and hydrophobic octanoic acid (OCT)) stabilized with 2 different surfactants, were studied at oil/water interface. A thin layer of deuterated (D) and hydrogenated (H) hexadecane (contrast matching Silicon substrate) oil was formed on a silicon block by a spin coating freeze process. The distribution of the NPs across the oil/water interface with CTAB surfactant is similar between the two systems. NPs coated with CTAB have more affinity towards the oil/water interface, which explains the oil recovery increase by around 5% when flooding the core with OCT-NP/CTAB system compared to the surfactant flooding alone. These results suggest that NPs/surfactant complexes can have potential usage in EOR recovery applications.

Chapter four addresses the challenge of the O/W Pickering emulsion formed with un/modified alumina nanoparticles adsorbed with surfactants showing longer stability. Alumina nanoparticles were modified by different carboxylic acids to acquire the different degrees of hydrophobicity. Dynamic light scattering and optical microscopy measurements were then performed to characterize the aggregation behaviour of alumina-NP/surfactant's mixture in an aqueous solution. The long-term stability of pickering emulsion stabilized by alumina modified nanoparticles was investigated directly after each time interval: 5 min, 1 hour, 1 week, and 1 month. The result indicated that adjusting the amount of modified alumina nanoparticles and

surfactants could be a suitable means for manipulating the stability of nanoparticles-surfactant based pickering emulsions. This would serve as a great application prospect for the preparation of pickering emulsion stabilized by eco-friendly nanoparticles (both MEEA and OCT) and surfactants.

The synthesis and characterization of two new families of amphiphilic graft copolymers (AGCs) are reported. The graft polymers were synthesized using the various molecular weight of polyethylene glycol (PEG) (as hydrophilic graft chains) and two different hydrophobic backbones (with a varied quantity of functional groups) using a *"graft onto"* technique. FTIR and ^{1}H NMR characterizations were used to indicate and validate the synthesis of grafted copolymers. The length of the PEG was observed to correlate with the hydrophilic ratio. Increasing the chain length of PEG was observed to increase the hydrophilicity ratio (more grafted PEG more hydrophilic). Consequently, both hydrophobic backbones wettability (⇠ 90 - 110) altered upon grafting onto synthesis and the contact angle data showed that the higher molecular weight of grafted chains led to higher hydrophilicity of grafted polymers (⇠ 11 - 65). The critical micelle concentrations (CMC) and surface activity (SFT) of AGCs in water were determined by the surface tension technique via the shape analyser (pendant drop method). It revealed that these polymers can act as polymeric surfactants with CMC of around 2-3 wt.%. Small-angle neutron (SANS) was used to examine the conformation of the AGCs in aqueous solutions which displayed the formation of ellipsoidal core-shell micelles. This research provides fundamental understandings of potentially important polymeric materials with a variety of applications from emulsifiers and drug carriers to enhance oil recovery additives.

The synergetic effect of combing low salinity water with polymer injection methods (polymer flooding) is a promising technique for oil displacement (enhanced

oil recovery) (EOR). The objective of this study was to investigate the effect of newly synthesized amphiphilic polymers on two potential applications: oil displacement and stabilized emulsion. To successfully displace the oil within the tested reservoir rock, the optimal concentration of NaCl ions was determined to be 1 wt.% in the low salinity polymer. To evaluate aggregation behaviour, the conformational change of the grafted polymers/amphiphilic polymers resulting from the effect of salt/NaCl addition was investigated by Small-angle X-ray scattering (SAXS). The polymers displayed an ellipsoidal core-shell micelles conformation. The copolymers with higher hydrophilic grafts had lower emulsion stability due to the size of the aggregation particles being smaller, despite having higher oil recovery capability. These findings have a significant potential impact on the oil industry which is to counteract current hazardous methods and overcome the high salinity environment of EOR.

List of Publications

Al-Shatty, W., Alexander, S., and Barron, A. R. (2022). Micromodel Evaluation of Nanoparticles for Enhanced Oil Recovery. *MiDAS Green Innovations.*.

Al-Shatty, W., Alexander, S., and Barron, A. R. (2022). Stability of carboxylic acid modified alumina nanoparticles for enhanced oil recovery applications. *AIP Conf. Proc. 2022*, in press.

Al-Shatty, W., Hill, D. A., Kiani, S., Stanulis, A., Winston, S., Powner, I., Alexander, S., and Barron, A. R. (2022). "Superhydrophilic surface modification of fabric via coating with cysteic acid mineral oxide. *Appl. Surf. Sci.* (2021): 152306.

Al-Shatty, W., Hill, D. A., Rogers, S. E, Alexander, S., and Barron, A. R. Novel CoreShell Polymeric Surfactants, Part 1: Synthesis and Characterisation. Submitted to *J. Colloid Interface Sci.*.

Al-Shatty, W., Campana, M., Alexander, S., and Barron, A. R (2022). Interaction of Surface Modified Alumina Nanoparticles and Surfactants at an Oil/Water Interface: a Neutron Reflectometry, Scattering, and enhanced oil recovery Study. *ACS Appl. Mater. Interfaces*, 14(17), 19505-19514.

Al-Shatty, W., Alexander, S., and Barron, A. R. Novel Core-Shell Polymeric Surfactants, Part 2: New Candidates for Enhance Oil Recovery and Emulsifiers Applications. [manuscript in process].

Al-Shatty, W., Alexander, S., and Barron, A. R. Eco Friendly Pickering Emulsion Stabilized by Carboxylic Acid Modified Alumina Nanoparticles. [manuscript in process].

Declaration of Authorship

- This work has not previously been accepted in substance for any degree and is not being concurrently submitted in candidature for any degree.

  Signed: [redacted]

  Date: 27/6/2022

- This thesis is the result of my own investigations, except where otherwise stated. Other sources are acknowledged by footnotes giving explicit references. A bibliography is appended.

  Signed: [redacted]

  Date: 27/6/2022

- I hereby give my consent for my thesis, if accepted, to be available for photocopying and for inter-library loans, and for the title and summary to be made available to outside organisations.

  Signed: [redacted]

  Date: 27/6/2022

- The University's ethical procedures have been followed and, where appropriate, that ethical approval has been granted.

  Signed:

  Date:

Contents

List of Figures

List of Tables

List of Abbreviations

TEOR	Thermal enhanced oil recovery
S_i	Saturation
S_{gc}	Critical Gas Saturation
S_{wc}	Critical Water Saturation
S_{org}	Oil Displaced by Gas
S_{orw}	Oil Displaced by Water
S_{gr}	Gas displaced
S_{wr}	Water displaced
S_{wir}	Irreducible Water saturation
K_a	Absolute permeability, a refer to material
K_{ra}	Relative permeability for material a
K_{rb}	Relative permeability for material b
IFT	Interfacial tension
WCA	Water contact angle
EOR	Enhanced oil recovery
NPs	Nanoparticles
SFT	Surface tension *g*
HPAM	Mixture of salt/surfactant/water/polymer
CNP	Silica Colloidal Nanoparticles
NSP	Silica nano-structure particle
PVP	Polyvinylpyrrolidone
DSNP	polyacrylamide
PAM	polymer
ZPT	Zeta potential
SDS	Sodium dodecyl sulfate
CNTs	Carbon nanotubes

SWCNTs	Single-Walled Carbon Nanotube
MWCNTs	Multi Walled Carbons Nanotubes
DWCNTs	Double-Walled Carbon Nanotubes
O/W	oil/water
HLB	Hydrophobicity
FTIR	Fourier Transform Infrared
FKM	Fluoroelastomer rubber
OOIP	Oil remain In Place
UV	Ultraviolet Light
SU-8	8 epoxy based negative photoresist
HF	Hydrofluoric acid
CAD	Computer-Aided Design
PDMS	polydimethylsiloxane polymer
PMMA	Polymethylmethacrylate polymer PVI
photoluminescent volumetric imaging μ-PIV Micro Particle Imaging Technique	
CM	Confocal Microscopy
CML	Carboxylate Modified Latex
LSES-iC18S(FO-180)	Low Surface Energy Surfactant
MEEA	2-(2-methoxyethoxy)ethoxy]acetic acid
HAPM	Anionic Hydrolysed Polyacrylamide Polymer
OCT	octanoic acid
CMC	Critical Micelles Concentration
BET	Specific Surface Area
SANS	Small Angle Neutron Scattering
Unf-Al_2O_3	unfunctionalized alumina

SLD	Scattering Length Density
NR	Neutron Reflectometry
DLS	Dynamic Light Scattering
QCM	Quartz Crystal Microbalance
AFM	Atomic Force Microscopy
CTAB	hexadecyltrimethylammonium bromide
L	Layer
AGCs	Amphiphilic Graft Copolymers
PEG	polyethylene glycol
PIP	polyisoprene
TGA	Thermogravimetric Analysis
SAXS	Small Angle X-ray Scattering
Octa	Poly (maleic anhydride-*alt*-1-octadecane)
IB	Poly (isobutylene-*alt*-maleic anhydride)
PDMS-g-PEO	poly(ethylene oxide)
M	Mobility
DI-water	Deionized Water
PES	Pickering Emulsions
MSC	Microbial Surfactant Complexes
TEM	Transmission Electron Microscopy
XRD	X-ray diffraction
FE-SEM	Field Emission Scanning Electron Microscope
HF	Hydrofluoric acid

Acknowledgements

I would like to extend my sincere gratitude to everyone who assisted me in the completion of my research. To all those who have inspired me and given me the selfconfidence to succeed in this journey. Firstly, and foremost, I would like to express

my greatest thanks to my supervisors Professor Andrew R. Barron and Dr Shirin Alexander who have been incredible in their support and guidance during the past three years. I believe and hope that the relationship I have developed with my supervisors will continue to grow even in the distance future in all aspects including work and collaboration opportunities to come. I could not have reached the position I am in today with my project without their valuable guidance and advice on all aspects of the work.

I would also like to extend a special thanks to all members of the Energy Safety and Research Institute (ESRI): Dr. Charles Dunnill, Merrie Barron, Enrico Andreoli, Alvin

Orbaek White, Dan Jones, Louise Hamdy, Donald Hill, Andrius Stanulis, Mabrouk Zanain, Waqas Tanveer, Katherine Glover, Mahboob Basha, Lucy Final, Ewa A. Kazimierska, Catheren E. Gowenlock, Saeid Khodabakhshi, and Varun Gangoli for being there when I needed them the most and for giving up their valuable time to help with training and advise on project directions.

I would like to dedicate profound gratitude to my family, who have been extremely patient for the duration of my academic journey away from home and in a different country. I would like to extend my appreciation to colleagues who were constantly encouraging me to successfully complete my postgraduate degree. My special thanks to my friends: Saja Ali Muhsin, Mariem Taher, Fatima Abed Al-Rita, Zainab Mehson, Najlaa Zaki, Nahaa Al-Otabi, Hussain Galeb, Jawad Kadhim and many others not mentioned. Thanks to my coalleages in ESRI and university: Blessing Nwanosike, Dan Stewart, Henery Apsey, Celina Vaniaand, and Odin Bian.

I would like to express further thanks to our project sponsors and collaborators: the Reducing Industrial Carbon Emissions (RICE) operations funded by the Welsh European Funding Office (WEFO) through the Welsh Government; the Core Oil Laboratory Team at Basrah Oil Company (Iraq) for assisting with the core flood experiments; Rutherford Appleton Laboratory (ISIS-STFC) for allocation of SANS and INTER beam time, travel and consumable funding at ISIS, Dr Sarah E. Rogers (ISIS) and Rob for their assistance with the small-angle neutron scattering (SANS) experiments, and Dr. Mario Campana for his assistance with the INTER experiment; Liverpool University for their assistance with SAXS beamtime measurements; Royce Student Equipment Access Scheme for their funding and equipment support; and AIM and CNH facilities for training and have access for number of facilities such as SEX, AFM, and NMR.

In addition, I would like to thank my landlord's (Mr and Norries for supporting me all time, especially during COVID-19.

Last but not least, I would like to offer a special thanks to my office colleagues, in particular Ebrima Sallah, Lucy Fisher, and Stephen Shearen, who were also there for me in both good and difficult times. Thank you for being someone I can always count on.

Dedicated to my Mum

and

My best friend: André Norries who passed away on the 26th of February 2021 with COVID-19.

Chapter 1

Introduction and literature review

1.1 Area of study

One of the main problems facing the oil industry today is the amount of remaining oil that is left behind after the deployment of the water flooding procedure. This is compounded by the difficulty; to increase oil recovery efficiently in a cost-effective way. As such about 65% of the oil is left unrecovered depending upon the mineral surface characteristics (Alnarabiji et al., 2018). However, the increase in population each year leads to an increased demand on hydrocarbon resources causing continuous price inflation on these resources. To meet these demands, industries have focused their efforts on increasing oil recovery by drilling new wells. In recent times, environmental concerns have shifted their focus to finding alternative routes to increase recovery in a more efficient, cost-effective and clean manner. This research aims to address the environmental challenge facing the industry by providing greener solutions to the most efficient oil recovery.

Chemical treatment is a common method used in industry as an oil recovery intervention. It often utilises surfactants, polymers, and nanoparticles, or combinations of these to achieve this. Adding surfactants to injected fluids leads to a reduction of interfacial tension between liquid-liquid or liquid-solid, which will cause the oil to be easily displaced by injected fluids (Figure 1.1 is a schematic diagram that shows the mechanism of the role of microbial surfactant complexes (MSC) in an oil production well (Mahmoud et al., 2020).

It is becoming more desirable for oil industry to use polymers in order to increase oil recovery to meet the oil demands. However, the polymers that are currently in use are designed to work under limited conditions such as low temperature, it is hence desirable to synthesise a new amphiphilic copolymer that works at high temperature and under a wider range of conditions. The addition of polymers to the injected water increases the injected water viscosity which would lead to a decrease in mobility (M) ratio between water and oil, and rock permeability (Ahmed, 2018). The decrease of these two factors improves oil recovery (Wang and Dong, 2009; Samanta et al., 2013). This is further discussed in section 1.8.3. Figure 1.2. Shows a schematic diagram of the polymer treatment mechanism.

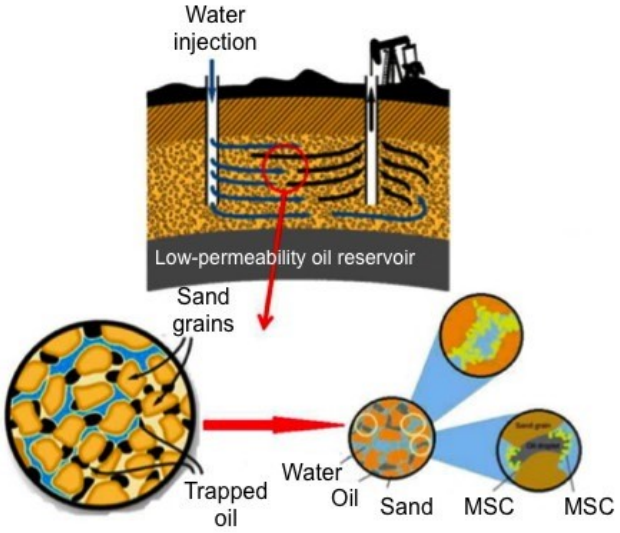

FIGURE 1.1: A schematic diagram showing the mechanism of microbial surfactant complexes (MSC) in an oil production well (Mahmoud et al., 2020) (Copyright: American Chemical Society, 2021).

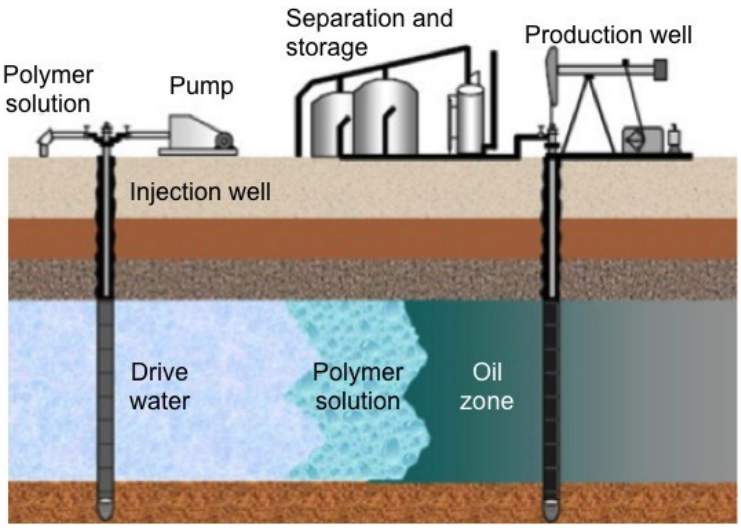

FIGURE 1.2: A schematic representation the mechanism of the displacement of oil (dark green area, 1) by a polymer solution (bubbly white area, 2), followed by displacement with water (white area, 3). Adopted from (El-Hoshoudy et al., 2017) (Copyright: Elsevier, 2017).

Injection of nanoparticles (NPs) has shown a promise in changing the reservoir properties through different mechanisms that include (but are not limited to) wettability alteration and reduced interfacial tension between interfaces (liquid-liquid, and liquid-solid). The primary objective of this thesis is to investigate the effect of modified alumina on the NPs size formed and their behaviour as a potential application for EOR.

This thesis focuses on the modification of alumina nanoparticles by different carboxylic acid groups to form different degrees of hydrophobicity on which to investigate the NPs size, shape and the resulting effect on the hydrophobicity. The role of different carboxylic acid on the functionalized alumina NPs will be tested for the first time as a nanofluid for Enhanced Oil Recovery (EOR) applications in reservoir cores. In addition, novel amphiphilic copolymers that are successfully synthesised via *grafted onto* method through esterification reactions taking place between the

terminal hydroxyl groups of the polyethylene glycol (PEG) and the alternating cyclic anhydride functionality present in Poly (maleic anhydride-*alt*-1-octadecane) (Octa) or Poly (isobutylene-*alt*-maleic anhydride) (IB) backbones. Consequently, it is possible that these copolymers can form core-shell micelles which make them a good candidate for various applications such as oil recovery.

This chapter is structured to provide the reader with an overview of the role of chemical addition particularly: nanoparticles, surfactants, and polymers in the oil displacement, and a description of the micromodel device that is currently used to mimic the oil displacement process. In addition, a review of some of the literature on chemical treatment that has been shown a positive impact on oil recovery is also given. However, background information relating to oil, type of reservoir fluids, and physical properties are provided in the following sections.

1.2 Oil

Hydrocarbon oil (petroleum) is defined as a thick black fluid, which consists mainly of a mixture of hydrocarbon (hydrogen + carbon) materials. It is highly effective as a source of chemical energy that can be converted to kinetic energy, for example, fuel for vehicles, ships, and airplanes or electrical energy, for example, oil-fired power plants. Hydrocarbon oil is a feedstock/precursor for many industrial applications, for example, plastic, leather, fabrics, lubricates, pesticides, fertilisers, vehicles tires, cosmetics, and medicine (Burcik, 1957). Oil explorations are a process by which hydrocarbons are found beneath the earth's surface and extracted for use in various industries.

Naturally, oil is found beneath the earth, oceans and seas in the source rock. Geologists and geophysicist researchers use reflection seismology surveys to search for geological structures that might form hydrocarbon reservoirs. The typical method involves setting off an explosion underneath the ground near the possible site and observing the seismic reaction. This will provide geological structure information (Burcik, 1957). However, geophysical seismic process waves can be used as a "passive" method to extract information. Other examples such as gravimeters and magnetometers are also used in the search for hydrocarbons. The main principle of oil extraction starts with drilling wells into subterranean reservoirs. The geologist, who is known as a mud logger will note the oil presence from a tapped well.

Mud logger is a computerized unit connected to surface and subsurface sensors. Geologist mud loggers collect and analyse drilling cuttings and work on gas percentage from shale shakers in order to define the rock lithology and hydrocarbon presence (Burcik, 1957).

1.3 Petroleum reservoir fluids classifications

Hydrocarbon reservoirs (petroleum) contain one or more of the three fluids phases: oil, gas, or water (brine). The preliminary distribution of fluid phases depends on pressure, temperature, historical migration, reservoir heterogeneity (the various reservoir rock properties), type of geological trap, and depth (Ahmed, 2018). Typically, there are five mains different reservoir fluids:

1.3.1 Reservoir water

The water found in a reservoir is mostly brine (saltwater). The salt present in the brine is primarily sodium chloride (NaCl) in concentrations ranging from 10 to 350 ppt

(seawater has about 35 ppt salt). Other compounds found in brine contain sulphate, SO_4, magnesium, Mg, bromide, Br, bicarbonate, HCO_3, iodide, I, and calcium, Ca. With increasing salinity (0.075 per 100 ppt), the brine specific gravity is increased (Ahmed, 2018).

1.3.2 Black oil

Black oils consist of a range of components such as heavy, large, and non-volatile petroleum. Figure 1.3. shows the phase diagram of the pressure/temperature variations for a black reservoir oil. At a constant temperature, the reservoir pressure has been declined, vertically illustrated in points (1, 2, and 3).

The temperature and pressure at the surface of a separator are also highlighted in the diagram. At point 1, the initial pressure is much greater than the bubble point pressure. The bubble point pressure is the pressure at which the first bubble of gas in the oil is released, the point is indicated on the diagram as point 2. Between points 1 and 2, the pressure is above the bubble point pressure, this point is called the undersaturated reservoir point. The undersaturated reservoir point is the point that indicates that the oil is not fully saturated with gas, and is able to absorb more gas. However, the saturated reservoir state occurs at below point 2. At the saturated reservoir, state gas starts to evolve out of the oil into the hydrocarbon reservoir. This means, the oil is not able to absorb more gas, even if more gases are presented. At point 3, the pressure decreases further, and more gas is released from oil into the reservoir. At this stage, the pressure inside the reservoir is not able to push the fluids out to the surface. For the black oil reservoir, more black oil is produced at the

surface. Black oil is classified depending on the components present, such as light or heavy oil (Ahmed, 2018).

1.3.3 Volatile oil

Figure 1.4. shows a phase diagram of the pressure/temperature dependence of a volatile oil reservoir. From the figure, it is clear that there are differences between black and volatile oil diagrams. They both have a similar starting point, however, the volatile oil reservoir starting pressure is much closer to the bubble point as it contains more lighter hydrocarbon materials. Further, points 1 and 2 are closer to each other meaning a small decrease in pressure below the bubble point pressure causes a large amount to be released from the oil. The volatile reservoir has gas released from the oil. So, less liquids (oil) recovery is signposted in Figure 1.4. Another difference is the oil recovered from a volatile reservoir is lighter than that from a black oil reservoir for similar reasons (Ahmed, 2018).

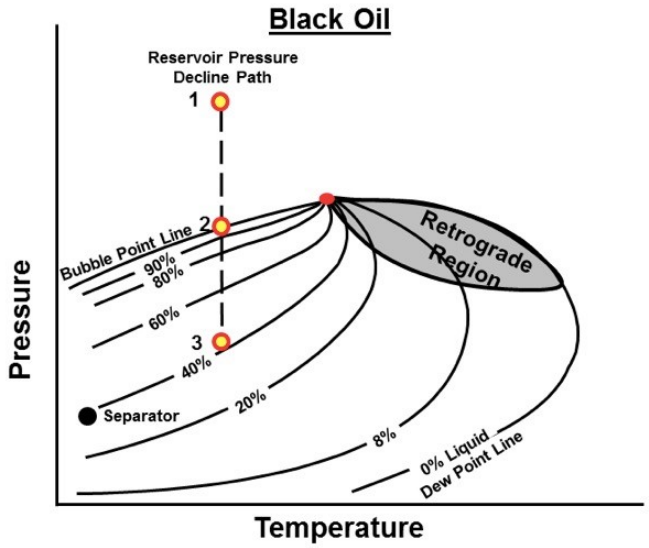

FIGURE 1.3: A typical pressure-temperature diagram for a black oil, showing the dependence between the pressure, temperature and composition of recovered oil. Adopted from (Ahmed, 2018) (Copyright: Gulf Professional Publishing, 2018).

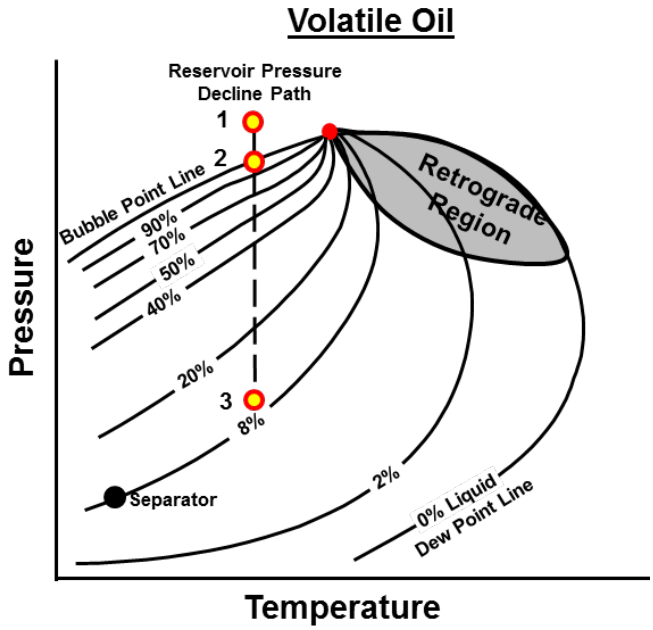

FIGURE 1.4: A typical pressure-temperature diagram for a volatile oil, showing the dependence between the pressure, temperature and composition of recovered oil. Adopted from (Ahmed, 2018) (Copyright: Gulf Professional Publishing, 2018).

1.3.4 Gas condensate

Figure 1.5. shows the phase diagram for the pressure/temperature dependence of a gas condensate reservoir. This type of reservoir is identified through its temperature. The reservoir temperature reduces between the cricondentherm and critical point temperature. As pressure decreases, the heavier hydrocarbons drop out as a liquid, this point is called the dew point. The liquid from this reservoir is less mobile as it is more bonded to the pore space near the wellbore. These reservoirs produce less gas as it is formed into liquid and the liquid is partially black (Ahmed, 2018).

1.3.4.1 Wet gas

Figure 1.5. b shows a phase diagram of the pressure/temperature dependence of a wet gas reservoir. A wet gas reservoir has a temperature dependence similar to a gas condensate reservoir, but its temperature is above the cricondentherm point. As the

pressure drops, the reservoir enters into the two-phase region. This means only gas will release into the reservoir without any liquid, but the liquid will fall from at the surface (separator conditions) hence, why it is called a “wet gas”.

1.3.4.2 Dry gas

Figure 1.5. c shows a phase diagram of the pressure/temperature of a dry gas reservoir. The phase diagram of the dry gas is condensed and short, it is primarily pure methane. As the reservoir is depleted, the pressure decline path never enters into the region of the two phases. Furthermore, the temperature and pressure at surface conditions drops outside of that region, meaning only gas is released at the reservoir and the surface

(separator).

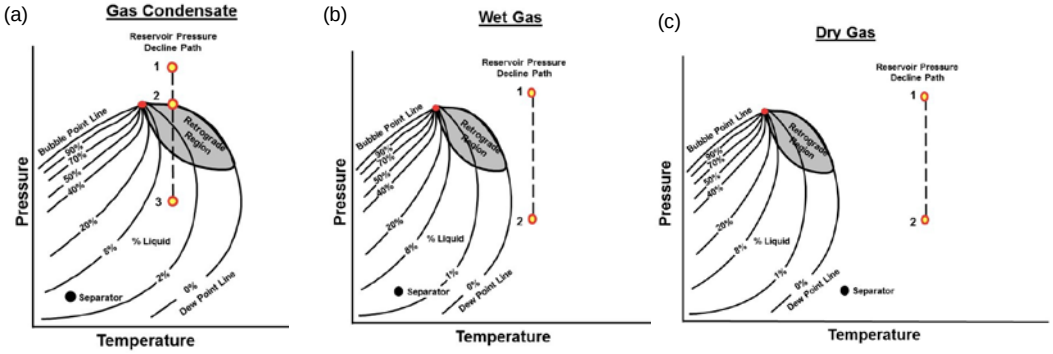

FIGURE 1.5: A typical pressure-temperature diagram for a gas condensate, showing the dependence between the pressure, temperature and composition of gas (a): gas condensate, (b): wet gas, and (c): dry gas. Adopted from (Ahmed, 2018) (Copyright: Gulf Professional Publishing, 2018).

1.4 Reservoir rock

As mentioned in section (1.2. oil), oil is naturally found in beneath the earth’s surface in source rock (reservoir rock). As a result of chemical reactions, environmental

changes and mechanical activities, the oil will migrate from source rock to reservoir rock, which is where we found it now. Figure 1.6. illustrates the migration of the oil, from the source rock to the reservoir. Most source rocks are black shale rock, Figure 1.7. shows an image for an ordinary shell resource rock (a), and a map of the countries with large oil shell resources (b). The same figure also demonstrates that the United States has the largest oil recourse, followed by China.

An oil reservoir with a reasonable commercial hydrocarbon flow can be formed where there is a porous and permeable medium saturated with adequate hydrocarbon. The reservoir rocks should be covered with cap rocks which are an impermeable formation to avoid hydraulic leaking of oil to the surface. Sections (1.6.1., and 1.6.3.) discuss these in more details. Porosity and permeability are the main physical attributes which describe the geometric properties of the rocks. These properties are the consequence of the rock's structure, composition behaviour, and lithological. The oil storage and how easily it can be extracted from reservoir rock is related to the different rock types and their properties. The following sections focus on reservoir rock types. Since practically all petroleum (hydrocarbon oil) occurs in sedimentary rocks, Sedimentary Geology forms one of the main foundations of petroleum geology. These sedimentary rocks are made of carbonates mud, dolomite, and sandstones (arksosic or quartz sand) (Burcik, 1957).

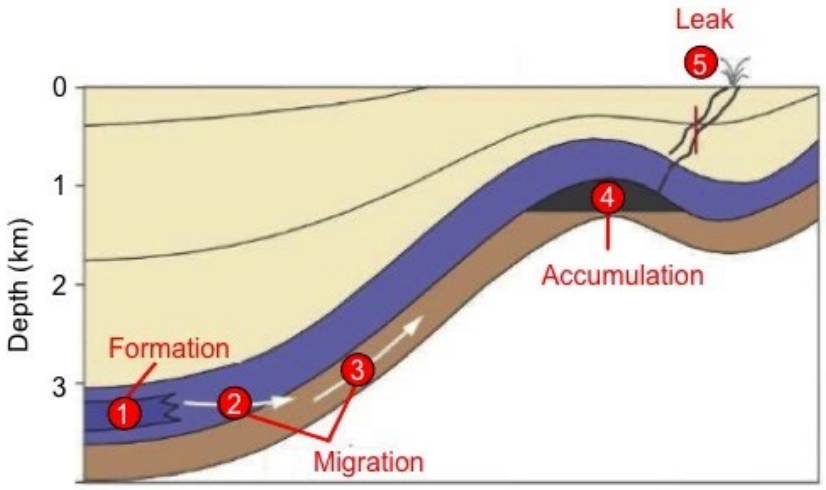

FIGURE 1.6: Formation of petroleum in the source rock (1), primary migration (2), secondary migration (3), accumulation in a hydrocarbon trap (4) and natural oil leak in consequence of the fracturing cap rocks (5), schematic adapted from references (Bjorlykke, 2010) (Copyright: Springer 2010).

(a) (b)

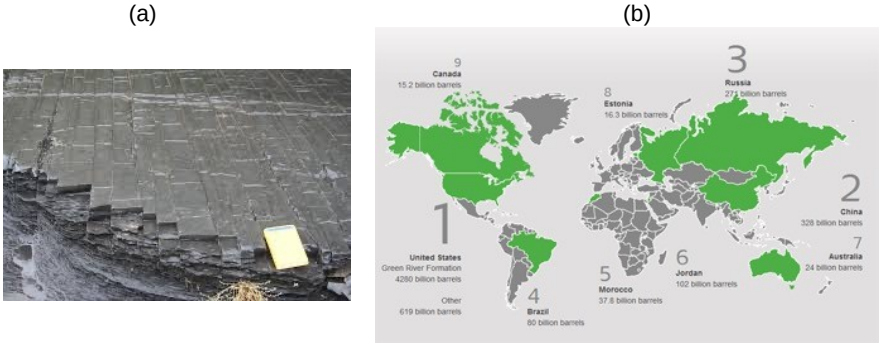

FIGURE 1.7: A photograph of the shale rock (a), and a geographical map that represent the countries with the largest oil shale resources (b) (Link, 2020).

1.4.1 Sandstone reservoir rocks

Any rock that has a grain size between 62 μm and 2 mm, is referred to as “sand”. An ideal sandstone is composed mostly of silica cement or quartz with equal-sized grains of sand and with minimal fragmented particles. The sandstone rocks are normally (25 m) thick. As explained in section 1.4 (Reservoir rock), the performance of the

sandstone rocks as a reservoir is dependent on a combination of its permeability and porosity arising from which type of sand dominates its composition (Bjorlykke, 2010).

1.4.2 Carbonate reservoir rocks

The two key differences between carbonate and sandstone reservoir rocks are:

1. The site of the sediment production, autochthonous for carbonate is defer than the autochthonous for sandstone.

2. The chemical reactivity is higher in Carbonate reservoirs and are more chemically reactive than sandstone reservoirs.

The second point presented as the difference has a large significance in the diagenesis (the physical and chemical changes) for a reservoir that occur during sedimentation, and overall reservoir quality (Peng and Zhang, 2007). As such, 60% of oil comes from sandstone reservoirs and 40% from carbonate reservoirs. As it is the more prevalent source of oil sandstone reservoir rocks were selected for this study.

1.5 Oil extraction and recovery stages

There are three stages for oil extractions and recovery, through following sections give a concise summary of each stage. The first part of oil extraction is known as an ‘oil well’. This is built by drilling a long hole underground from the well to the surface with an ‘oil rig’. A steel pipe is inserted into the hole to keep the wells structural integrity for the next drilling of the well bore, (this step is known as ‘casing’). To enable oil to pass thought the well bore holes are made in the well. Final step is called a ‘Christmas tree’ which is based on the collection of valves that are fitted to the top of the well. These valves control the pressure and fluids flow. In the oil industry,

drilling processes are known as a upstream, mid-stream, and downstream (Archer and Wall, 2012). Figure 1.8. illustrates the flowchart for the three stages of oil recovery to enhanced oil recovery.

1.5.1 Primary recovery stage

The recovery factor in this stage is usually between 5 to 15%. During the first recovery stage, hydrocarbon reservoir drive occurs from natural mechanisms. These mechanisms consist of: water displacing the descending oil into the well, underground pressure, expansion of the connected gas, which is initially disbanded in the crude oil, expansion of the connected petroleum gas at the upper of the reservoir, and the gravity drainage as a consequential of oil movement within the hydrocarbon reservoir from top to bottom parts of surface where the oil wells are located (Archer and Wall, 2012).

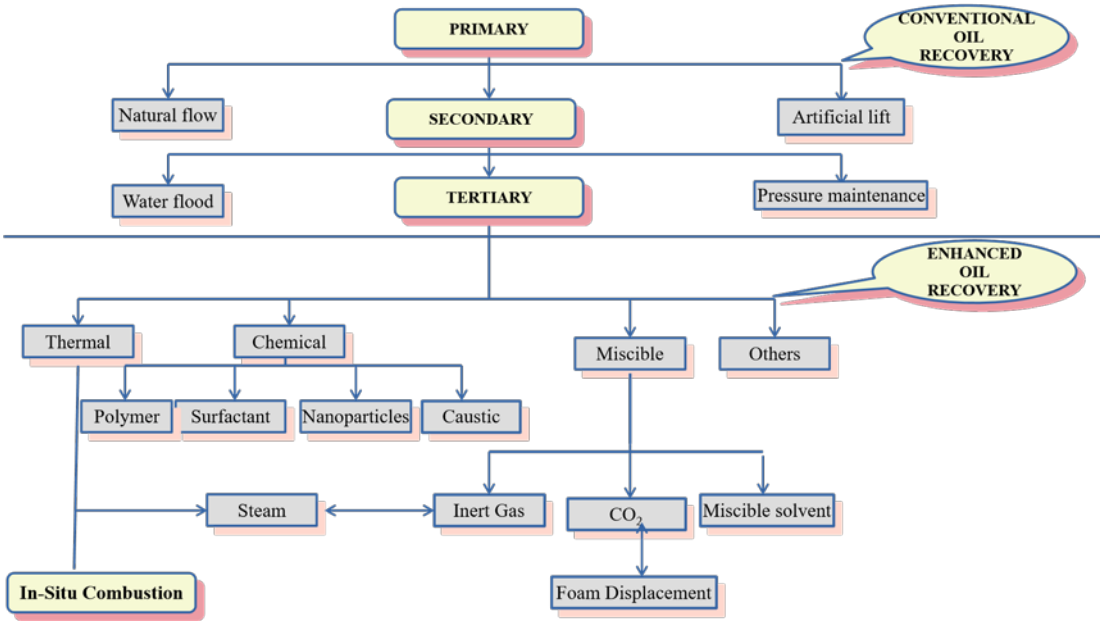

FIGURE 1.8: Flowchart to illustrate the classification for oil extraction recovery stages.

1.5.2 Secondary recovery stage

The oil recovery after primary and secondary operations is between 35 to 45%. As mentioned in the previous section, there is insufficiency pressure naturally occurring underground to force all the oil on the surface. Over the life cycle of the oil well, the natural pressure of the well gradually decreases, and secondary recovery processes are applied. These methods are carried out by injecting the well with fluids or gases that increase the reservoir pressure by applying external power (energy). Consequently, increasing or swapping it naturally hydrocarbon reservoir pressure with an artificial drive. Examples of secondary systems are gas re-injection, gas lift and water injection. For the first two methods (gas re-injection and gas lift), each use associated carbon dioxide (CO_2), gas or a different inert gas is injected to decrease oil-gas mixture density which leads to the improvement of oil mobility. The recovery factor depends on characteristics of the reservoir rock and oil properties, for example, the typical recovery from water injection 'water flooding' is approximately 30% (Archer and Wall, 2012).

1.5.3 Tertiary recovery or (enhance recovery) stage

Enhanced recovery begins when the secondary stage is not sufficient to continue satisfactory oil extraction, but the remaining oil is still of value. This relies on crude oil's current price and the cost of the recovery extraction methods. When the price is low, the extraction is curtailed, and when it is high, the unbeneficial wells are brought back into use. Tertiary recovery methods enable an increase in oil recovery to more than 15% of the remaining oil (Ehtesabi et al., 2014). This stage focuses on increasing the oil mobility ratio in order to increase oil recovery.

One of the techniques used is a 'Thermal enhanced oil recovery (TEOR)'. TEOR works by heating the oil which will decrease its viscosity making it easier to extract. For example, steam injection for TEOR is often used in a cogeneration plant, such as a gas turbine used to generate electricity. The associated heat from the electricity production is used to generate steam, which is fed into the reservoir for TEOR. San Joaquin Valley has a heavy oil as such TEOR is used to inject heat steam in order to increase oil extraction (Nazari Moghaddam et al., 2015). This accounts for 10% of the United State oil extraction. Another example of the TEOR method is fire flooding (In situ burning), in which some oil is burned to generate steam that will heat nearby oil.

Another tertiary technique is a chemical injection (which is the focus of this thesis). The chemical injection uses surfactants, polymers, and nanoparticles (individually or in combination) to alter the surface tension between interfaces (liquid-liquid, liquidsolid, or both) in the reservoir. This works to mobilise oil that would otherwise remain in the reservoir (residual oil). Another form of chemical injection uses carbon dioxide (CO_2) which is injected into the reservoir to reduce oil viscosity aiding in oil recovery.

In addition, microbial treatments are used as a tertiary treatment method. A special blend of the microbes is utilized to treat and break down the hydrocarbon chain in oil thus decreasing the viscosity making oil easier to extract. This method is more economical than other conventional methods (Archer and Wall, 2012).

Overall, the amount of oil recovery is determined by different factors, such as porosity and permeability of the reservoir rocks, interfacial tension, wettability and oil viscosity. Each of these factors is discussed individually in the following sub-sections.

1.6 Fundamental properties of porous medium

A porous medium is defined as a solid that contains an empty space (pores). These pores can be connected or unconnected which is distributed inside the pores, in either a uniform or random way. The pores may contain a mixture of phases, for example: a mixture of oil, water, or gas. The pores network is connected as such able to act as able to carry fluids (Heinemann and Mittermeir, 2013). Only these factors and porous media are discussed in this chapter. Porous Media can be named in various examples such as in a Petroleum Engineering is named as a reservoir rock and stores natural gas and crude oil.

1.6.1 Porosity

Two groups can be classified of porous media: fractured and intergranular-intergranular. Porous media might consist of one or both types of porosity groups, however, if they have both, intergranular-intergranular and fractured, they are called 'double' porous media. On the other hand, regarding to the mechanical properties related to porosity can be distinguished between consolidated and unconsolidated porous media. The particles 'grains' in a consolidated porous media are held together via a cementing substrate. Meanwhile, the grains are loose in an unconsolidated media. Porosity can be defined as the ratio of the pores volume to the total volume of the porous media, equation 1.1 is the mathematical expression of the total volume.

$$V_T = V_P + V_S \tag{1.1}$$

where: V_p and V_s are the pore and solid materials volume, respectively, and V_T is the total volume. Using equation 1.1 the porosity of a materials can be expressed as, equation 1.2 below:

$$f = \frac{V_P}{V_T} = \frac{V_T}{V_T} - \frac{V_S}{V_T} \quad (1.2)$$

where: *f* refer to porosity. Porosity can be classified into two types, total porosity and effective porosity. Total porosity is described as all of the material volume taken up by empty space. However, effective porosity is the most connected pores that can be utilised in fluid transport. As such, effective porosity is the most important parameter for any reservoir, as it gives information related to storage capacity of reservoir porous media and holds the reservoir fluids. Figure 1.9. show the schematic diagram of total and grain volume of the porous media.

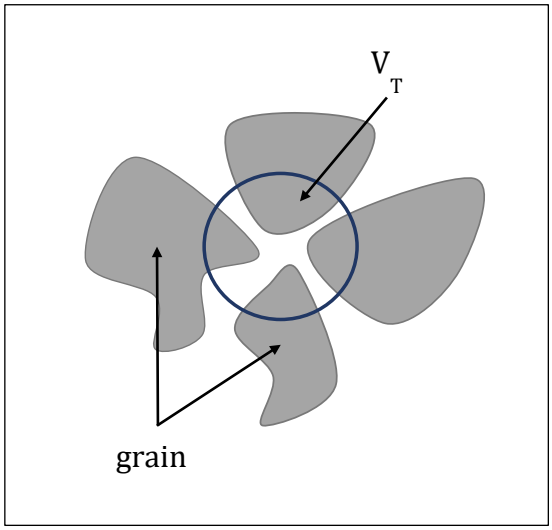

FIGURE 1.9: Schematic showing the total volume V_T and grain for the porous medium.

1.6.2 Capillary pressure properties

The following sections discuss the parameters that have a relationship with capillary pressure.

1.6.2.1 Saturation S_i

Porous space can include several phases. Saturation phase can be defined as a ratio of the volume of a phase to the effective pore volume of the porous medium, as illustrated in equation 1.3.

$$S_i = \left[\frac{Volume of the phase^i}{\text{Effective pore volume}}\right] \text{of the porous media} \quad (1.3)$$

where is the summation of the phases saturation, is result in $\hat{A}_i S_i = 1$, i refer to phase name.

1.6.2.2 Wettability

The wettability of a reservoir rock fluid system can be defined as the ability of one fluid to spread on the surface of the rock in the presence of another fluid. It plays an essential role in oil production, as it establishes the distribution of the initial fluid and the main flow processes in reservoir rocks. Water Contact Angle (WCA) is used to measure the wetting degree of solids via liquids (water or oil). It measures the contact angle of the liquid-liquid, or liquid-solid interface makes with the substrate, and it has different shapes depending on the surface. Figure 1.10. illustrates the comparison of a wetting droplet (water) and non-wetting droplet (mercury) on a glass surface. A contact angle of more than 90 represents a non-wetting surface. If the contact angle is less than 90 , it represents a wetting substrate.

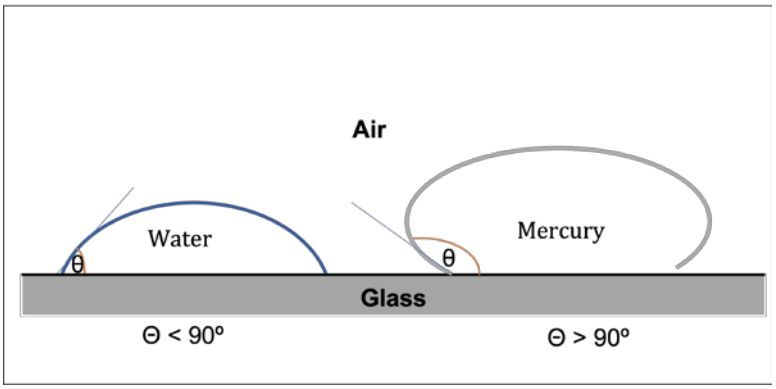

FIGURE 1.10: The comparison of a wetting droplet (water) and non-wetting droplet (mercury) on a glass surface.

As mentioned earlier in section (1.6.), reservoir rocks can be classified by wettability and it depends on several factors such as: pore geometry, reservoir rock materials, geological mechanisms, reservoir pressure and temperature, composition and quantity of brine and oil and variation in pressure, saturation and composition during production.

In oil reservoirs, it is vital to determine the particular rocks and fluids properties in order to regulate whether water or oil-wet the reservoirs. Rocks that are neither oil preferentially wet by oil nor water are called intermediate or neutral wet (Law and Zhao, 2016). Table 1.1 gives a list of reservoir wettability types based on water contact angle measurement.

TABLE 1.1: Reservoir wettability type for reservoirs in either sandstone or carbonate rock. Table is reproduced from (Treiber and Owens, 1972).

		Sandstone	Carbonate	Total
Water wet	0 - 75	13	2	15
Intermediate wet	75 – 105	2	1	3

Wettability	Contact angle ( )	Number of Reservoir	Investigated
Oil wet	105 - 180	15	22	37

Reservoir rock wettability can be measured from different methods, which are considered in the following sections. Water contact angle is used in this thesis to study the wettability of the liquid-liquid interface.

Wettability measurements

Measurement of wettability in the laboratory depends on the reservoir core handling. To achieve illustrative information on the wetting partialities in the porous media from the laboratory experiments, the following conditions should be accomplished:

- Substrate properties of the reservoir rock should be conserved.
- Technique should allow differentiation of the complete wettability range.
- Consequence should not be contingent on fluid viscosity and rock permeability.
- Outcome should be reproducible.

In core analysis, three different terms are used to describe the state of the core sample, native state, cleaned state and restored state. The native state represents a core status that is analysed directly after cutting, before any treatment methods are applied. The cleaned state represents a core after being cleaned by different methods, as all original and penetrated fluids are removed. After the cleaning

process, reservoir cores are strongly water wet. These cores have been used for porosity and gas permeability measurements, since the wettability does not affect the result. The restored state core is cleaned from all original, penetrated fluids, and then saturated with specific brine conditions, followed by oil injection. At the end, the core is kept at reservoir temperature for certain hours. The non-wetting surface and wetting fluid on the mineral surface are demonstrated in Figure 1.11. It shows SEM image of two surfaces (non-wetting-left) and (wetting-right). It is clear that the non-wetting surface has topography roughness (which like the Lotus plant) that prevents water droplets from spreading onto the surface, and vis-versa with the wetting surface (smooth surface)(Heinemann and Mittermeir, 2013).

The following sections will describe some of the techniques used to measure wettability in the laboratory:

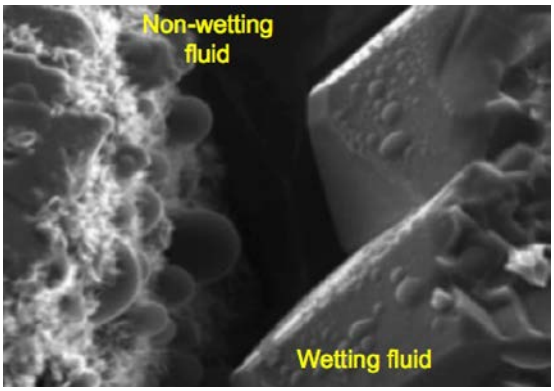

FIGURE 1.11: SEM image of the mineral surface shows the topography of the surface: (left) non – wetting surface, and (right) the wetting fluid on the surfaces. Adopted from (Heinemann and Mittermeir, 2013) (Copyright: PHDG Association, 2013).

1. Contact angle measurement

The contact angle measurement is illustrated in Figure 1.12, Young (Ahmed, 2018) defined the liquid contact angle as a result of the static equilibrium

between a liquid droplet and solid substrate. The shape of the liquid droplet depends on the interaction with the surface. These interactions result from the interfacial tension between liquid 1 and 2 (s_{12}), and between solid (substrate) and liquids (s_{S1} and s_{S2}).

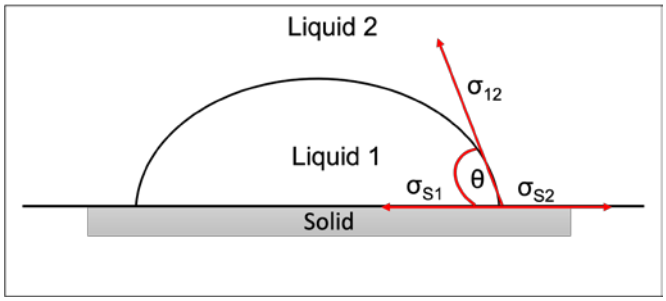

FIGURE 1.12: Drawing illustrates the Young definition for contact angle. Where s_{S1}, s_{S2}, and s_{12} are refer to interfacial tension between solid and liquid 1, solid and liquid 2, and liquid 1, and 2, respectively. They defined in equation 1.4

From Figure 1.8, following equations can be defined:

$$q = \frac{s_2 s_{S1} s}{s_{12}} \tag{1.4}$$

$$s_{S1}+s_{12}\cos q = s_{S2} \tag{1.5}$$

where q is the contact angle between two interfaces, s_{S1},and s_{S2} refer to interfacial tension between water droplet and substrate at liquid1-solid, liquid2-solid interface, respectively. s_{12} represent the interfacial tension between two liquids.

2. Amott method

The Amott method combines force displacement and imbibition to measure average core wettability. Both, the fluids and reservoir core can be measured using this method. In the Amott method, the chosen core sample is saturated with oil. The saturated oil core will be placed in an imbibition cell holder surrounded by water. The water is enabled to imbibe into the reservoir core

sample, replacing testing oil in the core sample till the equilibrium is reached. Water imbibed volume is measured subsequently after 20 hours. Subsequently, the reservoir core sample is taken out of the water and the residual oil is forced down to remain the saturation on displacement of water. Thus, can be done using centrifuging under the brine. Finally, oil displaced volume is measured directly by weighting the rock (Treiber and Owens, 1972).

The second part of the Amott method is to repeat the same procedure but using oil instead of water. Figure 1.13. shows the schematic of the Amott method, which is adapted from reference (Torsæter and Abtahi, 2003). The Amott method is fully described in (Hendraningrat, Li, and Torsæter, 2013a).

3. USBM (U.S.Bureau of Mines) wettability index

   The USBM method is a trial developed by (Anderson, 1986). It is dependent on measuring two capillary pressure curves. In this method, oil is displaced by brine until saturated by brine and the result is calculated from the remaining oil saturation. The displacement of oil in the converse direction is then measured. The last two methods (Amott and USBM (Donaldson, Thomas, and Lorenz, 1969)) are outside of this project area and as such contact angle is the only method used in this study. Table 1.2. shows a relationship between wettability measurements based on the three methods.

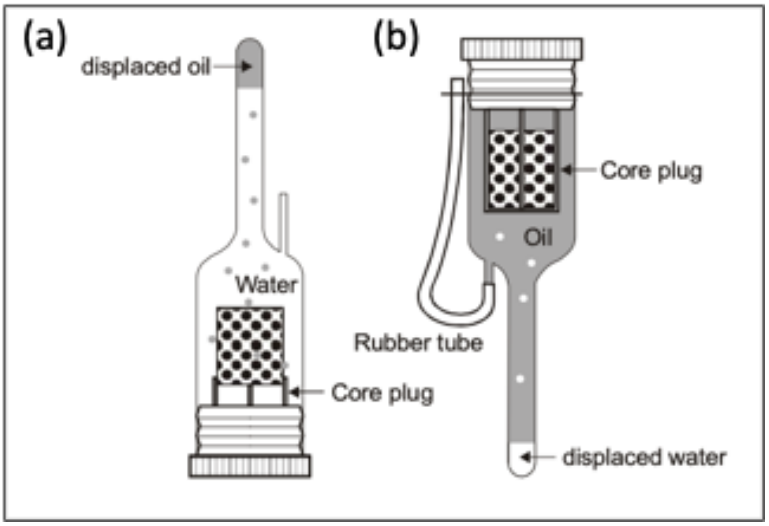

FIGURE 1.13: A schematic of (a) the imbibition Amott method cell among core oil saturated sample surrounding by water, (b) core water saturated sample by oil. Adopted from (Torsæter and Abtahi, 2003) (Copyright: Norwegian University of Science and Technology 2003).

TABLE 1.2: Wettability indexes defined by contact angle, USBM, and Amott methods. This table reproduced from (Donaldson, Thomas, and Lorenz, 1969).

Wettability Method	Water wet	Neutrally Wet	Oil wet
Contact Angle			
Minimum	0	60 to 75	105 to 120
Maximum	60 to 75	105 to 120	180
USBM wettability index	value ⇠ 1	value ⇠ 0	value ⇠ -1
Amott wettability indea			
Displacement-by-water-ratio	Positive	Zero	Zero
Displacement-by-oil-ratio	Zero	Zero	Positive
Amott-Harvery Wettability index	0.3 ? I ? 1.0	– (0.3 < I < 0.3)	–(1.0 ? I ? –0.3)

1.6.3 Permeability

It is important to characterise filtration and mass flow of the substrate because it represents the amount of oil that can be extracted from the reservoir. In the event of mass flow, all field particles are in motion. However, in the event of filtration, only a

portion of the mass particles are flowing, while the residual particles from the flooded framework. The first experiment for permeability was made by Dupuit in 1854 in London using urban water filters (Brown, 2004). He noticed the filtration velocity had been 5 m^3/m^2 per day. He realized that the drop in pressure initiated by the filter was related to the filtration velocity. In 1856, the hypothesis of Henry Darcy was proved using illustrated equipment in Figure 1.14 (Freeze, 1994). Different sand gravel packs have been used for investigations. He found that the following equation represents the motion of the flow through the sand filter.

$$Q = K \frac{S}{L} h \tag{1.6}$$

where is k represent the permeability coefficient, S and L are the cross section and length of the packing, respectively, and h is the difference in piezometric head.

However, the first definition for permeability in world oil congress was in 1933 by Fancher, Lewis and Barnes (Fancher, Lewis, and Barnes, 1933). In addition, Wyckoff, Botest, Muskat and Reed have suggested Darcy as a unit for permeability (Wyckoff et al., 1933). From that time, Darcy's Law is defined by the equation below.

$$q = A. \frac{K \, DP}{\mu \, L} (1.7)$$

where: q is instantaneous flow rate, A is the cross-section of the porous medium perpendicular to the direction of flow, K is the permeability as a material property of the porous medium, L is the length of the porous media in direction of flow, DP is the pressure difference along the porous medium μ is the viscosity of the flowing fluid.

However, the *Darcy's* Law has a limitation, it is only usable for a steady state and laminar on phase within a porous media. Likewise, the fluids have to be mainly incompressible. Figure 1.14. illustrated the schematic of the DARCY's experiment.

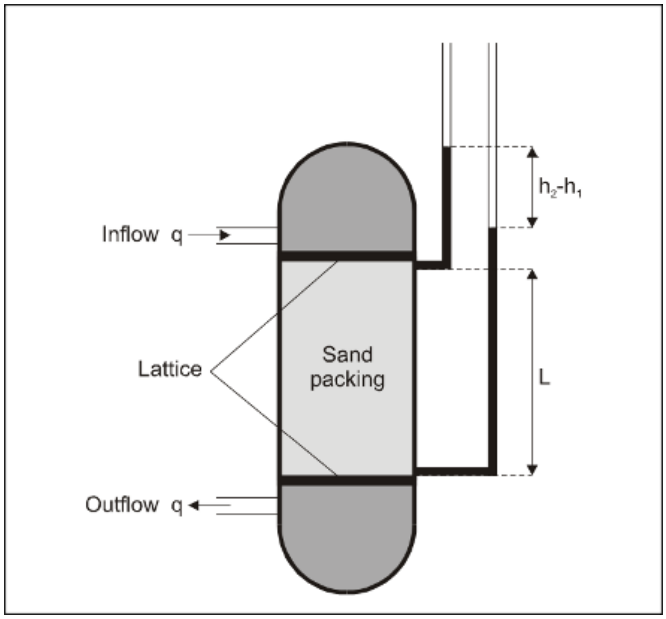

FIGURE 1.14: A schematic diagram shows the DARCY's experiment. Adopted from (Burcik, 1957) (Copyright: Springer, 1957)..

1.6.3.1 Permeability measurement methods

The permeability measured in the laboratory depends on the core size, fluid properties, consolidation of the medium, and applied pressure. Consolidation media samples can be cut as regular geometrical shape, like a cylinder (which this project used) in a different length, diameter, or as cube.

The permeability will be defined in the following section. (See definition in section 1.6.3.4.). Figure 1.15 shows a schematic flow diagram of the measuring permeability by air.

1.6.3.2 Relative permeability

The following sections discuss a historical background and a definitions of relative permeability:

1.6.3.3 Historical background on relative permeabilities

In 1933, *Funcher* and *Lewis* discovered the existence of gas, oil and water in a hydrocarbon reservoir. Later, in 1925, a patent was granted to *Nutting* who described how the surface forces between rock and oil might be modified for enhanced oil recovery.Later in the year 1927, experiments were conducted by *Uren* which simulated an oil with a gas drive using a tank filled with gas sand and gas saturated oil at lower pressure (several bards). The results indicate that the detached gas reduces permeability, and provides the energy needed for oil mobilization. (Uren and Fahmy, 1927).

In 1945, *Hassler* prepared experiments that contributed to the solution of the multiphase issues called Hassler core and was described earlier in Figure 1.15. The advantage of using a *Hassler core* holder as the sample holder is excellent scaling, fluids independency, various selection of core length, measurement of permeability in two directions and large pressure gradients. The experiment setup begins with testing the core while fully saturated with chosen oil derivates, which are then displaced by air. *Hassler* measured air permeability and determined the saturation through weigh measurement control of the reservoir core. Later, he observed that it is fundamental to establish permeability for a reservoir core with any saturation conditions. Hassler also discovered the retention of the wetting phase at the exit and this is called *end effect* (Hassler and Brunner, 1945).

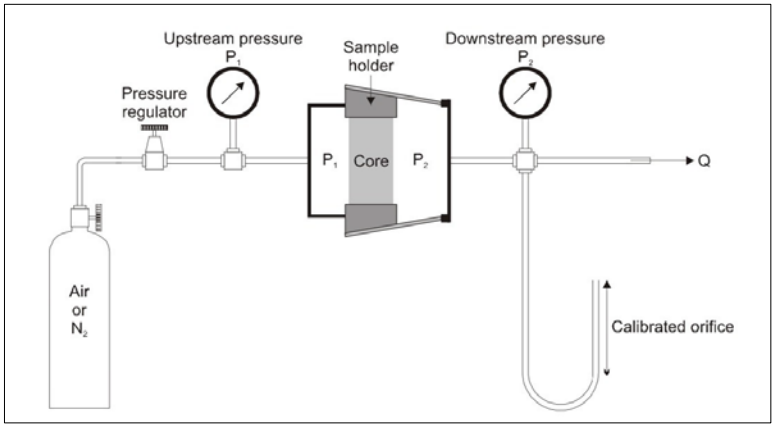

FIGURE 1.15: A schematic of a Hassler core. This equipment is used to measure the air permeability of a core sample. Adopted from (Monicard, 1980) (Copyright: Technip 1980).

In the same year, *Wyckoff* and *Botset* (Wyckoff et al., 1933)published research using carbon dioxide and brine. Brine was used to ensure the electrical conductivity for measurements. They measured the pressure at (10 equidistant points) determining the wetting K_w and non-wetting K_{nw} permeability phases as a function of saturation. They used the gas-oil ratio to determine the variation of the saturation and viscosity of the samples at steady state flow. *Wyckoff* and *Botset* made the statement that at a given gas-oil ratio, the saturation may be independent of the absolute permeability (Wyckoff et al., 1933).

1.6.3.4 Definition of relative permeability

As described in the historical review, all works were done to extend the Darcy Law validation to multi-phase filtration, and the following equations can be set up:

$$q_w = A\left[\frac{k_{rw}}{\mu_w}\right]\left[\frac{Kk}{L}\right]\Delta P \quad (1.8)$$

$$q_w = A\left[\frac{\frac{Kk}{\mu}}{\mu_{nw}}\right]\left[\frac{k_{rnw}}{L}\right]\Delta P \quad (1.9)$$

where K_{rw} and K_{rnw} are referring to the relative permeability of the wetting and nonwetting phase, respectively. A is the cross-section of the porous medium perpendicular to the direction of flow, K is the permeability as a material property of the porous medium, L is the length of the porous media in direction of flow, Dp is the pressure difference along the porous medium μ is the viscosity of the flowing fluid. Equation 1.10. illustrates the effective permeability (K_{rw}) for the wetting phase and equation

1.11. K_{rnw} for the non-wetting phase (Ebeltoft et al., 1998).

$$K_{rw}(S_w) = k_{rw}K(\underline{S_w}); q \quad K_w(S_w) \quad 1 \quad (1.10)$$

$$K_{rnw}(S_w) = k_{rnw}K(\underline{s_w}); q \quad K_{nw}(S_w) \quad 1 \quad (1.11)$$

where k is the air permeability, S is saturation, S_w is water saturation.

1.6.3.5 Definitions of End-Point saturations

At a given saturation, the relative permeability is zero, and for displacing saturation phases are called critical gas saturation and critical water saturation (S_{gc}) and (S_{wc}), respectively. For the displaced phase the minimum saturation is residual saturation: for oil displaced by gas (S_{org}) or displaced by water (S_{orw}) for gas (S_{gr}) and for water

(S_{wr}). S_{org}, S_{orw}, S_{gr}, and S_{wr} are the saturations which can be achieved in laboratory which is under reservoir conditions when left for enough time to equilibrate. At the maximum saturation reservoir phase, the pore volume which is occupied by water is irreducible water saturation (S_{wir}), and it is an equilibrium state. In water-wet reservoir rock surface, it represents adsorbing the water coating layer and the water that contacts around grains and at pore openings. S_{wir} differs from critical water saturation, and from remaining water saturation that measured by core analyses.

In conclusion, relative permeability can be measure by three methods:

- The Hassler method.
- The welge method (wherein at constant rate, two fluids are injected simultaneously).
- or PENN STATE method (which uses the calculation result from the displacement experiments).

1.6.3.6 Relative permeability theory

The concept of relative permeability is used to establish relationships between saturation and the conductivity of two or more phases, flowing in a porous media. Although, the Darcy equation was never meant to apply to multiphase flow. It has been extended to quantify relative permeability. This is done by assuming that the absolute permeability used in Darcy's equation may be replaced by a term that contains the absolute permeability and the relative permeability, as a function of the fluid saturation. The following equations are for two phases systems (a and b are referred to as two different fluids) are:

$$u_a = \frac{a \quad ra}{\mu_a} D P_a \quad r_a g) \qquad (1.12)$$

and

$$u_b = \frac{K_a K_{rb}}{K K} D P_b \quad r_b g) \qquad (1.13)$$

$$\mu_a$$

where: u_a and u_b are flow velocity for fluid a and b, respectively, μ_a and μ_b are the dynamic viscosity for each fluid, K_a is the absolute permeability (full definition in paragraph below), K_{ra} and K_{rb} are the relative permeability that refer to each fluid, DP_a and DP_b are pressure gradient, r_a and r_b are fluid density, and g is the gravitational acceleration constant. The subscript r refers to relative.

Relative permeability is an important factor to characterize the displacement of the hydrocarbons by water as well as in the displacement of oil by gas or water. It can be measured from: laboratory studies on core samples, calculated from production data, extracted from in situ flow tests, or derived from correlations.

These data are most useful in reservoir engineering evaluations and reservoir modelling (reservoir simulation). Relative permeability data are used to explain the primary, secondary, and tertiary recovery mechanisms (see section 1.5), and fluid displacements that occur during coring. In addition, these data are used to make engineering estimates of productivity, injectivity, and ultimate recovery for evaluation and planning of production operations. Furthermore, relative data can be

also used to diagnose formation damage problems, for example, water blocks. For the Darcy law to be valid for any system, three conditions must be satisfied:

1. The entire pore space of the porous media must be filled with a single-phase fluid, such as, the saturation must be equal to 100%. The extension of the Darcy's law assumes each phase will develop its own network to which a permeability can be assigned.

2. The fluid must be Newtonian, for example, viscosity is independent on flow rate.

3. The flow must be in the viscous or laminar region.

The permeability that is characteristic of the porous media at 100% single-phase fluid saturation is a constant known as the Specific or Absolute permeability, K_a. Reported differences in the permeability to different phases can be a result of the reaction with the porous media to one or more of the phases or intrinsic fluid properties. Sample size or sampling volume can also affect the absolute permeability results. The specific or absolute permeability is also referred to as a reference (Base) permeability. The Klingenberg corrected K_o, K_a @, S_{wi}, and K_w @ S_w = 100% are the most frequently used base permeabilities. Table 1.3 illustrates the type of the relative permeabilities for multi-fluids phase and their description.

Due to the fact that all hydrocarbon-bearing reservoirs contain some percentage of mobile or immobile water, it is necessary to extend specific permeability concepts to account for the flowing phase saturation. The presence of water on a rock surface will reduce the cross-sectional area available for oil to flow. The permeability of a particular porous media to oil, K_o, when S_o = 50% and S_w = 50% might be only 45% of the permeability measured when the same formation is at 100% S_o. At 40% S_w and

60% S_o, the K_o can be 70% compared to the permeability of the formation at 100% saturation S_o. The ratio of permeability at a specific saturation to the permeability at 100% saturation is known as the Relative Permeability, K_r. This means that when a formation contains two or more immiscible fluids, each fluid tends to interfere with the flow of the others. This decline in the ability of a fluid to flow through porous media which is termed a relative permeability effect (Kiani, Alexander, and Barron, 2021).

TABLE 1.3: List of the type of the relative permeabilities for multi-fluids phase and their description.

Permeabilities	Description
K_o at S_{wir}	K_{rw} and $K_{ro} – K_w/K_o$ relative permeability
	K_{rg} and $K_{ro} – K_g/K_o$ relative permeability
K_g at S_{wir}	K_{rw} and $K_{rg} – K_w/K_g$ relative permeability (imbibition)
K_w at S_w = 100%	K_{rg} and $K_{rw} – K_g/K_w$ relative permeability (drainage)

The effective permeability to a specific phase is the absolute permeability, K_a, multiplied by the relative permeability, K_r. The individual effective permeability of each phase, as well as their sum, is lower than the absolute permeability because of the mutual interference between fluids in the same pathways.

where:

$$K_o = K_a k_{ro} \tag{1.14}$$

$$K_g = K_a k_{rg} \tag{1.15}$$

$$Kw = Kakrw \tag{1.16}$$

$$\textit{RelativePermeabilityforanyof}\ \frac{K_{ro}}{}\ \textit{orK}_{rw} = \left(\frac{K}{K_{rg}}\right)\textit{Effectivepermeabilityfor}\ \frac{K_{ro}}{}\ \textit{orK}_{rw}\ (\textit{AbsolutePermeability}\ K_a) \quad (1.17)$$

Relative permeability is dimensionless and reported as a percentage or fraction. Generally, relative permeability varies from zero to one, when referenced to the proper absolute permeability. Data can be shifted to a new base such as K_{rw} at old base = K_w/K_{old} base and (K_{rw} at the old base to (K_{old} base/ K_{new} base) = K_{rw} at the new base.

Relative permeability has a first-order dependency on saturation level. Many interstitial fluid distributions are possible for each level of saturation, depending on the direction of the pore space geometry and saturation change of the formation.

The terminology used in capillary pressure curve evaluation also applies to relative permeability studies. Values of the saturation versus relative permeability obtained as the wetting phase saturation decreases are termed drainage. While as the increase in wetting phase saturation describes an imbibition displacement. The difference between the two displacements is known as hysteresis. The wetting phase normally occupies the smallest pores. While the non-wetting phases occupy larger pores.

Relative permeability pairs are ordered according to the increasing phases, such as K_o/K_w = water increasing, for a water-wet reservoir rock equal imbibition, and conversely, K_o/K_w oil increasing for a water-wet reservoir rock equal drainage.

Imbibition and drainage can be of the primary, secondary or tertiary EOR. The original oil displacement of a 100% water-saturated reservoir rock is primary drainage, as during the initial oil migration into a reservoir. Secondary drainage occurs during the drilling and completion process. As observed oil displaces non-reservoir fluids such as filtrate displacement (section 1.6.3.).

The type of relative permeability records needed to describe flow in hydrocarbonbearing reservoirs depends on the fluids present in reservoir and the natural or induced reservoir drive mechanism. Two-phase relative permeability measurements are adequate for most reservoir engineering purposes. Normally, data collected on at least two saturation pairs are sufficient to explain multiphase flow when more than two phases are present.

Various system measurements are used for relative permeability; however, this project is only focused on water-oil relative permeability, more details are in the following section.

1.6.3.7 Water oil relative permeability

Water and oil relative permeability is a water-oil system which are normally plotted as functions of water saturation; Figure 1.16. demonstrates the concept. The following points that are on the graph are worth explaining:

1. At S_{wir} (point A); The water relative permeability, K_{rw}, is zero and the oil relative permeability, K_{ro}, with respect to water is less than 1 indicating a reduction in the capability of oil to flow because of the appearance of water.

The effective permeability to oil with respect to water is less than the absolute permeability of the formation. At S_{wir}, the effective permeability to water is zero, only oil can flow. In a water displacing oil water wet system, previous to water encroachment (imbibition) by natural water drive or waterflood, interstitial water exists as a thin film on sand grains (Figure 1.17 a). The remainder of the pore space filled by oil and water has little effect on the flow of oil, K_{ro}, approaches 100%, and K_{rw} is zero.

2. At S_{wir} (Figure 1.16. point b); The relative permeability to oil, K_{ro}, is less than 1.
3. Recorded to the left of S_{wir} becomes portable via heating or additional conditions.
4. The relative permeability boundary point (aka equipotential flow point) is the point at which the relative permeability to both phases is identical, demonstrated in Figure 1.16. point c.
5. As water saturation, S_w, is increased, the water relative permeability, K_{rw}, increases, and the oil relative permeability, K_{ro} decreases with respect to water.

Water outflow results in water influx by small and large pores. Both of S_w and K_{rw} increase through imbibition and oil saturation S_o decline, as does oil relative permeability, K_{ro}. Water outflow might be from filtrate invasion, waterflood, natural water drive, or combination of all variables (Figure 1.17 b).

6. Point d: Notes where K_{rw} is at S_{or} (remaining or residual oil saturation).
7. Point e: Notes the point of maximum S_w or S_{or} end point (flood-out) for an oil reservoir. In an aquifer, water saturation is equal to 100%, and the consequent water relative permeability is 1. After water flood out, oil saturation residues are

trapped and disconnected oil drops. The water relative permeability reaches a maximum, however residues less than the specific permeability since oil saturation occupies pore centres obstructing water flow (Figure 1.17 c).

8. Both of phases have a residual saturation at which K_r to that phase is zero. K_r at 100% saturation of a specific phase is equal to 1.

9. The endpoints and shapes of the K_r curves are distinguishing of the wetting qualities of the two fluids, and the intrinsic rock properties, such as pore geometry.

10. Relative permeability curves can be fitted by semilog or arithmetic scales.
11. K_r characteristics are exceptional to each multiphase fluid reservoir rock system.

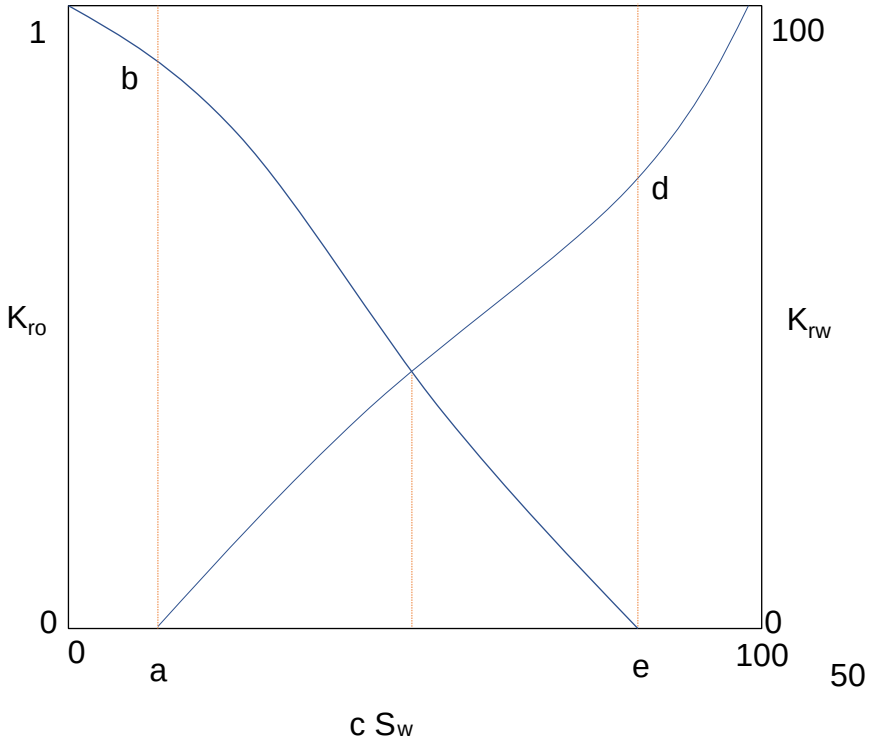

FIGURE 1.16: Diagrammatic plot shows a typical oil/water relative permeability relationship. Where K_{ro}, K_{rw}, and S_w are oil relative permeability, water relative permeability, and water saturation, respectively.

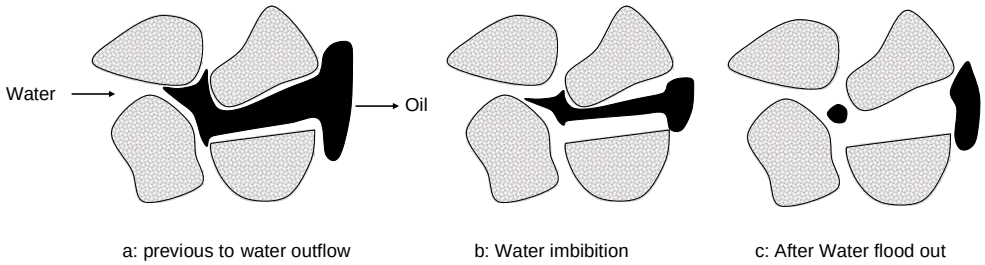

FIGURE 1.17: A schematic view demonstrating the oil displacing in a water wet system.

1.6.3.8 The Influence of reservoir parameters on relative permeability

The following point are the main factor the influence the relative permeabiity of reservoir:

1. Wettability

   Relative permeabilities represent the macroscopic fluid-fluid and rock-fluid interactions during multiphase fluid distribution within the porous media. This fluid distribution is governed by wettability of the porous media, pore geometry (structure) of the porous media, saturation history, ratio of the capillary to viscous or gravitational forces at the pore scale, and viscosity ratio.

2. Fluid wettability

   The wetting state or wettability of the porous media is the single most important factor that determines the character, shape, and the end point for relative permeability curves. Figure 1.18. illustrates the differences between oil-wet K_o and water wet K_w data collected on the same rock with two extreme wetting conditions. Figure 1.18. (a) is strongly water-wet and Figure 1.18. (b) is strongly oil-wet. The most obvious difference between the data sets is the location of the endpoints, initial and terminal conditions.

In the water-wet rock, water at low saturations tends to fill small pores and has relatively little effect on K_{ro}. Areas that would not contribute appreciably to flow because of capillary pressure constraints. The finite amount of wetting fluids could be water or oil. Thus, will be immobile in any system and only saturations above this amount are available for flow. To understand the mechanism behind this effect, the surface forces of the system must be considered.

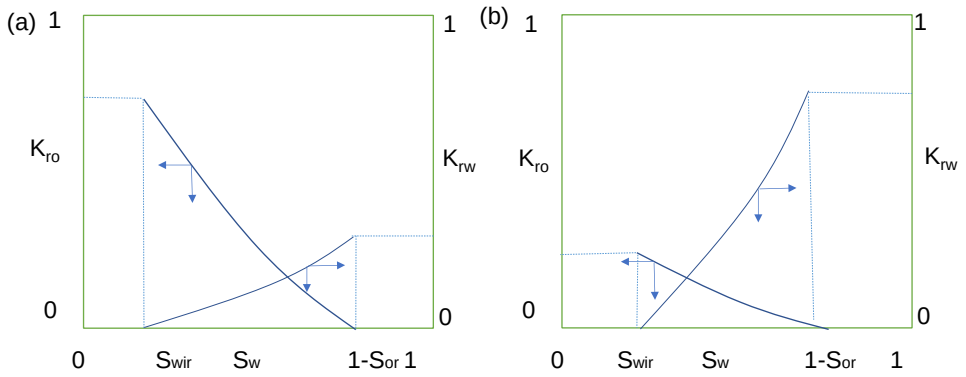

FIGURE 1.18: The effect of wettability on oil water relative permeability: (a) strongly water wet, and (b) strongly oil wet.Where K_{ro}, K_{rw}, and S_w are oil relative permeability, water relative permeability, and water saturation, respectively.

If oil and water are flowing through a straight capillary, the relative amounts of the two fluids flowing are dependent upon: which fluid preferentially wets the capillary wall and thereby flows along the wall. And the non-wetting phase fluid flows through the centre of the capillary since the flow velocity in a laminar system is zero at the boundary, and at a maximum in the centre. Figure 1.19. illustrates the effect of the wettability on oil water relative permeability for both systems.

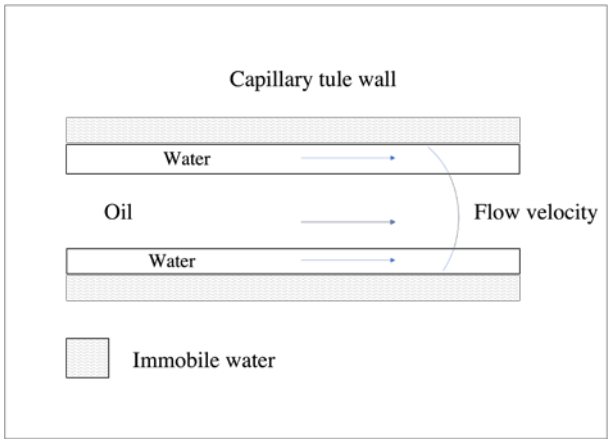

FIGURE 1.19: An idealized capillary tube and the effect of the wettability on fluid flow velocities -water wet case.

Water tends to streamline the flow of oil in a water rock. A reduction in K_{ro} can be attributed to the reduced cross-sectional area available for oil flow. The disconnected oil globules at S_{or} effectively causes a reduction in K_{rw}. In an oilwet rock, the processes are reversed note that a and b are near mirror images of each other, as clearly shown in Figure 1.20.

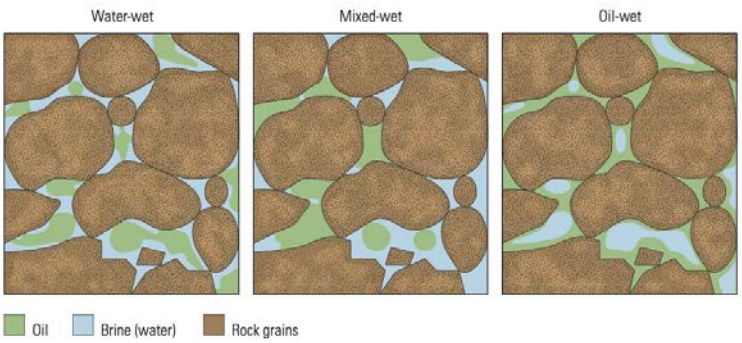

FIGURE 1.20: Schematic shows the wetting phase in pores, left: water-wet state (oil residues in the centre of the pores), middle: mixed-wet state (all of the three phases displayed similar of the water/oil saturations), and right: oil-wet state (water residues in the centre of the pores). Adopted from (Bhattacharya et al., 1994) (Copyright: Elsevier 1994). .

3. Pore structure

Pore geometry (structure) has long been recognized as one of the predominate factors affecting the character of relative permeability curves. The following rock properties affect relative permeability, Figure 1.21. shows a schematic diagram of pore geometry.

I The ratio for the pore size to pore throat, which control the snapping off of the non-wetting phase. The later results in the trapped or isolated phase no longer flowing with oil. Large pore size to pore throat ratios (snap-off) and lead to high non-wetting phase residual saturations.

II Connectivity of the pore structure, high connectivity normally results in lower residual saturations.

III Grain shape, size, packing, solution, sorting and alteration, and diagenesis, for example quartz overgrowths.

IV Pressure compaction or solution.

V The mineralogy and lithology, such as, clay and shale streaks.

VI The detrital or authigenic pore fillers.

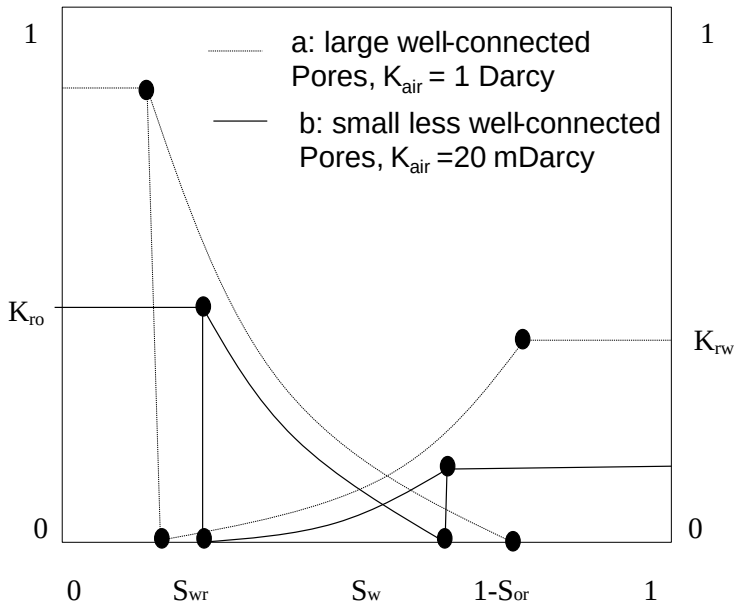

FIGURE 1.21: Schematic illustrates the effect of pore size on the oil/water relative permeability. Large well-connected pores (dashed), small less well-connected (solid).

4. Saturation history (hysteresis)

   The distribution of fluid phases in porous media depends on the history of the saturation changes. This was demonstrated in capillary pressure theory, section 1.6.2., which showed distinct differences, depending on whether the wetting fluid saturation increases (imbibition) or decreases (drainage).

   Hysteresis is defined as "A phenomenon exhibited by a system or material in which response depends nonlinearly on past responses". Furthermore, several other Influences on Relative Permeability and these include capillary or viscous forces, viscosity ratio, reservoir conditions, scaling effects and capillary end effects.

1.6.3.9 Laboratory measurement techniques of relative permeability

As mentioned early, relative permeability can be measured in the laboratory or by data calculation; this thesis focus on laboratory measurement, there are two different techniques; the steady state and un-steady state methods, both present fundamental advantages and disadvantages. Each has been described in detail in following sections.

1. Steady state

   Generally, the most reliable relative permeability data is obtained by steady state techniques. Two or more immiscible fluids are injected simultaneously at constant pressure or rate of extended time, until equilibrium conditions are attained. The flow rate, pressure gradients, and saturations are measured and used with Darcy's low to find the effective permeability, K_r, for each phase.

Relative permeability curves versus saturation are found in a stepwise manner, which is from changing injection ratio rates and replicating the measurements as equilibrium is reached. Saturation changes are unidirectional in a drainage or imbibition mode to avoid hysteresis. When the rate distribution and pressure in the sample (reservoir) remain constant during time, the steady state conditions are met. In reservoir studies, this is established when the differential pressure across the sample remains constant.

The steady state technique is experimentally time consuming and complex because it takes several hours or days, to reach equilibrium at each phase saturation. The key experimental problem that occurs uniform saturation. Saturations can be measured by; electrical resistivity, materials balance, microwave attenuation, radio waves (sonic), gamma-ray attenuation, nuclear magnetic resonance imaging, and x-ray computerized/absorption tomography.

Each procedure has specific benefits and drawbacks; however, all are rather complex and require more advanced skilled technicians. The figure 1.22 illustrates the major components of an X-ray absorption K_r saturation monitoring technique. A calibration curve is established by scanning the sample at dry conditions and repeated when it is fully saturated, with testing fluid to be monitored. However, using magnetic resonance computerized tomography or imaging has been added to the advantage of multidimensional image reconstruction capabilities for flood monitoring.

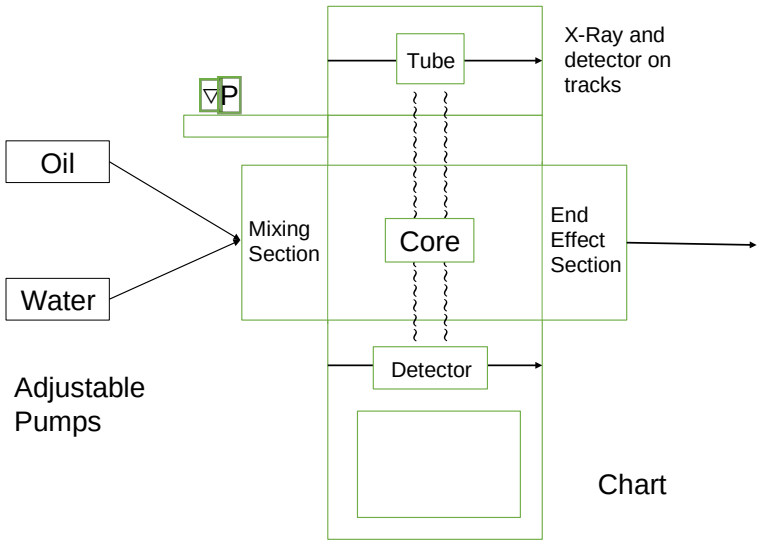

FIGURE 1.22: Schematic of the steady state X-ray absorption of relative permeability equipment. The schematic adapted from reference (Oak, 1988) (Copyright: Society of Petroleum Engineers 1988).

2. Water flood state

In addition to steady state and un-steady state, water oil relative permeability tests, numerous testing options which are available to evaluate water-flood efficiency. (Water-flood is used in this project to measure relative permeability). The water-flood tests can include water and oil saturations, effective permeability, oil recovery versus water pore volume injected, and oil recovery versus water cut.

Basic water-flood tests are useful and cost effective as many tests are to be run, such as, in highly heterogeneous reservoirs. At reservoir modelling, it is practical to run basic water-flood in conjunction with water oil relative permeability tests.

The following record data are normally supplied, water saturation, oil saturation at 99.9% oil recovery and water cut, oil effective permeability at water saturation, and water effective permeability at oil saturation.

1.7 Nanotechnology and their usage in oil recovery applications

Nanotechnology has been defined as (the construction of functional materials, devices and systems by controlling matter at the nanoscale level (one-billionth of a meter), and the exploitation of novel properties and phenomena which emerge at that scale. Research into the synthesis of nanomaterials has been centred on readily available materials of low cost (Latiff et al., 2011; Tetteh, Janjang, and Barati, 2018).

Nanotechnology has been applied in various areas such as medicine, chemical engineering, pharmacology and biotechnology (Niosi and Reid, 2007). Novel applications of nanotechnology were also proposed in the petroleum industry for exploration (Kapusta, Balzano, and Te Riele, 2011), refinery (Kwon et al., 2008), drilling (DargahiZaboli, Sahraei, and Pourabbas, 2017) and enhanced oil recovery (Alvarez-Berrios et al., 2018). Of these, nanotechnology stands out as a particularly flexible option due to its propensity to form nanomaterials, providing a great specific surface area for reducing interfacial tension between oil/water or water/oil (Nwidee et al., 2017; Songolzadeh and Moghadasi, 2017). Through the application of experimental techniques such as (flooding) and the studying of scientific properties such as interfacial tension and wettability, it is possible to find a variety of nanomaterials which have the potential for applications in the oil and gas industry (Fu et al., 2016; Binks et al., 2010).

Since the turn of the century, a considerable body of work has been published regarding the practical use of nanoparticles for enhanced oil recovery (Dai et al., 2018a). Our previous publication explored the properties of functionalized alumina

oxide nanoparticles and showed them to have a significant impact on wettability and interfacial tension between different light oils and water (Al-Shatty et al., 2017). In addition, several publications have shown that using nanoparticles alone or in combination with one or both of: surfactants or polymers will decrease interfacial tension and thereby increase the production rate (Cheraghian et al., 2014).

A significant advantage of these nanoparticles is alteration of the contact angle (refer to section (1.6.3.4) for definition) between oil droplets and the rock surface, Figure 1.23. (Alvarez-Berrios et al., 2018) below demonstrates contact angle reduction during injection SiO_2 nanofluid. Their results showed that the hydrophilicity and wettability increase with increasing nanoparticle concentration and also cores saturated with oil and water were initially mixed-wet, but nanoparticles injection made the rock waterwet, which means water wettability increases at higher concentrations.

The nanoparticles that are used to form reduction in interfacial tension (IFT), and water contact angle (WCA) in this thesis possesses suitable nanomaterials that allow the NPs to penetrate onto rock surface molecules from nanofluid solution. To achieve a more marketable product, it is essential for enhanced oil recovery applications to be environmentally friendly and cost-effective.

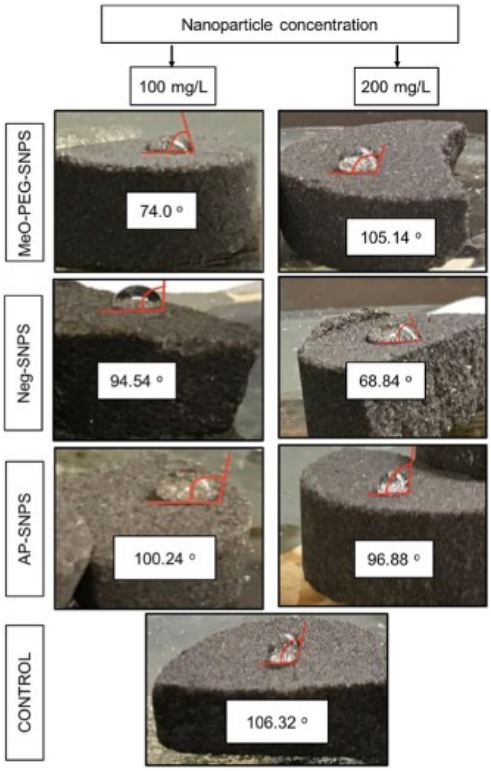

FIGURE 1.23: A photograph that shows the contact angle of a water droplet on the reservoir rock after treatment with silica nanoparticles at different concentrations. Adopted from (Alvarez-Berrios et al., 2018) (Copyright: Springer 2018).

EOR chemicals are evaluated using interfacial tension, salinity, core flooding and wettability alteration experiments. The research on implementations of nanoparticles in enhanced oil recovery is focused on how these nanoparticles alter the previously mentioned properties during oil recovery. Some reviewers have also summarized the different aspects of nanoparticles research in EOR (Negin, Ali, and Xie, 2016; Ko and Huh, 2019; Yekeen et al., 2018). The following sections present a review of the most recent applications of micromodels and nanoparticles that are studied in hydrocarbon recovery and aims to provide insights for scientific researchers who are working in the nano-EOR field. In addition, the influence of

nanoparticles employed oil recovery and understanding the mechanism of elements and factors that affect oil recovery is looked at.

1.8 Some of literature review of using nanoparticles studied in oil recovery applications

Interfacial tension and wettability alteration are the main key factors that have a high effect on oil recovery. The following sections will discuss each one in more details.

1.8.1 NPs studied in modification of the interfacial tension

The interfacial tension is defined by Monicard (Monicard, 1980) as the surface free energy that occurs between two immiscible liquids or liquid and gas. Figure 1.24 illustrates nanoparticles schematic and structure disjoining pressure gradient mechanism between oil, nanofluids and solid. He relates the surface phenomena to the interaction of molecules that occur between two non-homogeneous liquids. This phenomenon (force or energy) is called “surface tension (SFT)” for liquid-air interface or “Interfacial tension (IFT)” for the liquid-liquid interface. Monicard calculates the SFT to 73 dyn/cm for liquid (water) and air interface and IFT of between 28 to 30 dyn/cm for liquid-liquid (water-oil) interface (Monicard, 1980). Moreover, four factors influence IFT:

1. Temperature (T), IFT decreases as temperature increases, due to decrease the cohesive forces between the molecules and kinetic energy increases as temperature rise (Dillan, 1984). An empirical equation 1.18 express the relationship between the temperature and interfacial tension.

$$T \uparrow aT_r + b \quad (1.18)$$

where T refer to temperature, a, and b are positive constant. T_r is relative temperature.

2. Pressure (P), IFT change in the same way as temperature, the binomial equation below expresses the relationship between the pressure and IFT. In general, dissolved gases in liquids led to increase the IFT.

$$T \uparrow aP + b \quad (1.19)$$

where P is pressure and (a and p) are positive constant.

3. Dissolved gases in either oil or water; and the addition of a surface-active agent (surfactant) in either reservoir oil or water. Adding surfactant led to decrease the attendant in the overall surface activity (Dillan, 1984).

In addition, Monicard (Monicard, 1980) explained that oil recovery depends on capillary number (N_{ca}), which is defined as the ratio of viscus forces to surface tension forces (an empirical equation 1.20 can be express the calculation of capillary number). To explain these forces, when there are two immiscible fluids (oil/water) flowing through reservoir rock, there are three main forces that determine the flow behaviour. They are viscous, gravity and capillary force. Where capillary number is a higher value, viscous forces dominate and the IFT between fluids (water/oil) in the reservoir rock is reduced, thus augmenting recovery. So, in oil recovery experiments, N_{ca} is an important factor to consider.

$$N_{ca} = \frac{Viscous forces}{Capillary forces} = s\frac{v\mu}{\cos q} \quad (1.20)$$

where u and μ are the velocity and the dynamic viscosity, respectively, s is IFT between oil and water, and q is the contact angle of water and substrate. Capillary number it is dimensionless group.

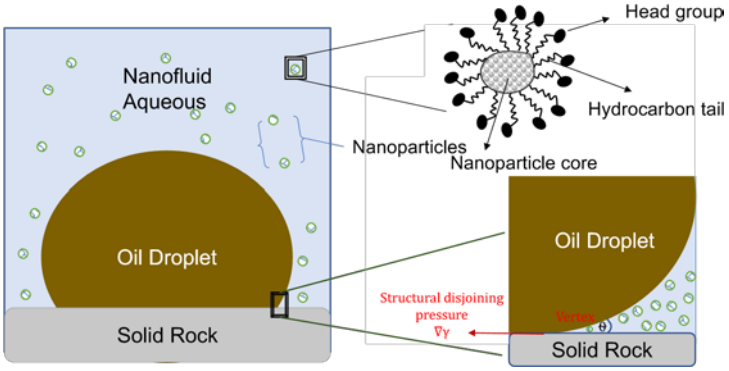

FIGURE 1.24: Schematic diagrams which illustrate of nanoparticles and structure disjoining pressure gradient between an oil droplet, nanofluids and solid rock.

A study was done by (Joonaki and Ghanaatian, 2014) which investigated the effect of aluminium oxide, iron oxide, and silicon oxide on the IFT. They found that increasing the concentration of NPs reduce IFT. Silicon oxide was more efficient in reducing the interfacial tension between water and oil due to its high surface area and small particle size. This reduction of the IFT leads to the easy flow of residual oil in place, because it lowers the work that is required for oil phase to move through pore rock.

1.8.2 NPs studied on the oil saturation

Based on the investigation performed by Hendraningrat and his co-researchers (Hendraningrat, Li, and Torsæter, 2013a), a higher capillary number of results in a lower oil saturation of water, such that by reducing IFT to an ultra-low value (e.g. 10^{3} mN/m) the factors mentioned above can be influenced. Furthermore, Hendraningrat, Li, and Torsæter tested the effect of adding lipophilic and hydrophilic

silicon dioxide nanoparticles (SiO_2) of 7 nm diameter on the IFT of brine-oil fluids in low-medium Berea sandstone permeability. In this work, they prepared different concentrations of Nanofluids (arrange number between 0.01 and 0.05 wt.%) which were dispersed on brine. The brine was made from 3 wt.% of NaCl dissolved in deionized water. The IFT between nanofluids-brine and crude oil is measured by using spinning drop video tensiometer (which is a solid optical measuring device for the determination of low to ultralow IFT and rheological interface properties) at ambient conditions using the following formula.

$$s = \mathrm{D}rw8\overline{n3^2J.(_D D(_{app}{}_{DL})}\,)^3 \qquad (1.21)$$

where: *s* is the interfacial tension, D *r* is the density difference, *w* is the rotational rate of the cylinder, n is the refractive index, D_{app} is the measured drop diameter, D is the true droplet diameter, J_D is the correction factor and L/D is the aspect ratio. Their results indicated that introducing nanofluid of SiO_2 NPs into the brine/oil system reduces the IFT from 19.2 to 10.9 mN/m when 0.01 wt.% is used and to 7.9 mN/m when 0.05 wt.% of nanofluid is used. They indicated that the reason of IFT reduction can be the diffusion of the SiO_2 NPs into brine and oil interface, and the fact that IFT decreases might be enough for increase oil recovery. Similar to (Hendraningrat, Li, and Torsæter, 2013a), Li and Torsæter (Li and Torsæter, 2014) have also established that these nanoparticles (Colloidal nanoparticles (CNP) and nano-structure particle (NSP)) can decrease IFT and cause significant alteration in wettability. Their results show that both nanoparticles can reduce IFT, but at the same concentration, CNP lowers IFT more than NSP. They indicate that, the mechanism for IFT reduction can

be related to the hydrophobic part of NPs tends, which like to exist in crude oil phase and the hydrophilic part like to be present in the nanofluid aqueous phase.

1.8.3 Polymer studied on the modification of interfacial reduction

(Hendraningrat and Torsæter, 2015b) researched on the emulsion stability of nanofluids made from three different nanoparticles: Al_2O_3, TiO_2 and SiO_2. These nanoparticles were dispersed in 3 wt.% NaCl with 0.05 wt.% concentration. In this work, they found these nanoparticles in brine were not stable, so they added 1 wt.% of Polyvinylpyrrolidone (PVP) and the PVP works to prevent the agglomerate of NPs and increasing the number of small size NPs that dispersed in brine. They found that, the size of NPs in aqueous phase is 29 and 26 nm for TiO_2 and Al_2O_3, respectively. The chemical structure and molecular of PVP, and the advantage of having a high solubility in hydrophobic and hydrophilic solvents has caused size stabilization of nanofluids (made of metal oxides nanoparticle dispersed in PVP solution) for 7 days. The mechanism of how polymer works as NPs stabilizer is illustrated in Figure 1.2.

Moreover, they indicated that all nanoparticles have the ability to lower IFT value between the aqueous phase and crude oil. According to their results, Al_2O_3 NPs reduced IFT more than the other two nanoparticles. Therefore, their research indicated that Al_2O_3 NPs is a good agent for EOR from a sandstone reservoir. Table 1.4 below lists other researchers who have done an experimental study which represented that the nanoparticles have the ability to reduce IFT either alone or in combination with chemical such as (polymer or surfactant).

Later, (Yousefvand and Jafari, 2018) showed, by using a five-spot glass micromodel, the addition of nanosilica did not change IFT between the injection fluid and crude oil.

To obtain a further reduction of IFT, they investigated the injection of complex mixture made of nanofluid, salt, Sodium dodecyl sulfate (SDS) surfactant, deionized water, and mixture of salt/surfactant/water/polymer (HPAM). They were the first research to test these materials together in EOR. Their research indicated that salt is the main reason of reducing NPs stability, however, SDS increase the NPs stability due to the ability of the SDS to adsorb into silica NPs and increase NPs charge which leads to increase stability of suspension. Interestingly, they found that silica NPs does not change the IFT of oil/nanosilica.

TABLE 1.4: Selected NPs, polymers and surfactants and the interfacial tension (IFT) of the suspensions.

NPs	Dispersion media	Surfactant Con. wt.%	IFT without NPs	IFT with NPs	Ref.
metal nanoparticles	solution	0.05	10.9	5.5	(Suleimanov, Ismailov, and Veliyev, 2011)
IIT⇤	Brine	0	NA	1.5	(Zhang, Nikolov, and Wasan, 2014)
SiO_2	water	0	35	7.9	(Hendraningrat, Li, and Torsæter, 2013a)
Fe_2O_3	PVP solution	0	19.2	15.2	(Hendraningrat and Torsæter, 2015a)
Fe_2O_3	SDS	1	6.5	3.5	(Hu et al., 2017)
NSP	Brine	0	13	10	(Li and Torsæter, 2014)
CNP	Brine	0	13	4.8	(Li and Torsæter, 2014)
ethanolamine	Brine	0.1	3	0.003	(Xie et al., 2016)
SiO_2	PAM solution	0.14	50	19	(Sharma and Sangwai, 2017)
IIT	Brine	0	NA	1.5	(Cheraghian et al., 2014)
SiO_2	water	0	35	7.9	(Nazari Moghaddam et al., 2015)
Al_2O_3	water	0	35	10.9	(Nazari Moghaddam et al., 2015)
TiO_2	water	0	35	19.2	(Nazari Moghaddam et al., 2015)
SiO_2	PVP solution	0	19.2	16.5	(Alvarez-Berrios et al., 2018)

where ⇤refers to nanosized hydrophilic silica dioxide particle.

1.8.4 Nanoparticles studied on their effect on wettability alteration

Wettability of reservoir rock system is defined as the tendency of rock surface to preferentially a particular liquid to occupy the pore space in the presence of two or

more immiscible liquids in a multiphase fluid system, (oil, water, or gas phase) (Bayat et al., 2014; Sakthivel et al., 2017). It is a key parameter which controls the location and distribution of fluids in the formation (Huibers et al., 2017). Based on wettability, oil reservoirs characterize as strongly oil-wet, weakly oil-wet, strongly water-wet, weakly water-wet or mixed-wet, see section (fluid wettability) above. Wettability is well recognized that the oil recovery from wet reservoirs is high and oil recovery level becomes lower as reservoir core becomes more oil wet (Ju, Fan, and Ma, 2006). Nonetheless, most of carbonate reservoirs rock are oil-wet to mixed wet (Abhishek, Hamouda, and Murzin, 2018). Consequently, in the oil industry, wettability alteration term means changing reservoir petro-physical characteristics rock properties such as (relative permeability and capillary pressure) from oil-wet to extra water-wet, return to section (1.6.3.8.) (Maghzi et al., 2014). Information about wettability is fundamental to understanding the multiphase flow problems ranging from oil migration from source rocks through primary production mechanisms to secondary/tertiary recovery. Wettability alteration for reservoir surface was determined by using contact angle, displacement study, spontaneous imbibition, surface imaging tests, and zeta potential measurements. Scanning electron microscopy, nuclear magnetic resonance spectroscopy and Atomic force microscopy are able to provide changes in rock properties due to wettability al-

teration.

1.8.5 Surfactants studied on the wettability influence of liquid-liquid or liquid-solid interface

Before going further to wettability influence by adding surfactant, let's give a brief definition, classification and surfactant flooding mechanism. Surfactant can be defined as a long chain molecule, that has a hydrophobic tail group (oil soluble), and a hydrophilic head group (water soluble). The tail group may be a long chain by fluorocarbon, hydrocarbon, short polymer chain, or a siloxane chain. The head group may be amphoteric, anionic, non-ionic, or cationic. In cationic and anionic types, the hydrophilic group are positively and negatively charged, and in non-ionic surfactants, the head group is of non-dissociative nature. Table 1.5 summarized common hydrophilic surfactant groups. Surfactant usage to change wettability is one technique that was adopted by scientist researchers to increase oil recovery from oil-wet fractured sandstone and carbonate reservoirs (Gong et al., 2016). Surfactant that preferentially adsorbs at an interface, decreasing IFT, or SFT between fluids or fluid/sloid, by improving mobility ratio and increasing the Capillary number N_{ca}, section (1.6.2.) has discussed with the entail details.

TABLE 1.5: A summary of common hydrophilic surfactant types and the associated chemical groups.

Surfactant type	Hydrophilic group
Anionic	carboxyl ($RCOO^-M^+$), sulfonate ($RSO_3^-M^+$), sulfate ($ROSO_3^-M^+$), phosphate ($ROPO_3^-M^+$).
Non-ionic	Polyoxyethylene, polyols, Sucrose esters, polyglycidyl esters
Cationic	Ammonium quaternary ammonium halides ($R_4N^+X^-$)
Amphoteric	Betaine, Sulfobetaine $RN^+(CH_3)_2CH_2CH_2SO_3^-$ Imidazoline Derivatives

A various series of investigations have been made through studying how nanofluids can change rock wettability (Karimi et al., 2012; Hendraningrat, Li, and Torsæter, 2013b; Onyekonwu and Ogolo, 2010; Giraldo et al., 2013; Taborda et al.,

2016). A major example is silicon oxide nanoparticles dispersed in propanol that was reported to change core wettability. Lipophilic polysilicon NPs alter rock wettability from oilwet to water-wet, and it can increase rock wettability to be more water-wet due to hydrophilic and hydrophobic appearance (Onyekonwu and Ogolo, 2010).

Onyekonwu et al., 2010, proved that the hydrophilic should be limited to oil-wet formation whereas the hydrophobic restricted to water-wet formation to extra waterwet and delay oil production that causes poor recovery. Also, silica nanoparticles modified with different silane could change rock wettability and have shown better results in water/wet formation (Jang, Lee, and Lee, 2018). (Ju, Fan, and Ma, 2006), theoretically studied lipophilic and hydrophilic polysilicon NPs for wettability alteration of rock. Their result was hydrophilic polysilicon nanoparticles adsorb water toward pore walls and alter sandstone wettability, while the lipophilic had no effect on reservoir wettability. To better interpret the core flood results, (Cheraghian et al., 2017) investigated the effects of SiO_2 nanoparticles with anionic surfactant SDS on contact angle and interfacial tension, and experimental oil displacement performance in five spot glass micromodels. They established that the enhanced oil recovery results from the alteration of the rock wettability to a more hydrophilic condition. In addition, they had argued that rock wettability changes from oil-wet to water-wet due to an increase surface free energy because of a strong hydrogen bond between water and SiO_2 nanoparticles. Figure 1.25 illustrates the effect of surfactant on surface wettability behaviour.

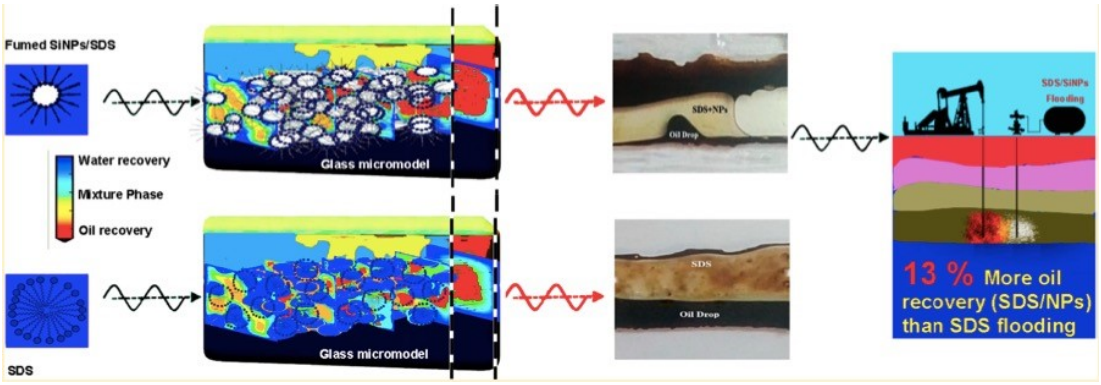

FIGURE 1.25: Schematic diagram shows the effect of surfactant on surface wettability behaviour. Adopted from from reference (Cheraghian et al., 2017) (Copyright: American Chemical Society 2017).

Other parameters effect on wettability alteration with nanoparticles: oil type, rock type, NPs and their concentrations. (Huibers et al., 2017), studied silica oxide NPs effect on light and heavy oil on two-sandstone core, return to section (1.4.1.). The largest wettability alteration observed on intermediate light crude oil by SiO_2 than Lloydminster heavy crude oil. Furthermore, (Ehtesabi, Ahadian, and Taghikhani, 2015) and his group studied the impact of TiO_2 NPs to alter wettability alteration for sandstone cores, the hydroxyl groups on the nanoparticles make the sandstone core surface water-wet. In addition, TiO_2 NPs effectively modify sandstone rock wettability from oil-wet to water-wet. (Bayat et al., 2014), investigated SiO_2, TiO_2 and Al_2O_3 NPs dispersed in deionized water to study wettability alteration for an intermediate limestone by contact angle measurements. They noticed Al_2O_3 NPs are efficient in reducing contact angle of rock. However, (Dehghan Monfared et al., 2018) found SiO_2 nanoparticles alter wettability of carbonate rock by surface adsorption.

To sum up, hydrophilic nanoparticles are preferred in oil-wet formation case, while hydrophobic nanoparticles are preferred in water-wet case. In both cases, NPs

concentration is the key factor to alter reservoir rock wettability. The NPs should reach a threshold to be able to change the wettability. Figure 1.26. is a plot for SiO_2 NPs Vs oil recovery and contact angle in different sizes, and Table 1.6. a list of the common NPs that studied on changing rock wettability. Nearly wettability alteration literature is used NPs on sandstone systems. However, the wettability alteration literature on carbonate rocks is limited. As the vital significance of carbonate core, it is essential to understand NPs carbonate interfaces by variable different parameters such as core type, geological condition, salinity, stability, size, shape and different types of NPs and method of NPs preparation. Few publications reported studying pore scale effect on wettability alteration and required further experiment (Jang, Lee, and Lee, 2018). The contact angle method has limitations: its absence for standard reference and its required length for equilibration time that cannot be reproduced in lab.

TABLE 1.6: The water contact angle (WCA) of dispersion media on surfaces before and after the injection of NPs.

NPs	Dispersion media	WCA before NPs	WCA after NPs	Ref.
IIT	Brine	74	1.2	(Hendraningrat and Torsæter, 2015a)
SiO_2	SDS solutions	102	9.8	(Cheraghian et al., 2017)
SiO_2	Brine	140	100	(Alnarabiji et al., 2018)
Al_2O_3	Brine	90	8.2	(Bayat et al., 2014)
SiO_2	Brine	48	33	(Hendraningrat and Torsæter, 2014)
CNP	Brine	137.7	50.8	(Jang, Lee, and Lee, 2018)
FC-NPs↞	Seawater	38	29.8	(Li et al., 2017)
Al_2O_3	anionic surfactant	142	110	(Giraldo et al., 2013)
TiO_2	electrolyte solution	200	40	(Whitby, Fornasiero, and Ralston, 2010)
Fe_2O_4	Brine	160	100	(Rezvani et al., 2018)

where ↞ refers to Fluorescent carbon NPs.

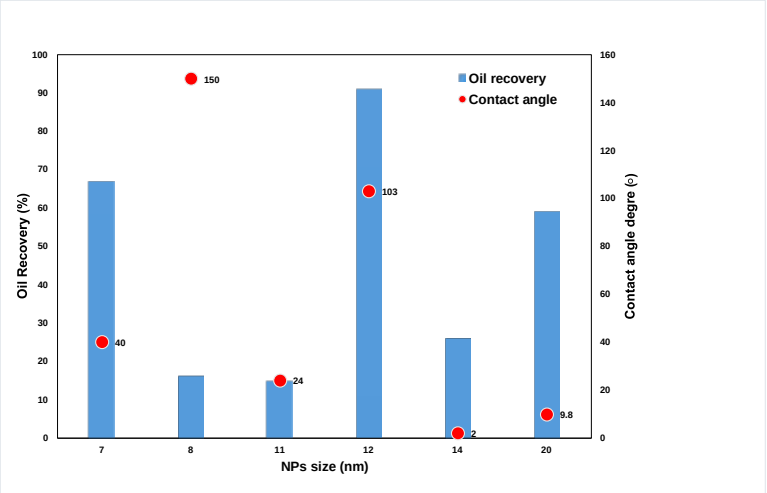

FIGURE 1.26: A plot showing that SiO_2 nanoparticles size, contact angle and percentage oil recovery are not correlated. The plotted data are taken from references (Songolzadeh and Moghadasi, 2017; Fu et al., 2016; Hu et al., 2017).

1.8.6 Nanoparticles studied on core flooding experiment

Core flooding experiments are used widely in the oil and gas industry to determine the petroleum recovery at limited reservoir conditions such as: high pressure, temperature, and salinity (Nazari Moghaddam et al., 2015; Manesh et al., 2017; Sun et al., 2017). Since its time consuming and is not conductive to performing a large number of experiments, data collected from previous initial inspection experiments such as: IFT, wettability, and rheology measurement are required to reduce the number of core flooding tests (Alnarabiji et al., 2018; Nazari Moghaddam et al., 2015).

Considerable core flooding tests have been achieved by NPs injection (Emadi et al., 2017; Ramezanpour and Siavashi, 2019): SiO_2, Fe_2O_3, and Al_2O_3 are the most NPs that are studied for oil recovery application due to their low-cost and ready availability. However, the injection of NPs may have a negative impact on the oil recovery. There are different factors that influence: such as NPs aggregation, low

stability, and surface charge. For instance, a large aggregation size (bigger than pore space) leads to blocking the pore space, reducing porosity and leads to reduce oil displacement. Similarly, short time nanofluids stabilization has same effect but for long term.

Table 1.7. collects data from several sources for easy comparison of the percentage oil recovery for different NPs and dispersion medium. It can be seen that the injection of NPs may have a negative impact on EOR and the addition of SiO_2 which has a position charge decreased oil recovery by 6.7% (Alvarez-Berrios et al., 2018). The following sections will highlight various factors that affect hydrocarbon recovery. In classification, one can attribute this dependence to the following: NPs type, size and concentration, polymer or surfactant concentration, stone characterization and solution salinity. Each of these points will be discussed in details on the following sections.

TABLE 1.7: Various NPs studied in oil recovery.

NPs	Dispersion media	NPs Con.	surfactant Con.	Core	Recovery (%)	Ref.
$CaCO_3$	water + alcohol	1	0	Carbonate substrates	20	(Nazari Moghaddam et al., 2015)
SiO_2	paraffin/heptane	1	0	Carbonate substrates	25	(Nazari Moghaddam et al., 2015)
SiO_2	ammonium hydroxide	100	MEO-PEG-SNPs⇤	Berea sandstone	12	(Alvarez-Berrios et al., 2018)
Silica Nanofluid	Brine	1	0	Berea Sandstone	55	(Zhang, Nikolov, and Wasan, 2014)
SiO_2	Brine	1	0	micromodel NP	35	(Yousefvand and Jafari, 2015)
SiO_2	Brine	0.05	0	Berea as core plugs	67.02	(Hendraningrat, Li, and Torsæter, 2013a)
TiO_2	NaCl	0.01	0	Sandstone Core	80	(Ehtesabi et al., 2014)
TiO_2	NaCl	0.01	1	Sandstone Core	23	(Ehtesabi et al., 2014)
SiO_2	PVP solution	0	0	Quartz plates	67.02	(Hendraningrat and Torsæter, 2015a)
Fe_2O_3	surfactant solution	4	10	the glass column	85.1	(Hu et al., 2017)[Hu et al., 2017]
SiO_2	Brine	0.1	3	Sandstone cores	55	(Yousefvand and Jafari, 2018)

where ⇤ refers to methoxy polyethylene glycol-Silica nanoparticles.

1.8.7 The effect of the NPs concentration

The NPs concentration is of utmost importance in flooding experiments. Occasionally, the ideal concentrations are changeable using initial examination techniques for example: IFT, rheology and adsorption (Ehtesabi, Ahadian, and Taghikhani, 2015; Ehtesabi et al., 2014). Wettability alteration occurs when the attractive forces between the brine, the NPs, the repulsive forces between the NPs, and the reservoir rock surface are balanced (Ehtesabi, Ahadian, and Taghikhani, 2015). Accordingly, the disjoining pressure and the contact force of the particles-fluid and the particle-particles and interactions leads to prevention of the coalescence of the nanofluid droplet from forming an inter-droplet layer, which diverges the medium wettability layer. The NPs concentration (volume fraction) dispersed in solutions correlates with the solution thermodynamic properties. NPs are affected by the contact force (between interface) and the disjoining pressure (Ehtesabi et al., 2014).

According to an experiment done by (Caldelas et al., 2011), increasing NPs concentration remain to increase disjoining pressure, thus led to a rise in repulsive force.

The wettability modification occurs when the repulsive forces between nanoparticles and the reservoir rock surface and the attractive force between the brine and the nanoparticles are balanced. Accordingly, the disjoining pressure and the contact force of the particles-fluid and the particle-particles and interactions, this leads to prevention of the coalescence of the nanofluid droplet from forming an inter-droplet layer, which diverges the medium wettability layer. All previous mechanisms make it easy to release oil from reservoir rock. Moreover, increasing NPs concentration has the ability to improve the displacement efficiency as spreading NPs on rock grain surface and enhanced nanofluids viscosity (El-Diasty and Aly, 2015).

However, the hydrocarbon recovery will reduce at a certain concentration of NPs. In that, the NPs will block the reservoir pore, so the oil recovery is reduced. Moreover, at higher concentrations the NPs will aggregate and accumulate around the inlet this leads to reducing the displacement efficiency, Figure 1.27 demonstrates the mechanism. (Ehtesabi et al., 2014) reported that porosity, permeability and oil recovery of sandstone improve 31% after injection TiO_2 NPs with 0.1% concentration in core flooding experiment, Table 1.8 illustrates all parameters in details. Changing in the NPs concentration to 1 wt.% slightly show changes on oil recovery factor and lower recovery was achieved when compared to what was obtained from using brine only. The recovery factor was up to 23%, which is less than from injection brine into the system (Table 1.7, Entries 7 and 8). This concentration various controlled by porous medium, type of NPs and reservoir environmental conditions. There is a

strong relationship between NPs concentration and Oil recovery result, as Figure 1.28. shown below.

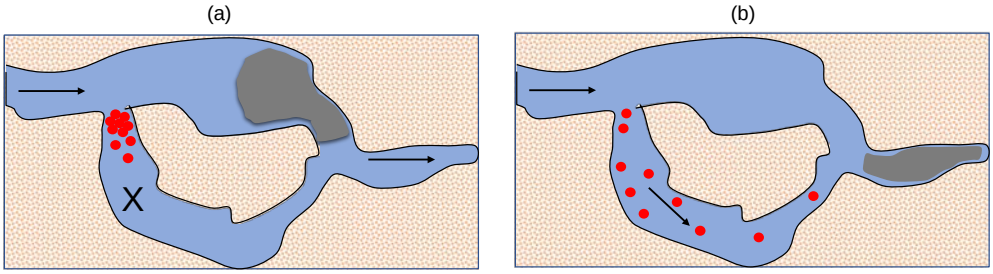

FIGURE 1.27: A schematic diagram showing (a) a high concentration of NPs in the fluid causing pores to block, and (b) free flowing fluid containing a low concentration of NPs.

TABLE 1.8: Oil recovery factor after injection with water and TiO_2 nanofluids at different shape and concentrations. Table reproduced form reference (Giraldo et al., 2013).

Injected Aqueous	Oil recovery factor (%)
Water	49±10
TiO_2 anatase (0.01%)	80±10
TiO_2 anatase (1%)	42±10
TiO_2 amorphous (1%)	23±10

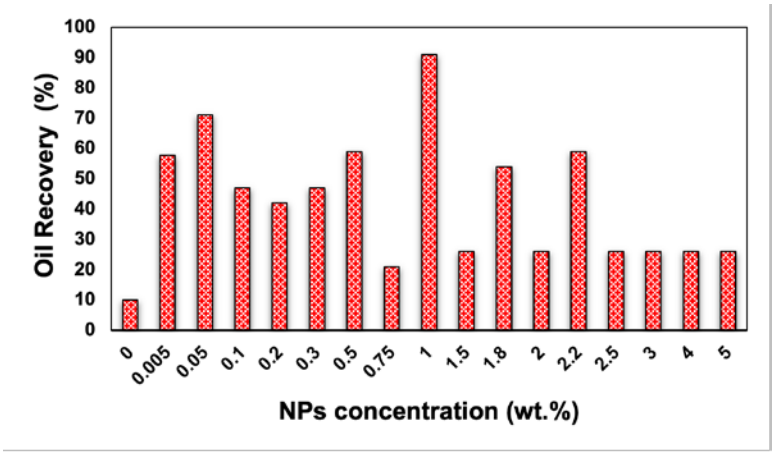

FIGURE 1.28: A plot summarising data from (Nwidee et al., 2017; Hendraningrat, Li, and Torsæter, 2013a; Xie et al., 2016; Cheraghian et al., 2017; Al-Anssari et al., 2018; Yousefvand and Jafari, 2018). It shows oil recovery percentage after injection of SiO_2 NPs at different weight percentages.

1.8.8 Effect of type and size of nanoparticles on oil recovery

The NPs types are the most important parameter for the outcome of oil recovery and choosing the appropriate NPs for common reservoir conditions. A lower contact angle and a higher particles density can be achieved based on small NPs at the same concentration. A higher nanofluid density significantly improves the disjoining pressure (which is defined as the repulsive and attractive force that occur between two layers of reservoir fluid surface) (Monicard, 1980). (Hendraningrat, Li, and Torsæter, 2013a) studied the displacement effects of three metal oxides NPs (Al_2O_3, TiO_2, and SiO_2) on the quantity and quality of the produced oil from an intermediate limestone sample at different temperatures. They highlighted that smaller NPs not only approve to increasing hydrocarbon recovery considerably, but also develop the displacement result due to the physicochemical adsorption which occurs between the porous medium and particles. The displacement results showed that the use of brine for water flooding resulted in an average of 47.3% oil recovery at 26 C. But when nanofluid of: Al_2O_3, TiO_2, and SiO_2 NPs were injected, the hydrocarbon recovery was improved to 52.6%, 50.9%, and 48.7%, respectively. The highest oil recovery exhibited by the Al_2O_3 nanofluid was attributed to its ability to lower the capillary force of oil during the displacement test on the recovery of heavy crude oil (Hendraningrat, Li, and Torsæter, 2013a).

However, (Mohd et al., 2016) reported that the NPs shape and size affect nanofluid properties. It has found that the viscosity of the nanofluid increased with decreasing particle size and increasing volumetric concentration of nanoparticles in nanofluid injection solution. They investigated the effect of different dispersion media such as distilled water, ethanol, ethylene glycol and brine solutions on

recovery. They sighted that decreasing NPs size led to an increase of solution viscosity. Whereby sphericalsolid shape provided higher nanofluid viscosity than the sample with porous shape. As NPs concentration increase viscosity, EOR increase as well from 7 to 18%.

Other researchers examined Al_2O_3, TiO_2, SiO_2, and NiO NPs and their influence on heavy oil recovery from sandstones core (Alomair, Matar, and Alsaeed, 2014). Flooding experiments was done for each NPs at different concentrations. All NPs showed an improvement on recovery when compared to the base recovery (water injection). Both SiO_2 and Al_2O_3 NPs increased hydrocarbon recovery to 0.958%, and 4.895%, respectively. In that case, the researchers decided to mix both NPs for flooding testing. They observed more substantial oil recovery which was higher than the water injection recovery by 23.724% (Alomair, Matar, and Alsaeed, 2014).

It was reported that the flooding based on injected nanofluid made of SiO_2, NiO, and Fe_3O_4 NPs improved the oil recovery by 22.6%, 14.6%, and 8.1%, respectively, when water injection was set as the reference point (Alomair, Matar, and Alsaeed, 2014). The greater oil recovery displayed by SiO_2 was probably due to its effectiveness to reduce interfacial tension and wettability alteration in porous media. Figure 1.29. and Table 1.9. below shows oil recovery by different nanoparticles with and without surfactant. As it is seen that, the same NPs size, the SiO_2 NPs has higher oil recovery than Fe_2O_3, Al_2O_3, ZnO and TiO_2 NPs. However, TiO_2 NPs has a bigger NPs size when compared to other NPs without using surfactant, (Hu et al., 2017) used KCl because TiO_2 NPs are stable at high temperature and salinity. Oil recovery increase by adding surfactant and this is due to the nanoparticle's aggregation in the present surfactant

which is better than when compared to nanofluid without surface agent. Furthermore, Figure 1.30. shows the plot for NPs (in different sizes) and the effect of present surfactant on oil recovery. It is clearly that oil recovery has improved when surfactants are present in dispersion media.

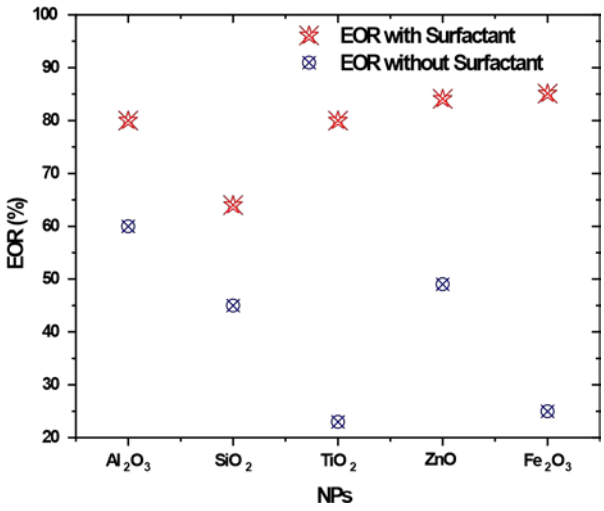

FIGURE 1.29: A plot of maximum EOR percentage achieved with different NPs materials, with and without surfactant. Blue squares with surfactant, Red circles without surfactant. The plotted data are taken from (Hu et al., 2017; Latiff et al., 2011; Ehtesabi et al., 2014; Yang, Wang, and Fan, 2017; Wu et al., 2017).

TABLE 1.9: Common NPs used in oil recovery showing an improved EOR after a surfactant is added.

NPs Type	Size(nm)	Core	EOR(w-out surfactant)%	EOR(with surfactant)%	surfactant	surfactant con. (wt.%)	Ref.
Al_2O_3	10	Sand pack	60	80	Sodium Cumenesulfonate	0.02	(Yang, Wang, and Fan, 2017)
SiO_2	15	Quartz sand	45	64	SDS	0.2	(Wu et al., 2017)
TiO_2	63	Rock surface	23*	80*	N/A	0.0855	(Ehtesabi et al., 2014)
ZnO	5	Glass Beads	49	84.1	SDS	0.1	(Latiff et al., 2011)
Fe_2O_3	7	Glass Column	25	85.1	anionic surfactants(SDS)	10	(Hu et al., 2017)

Where: * mean TiO_2 NPs do not use surfactant but different NPs concentration (1, 0.01wt.%), and w-out

refers to without surfactant.

(a) (b)

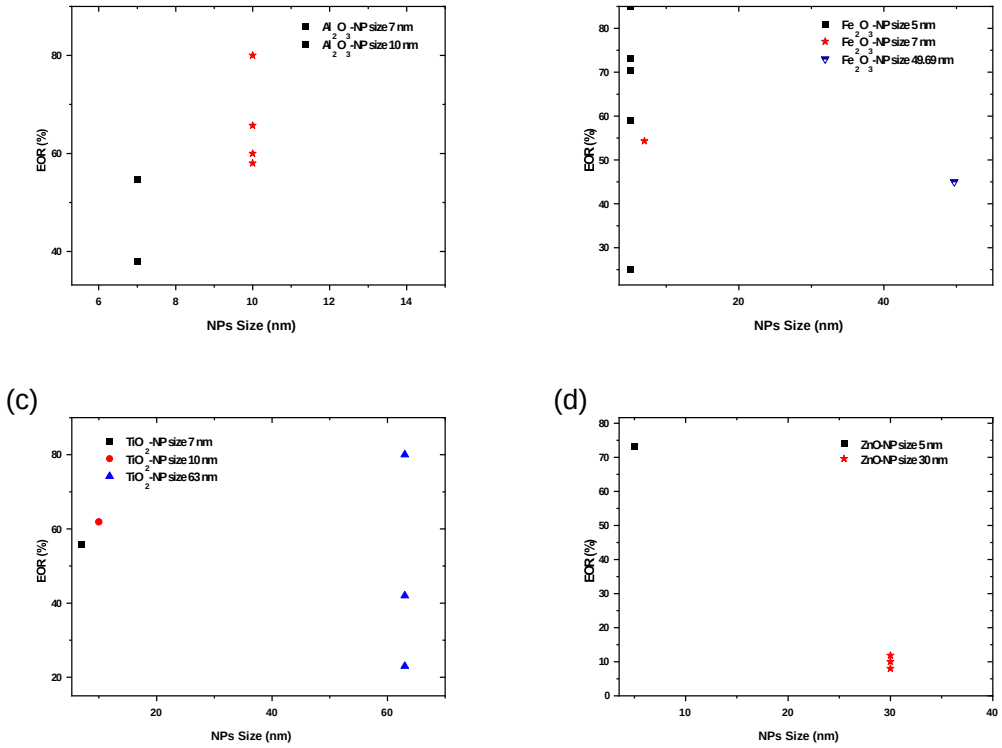

FIGURE 1.30: A plot that shows the EOR percentage after injection with NPs of different sizes made of: Al_2O_3 (a), Fe_2O_3 (b), TiO_2 (c), and ZnO (d). The plotted data are taken from (Nwidee et al., 2017; Fu et al., 2016; Songolzadeh and Moghadasi, 2017; Yousefvand and Jafari, 2018; Hendraningrat and Torsæter, 2015a; Dai et al., 2018a; Ju, Fan, and Ma, 2006; Giraldo et al., 2013; Emadi et al., 2017).

1.8.9 Effect of surfactant concentration on nanoparticles of oil recovery

The effect of NPs on surfactant efficiency has been investigated in different articles (Cheraghian et al., 2017; Parizad, Shahbazi, and Tanha, 2018). Several studies have reported using surfactant flooding to improve wettability of reservoir rocks. Nevertheless, using surfactants on hydrocarbon field is uneconomical for many aspects, such as, oil price is cheaper than chemical price, cannot apply one surfactant

on all reservoirs, because each one has different properties, (return to section 1.8.5., for full details).

Thus, many experimental research have proposed NPs as an alternative to oil recovery. (Huibers et al., 2017) investigate silica NPs on light and heavy oil for wettability with brine of two sandstone cores with nonionic surfactant for different concentrations. They reported that oil recovery improves about 57%, 43% for both light and heavy oil, respectively with the addition of 0.01 wt.% surfactant. In addition, by adding surfactants, the IFT decreases, and increase contact angle.

(Yousefvand and Jafari, 2018) studied the stability and displacement behaviour of SiO_2 NPs with sodium dodecyl sulphate (SDS) using a five-spot glass micromodel flooding setup. The flooding results showed that SiO_2/SDS foam flooding displaced more oil than water flooding or SDS foam flooding. The high recovery is attributed to the improved foam stability and viscoelasticity caused by attached particles. Furthermore, sand pack flooding tests indicate that SiO_2/SDS foam has good properties for oil displacement in both homogeneous and heterogeneous formations. Silica nanoparticles adsorbed by SDS and supercharge the interface which led to long term stabilization for silica nanofluid. The increase in differential pressure and profile control effect exhibited a favourable correspondence with the increase in SiO_2 NPs concentration, which led to higher oil recovery.

In the work of (Hu et al., 2017) the effects of Iron oxide Fe_2O_3 NPs on the anionic surfactant-stabilized emulsion were studied for enhanced heavy oil recovery. They used the core flooding system and microscopic visualization tests to investigate the displacement mechanisms by Fe_2O_3 NPs surfactant-stabilized emulsion. They conducted a series of flooding tests in cores with absolute permeability 98.0± 17.3

mD. In all of the cases that were tested in their study, 20 PV Emulsion slug was injected after the initial water flooding. While 4 wt.% of pure anionic surfactant SDS was employed for surfactant-stabilized and n-hexane as the oil phase, with the addition of 1% Span 80 as the co-surfactant in order to achieve an ultra-low interfacial tension between the oil and water phases. As for the plot shown in Figure 1.31. below the oil recovery increases as the concentration of present surfactant increases.

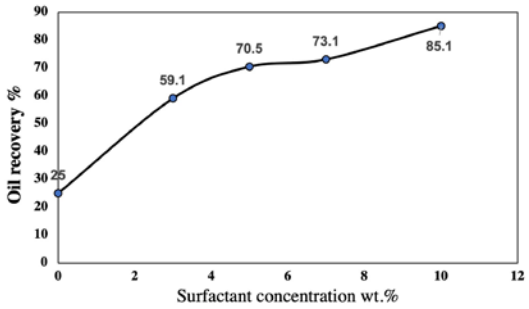

FIGURE 1.31: A plot showing the increase in EOR percentage with increasing surfactant concetration in the nanofluid. In this case the nanofluid is made up of iron oxide nanoparticles and SDS. The plotted data are taken from (Hu et al., 2017).

1.8.10 Studied of the salinity effect on NPs aggregation and oil recovery

The ionic contents in a reservoir vary depending upon the nature of reservoir and formation. Occasionally, seawater is usually used as a major component of flooding liquid. Thus, the impact of salinity on oil recovery is determined for different types of chemical core flooding tests (Shah, 1981). (Alnarabiji et al., 2018) evaluated the effects of two salinity concentrations (or ionic concentrations) and ionic compositions on oil recovery using ZnO NPs based Nano fluids. They observed that the oil recovery at low salinity 3000 ppm of NaCl, has higher recovery than at high salinity 30 000 ppm, 50.0% and 28.3%, respectively. Similarly, (Maghzi et al., 2014) investigated the

impact of silica NPs on polymer performance at EOR flooding operation in the presence of salts by conducting a number of polymer flooding tests. They conducted flooding experiments in the presence and absence of SiO_2 NPs in polyacrylamide (DSNP) solutions with different salinities. The experiment results showed that oil recovery decreased with the increase in salt concentration during the DSNP flooding without NPs, which was ascribed to increasing solution viscosities in salt present. In fact, adding salts has a reverse effect, and the aqueous solution becomes more viscous. Whereas in the case of polymer (PAM) flooding in the presence of NPs, the decreasing rate of oil recovery reduced.

Figure 1.32. shows a list of common NPs that have employed in oil recovery and salinity effect. It can be seen, salinty concentration and oil displacement are not correlated. In case of injected nanofluid made of TiO_2 NPs at 3000 ppm the recovery was 61% (Bayat et al., 2014), however, it decreases to 55% the salt is increased to 5000 ppm (Ehtesabi et al., 2014) and increases again to 80% at 10000 ppm salinity (Ehtesabi, Ahadian, and Taghikhani, 2015). For Al_2O_3 NPs, the percentage of oil recovery increases from 65 to 85% when the salinity increases from 30000 to 50000 ppm (Hendraningrat and Torsæter, 2015a; Yang, Wang, and Fan, 2017). It is difficult to conduct the relation because the number of elements should be considered.

In addition, as reservoir have a high pressure and a high temperature more than 150

C. An experimental study by (Caldelas et al., 2011) highlighted that temperature has an inapplicable effect on NPs retention. Thus, due to desorption and adsorption of NPs has a weak dependence on temperature for NPs detachment (due of Brownian motion) and attachment (due of van der Waals forces). Their outcomes depend on

experiments they did, which are comparisons between two experiments they did at 55 C and 80 C and room temperature (21 C). As clearly shown in Figure (1) at 55 C and 21 C the same recovery is observed, however, at 80 C was a few less when compared to them.

However, (Hendraningrat, Li, and Torsæter, 2013a) argue that temperature has potential effect on hydrocarbon recovery. A higher oil recovery result from a higher temperature, because it will modify the reservoir fluids at pore scale level. In that case, the contact angle between the fluids reduced.

Temperature is affecting both hydrocarbons system and nanofluids, the influence hydrocarbon recovery cannot be popularized. Each reservoir has different temperature, applying nanofluids on reservoir results in lower temperature might not led to the same recovery when applying to reservoir that has lower or higher temperature. As the nonfluid behaviour with different temperature such as increase of the particle aggregation or decompose the materials. It is worth to characterize nanofluid in arrange of temperatures in order to know the threshold of nanofluids injection. Hence, further experimental research for understanding the influence of temperature on oil recovery should studied.

In summary, various studies have shown that NPs have a positive effect on enhance hydrocarbon recovery. Different factors have recognized influence on EOR such as the type, size, concentration of NPs and the nature of the additives (polymer and surfactant). The most common NPs have used EOR in SiO_2 NPs; and it has shown an improvement on hydrocarbon recovery up to 20% from oil in place.

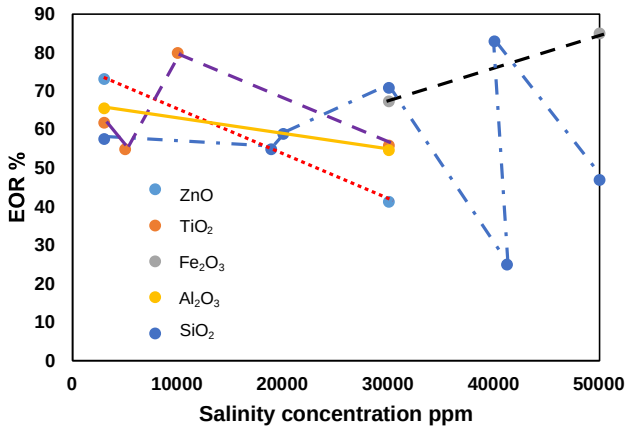

FIGURE 1.32: The EOR% after injection with nanofluid with different salinities and nanoparticles made from different materials. Nanoparticles are either ZnO, TiO_2, SiO_2, Al_2O_3, and Fe_2O_3. The plotted data are taken from (Bayat et al., 2014; Hendraningrat and Torsæter, 2015b; Yang, Wang, and Fan, 2017).

1.8.11 Studied of nanoparticles stability that effect on oil displacement

The stability of NPs is often referred to as the ability of nanoparticles to maintain their stabilization in the face of changing environmental conditions. Or as the ability of NPs to cope with varying environments in different porous media. The study of NPs stability in porous media has many critical contributions in many different EOR applications. For example, in emulsion and foam measurement, the NPs can be evaluated to improve their stability. The reservoir environment has high temperatures and high salinity. Previous investigations evaluated the effect of NPs for EOR purposes; by using either water or deionized water at low ionic concentrations. However, increasing salinity decline the Zeta potential (ZPT) of the nanoparticles, which leads to easy NPs agglomeration (McElfresh, Holcomb, and Ector, 2012). High ionic strength (salinity) in dispersion media results from the presence of salt, which leads to decreased electrical repulsion between nanoparticles

and the Van der Waals force attraction force will dominate. Reservoir rocks are surface charge, and the attraction is more likely to be between particle/particle, but not particle/surface. For all aspects above, it is necessary to maintain nanoparticles stabilization in a high salinity environment, which can be obtained by ionic control, surface modification such as surface-active agent(surfactant), or a combination of both (El-Diasty and Aly, 2015). The ionic strength is illustrated in Figure 1.33., which shows the schematic diagram for a new method for stabilized silica nanoparticles, done by (Sofla, James, and Zhang, 2018).

NPs stabilization has been studied in the aqueous phase in EOR applications such as wettability alteration and interfacial tension reduction and found to be challenging due to reservoir, that is, at high temperature and extreme salinity. Typical temperatures range from 40 C to 150 C, while salinities range from 30,000 ppm to 215,000 ppm (divalent and monovalent ions). (Songolzadeh and Moghadasi, 2017) investigate the stability of SiO_2 and *g*-Al_2O_3 NPs with two surfactants on carbonate rock at harsh environments. They used the UV adsorption and zeta potential to study NPs stability in high salinity experiments. They showed that the Sodium dodecyl sulfate (SDS) improve SiO_2 NP stability in highly concentrated electrolytes as the mechanism above showed (Songolzadeh and Moghadasi, 2017). (Emrani and Nasr-El-Din, 2017) performed their experiments with soft foam stabilized by Fe_2O_3 and SiO_2 NPs and two surfactants in different concentrations. Both the contact angle and foam mechanisms were examined to evaluate NPs performance. The SiO_2 and Fe_2O_3 NPs stabilized foams offered promise as suitable substitutes for polymers as they do not damage the formation of porous media (Emrani and Nasr-El-Din, 2017).

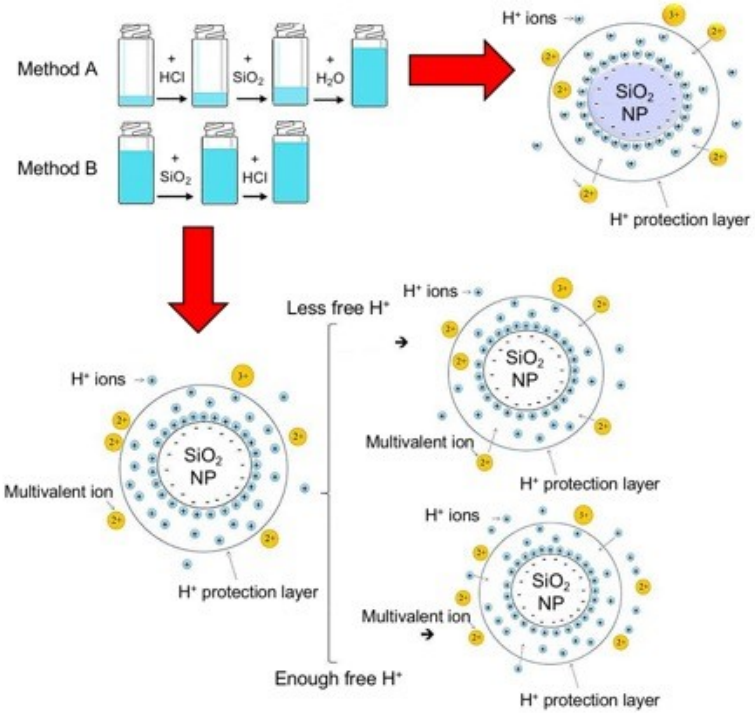

FIGURE 1.33: A schematic diagram for a new method for stabilized silica nanoparticles. Adapted from (Sofla, James, and Zhang, 2018) (copyright: Elsevier 2018)

The impact of nanoparticles on wettability alteration (contact angle), interfacial tension reduction and oil recovery is still under investigation. The use of nanoparticles in fluid displacement agents could reduce the interfacial tension; enhance the wettability of the core to an extra water-water state. Stability of nanoparticles dispersion is one of the principal challenges that need to be addressed. Further, the cost of nanoparticles is another crucial issue in practical applications. Some of the nanoparticles are synthesised from complex and expensive chemicals. Or it required added stabilizer due to low stabilization such as hydrophobic SiO_2 (Hendraningrat and Torsæter, 2015a). The addition of the stabilization also led to an increase in the cost of the treatment. In conclusion, ZnO, SiO_2, Al_2O_3 and TiO_2 NPs are the most tested nanoparticles for oil recovery applications.

1.9 Carbon nanotubes for enhanced oil recovery applications

Enhanced oil recovery is of worldwide importance within the Oil and gas industry and is becoming increasingly important as the discovery and production of fossil resources become more costly. In comparison to nanoparticles that have been discussed earlier, Carbon nanotubes (CNTs) are considered as a newer generation of nanoparticles. Carbon nanotubes are categorised into three types; single-walled carbon nanotube (SWCNTs), double-walled carbon nanotubes (DWCNTs) and Multi walled carbons nanotubes (MWCNTs) Figure 1.34. Radushkevich and Lukyanovich were the first researchers to discover these in 1952 (Qin, 1997). They have shown the first image for MCNTs, and it was a 50 nm diameter. MWCNTs have unique electrical, mechanical, optical, magnetic, and thermal properties. MWCNTs structures are a suitable material for EOR due to their unique interfacial activity, which allows surface tension of the oil/water (O/W) interface to be altered and bring together the oil in a reservoir (Endo et al., 2008). Initially, it might seem that using MWCNT is uneconomical, however, the research into CNTs has increased in the last 20 years, the cost of these nanotubes has greatly reduced along with development in process skill (Bornaee et al., 2014; Hou et al., 2009). However, the value of EOR becomes more apparent when one considers that two thirds of oil in a reservoir is extracted using these CNTs methods. A 1% increase in oil production from EOR methods could increase income by 200 billion US dollars, approximately (£150 billion) (Ershadi et al., 2015).

Due to their relatively lower cost, MWCNTs are more commonly used in EOR research than SWCNTs. To reduce the cost of raw materials, the Research Institute of

Petroleum Industry has constructed the MWCNT production pilot plant with high output capacity (Bornaee et al., 2014). MWCNTs have been heavily studied in recent years and have been shown a promise to use as nano-fibres to reinforce innovative composite. As mentioned early, the wettability alteration and IFT are one of the main factors that effects the oil recovery reduction (section 1.8.4.). The CNTs have been tested for that purpose, and the result shows that CNTs are able to be adsorbed into reservoir grains. (Ershadi et al., 2015) have prepared MWCNTs-silica Nanohybrid using ultrasonic assisted, with sol-gel method, which means adding a suitable amount of MECNT to silica nano-structure. Then, they have characterized it by using Transmission electron microscopy (TEM), X-ray diffraction (XRD) and Field emission scanning electron microscope (FE-SEM). In addition, the effect of nanofluid (MWCNT-silica-nanohybrid) on the wettability of sandstone and carbonate reservoir rocks has been investigated. The crystalline structure of the anticipated materials has been studied using the X-ray diffraction technique, shown in Figure 1.35 (a, for silica b, MWCNT, and c for MWCNT-silica, respectively).

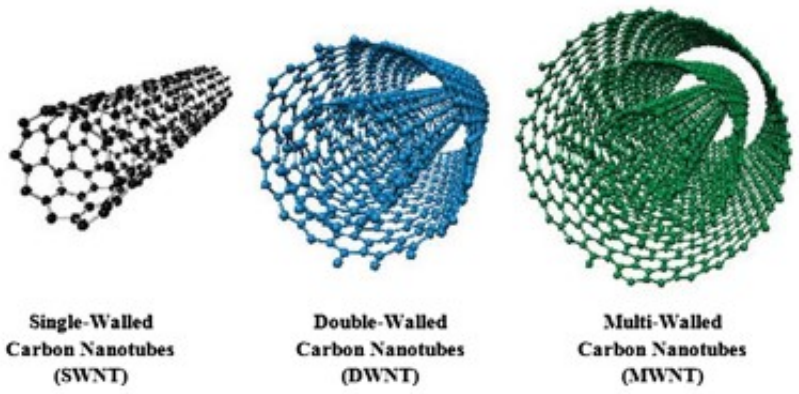

FIGURE 1.34: Carbon nanotubes are classified as either single-walled, double-walled or multi-walled. The image shows an example of the three different types. Adopted from (Khalil et al., 2017) (Copyright: Elsevier 2017).

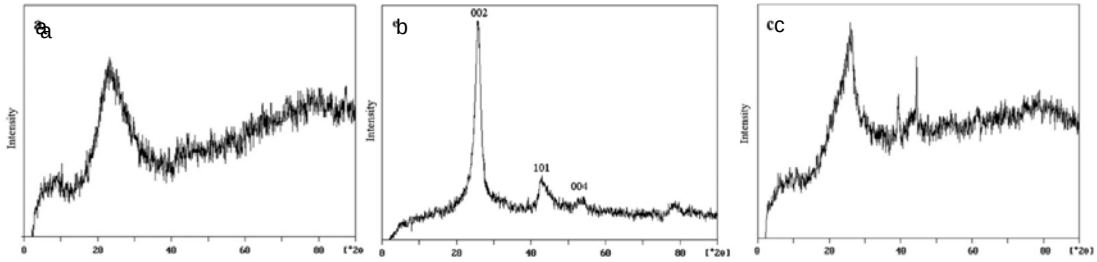

FIGURE 1.35: XRD images of a: silica, b: MWCNTs, and c: MWCNT-silica. The images have been copied from reference (Ershadi et al., 2015).

As seen in XRD image (Figure 1.35, a), the silica nanohybrid has an amorphous structure, and MWCNT-silica has mean peaks at 26 and 41 with attention to silica nanohybrid peak. In this work, the contact angle between Kerosene (oil phase) and reservoir rock sample was shown to increase from 115 to 128 for sandstone rock in the presence of saturated nanofluid, there was also, a corresponding increase from 82 to 140 in the case of carbonate rock. These results indicate that MWCNT-silica nanofluids could change the wettability of sandstone and carbonate reservoir rocks from hydrophobic to hydrophilic without using surfactants (Ershadi et al., 2015).

Moreover, research done by (Bornaee et al., 2014) showed that MWCNTs able to act as a stabilizer for an oil /water emulsion by functionalized MWCNTs with a silica nanohybrid using sol-gel method. The water phase in their research was taken from two-reservoir oil. According to their results, the weight ratio of CNTs to silica was the crucial factor for synthesis. The authors found that the best ratio for MWCNT/silica nanohybrid was less between 28 to 33 wt.% for achieving hydrophilicity and hydrophobicity (HLB). Furthermore, they found the optimum time for stabilization without ultra-sonication was 12 days whereas with ultra-sonication it was 4 hours (Bornaee et al., 2014).

Another factor affecting the hydrophobicity of a surface is the presence of cations such as Mg^{2+} and Ca^{2+} in the water. These divalent ions affect the hydrophobic balance more strongly than univalent cations such as Na^{+}. As mentioned above, silicananohybrid has been achieved stable emulsion only with change cations concentration, and without chemical addition (emulsifier), it holds promise for EOR applications. Emulsifier addition increase treatment cost and time, and the emulsion are eventually will separate because they are still inherently unstable on their own. In addition, (Esmaeilzadeh et al., 2015) have studied the liquid-wetting of SiO_2, TiO_2 and CNT nanostructures (Figure 1.36. SEM images of nanofluids on reservoir rock) by investigating their effects on the wettability of carbonate rock by testing different concentrations. Nanoparticles synthesized by the sol-gel methods were characterized by FTIR, SEM, TEM and XRD analysis. The authors observed that while untreated rock yielded a contact angle of zero when wetted by drops of n-decane or water, rocks treated by nanofluids 0.06 wt.% in an alcoholic medium produced water contact angle of 161º, 164º and 163 for SiO_2, TiO_2, and CNTs, respectively. In addition, they investigated the thermal stability of these nanofluids on carbonate rock and heated them at 160 C. According to their results, all nanofluids showed excellent nanostructure stability at that testing temperature (160 C).

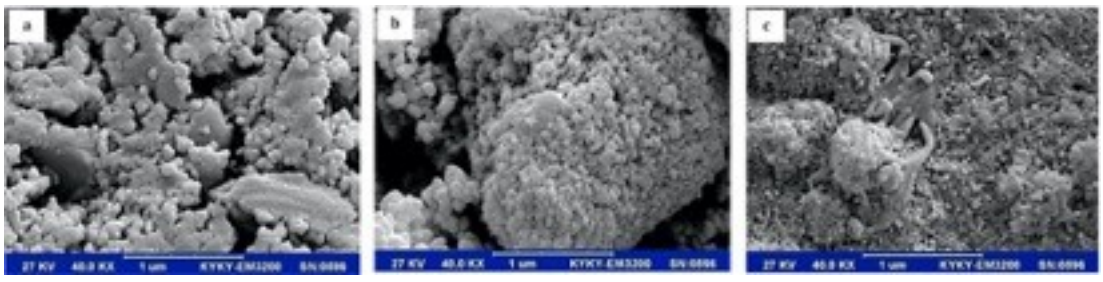

FIGURE 1.36: SEM images of nanofluids: SiO_2(a), TiO_2(b), and CNT nanos- tructures (c) on reservoir rock. Image copied from (Esmaeilzadeh et al., 2015).

Furthermore, the multi-carbon nanotubes have generated much attention as a novel type of adsorbent because of their high capacity for oil-water separation (Pourjavadi and Doulabi, 2013). In order for oil absorbing to be swollen by nonpolar oil medium, it must be hydrophobic and the Van der Waals interactions between oil and absorb ants is the driving force. In their study, they used cross linked co-polymers to establish hydrophobic moieties (alkyl or phenyl) groups, where synthesized and modified for swelling purposes for oil absorbent application. (Pourjavadi and Doulabi, 2013) tested their cross-linked co-polymers on pure toluene, and dilute crude oil. Their results indicated that, the oil absorbents including CNTs showed the highest oil absorbency: 42.6 g when used in toluene and 36,0 g when used in crude oil. In addition, the high hydrophobicity of MWCNTs makes them a candidate for the removal of oil from wastewater.

An experiment by (Fard et al., 2016) showed that doped CNTs, where doping was with iron oxide nanoparticles using a wet impregnation technique, were effective in removing oil from water, exhibiting sorption capacities of more than 7 g/g for gasoline oil. Consequently, increasing the percentage of iron oxide on the CNTs surface led to increased separation of the emulsified oil from the water. Figure 1.37. below shows the synthesis of the Fe-doped CNTs.

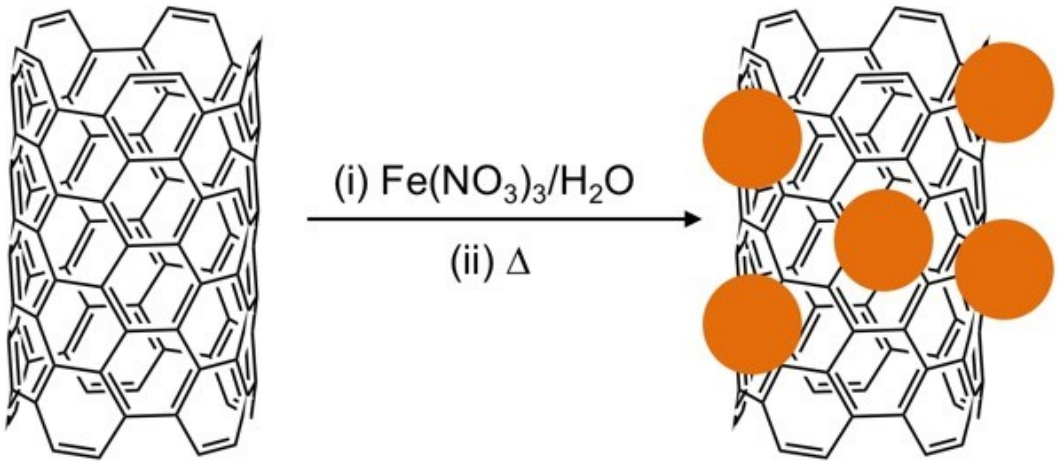

FIGURE 1.37: Schematic illustration of the synthesis processes used to produce hematite nanowires using CNTs as support. Adopted from (Fard et al., 2016) (Copyright: Elsevier 2016).

A novel material established from a composite of MWCNTs and Fluoroelastomer rubber (FKM) has been developed by (Ito et al., 2011) to recover oil from deep and hot reservoirs. They overcame the sealing technique issues and clarified the mechanism of Nano-network reinforcement based on experimental data from oil fields around the world. They studied the reinforcing effect of MWCNTs concentration on FKM matrix due to their low glass transition temperature. Ito and co-workers used MWCNTs of 80 nm diameter and 10-μm length to define their storage modulus with different concentrations. Their result indicated that as concentration increase, the storage modulus increases. Furthermore, they found 9 wt.% has a critical point of the storage modulus, and an efficient network of MWCNTs. In addition, the resulting sealing solution underwent field tests around the world and marks a rare success story for the use of nanotechnology in the oilfield. Sealing tests were carried out at depths of over 4000 m at offshore sites in the Gulf of Mexico,

North Sea and North Africa (Ito et al., 2011). The result has considered the success of increasing the efficiency of drilling fluid (this is out of this project area).

In spite of the advantages of applied CNTs/MWCNTs in the oil and gas industry, it is important to take consideration of the relationship between density and weight of CNTs with geometric features: length, inside/outside diameters, and the number of walls, which is not easy to prepare (Laurent, Flahaut, and Peigney, 2010). More, the purification and separation are remarkable during the synthesis of CNTs. For example, Duque and co-authors have found that the SWCNTs diameter might highly influence their solubility in aqueous solution (Duque et al., 2010). Their results showed that the larger diameter of SWCNTs is less soluble than CNTs with smaller CNTs in a hydrous solution.

1.10 Micromodels and their usage in oil recovery applications

Developing hypothetical models of reactive transport and multi-phase flow in porous media at the pore scale is an important and common challenge to various areas within science and engineering (Oostrom et al., 2016; Soll, Celia, and Wilson, 1993). Progressively, it has developed remarkably in underground dynamic flow and transport research because of its relevance to multiple areas such as: wastewater treatment, oilwater separation processes, transport of oil-soluble pollutants in land and subsurface water, generation of foam (Almajid and Kovscek, 2016), and emulsion for food production (Yun et al., 2017). All these applications involve multiphase flow. In addition, hydrocarbon recovery from reservoir, conformance control, water flooding and oil recovery are multiphase processes (Yun et al., 2017).

The studying of multiphase flow is known for using realistic porous substance applications like oil displacement core flood and micromodel devices. Core flooding is a method which uses actual reservoir oil rock to measure oil displacement and residual (how much oil will remain in place OOIP). However, micromodel devices, is another method which uses a pattern (geometry or classic) to mimic the reservoir rock in order to study the mechanism of oil displacement. Using micromodel can save a lot of time, however, the interaction between the tested materials and porous medium cannot predict.

In these investigations, macroscale data including physical properties (porosity and permeability), saturation profile and pressure drop are regularly measured. Due to the multiphase fluid scale variability of wettability in such properties, and because the 3D geometry of actual porous media (surface rock) is complex, the direct visualizations and quantitative description are often difficult. In that case, the direct carbonate and sandstone reservoir visualizations and quantitative description are often difficult due to multiphase fluid scale variability in such properties.

In the last 30 years, micromodels have been used more by researchers for studying multiphase fluid behaviour inside microstructures. Micromodels provide a tool that can be used to investigate and visualize multiphase flow at the pore scale. For example, surrogates for pore bodies and throats. In addition, micromodels have been used in studying a number of fundamental flow phenomena such as foam coalescence, cross section interface, capillary pressure (trapping or fingering), fluid analysis single-phase flow and Newtonian and non-Newtonian multiphase flow (Geistlinger, Ataei-Dadavi, and Vogel, 2016).

Many methods are generating patterns that are used in micromodels such as perfectly regular, partially regular, fractal or irregular patterns (simulate microstructure of real porous media). Various fabrication materials and approaches were used in making micromodels. For example, glass beads and Hele-Shaw, optical lithography, soft lithography, dry/wet/ plasma or laser etching and stereo lithography. Micromodels can be visualized by using microscope techniques and digital camera imaging.

Chatenever and Calhoun 1952 first studied the mechanism of microscale fluid in porous media using micromodels. Subsequently, micromodels have become used for investigating various applications and processes in multiphase flow. Generally, micromodel is a 2D representative porous media network at the micron dimension in which solutes and fluids flow. Visual observations are made of micromodels to study the movement or flow of fluid and solute or colloids. Therefore, it is necessary that transparent materials are used to manufacture micromodels. Typically, these are glass or quartz, but silicon or polymeric substrate with a glass cover to enable visual observations can also be used.

1.10.1 Fabrication of micromodels

The following section discuss the micromodule fabrication methods in details:

1. Glass bead and Hele-Shaw models

   Micromodels are in the centimetre squared (cm^2) area scale and have various geometries. At the early stage, (Chatenever and Calhoun, 1952) fabricated micromodels with regular and simple geometries. Later, the computer generation of micromodels has been used to study complicated geometric

patterns. The glass beads and Hele-Shaw model were one of the first models developed to fabricate micromodels. This model consisted of a single glass layer (observation cell) and spheres sandwiched between two plates. (Chatenever and Calhoun, 1952) noticed that adding more layers made the visualization of the fluid's behaviour very complicated. To minimize this challenge, two different flow observation cells were used. This micromodel consisted of a Lucite base (Lutie is a solid transparent plastic that is made of polymethyl methacrylate), a gasket, an observation window and a compression. The Lucite base is composed of glass (top, spheres and base), an observation window (top cover), a gasket, and a compression cover. There was a hole in the centre for inter fluid (exchange) and also at the end as the fluid outlet. These micromodels are easy to create, but they are difficult to use for 3D visualizations of fluid flow using optical microscopy.

2. Photolithography (optical lithography)

   Later, photolithography was developed for micromodels of the preferred dimensions such as pore number and size geometry at micrometres or smaller (Cheng et al., 2004). In this method, the micromodels started with a digitally produced pattern, which based the statistical distribution of the pores either with or without a spatial correlation for dimension to network pattern. The required pattern was printed (with a *photoresist* layer) on transparent materials such as glass or quartz to produce a 'mask'. For a small network pattern, the mask was printed based on the magnified image. Otherwise, for the large and deep networks, the mask has the same network dimensions. The photolithography method can be summarized into steps: application of the photoresist onto the glass substrate; soft bake; mask aligner setup (the mask is

exposed to photoresist by ultraviolet light (UV)); exposure; development; and hard bake. The materials that have been used for photoresist masks are generally polymeric substrates. The substrate should be perfectly clean before using a thin photoresist layer. SU-8 (8 epoxy based negative photoresist) is usually used as a photoresist layer and is spun on the glass substrate. The thickness of the photoresist layer, and the final network depth, depends on the duration of the spinning time, spinning speed, and the photoresist that has been used. Similarly, to the glass beads and Hele-Shaw model, there is an inlet and outlet hole drilled into the glass to introduce and release flow fluids.

Figure 1.38. is a schematic diagram for micromodel.

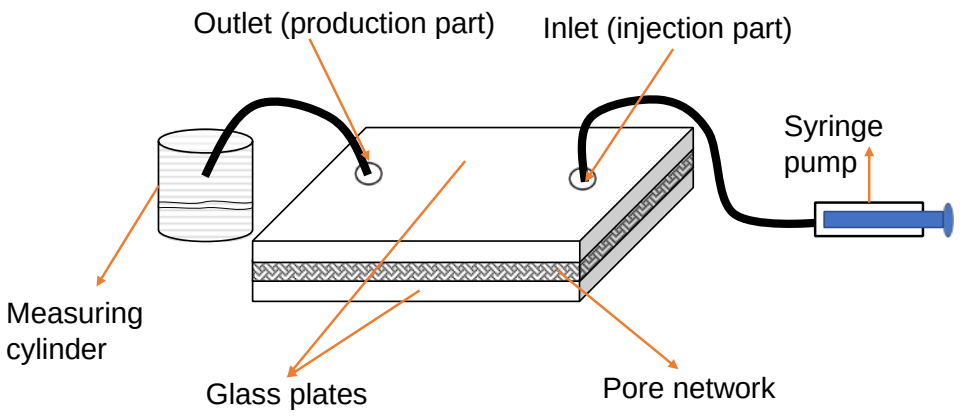

FIGURE 1.38: A schematic diagram showing the basic setup of a micromodel. The small lab set-up mimics the injection of fluid into reservoir rock.

This method is attractive as it is easy to make, inexpensive and there is no mixing wettability, since it is made from one material. In another word, as has been explained in wettability section that each surface has its own wettability, that's means glass substrate wettability is different from silicon and polymer substrate, thus, mixing wettability occur when using two different substrates. However, it is more likely the whole procedure can fail at any step, especially

for a very small scale, because there is not enough space on the surface for binding between the photoresist that forms a solid substrate and the thin film of photoresist that can be used as a glue. In addition, there is a problem that emerges from the photo-resistivity natural of photoresist material. The latter is able to produce N_2 bubbles (also called pockets), when its exposed to light, that has UV spectrum or is close to the Violet wavelength. That is by the pockets grow in size and breaking photoresist which damage the network pore. In that case, to prevent light from damaging the photoresist, the micromodel should be put inside the place that has a filter or replace any source that makes UV spectrum in the laboratory. An experiment done by (Karadimitriou and Hassanizadeh, 2012), where they filled the testing micromodel with water, and left it the exposure into light, and then after three days, the defaults were clearly seen (red circle outlined in Figure 1.39-a: the testing micromodel first day, and b: the same micromodel after three days. In conclusion, neither using high-quality light nor filter, both solutions make fabrication micromodel following this method an expensive technique.

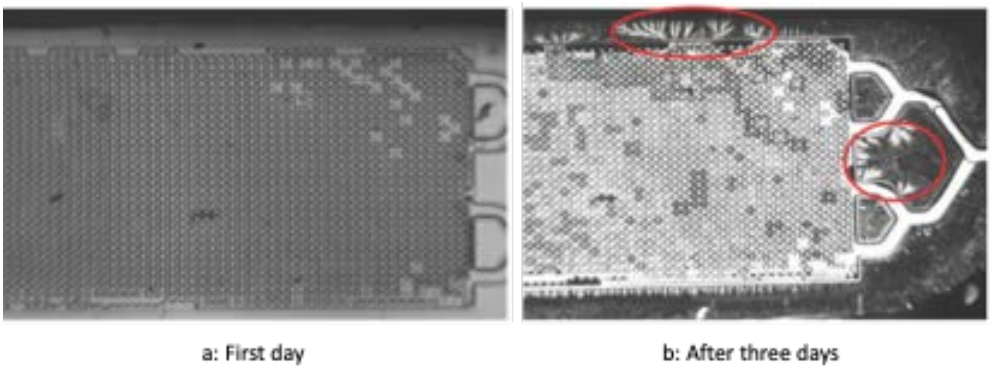

FIGURE 1.39: Photo images of micromodel filled with water, a: first day, and b: after three days of light exposure. Sections highlighted by red circles show damage of micromodel by UV light. Adopted from (Karadimitriou and Hassanizadeh, 2012) (Copyright: Soil Science Society of America 2012).

3. Micromodel produced through etching

This technique is based on plasma radiation, chemical interactions, and laser interaction with substrate, such as glass, polymer, and silicon (Zhang et al., 2010). The etching method can be summarized into steps: produce desired pattern for the micromodel from previous method described in sections (1.10.1.1.and 2), as well mask is prepared following one of the techniques that was described in section 1.10.1.2. After that, on a glass substrate, the chosen network pattern is formed, and covered with a thin layer of photoresist. Mask resolution affects the etching process result. The development of the pattern network through using solvents, is affected by the thickness of the photoresist layer, which determines the depth of the chosen flow network. After that, the desired network is ready for the etching method, there are two types of etching: wet and dry etching, the following which will be described.

In 1961, Mattax and Kyte first etched a micromodel based on a chemical reaction. Etching rate and duration time are responsible for etching depth. Wet etching (using acid, such as hydrofluoric acid (HF) (Xu et al., 2017) and laser/plasma etching (dry etching (Cheraghian et al., 2017)) have been used on silicon, glass or polymer substrates. HF acid is used in chemical/wet etching to etch silicon or glass. In wet etching, copper or photoresist layer are used to cover the area from effect by acid, copper can be removed later by using chemicals. The wet etching occurs in an acid bath, the setup can be broken into three steps: etchant diffuses into the surface for subtraction, the reaction between the materials being subtracted and the etchant, finally, the diffusing of the result by-products from the surface reaction. The wet method is a very

common process of micromodels fabrication; however, it has some limitations, such as: the topography of the pore walls is sloped not vertical, acids liquids are an isotropic, which lead to making a curve at the bottom of the selective pore, and this erodes substrate in all directions.

Dry etch is another way of etching silicon or glass by electromagnetic radiation. This can be done by using plasma beam ion milling or laser source (Kolari, Saarela, and Franssila, 2008). Ion milling generated by an ion gun especially argon ion (Ar^{+e}. This method can be summarized into steps: etchant surface by ion, transfer momentous or reaction with surface, by-product desorption and spread of the by-product to bulk gas (Cottin, Bodiguel, and Colin, 2010). The etching from the dry method is called as anisotropic. Combinations between isotropic and anisotropic etching is an illustration in Figure 1.40, and the schematic diagram for ion-milling beam (dry etching) is shown in Figure 1.41.

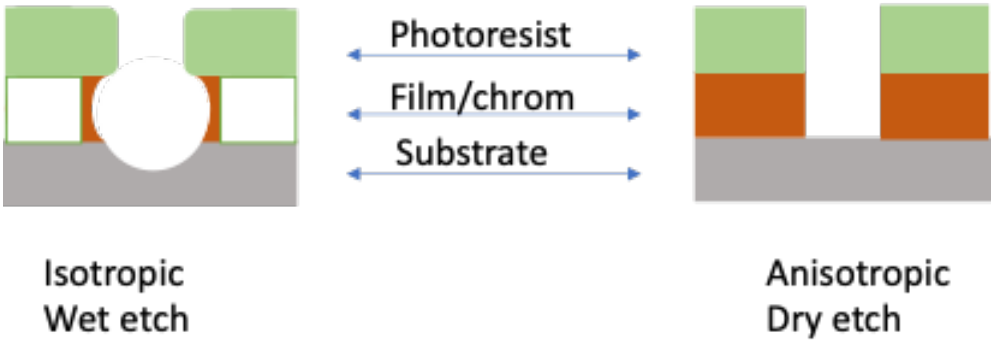

FIGURE 1.40: Schematic showing the difference between wet (left) and dry etching (right). Dry etching is preferable due to the sharp edges of the channel. Images adapted from reference (Kao et al., 2013).

However, if the etching is done by a laser beam this method called lithography, which was introduced by (Ehrfeld, 1987). The geometric pattern formed on the glass or silicon and the procedure is controlled by a computer. The controlling

pore walls feature from using both techniques (laser and ion) are not straightforward. However, they are very anisotropic, which mean the pore walls diminished. It reserved for very shallow and small channels, then the desired pattern has been shaped on the substrate, the inlet (injection part) and outlet (production part) are produced as discussed in previous techniques, finally, cover etching micromodel layer with second plate that has two holes (inlet and outlet). The sealing can be done using a muffle furnace (or high temperature oven) or placing a thin layer of polymer between two-glass substrate and baking in an UV oven. Glass and silicon bonding can be obtained by heating around 400 C whilst applying an electric field towards the glass-silicon substrate to ensure better contact through correlate electrostatic force. This technique is known as anodic bonding or field assisted.

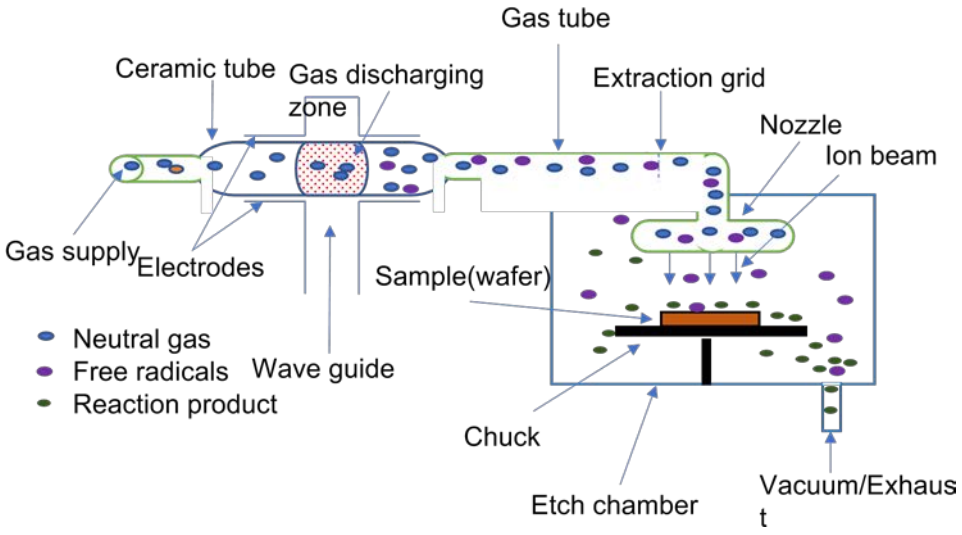

FIGURE 1.41: A schematic diagram for ion milling (dry etching).

4. Stereo lithography

Another method done computationally is called Stereo Lithography and has been developed by (Hwang et al., 2008). An additive fabrication technique

allows the fabrication of parts using a computer-aided design (CAD) file. In this method, the manufacturing of 3D micromodels by stereo lithography is based on the spatially controlled solidification of a liquid resin by photo polymerization. The setup consists of a computer-controlled digital light projector or laser beam, this is firstly placed under the resin surface, depending on the required depth of the resin reservoir layer. This method consists of five steps: laser beam formation of the desired pattern on the resin surface; photo-polymerization; incremental lowering of the platform; and finally, cleaning excess resin from the structure as soon as construction is finished. This fabrication is an effective method for large structure at micrometre. In addition, the manufacturing can be completed in 1 day. However, it is an expensive technique and less widely used.

Last technique that's brief summarize in this section is Soft Lithography (Senn et al., 2010). It used soft materials such as molds, photo mask and elastomeric to fabricate substrate. The differences of this method include microcontact printing, replica molding, micro transfer molding, solvent assisted micromolding, and micromolding in capillaries. The soft lithography method is the most desirable technique for fabrication micromodels that has two phase flow scale. These are the following steps for manufacturing: creating digital micromodels channel and printed on transparency materials; a glass/silicon wafer is spin-coated with photoresist to create a patterned of glass/silicon wafer (called a master) by using photolithography; the master wafer is insert in a petri dish and a mixture of liquid PDMS and curing agent is prepared, which then poured over the master wafer in the petri dish. The PDMS polymer is

degassed under vacuum and then cured; after curing, the polymer is peeled from the master, and the PDMS slab with the desired network is placed on a pre-cured thin slab of polymer to close the network and is exposed to an ion (O_2) plasma so that bonding can take place. This method is an easy and cheap to make, highly accurate and can mimic any network pattern. However, it requires a clean room to fabricate silicon and treatment to fix wettability problems. PDMS polymer is a hydrophobic behaviour, although after bonding the plates using O_2 plasma, it becomes hydrophilic. Over time, the PDMS recover its hydrophobics.

1.10.2 Micromodel's materials and visualization methods

Quartz and glass have been shown to be suitable substrates for micromodel experiments. These materials are widely used in glass beads and Hele-Shaw micromodels. The advantages for these materials are that they are cheap, easily polished at given dimension, have chemical and mechanical stability and stabile wettability properties (Xu et al., 2017). The disadvantages of creating a network from glass and quartz materials is that due to their physical properties. Their preparation has to be carried out in a clean room/ space to prevent any environment contamination. Alternative materials such as polydimethylsiloxane (PDMS) and polymethylmethacrylate (PMMA) have also been used.

Pictures and videos are collected in order to study fluid flow, fluid configuration and other variables inside the micromodel. There are four methods for data analysis: either visualization by microscope/camera alone (Cheraghian et al., 2017) or combined together with fluorescent microscopy and the photoluminescent

volumetric method (Yun et al., 2017; Roman et al., 2016). The choice of visualization approach is related to the experimental data required, such as: vertical walls, chemical and mechanical stability, or stable wettability properties, then quartz or glass is the most suitable materials. First the micromodel is placed under the microscope objective lens, then the camera is fixed on the outward the microscope and connected to a computer to collect data. Software is then used to analyse images and videos.

The difference from camera and microscope is that the camera captures the images directly. The camera can be fixed to all micromodels without requiring to move the micromodel. In that case, camera is the most suitable instrument to study the movement of fluid through the micromodel when compared to microscope. Table 1.10 shows the compaction between visualization methods.

1.10.3 Volumetric imaging and confocal microscopy

The photoluminescent volumetric imaging (PVI) has been introduced by (Montemagno and Gray, 1995), which is to construct their micromodel media. An optical quality quartz has been used as a micromodel grains, with two immiscible fluids having a refractive index that matched to quartz substrate. Onto fluid-fluid interface, they used dopped with specific fluorophores properties that are preferentially partitioned into the wetting phase. A planar laser source has surveyed the system at successive planes. The fluorophores getting excited by laser beam which then the fluid-fluid interface is illuminated. As seen in Figure 1.42., a CCD camera is used to take the fluorescent images. Then, captured images goes through the process of being able to use the captured images to generate a 3D data set, that shows the fluid-fluid interface location, as well as the pore space.

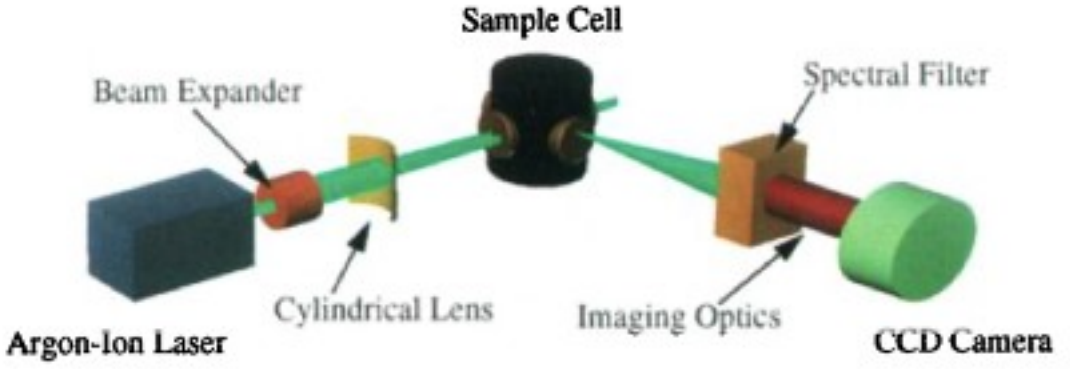

FIGURE 1.42: A schematic setup diagram for the photoluminescent volumetric imagining method of experiments. An argon-ion laser is focused on a sample, and a CCD camera takes. Adopted from fluorescent images (Montemagno and Gray, 1995) (Copyright: Wiley 1995).

Later (Stöhr, Roth, and Jähne, 2003), used the PVI method to accomplish 3D measurements of the transportation of single-phase flow at the pore scale. Their work was the first one with high resolution technique which visualize flow of two immiscible fluid at the same time.

A micro particle imaging technique (μ-PIV) is one of the fluorescent applications. It is used to examine mixing of fluidic and their transport at micrometre scale. μPIV is also used to: examine the pressure driven flow, electroosmotic flow, capillaries of the blood fluid dynamic flow in vitro (Sugii and Okamoto, 2004), and in vivo (Sugii, Nishio, and Okamoto, 2002). As seen in Figure 1.43, the schematic diagram for μ-PIV (Wereley and Meinhart, 2005).

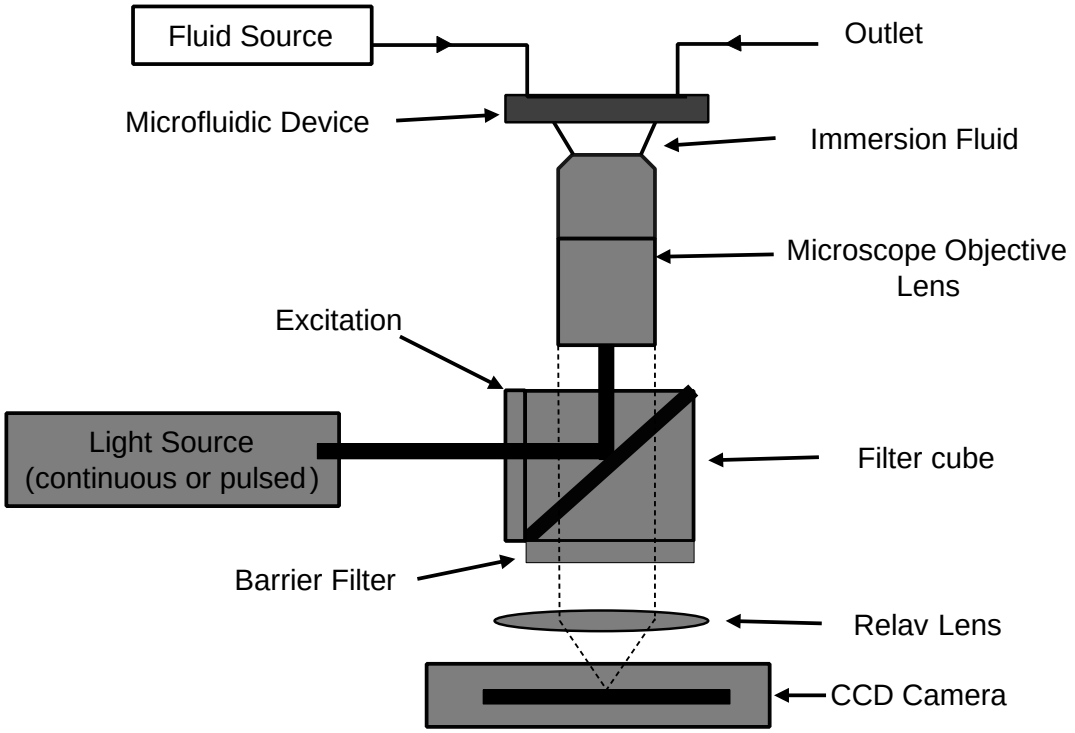

FIGURE 1.43: Schematic description of typical μ-PIV hardware, where a microfluidic device is imaged using a series of lenses Adapted from (Wereley and Meinhart, 2005) (Copyright: Springer 2005).

Another technique based on laser induced fluorescence is confocal microscopy (CM) but is point by point image which is different than PIV method. Sharp images have been created by confocal microscopy of specimens that allows the instruction of 3D image. Thus, done by supporting 2D image which obtained at following layers. In

1957, Marvin Minsky patented CM (Minsky, 1996), and in 2005, Semwogerere and Weeks (Wnek and Bowlin, 2008) presented the principle concepts of CM. As seen in Figure 1.44 a schematic of CM, the light comes from monochromatic laser source is reflected from a dichroic glass and projected through an objective lens onto specimen. The fluorescent dye or fluorescent particles are used to dye sample. There dye particles absorb the laser light from the laser source, then emit, when the

wavelength of absorb light is lower than the emit light, the light get de-excited. The emitted light crosses through the dichroic glass while the light from laser source is reflected back to the main source. Two filters are applied to prevent other light from passing through to the sample point and only light along this axis is used.

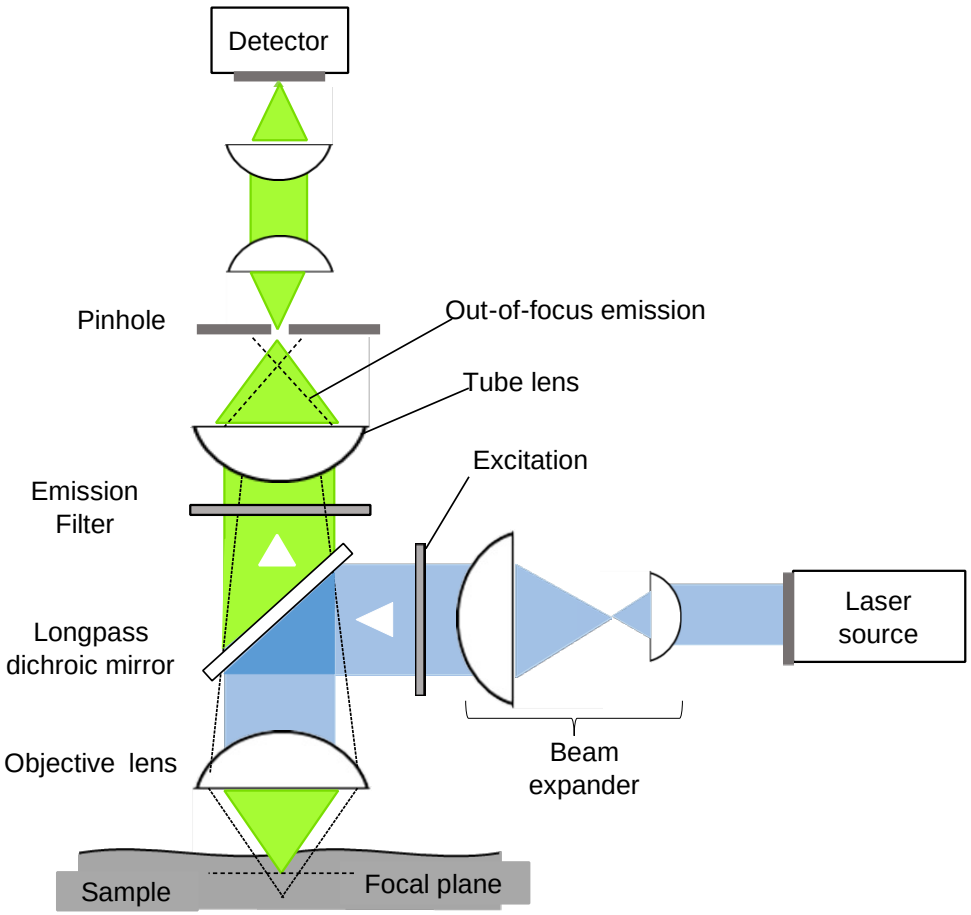

FIGURE 1.44: A schematic diagram of confocal microscopy. Adopted from (Wnek and Bowlin, 2008) (Copyright: CRC Press 2008).

TABLE 1.10: Comparison of different visualization techniques.

Visualization method	Advantages	Disadvantages
Microscope and camera	• Any transparent (partially) 2D Micromodel. • High resolution optical image.	• Not suitable for 3D Models. • limited in resolution >1 μm.
Direct visualization with a camera	• Low memory requirements. • High acquisition rate.	• Not suitable for 3D Models. • very low resolution.
Photoluminescent volumetric imaging	• 3D porous media.	• Refractive index matching is necessary.

	• High resolution.	• Relatively, slow result. • Relatively expensive
Confocal microscopy	• Very high resolution (submicron). • Quasi-static and very low speed effects.	• Effective for depths up to 250 μm. • Relatively expensive and very low acquisition rate. • not suitable for dynamic effects.

1.10.4 Micromodels applications in multiphase flow

The following subsections discuss the multiphase flow studies that done using micromodels devices:

1. Two phase displacement processes

   Most studies with micromodel applications have used the multiphase flow and immiscible displacement. In addition, the mechanisms that dominate drainage and imbibition such as capillary fingering, viscous and snap-off have also been investigated using micromodels. The first studies of multiphase flow at quasistatic conditions were carried out by (Lenormand, Zarcone, and Sarr, 1983) who used photographically etched molds and transparent polyester resin. They noticed displacement of fluids created by multiphase flow at different conditions: snap-off and piston type motion. In the pore throat, when the wetting phase collars and the gas bubble move through the pore throat, that mechanism is called “snap-off”. Furthermore, normally it uses a high flow water injection from high pressure pumps, which are placed close to the tower of deoxgenation. As the pressure is very high, water play like a piston pushing oil toward to walls. These types of defects could occur depending on the space occupied by the non-wetting phase and the number of ducts. Later, (Ghazanfari et al., 2007) used a glass micromodel, which is considered a porous media, to study the capillary pressure curve that influenced the pore scale dynamics and pore size characteristics of the porous model. Their findings were that the trends line of the extraction for the distribution of the pore size are close but

not well fitted, thus due to that the estimation of dynamic capillary pressure is not sufficient for pore size distribution.

Cottin and his co-authors, 2010 investigated the movement of more viscous fluid during drainage experiment; They discovered that fluid displacement depended on the capillary number. Their studies used two types of micromodels: a glass micromodel, fabricated by the soft lithography method, and a PDMS micromodel, fabricated by the wet etching method. In this work, they provide evidence for the influence of the viscous forces on the invasion procedure and the capillary force. If the capillary number is large, the viscous forces are increased, while at low capillary number, the time when the injection liquid flowed cross a single channel and built a wide-open structure (Cottin, Bodiguel, and Colin, 2010).

2. Measurements of rocks wettability and interfacial tensions

   The wettability of reservoir rocks wettability and interfacial tensions (IFT) of interfaces (liquid/liquid, and liquid/solid) are key factors in hydrocarbon recovery (Schembre, Tang, and Kovscek, 2006). In these phase studies, the fluid saturation and IFT area are the main variables that influence oil recovery. The reservoir wettability converts strongly water/wet to either oil/wet or mixed wet because of the interaction between hydrocarbon component, mineral surface and connate water in reservoir. Micromodels have made studying the IFT of fluid-fluid interactions possible. Yun and Kovscek, 2015 replicated realistic surface interactions between rock and fluid reservoir in 2015. They modified a silicon micromodel to become a strongly water/wet surface. Others fabricated $CaCO_3$ to build/design a micromodel that replicated the tunable

geometry surface of the carbonate reservoir, in simple micro-fluids channel, with homogenously aligned posts (Lee et al., 2016).

3. Relative permeability

Buchgraber et al., 2012 created an etched silicon 2D micromodel based on photolithography to investigate characteristic dual porosity. Dual porosity (microporosity) is defined either as a size threshold (>1 μm) or any pore dimeter of less than 62.5 μm (Cantrell and Hagerty, 1999). The 2D Buchgraber micromodel was created from a mosaic of silicon wafer based on a backscattered SEM image of a carbonate reservoir section. The microporosity studied for Arab-D (Ghawar field of Saudi Arabia from Arab Formation) reservoir pattern that has a pore size >21μm. Their model showed that dual porosity micromodel at pore level mechanism of interpret with petro-physical and multiphase flow properties. Furthermore, Buchgraber investigated permeability using Darcy's law by changing etching depth. They showed that permeability changes as etching depth changes as shown in Figure (1.46 and 1.45). The fluids that used in permeability experiments are ultralow interfacial tension surfactant systems.

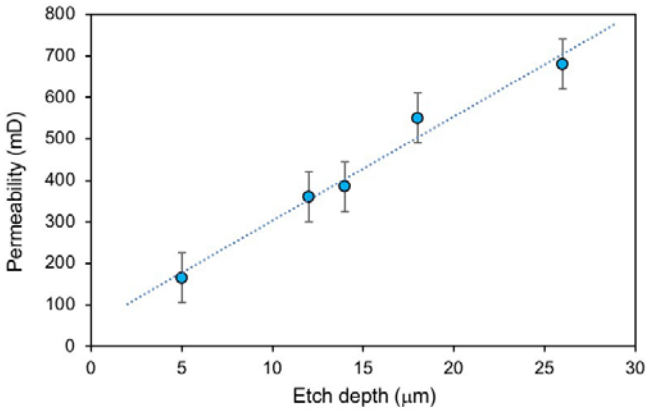

FIGURE 1.45: Relationship between permeability (mD) and etching depth (μm). Adapted from (Xu et al., 2017) (Copyright: Royal Society of Chemistry, 2017).

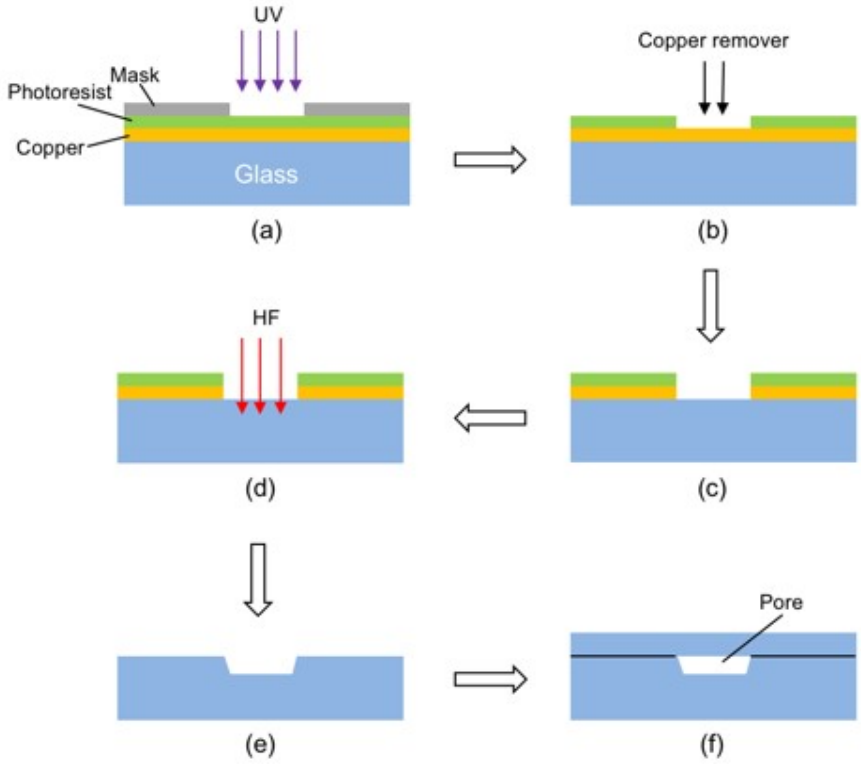

FIGURE 1.46: Schematic representation of the HF etching procedure for a 2D micromodel comprising: (a) exposure to UV of the photoresist through a mask, (b) expos-ing the copper to the pattern of the mask, (c) removal of the copper layer, (d) HF etching the silicon substrate, (e) creation of a trench, and (f) formation of a pore structure by bonding a cap layer to the etched substrate. Adapted from (Xu et al., 2017) (Copyright: Royal Society of Chemistry, 2017).

This technique has been successfully used by (Yun et al., 2017) for creation of a dual depth and dual porosity micromodel from silicon wafer. They developed silicon-etched micropores of 1.5 – 21.0 microns in width which is less in depth than macrospore, that's improve the realistic of a single pore micromodel for carbonate pore structure. They used the same micromodel fabrication as Buchgraber (μ-PIV) measurements for the first mask, called complete-pore, which included micro and macro pore sized structures. The second mask (dual depth) was prepared by exposing the first mask to duplicate erosion and dilation seven times to remove throats and surface roughness. This mask was called a partial pore. According to their results, the porosity difference between

partial and complete pore is 11.2% by measuring throat size distribution of backscattering SEM image after mercury injection. In this work, relative permeability, real time velocity of injection fluids and pore scale observations were characterized. They found a reduction in the relative permeability results for oil saturation from (0.52 to 0.39) and water saturation from (0.44 to 0.34) in single and dual depth respectively. This was due to the trapping of residual oil in the micro-pores for the single etched depth and macro-pores for the dual etched depth.

Roman et al., 20162016 investigated two patterns etched on silicon wafer: (1.88 mm ⇥ 0.6 mm) to study a thin sandstone section with homogeneously distributed cylindrical grains of 40 μm in diameter. Both micromodels contained two microchannels of 500-μm width to allow fluid to enter and exit the porous medium. They tested the comparison fluid which was between single-phase flow and twophase drainage. The single-phase flow rate was 5⇥ 10^{4} to 1⇥ 10^{2} mL/min for water seeded with CML (Carboxylate Modified Latex), which is microparticles (Polybead carboxylate Microsphere with 1μm diameter); Carboxylate functional groups which is contained microparticles, gives the microparticles negative charge, and hydrophilic surface behaviour. In addition, the density is close to water at 1.05 g/cm^3. However, they used a mixture of water and glycerol as the wetting phase and n-heptane as the non-wetting phase for a two-phase flow. The IFT value of the micromodel was between 30 to 50 dyn/cm, resulted in a capillary number (N_{ca}) near to 1⇥ 10^6 using Equation 1.22, where μ_{nm} is the viscosity of the non-wetting fluid, u is the injection fluid velocity (L/min), and *g* is the interfacial tension.

$$N_{ca} = \mu_{nw} u / g \tag{1.22}$$

The injection fluid velocity (u) is define by Equation 1.23, where Q is the flow rate (mL/min) and A is the section area define by Equation 1.24, where W is the width (mm), D the depth (mm), *f* is the micromodel porosity (dimensionless).

$$u = \frac{Q}{A} \tag{1.23}$$

$$A = W \rightarrow D \rightarrow f \tag{1.24}$$

In addition, to validate the two-phase fluid velocity measurements, they compared the experimental data and numerical simulation of different geometries.

The numerical simulation was in agreement with experimental measurements.

4. Enhanced oil recovery

Another potential usage for a micromodel is a visualization tool for flooding (oil Recovery). The visualization tool for studying the displacement of oil from another liquid (water, nanofluid), or gas near an oil well. The majority of the media involved in EOR are the injection of chemical agents such as foam, polymer, surfactant and nanofluids or gases. The media used depend on the physical properties of the phase, capillary number, reservoir conditions (pressure and temperature), and the viscosity and dynamic flow of fluid. Several researchers have studied these factors using micromodels (Yousefvand and Jafari, 2018; Cheraghian et al., 2017; Yousefvand and Jafari, 2015; Tajik et

al., 2018; Maghzi et al., 2012) .Tajik et al., 2018 employed a glass micromodel with regular repeating pattern (6 cm length, 4.5 cm width and 0.1 mm depth) as a porous media. Firstly, they injected crude oil with a 0.03 ml/hr flow rate, then a 4 wt% of NaCl solution containing 1 wt% silica-graphene nanohybrids. They obtained images from a digital microscope imaging system over different period. According to their results, oil recovery obtained from the injection of nanofluid was 83% which is higher than from the injection of water 53%.

(Yousefvand and Jafari, 2015; Maghzi et al., 2014) investigated oil flooding using the five-glass micromodel. Both outlined those micromodels are a useful, easy, and direct tool for demonstrated oil recovery mechanism. The effect of nanosilica in polymer flooding on heavy oil was carried out by (Yousefvand and Jafari, 2015). They used an image processing technique to visualize and analyse the displacement mechanisms and the efficiency of oil recovery. The oil recovery improvement was increased by 10% from injection of 0.5 wt.% nanofluid (which was made from disperse Silica nanoparticles with water), with 0.08 wt.% anionic hydrolysed polyacrylamide polymer (HAPM) comparing with water flooding (Yousefvand and Jafari, 2015). This result was due to an increase in fluid viscosity and change wet behaviour from oil-wet to water-wet. They found a thin layer of oil when they inject nanofluid, which mean nanofluid can isolate oil so it will be easy to remove. Table 1.11. shows a list of studied that tested NPs using Micromodel device.

TABLE 1.11: Studies reporting on NPs use in micromodel device.

NPs	Dispersion media	NPs Con.	surfactant Con.	Recovery (%)	Ref.
SiO_2	Brine	1	NA	35	(Garcia et al., 2018)
SiO_2	SDS solution	2.2	0.18	59	(Ko and Huh, 2019)

Fe_2O_3	Surfactant solution	4	10	85.1	(Dai et al., 2018b)
ZnO	DI-water	0.01	NA	73.3	(Hendraningrat and Torsæter, 2015a)
ZnO	Brine	1	5	26.2	(Suleimanov, Ismailov, and Veliyev, 2011)
SGNs↞	Brine	0.01	NA	53	(Hendraningrat, Li, and Torsæter, 2013a)
ZnO	Brine	0.3	0.4	11.82	(Giraldo et al., 2013)
SiO_2	Brine	0	0.1	50.6	(Li et al., 2017)
SiO_2	Brine	1	0.2	72	(Li et al., 2017)
SiO_2	NaCl solution	0.1	0.1	4	(Manesh et al., 2017)
SiO_2	Brine	NA	0.025	23	(Yousefvand and Jafari, 2015)
SiO_2	Brine	NA	0.75	25	(Yousefvand and Jafari, 2015)

where ↞ refers to silica-graphene nanohybrids.

It is true that 3D geometry for porous media is complex and difficult to model, but single channel or single pore flow experiments can be useful (Avraam and Payatakes, 1999). They are insufficient for a complete understanding of the flow behaviour through porous media. Xu and his co-researchers in 2017 developed a novel method (2.5 D) for glass slide of micromodel fabrication with different depths. This method better represented the 3D geometry of real porous media. In 2D models the researchers either accounted for the defaults or aimed to avoid it by the application of complex and expensive technology such as laser, whereas in the 2.5D method used isotropic etching of hydrofluoric (HF) acid and controlling the gap between pores and depth. They fabricated the micromodel by taking the 2D blueprint and joining the main body with four rectangular edges. The neighbouring ”pores” are not connected on the blueprint but connected by a small throat, which is vertically shallower and horizontally narrower than the pore body, as illustrated in Figure 1.47.b. The pore body is then exposed to UV light. Their etching method result, micromodel was connected on the top ” jagged” and not connected from the

bottom. They demonstrated three examples: wetting phase imbibition, emulsion flooding and IFT surfactant flooding. They are pre-saturated both micromodels (2D and 2.5D) with n-octane (viscosity 0.52 cP) as a non-wetting phase before water flooding. The water flooding injection/introduction of a blue dyed water (viscosity 1.0 cP) with a flow rate of 7 mL/h. They found that the 2D model completely saturated under either the water or oil phase (also observed by (Zhao, MacMinn, and Juanes, 2016)); however, 2.5 D had an isolated oil droplet ”snap off” that was occupied with water at throats and pore edges (as described in their theory) (Fig. 12). In addition, oil-water-emulsion was successfully demonstrated by 2.5D micromodel, where the large droplets were breaking into smaller ones at short distance near to the inlet (snap off).

In summary, micromodels are an important technique to study different applications of multiphase flow inside porous media. Different materials, fabrication techniques have been used for micromodels and various applications. The fabrication methods have limitations and are chosen depending on the pattern geometry and size distribution of experimental purpose. For example, dry etching method, provide vertical walls, and this technique is not suitable for deep feature. All manufacturing techniques requiring a mask have greatly affected by the accuracy of network for mask and the materials made from. The actual network will be in low resolution if the mask in poor resolution and reversely.

In addition, Micromodels provide and will continue to be used as a tool for investigating and visualizing multiphase flow at the pore scale. Further research

is required however, to produce cheap and easy-to-use micromodels and develop it as using new technology to produce one as real prose media pattern.

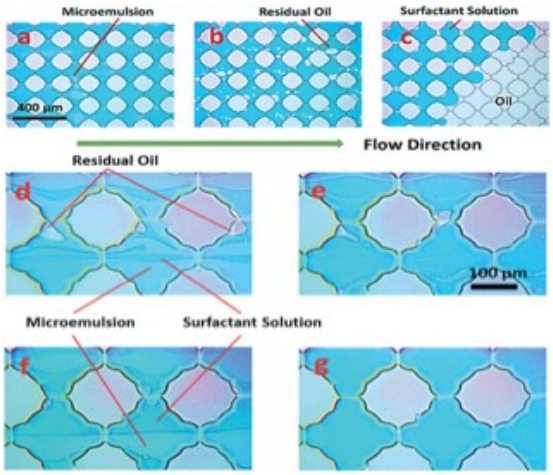

FIGURE 1.47: 2.5D micromodel shows the snap off regain, and oil has isolated by microemulsion. Adopted from (Xu et al., 2017) (Copyright: Royal Society of Chemistry, 2017).

1.11 Research objective and thesis outlines

In this thesis, the size, shape, and degree of hydrophobicity of functionalized alumina are investigated by Small Angle Neutron Scattering (SANS) and dynamic light scattering (DLS), their usage/or influence in oil recovery applications are to stabilize emulsions and increase oil recovery. In addition, the alumina nanoparticles are functionalised with different carboxylic acid and tested for the first time as a nanofluid for EOR applications in reservoir cores (chapter 2). Furthermore, the influence of high salinity condition combined with novel low surface energy surfactant iC18S(FO-180) is investigated.

Chapter three focuses on the use of neutron reflectometry to elucidate the behaviour of different surface modified alumina nanoparticles dispersed in surfactant

solutions. These alumina surfaces have been modified with carboxylic acids, 2-[2-(2methoxyethoxy)ethoxy]acetic acid (MEEA) and octanoic acid (OCT) to exhibit different degrees of hydrophobicity. The rational for choosing two different functionalities with different hydrophobicity is to determine whether the degree of wettability affects the NPs adsorption on the oil interface and results in the removal of the oil from the substrate (i.e., reservoir mineral surface). In addition to the two functionalities of the NPs, both cationic and anionic surfactants were used as a stabilizer, i.e., hexadecyltrimethylammonium bromide (CTAB) and sodium dodecyl sulfate (SDS). These surfactants were chosen because of their current ubiquitous use in oil recovery. The focus of the study is to determine the interaction and the distribution of the modified alumina NPs at the oil/water interface; as well as their interaction with surfactants. The adsorption and volume fraction of the NPs/surfactant complexes at the oil (hexadecane) interface were calculated using the scattering length density.

Chapter four examine the use of functionalized alumina NPs that are nontoxic, safe, and eco-friendly, as emulsifiers. This chapter focuses on the use of alumina NPs, modified with carboxylic acid with and without surfactants to synergistically stabilize O/W and W/O emulsions. The influence of the NPs concentration, oil properties and surfactant type on Pickering emulsion stability, phase behaviour, and size is also investigated.

In a previous study, it was shown that reacting side chains, containing two primary hydroxyl groups at either end of their chains, with a functionalized backbone would result in cross-linking and formation of gel networks, unless a large excess of the side chain is used. Chapter four builds on this previous work. In order to minimize this side

reaction, methyl terminated PEGs (having only one hydroxyl group) with different molecular weights (Mn = 550, 2000, and 5000) were selected in order to investigate the effect of chain length on the wettability of the grafted copolymers, the critical micelle concentration, and their aggregation structure. Characterization of the copolymers was performed spectroscopically using ^{1}H NMR and Fourier transform infrared (FTIR) spectroscopy and thermally using Thermogravimetric Analysis (TGA). Analysis of the size and aggregation structures were studied using Small Angle Neutron and X-ray (SANS and SAXS) techniques.

Chapter six, focuses on investigating the effect of salt concentration (NaCl) and seawater on the surface tension (SFT) and critical micelles concentration (CMC) of grafted polymers by studying the effect of interfacial tension between polymer and of oils mainly: hexadecane, decane, hexane, and flooding oil. Further to this, their ability to displace oil for EOR and stabilize emulsion is investigated. Small angle X-ray scattering has been used to investigate the structure of these copolymeric surfactants in the presence of ions. The analysis of surface tension and interfacial tension are performed by the pendant drop method.

The fitting model of the INTER experiment is in the appendix as well as, the SANS and SAXS fitting model.

Chapter 2

Stability of Carboxylic Acid Modified Alumina Nanoparticles for Enhanced Oil Recovery Applications

Portions of this chapter have been previously published as a paper in Brunei international conference: Al-Shatty, W., Alexander, S., & Barron, A. R. (2022). Stability of carboxylic acid modified alumina nanoparticles for enhanced oil recovery applications.

AIP Conf. Proc. 2022, in press.

2.1 Introduction

Interfacial properties between minerals and liquids control a wide range of phenomena like sorption, weathering and chemical interactions. Such phenomena are crucial in applications such as nuclear waste management, storage of CO_2 and oil recovery (Kiani, Alexander, and Barron, 2021). Regarding the latter, there is still no comprehensive theory for the intermolecular forces between a mineral surface and oil but the surface properties of both solids as well as the liquid characteristics determine the potential outcome of an oil recovery application. It is well known that approximately 35% of the oil is recovered by water flooding whilst the remaining 65% is dependent upon the mineral surface characteristics (Alnarabiji et al., 2018). The goal of enhanced oil recovery (EOR) is to extract the remaining oil with a chemical flooding procedure that is economically feasible. Core flooding experiments are used widely in the oil and gas industry to determine the petroleum recovery at limited reservoir conditions since core testing is time consuming and is not conducive to

performing a large number of experiments (Nazari Moghaddam et al., 2015; Sun et al., 2017). Minimization of the number of core flooding tests is facilitated by interfacial tension (IFT), wettability alteration and rheology measurements.

NPs offer a promising way of increasing accessibility to oil that is currently locked in reservoir rocks and act as a supplemented to the current extraction methods (Alnarabiji et al., 2018; Kiani, Alexander, and Barron, 2021). A considerable number of core flooding tests have been achieved by nanoparticles (NPs) injection (Emadi et al., 2017; Ramezanpour and Siavashi, 2019): SiO_2, $CaCO_3$, Al_2O_3, Fe_2O_3, and TiO_2 NPs are the most common candidates to be tested for oil recovery applications due to their low cost and ready availability.

However, the injection of NPs may have negative impact for EOR. For instance, Alvarez-Berrios et al. reported water flooding experiments performed with the addition of a nanofluid, made from SiO_2 dispersed in aqueous solution, decreased oil recovery by 6.7% (Alvarez-Berrios et al., 2018). It is important to determine the size and structure of nanoparticles in aqueous phase with/without chemical agents (polymer (Yousefvand and Jafari, 2015) or surfactant (Cheraghian et al., 2017)), as this determines a suitable formulation for flooding purposes. It is experimentally very challenging to characterize these behaviors at the molecular level. However, small angle neutron scattering techniques (SANS) is the best technique to determine these properties and provide information that is essential for better insight on successful oil recovery application using NPs.

In this study, the size, shape, and the degree of hydrophobicity of functionalized alumina were investigated by SANS and DLS, and in their usage/or influence in for

oil recovery application (stabilize emulsion and increase oil recovery). In addition, the role of different carboxylic acid on the functionalized alumina nanoparticles is tested for the first time as a nanofluid for EOR applications in reservoir cores. Furthermore, the influence of high salinity condition combined with novel low surface energy surfactant iC18S(FO-180) (Scheme 2.1. denoted as LSES) (Kiani et al., 2019) is being investigated herein for the first time.

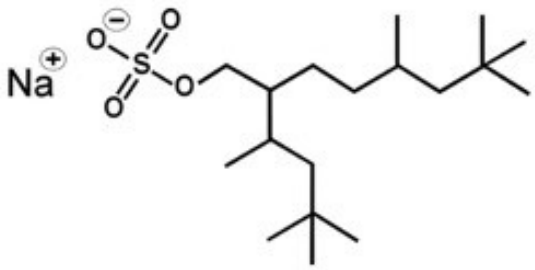

SCHEME 2.1: Chemical structure of low surface energy of the anionic surfactant (iC18S(FO-180), LSES).

2.2 Experimental methods

Aluminum oxide nanoparticles (13 nm, 99.8%), 2-(2-(2-methoxyethoxy)ethoxy)-acetic (MEEA, Scheme 2.2-a), octanoic acid (OCT, Scheme 2.2-b) and all solvents were purchased from Sigma Aldrich (United Kingdom) and used as received without further purification. The low surface energy of the anionic surfactant (iC18S(FO-180, LSES)) has been synthesized as per previous methods (Kiani et al., 2019) . Table 2.1 contains the list of the reservoir rocks (Iraq Basrah well) along with their measure properties; where Ka, f, and V_p represent the air permeability, porosity and pore space, respectively. In terms of oil and brine both density and viscosity were measured at 10, 20 and 30 C (see Table 2.2).

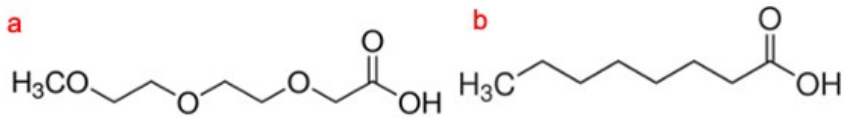

SCHEME 2.2: Chemical structure of carboxylic acid used for functionalized alumina nanoparticles with: (a) 2-(2-(2-methoxyethoxy) ethoxy) acetic (MEEA) and octanoic acid (OCT) (b).

TABLE 2.1: Reservoir rocks properties.

Sample	Depth (m)	Length (cm)	Area (cm^2)	Ka (md)	*f* (%)	Vp (cm^3)
R1	2806.1	5.48	11.46	968	27	17.79
R2	2807.13	5.5	11.34	1991	27.4	17.09
R3	2809.13	5.61	11.34	1634	27.3	17.3

TABLE 2.2: Reservoir rocks properties.

Injected Fluid	Density (g/(cm^3) at C			Viscosity (cp) at C		
	10	20	30	10	20	30
Oil	0.834	0.827	0.819	5.511	4.511	3.497
Brine	1.141	1.136	1.131	1.751	1.460	1.204

2.3 Modification and characterization of alumina nanoparticles

The synthesis procedure is based upon a modification of previous reported method (Maguire-Boyle et al., 2012; Al-Shatty et al., 2017). Aluminum oxide nanoparticles (10 g, 1.3 mol) were dispersed in toluene (200 mL). The appropriate amount of carboxylic acid (1 to 1.5 molar ratio) was added, and the mixture heated at (90 C) overnight. After cooling to room laboratory temperature, the sample was centrifuged at 5500 rpm for 30 min, and the solid was recovered. The solid was re-suspended in

isopropanol, and then agitated to remove physiosorbed carboxylic acid from the functionalized NPs. The solid was then recovered by centrifugation at 5500 rpm for 30 minutes and the supernatant discarded. This step was repeated twice with isopropanol and then repeated with ethanol. The functionalized alumina NPs were dried at 90 C for 10 hours, yielding (8 - 9 g) of solid product depending on which carboxylic has been used.

2.4 Characterization of alumina nanoparticles

SANS measurements were carried out on Larmor at ISIS, Didcot, UK (LARMOR, 2020). Larmor is a fixed-sample detector instrument that use neutron with wavelengths 8 Å; and two samples of placement detector (1.2 and 8 m) to provide a Q range of 0.002 – 0.4 Å. All samples were measured in 2 mm path-length rectangular quartz cells in D_2O or d6-ethanol. The raw SANS data were normalized by subtracting the scattering of the empty 2 mm cell and a D_2O (scattering length density, Þ = 6.33 x 10^{6} $Å^{2}$) or deuterated ethanol in the case of OCT-NP (scattering length density, Þ = 6.16 x 10^{6} $Å^{2}$) as a solvent background at 25 C. Data reduction used the Mantid data analysis package (Arnold et al., 2014) program and fitting of the SANS was carried out using SASVIEW program (SASVIEW, 2021), and data were fitted using an Ellipsoidal model (Sagisaka et al., 2019). Dynamic light scattering (DLS), and zeta potential were used to determine the NPs size and charge in dispersed solutions. For estimating NPs size, and charge, (2, 1 and 0.5 wt.%) concentrations of each NPs sample was dissolved in 5 ml of deionized water or isopropanol (considering the density, in the case of hydrophobic NPs (OCT-NP)) and left magnetically stirring for 24 hours to create homogenous fluid. The analysis was performed using a Zetasizer Nano Zs equipped with a He-Ne laser operating at a wavelength of 633 nm, at 20 C with 120 s

equilibration time and 173 scattering angles. Data processing was performed by the Zetasizer software. The data was average of 10 measurements.

2.4.1 Surfactant/Nanoparticles mixtures and emulsion preparation

LSES at critical micelles concentration (CMC) (2.7 mM, 1.0058 g/L) was placed in a glass vial, and Milli-Q water (20 mL, 18.0 MW) and stirred for 24 hours, to reach equilibrium. The appropriate NPs solution (0.3 or 0.5 wt.%) was added to the surfactant solution and left to stir for 24 hours in order to fully mix NPs in the surfactant solution. Emulsions were prepared by initially dispersing (0.3 and 0.5 wt.%) MEEA-NP (in water) or OCT-NP (in decane). In order to study the influence of surfactant on emulsion suitability, a surfactant solution was prepared at CMC, then (0.3 and 0.5 wt.%) of NPs added to surfactant solution. For each type of emulsion, five different water:decane ratios were used (10:90, 25:75, 50:50, and 90:10). The emulsions were then made using a probe sonicator (Cole Palmer Ultrasonic Processor) for 4 min at 30% amplitude. The resulting emulsions and the phase diagram were examined after 5 minutes, one hour, one day, and one week.

2.4.2 Fluid's formulation, reservoir rock cleaning and modification

MEEA-NP and OCT-NP (0.5 wt.%) solutions were prepared at room temperature with a magnetic stirrer with DI water as a dispersing agent for MEEA-NP and ethanol for the OCT-NP. Nanoparticle's surfactant mixtures (MEEA-NP/LSES, OCT-NP/LSES) were formulated by preparing a surfactant solution at CMC (2.7 mM, 1.0058 g/L) by stirring for 24 h to reach equilibrium. Following that, NPs powder (0.5 wt.%) was added to surfactant solution and left with a stirrer for 24 h at 25 C to create a homogeneous fluid. Brine solution was made at 20 wt.% NaCl in DI water. The reservoir rocks were

cleaned via Soxhlet extraction using toluene for two weeks to remove all organic compounds. The rock samples were then dried at 60 C in air. The samples were further cleaned by DI water to remove salt twice daily, and at each time tested for the presence of salts with aqueous of 1M of silver nitrite $AgNO_3$. After removing all ions/salts from reservoir rock, it is then dried with air oven at 60 C for 7 h.

2.4.3 EOR core flooding

Figure 2.1. shows a schematic representation of the core flooding experiments setup. The aim of the core flooding tests was to evaluate the capability of the functionalized alumina nanoparticles as potential agents of enhancing oil recovery in reservoir rocks after flooding with high salinity brine solution. At the beginning of each test, a core was fully saturated with Brine solution (20 wt.% NaCl) in a close high-pressure stainlesssteel cylinder at 1500 psi for 2 days. The core flooding system is characterized with an oven for adjusting the temperature, four piston cylinders for accommodating the injection fluids. In addition, a core holder was used to enable the system to perform different injection scheme. In this experiment, only three of the cylinders are used and at temperature 25 C. The first accumulator cylinder was filled with brine, while the second and third was used for oil and testing nanofluids, respectively. Each core sample was cleaned after every use by Soxhlet extraction (refer to section: Fluid's Formulation, Reservoir Rock Cleaning and Modification).

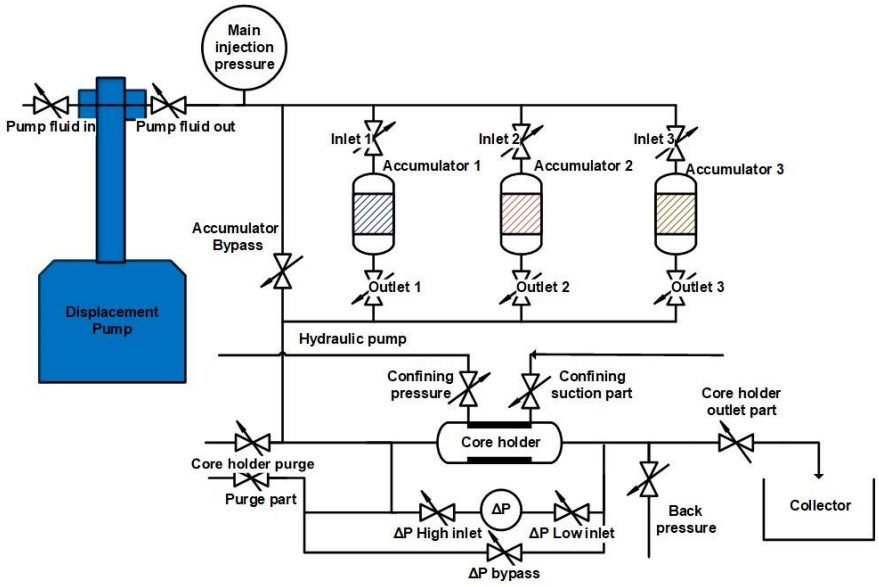

FIGURE 2.1: Schematic of oil displacement experiment.

A series of core-flooding experiment were performed to evaluate the effect of the functionalized alumina (MEEA-NP, and OCT-NP) alone and with surface-active agent (LSES) present on flooding performance. The system was pressurized to 1500 psi, supported with 100 psi as a backpressure. The procedure for oil flooding test includes air evacuation, initial saturation of the core with brine (20 wt.% NaCl), and then oil flooding until the water saturation was reached (Gbadamosi et al., 2019; Bayat et al., 2014). Air compressor pump was used for pumping the injection fluids from accumulator through the core flooding system. Medium oil was injected at a flow rate of 0.3 mL/min. The system was then aged for 2 weeks to establish equilibrium and attain uniformity. Subsequently, brine was injected at same flow rate until breakthrough occurred. This was followed by more brine injection until the oil amount was 0.05 mL. Afterward, the test/synthesized nanofluid was injected at a flow of 0.3 mL/min to recover remain oil.

2.5 Results and discussions

2.5.1 Stability of nanoparticles in surfactant solution

The specific surface area (m^2/g) by BET for solid MEEA-NP, and OCT-NP are 87.06 and 87.94, respectively. The stability of the native alumina, MEEA-NP, and OCTNP in the surfactant solution has been determined. The LSES surfactant was able to stabilities both NPs for up to 2 hours, which is enough time for flooding experiment (Pisárcik et al.,˘ 2018). Figure 2.2 contains density (a) and viscosity (b) results for testing nanofluids at 10, 20, and 30 C.

2.5.2 Shape and size of the nanoparticles

SANS is an ideal technique to study the size and shape of NPs in the presence of surfactant and high salinity aqueous conditions. The SANS fitting of the results for unfunctionalized alumina (Unf-Al_2O_3, 0.5 wt.%), along with MEEA-NP (in D_2O solution), and OCT-NP (in d6-ethanol) are shown in Table 2.3 and Figure 2.3. As can be seen from the fitting results, the nanoparticles shape is close to ellipsoidal (plate-like or needles) with radius increasing by functional group. The ellipsoidal shape of the NPs (without any chemical additives) has a polar radius of 42-45 Å and an equatorial radius of ca. 400 Å (Figure 2.3). Additionally, the influence of the NPs concentration has been tested, to study if they alter shape in higher concentrations. Generally, the long length (equatorial radius) does not change except for MEEA-NP that gets shorter, but this is in D_2O and it may be due to a solvent/solubility effect. While the width (polar radius) increases with wt.%, indicating an increase in NPs aggregation. The size by DLS, however, tends to stay essentially constant across concentration, and any variation tends to become less between types at highest wt.%

concentration (see Table 2.4). In addition, native alumina and functionalized alumina with (MEEA-NP, and OCT-NP) have a positive charge, and the positive charge increased slightly with concentration, in other words it become more stable (Al-Shatty et al., 2017).

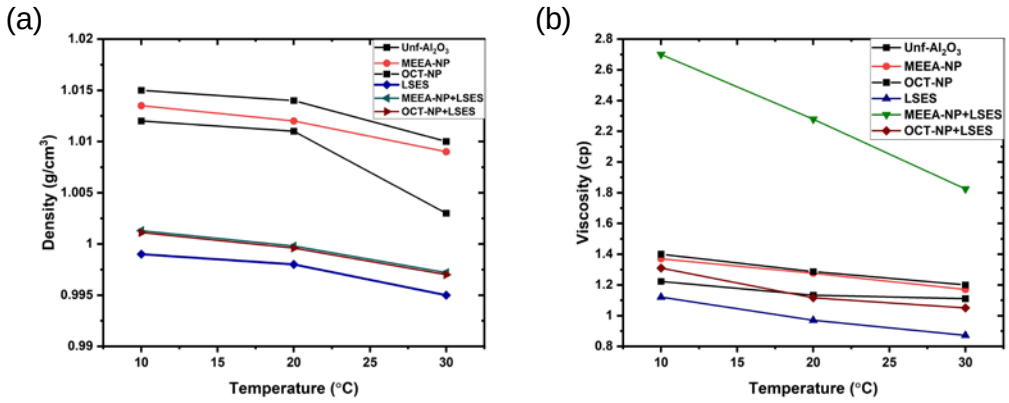

FIGURE 2.2: (a) density and (b) viscosity for injected nanofluid at temperature: 10, 20, and 30 C.

TABLE 2.3: SANS Parameters for unfunctionalized alumina (Unf-Al2O3) nanoparticles and functionalized with MEEA, and OCT at 0.5, 1 and 2 wt.% at 298 K in D_2O for Unf-Al_2O_3 and MEEA-NP and d6-ethanol for OCT-NP. X^2 is a statistical parameter that quantifies the differences between an observed data set and an expected dataset. Data were fitted using an ellipsoidal model.

Sample	Radius (Å) at 0.5 wt.% at C		Radius (Å) at 1 wt.%		Radius (Å) at 2 wt.%		X_2
	R1	R2	R1	R2	R1	R2	
Unf-Al_2O_3	42.3±0.5	290.2±0.7	-	-	-		-5.2
MEEA-NP	55.8±0.2	408.2±0.3	60.4±0.8	392.5±0.1	63.7±0.3	352.6±0.5	4.3
OCT-NP	45.1±0.2	346.5±0.2	61.4±0.9	372.2±0.1	65.6±0.4	329.8±0.5	6.4

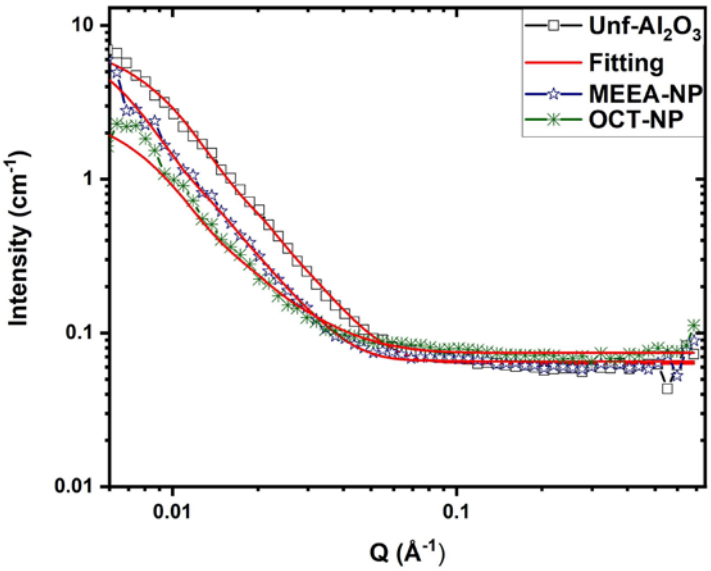

FIGURE 2.3: (SANS profiles (intensity (cm ^{1}) versus momentum transfer (Q, Å ^{1})), for unfunctionalized and functionalized alumina NPs at 25 C in D_2O (for Unf-Al_2O_3 and MEEA-NP), and d6-ethanol (for OCT-NP).

TABLE 2.4: Nanoparticle's size and zeta potential for un and functionalized nanoparticles at different concentrations.

Functional Group	Size (nm) at different Con.			ZPT at different Con.		
	2 wt.%	1 wt.%	0.5 wt.%	2 wt.%	1 wt.%	0.5 wt.%
Unf-Al_2O_3	160.3	140.1	135.6	39.8	44.2	45.1
MEEA-NPs	196.2	187.6	151.8	39.6	41.3	42.7
OCT-NPs	218.7	215.5	164.4	25.8	34.8	30.1

2.5.3 Emulsion stability

The influence of NPs concentration (0.3 and 0.5 wt.%) and the addition of low surface energy surfactant (LSES) on emulsion stabilization have been studied. MEEA-NPs were dispersed in DI-water, and various fraction (10-90%) of decane (used as an oil simulant) were added before emulsification. Due to the hydrophobicity of the OCTNP, it had to be dispersed in decane and various fraction of deionized water (10-90%)

were added before emulsification. The phase and emulsion stabilization with time are listed in Table 2.5. The results focus on the (50:50, 25:75, and 10:90) oil to water ratios. For emulsion made from 0.3 wt.% of MEEA without LSES addition, three-phase emulsion (type-III)(Kittithammavong, Charoensaeng, and Khaodhiar, 2021) across all times, where at (25:75, and 10:90) was formed excess water (type-II) for all tested times. In comparison with higher concentration (0.5 wt.%) were formed excess water for all ratios and at all tested times, except the (50:50) ratio phase transfer to (three phase- type III) after a week. In the other hand, OCT-NP behaves same, at both concentrations (0.3, and 0.5 wt.%): excess water (type-II) at all cases and changed to three-phase (type-III) after 1 day for both ratios (25:75 and 10:90).

The emulsion, which was made from LSES formed one-phase (type IV) (Kittithammavong, Charoensaeng, and Khaodhiar, 2021) for three focusing ratios and phase changed to one-phase (excess water) at 25 and 10 oil ratios. The hydrophobic NPs (OCT-NP) with LSES addition at both concentrations followed same trends which were: one-phase (excess-oil-type I) for 50:50 ratio, and three-phase (type IV) for 25:75 and 10:90 oil ratios until one week and there was phase changed from three-phase to one-phase (excess water, type-II) for 25:75 and 10:90 oil addition (see Table 2.5). Hydrophilic NPs (MEEA-NP) with LSES addition, the emulsion was formed two-phase (excess-oil, type I) for 50:50 and 25:75 ratios (at 0.3 and 0.5. wt.%), were formed one phase (type IV) at lower ratio (10:90). Interestingly, emulsion made from (0.5 wt.%) MEEA-NP and LSES formed a complete separation after a week for all ratios.

TABLE 2.5: Microemulsion phase behavior stability with time.

			Emulsion type[1] after time			
			5 min	1 h	1 day	1 week
MEEA-NP	0.3	50:50	III	III	III	III
		25:75	II	II	II	II
		10:90	II	II	II	II
MEEA-NP	0.5	50:50	II	II	II	III
		25:75	II	II	II	II
		10:90	II	II	II	II
MEEA-NP/LSES	0.3	50:50	I	I	III	III
		25:75	I	I	I	III
		10:90	IV	IV	IV	II
MEEA-NP/LSES	0.5	50:50	I	I	III	x
		25:75	I	I	III	x
		10:90	IV	IV	IV	x
LSES	CMC	50:50	IV	IV	IV	IV
		25:75	IV	IV	IV	II
		10:90	IV	IV	IV	II
OCT-NP	0.3	50:50	II	II	II	II
		25:75	II	II	II	II
		10:90	II	II	III	III

[1] type I = excess-oil; type II = excess-water; type III = three-phase emulsion; type IV = one-phase; x = full separation.

Sample	NPs weight (%)	O:W ratio				
OCT-NP	0.5	50:50	II	II	II	II
		25:75	II	II	II	II
		10:90	II	II	III	III
OCT-NP/LSES	0.3	50:50	I	I	III	III
		25:75	IV	IV	IV	II
		10:90	IV	IV	IV	II
OCT-NP/LSES	0.5	50:50	I	I	III	III
		25:75	IV	IV	IV	II
		10:90	IV	IV	IV	II

2.5.4 Oil flooding core displacement experiments

Oil displacement experiment of functionalized alumina nanofluid was conducted in reservoir rocks at 25 C. The results obtained were compared with surfactant LSES. The chemical tests were injected after brine flooding process. For testing parameters, conditions such as temperature, pressure, flow rate, pore volume injection and salinity remain the same for all core flooding tests. Figure 2.4 shows the oil recovery by the injected nanofluid alone (Figure 2.4-a) and with LESE surfactant (Figure 2.4-b). The recovery form of functionalized nanofluid indicates that the hydrophilic NPs has not changed the oil recovery, however, the hydrophobic NPs has increased the oil recovery to 10%. Thereafter, the focused was shifted on the two NPs (MEEA-NP, and OCTNP) that were mixed with LSES surfactant at CMC. There was an improvement in oil recovery for injected MEEA-NP with LSES from MEEA-NP alone (see Figure 2.4b). The recovery has been increased from 52% to 56% (around 4% more oil removed from reservoir rock); however, OCT-NP has shown a dramatic increase. The results indicate that hydrophobic NPs (OCT-NP) works as surfactant itself and compliments added surfactant, while hydrophilic NPs (MEEA-NP) probably binds to surfactant so basically removes if from the system (Pouryousefy, Xie, and Saeedi, 2016; Amirsadat et al., 2017).

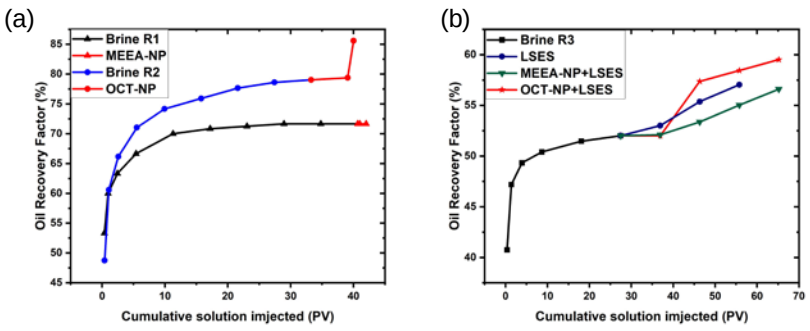

FIGURE 2.4: (Oil recovery factor in brine solution using reservoir core (water flooding experiment) for (a) NPs alone, (b) NPs mixed with LSES surfactant solution.

2.6 Conclusions

The suitability of native and carboxylic acid functionalized alumina NPs for improving the oil displacement properties of oilfield has been investigated. The size and shape of these nanofluid system at different concentration was ascertained by SANS data to provide theoretical understanding of the interaction between oil and the active agent (functionalized alumina). Oil recovery has been increased by 8% and 10% from injected with OCT-NP alone and OCT-NP/LSES, respectively; however, only 4% oil recovery occurred with injection with MEEA-NP/LSES while no improvement was observed with MEEA-NP alone. These results indicate that the hydrophobicity has a positive effect on the oil recovery and the OCT-NP being the active surface agent herein. To the best of our knowledge, we report herein, for the first time, the use of functionalized alumina NPs as a nanofluid as good candidate for enhanced oil recovery.

Chapter 3

Interaction of Surface Modified Alumina Nanoparticles and Surfactants at an Oil/Water Interface: a Neutron Reflectometry, Scattering, and Enhanced Oil Recovery Study.

Portions of this chapter have been submitted as a paper: Al-Shatty, W., Campana, M., Alexander, S., & Barron, A. R. Interaction of Surface Modified Alumina Nanoparticles and Surfactants at an Oil/Water Interface: a Neutron Reflectometry, Scattering, and Enhanced Oil Recovery Study. Published to *Appl. Mater & Interfaces.*.

3.1 Introduction

The observation that nanoparticles (NPs) readily adsorb at interfaces has led to their potential large-scale application in enhanced oil recovery (EOR) (Sun et al., 2017; Panchal et al., 2021; Kiani, Alexander, and Barron, 2021). A key to this use is an understanding of the relationship between a particular NP's displacement properties and its structure and surface functionality (Alnarabiji et al., 2018; Nazari Moghaddam et al., 2015; Cheraghian et al., 2017). Despite extensive literature dealing with NPs adsorption at air/liquid, liquid/solid, and liquid/liquid interfaces, attention has only recently moved to studying the conformation of nanoparticles upon adsorption (Yousefvand and Jafari, 2015; Petosa et al., 2010). This has been due to the lack of

suitable techniques to probe such buried interfaces (Williams and Beattie, 2002; Luo et al., 2010). Unlike other experimental techniques, neutron reflectometry (NR) provides structural information on interfaces (air/liquid, liquid/solid, liquid/liquid) (Chung et al., 2012). Eunhyea et al. established that neutron reflectivity experiments of the interfacial interaction of aqueous solutions of silica NPs with flat silica surface allowed for the determination of such parameters as thickness of NPs layers, and NPs particle size aggregation (size of the aggregates and particle distribution at interface) (Chung et al., 2012). The reflectometry technique comprises an incoming neutron beam (from a neutron source) impinging a flat surface, from which the reflection is measured in term of scattering length density (SLD) as a function of depth in the sample (Russell, 1990). The reflectivity profile, thus acquired, is used to establish the materials' composition, thickness, periodicity, and the roughness of the thin film which is layered on the substrate being examined (Zhou and Chen, 1995).

Techniques that have been used to determine the particle size aggregation in colloidal systems such as NPs in solution, are dynamic light scattering (DLS) and Quartz Crystal Microbalance (QCM). DLS measurement provide information on the particle size (Lim et al., 2013; Vanoyan et al., 2010), while QCM provides information on colloidal particles that are removed or deposited on to a surface (Gomez-Flores et al., 2020; Fatisson et al., 2009). Researchers have used both techniques as a complementary method to investigate the aggregation and deposition kinetics of colloidal system in an aqueous solution (Olsson et al., 2013; Gutierrez et al., 2010). In comparison to these methods, neutron reflectivity is able to provide supplementary information on particles clusters in solution and materials deposited onto a surface (Kalonia et al., 2018; Schaefer et al., 1995); most importantly the structure of the

materials under study as they are deposited onto a surface (Russell, 1990; Peillon et al., 2019). Atomic force microscopy (AFM) is commonly employed to determine particle/surface interaction but only under ideal conditions, by contrast, NR provides is more comparable to the performance of a real world system making it ideal as a method for studying multi-phase systems with buried interfaces (Schaefer et al., 1995).

A range of colloidal systems have been investigated by neutron reflectometry (including: surfactants, polymers, and biomolecules (Kalonia et al., 2018; Braun et al., 2017; Jo et al., 2020; Lakey, 2019)) in order to investigate the structures of proteins or amphiphilic particles monolayers on solid substrates or at an air/water interface as well as the interdiffusion in thin polymeric film (Delcea and Helm, 2019; Shimokita et al., 2021). To date, however, NR has not been used to study the interaction of the NPs with a surfactant for oil recovery applications. This study is the first to address the aggregation, destabilization and stabilization of NP/surfactant combinations at an oil/water interface.

Herein we use neutron reflectometry to elucidate the behavior of the different surface modified alumina nanoparticles dispersed in surfactant solutions. These alumina surfaces have been modified with carboxylic acids, 2-[2-(2methoxyethoxy)ethoxy]acetic acid (MEEA) and octanoic acid (OCT) to exhibit different degrees of hydrophobicity (Al-Shatty et al., 2017). The rational for choosing two different functionalities with different hydrophobicity is to determine whether degree of wettability affects the NPs adsorption on the oil interface and causing the removal of the oil from the substrate (i.e., reservoir mineral surface). In addition to

the two functionalities of the NPs, both cationic and anionic surfactants were used as a stabilizer, i.e., hexadecyltrimethylammonium bromide (CTAB) and sodium dodecyl sulfate (SDS), respectively. Their choice was because of their current ubiquitous use in the oil recovery (Kumari et al., 2018). The focus of the study is to determine the interaction and the distribution of the modified alumina NPs at the oil/water interface; as well as their interaction with surfactants. The adsorption and volume fraction of the NPs/surfactant complexes at the oil (hexadecane) interface were calculated using the scattering length density.

3.2 Experimental Section

3.2.1 Materials

Aluminum oxide nanoparticles (13 nm, Aeroxide-Alu), 2-[2-(2-methoxye-thoxy)ethoxy]acetic acid (MEEA), octanoic acid (OCT), hexadecyltrimethylammonium bromide (CTAB), sodium dodecyl sulfate (SDS), 2-propanol, n-hexadecane, d_{34}hexadecane, toluene, and ethanol were purchased from Sigma-Aldrich and used as received except n-hexadecane, which was purified by passing it through an alumina column (three times) before its use to remove all impurities. Distilled water (18 MW.cm; Millipore) was used throughout the experimental process. D_2O was obtained from Cambridge Isotopes Laboratories (>98 atom% D). Deuterated CTAB and the deuterated SDS was obtained from Santa Cruz Biotechnology and used as received. For oil displacement experiment, two sandstone rock samples from Basra reservoir well were used, and selected properties are provided in Table 3.1. The viscosity and density of brine and oil were measured at 10, 20, and 30 C in Table 3.2. The covalently functionalized carboxylate nanoparticles, MEEA-NP and OCT-NP were

synthesized using previously reported procedures (Al-Shatty et al., 2017; Kumari et al., 2018; MaguireBoyle et al., 2012).

3.2.2 Fitting for NP-surfactant mixtures at oil/water interface

Neutron reflectivity experiment at the oil/water interface were performed using the methodology developed by Zarbakhsh et al (Zarbakhsh, Bowers, and Webster, 1999). using the INTER reflectometer at ISIS, Ral, Didcot, UK (Webster et al., 2011) (INTER, 2021). The oil layer was spin coated onto a hydrophobic silicon block modified by a layer of trimethylchlorosilane silane as previously detailed (Campana, 2012). The oil layer was then sandwiched between the silicon layer and the aqueous phase. The samples were allowed to equilibrate for at least 45 minutes prior to measurement. Measurements were performed at two incident angles, 0.7 and 1.4 ; and stitched together after subtracting the wavelength dependent oil transmission. The data was analysed using Rascal, then replotted by MATLB. The interface is divided into discrete layers, each characterized by a roughness *s*, thickness t and scattering length density *r*, which is a function of layer composition as shown in equation 3.1, where f_i is the volume fraction of species i.

$$r_{layer} = \hat{\mathrm{A}}_i r_i f_i \qquad (3.1)$$

TABLE 3.1: Reservoir rock properties.

Sample no	Depth (m)	Length (cm)	Area (cm^2)	Air permeability Ka (md)	Porosity *f*(%)	Pore space Vp (cm^3)
R1	2806.1	5.48	11.46	968	27	17.79
R2	2807.13	5.5	11.34	1991	27.4	17.09

TABLE 3.2: Viscosity and density for fluids formation.

Injected Fluid	Density (g/cm^3) at C	Viscosity (cp) at C

	10	20	30	10	20	30
Oil	5.511	4.511	3.497	0.834	0.827	0.819
Brine	1.751	1.460	1.204	1.141	1.136	1.131
CTAB	1	0.865	0.799	1.001	0.996	0.997
SDS	1	0.875	0.789	1.002	0.997	0.997
MEEA-NP/SDS	1.08	0.97	0.86	1.004	0.999	0.997
MEEA-NP/CTAB	1.1	0.97	0.88	1.005	0.999	0.9965
OCT-NP/SDS	1.23	1.18	0.99	0.988	0.997	0.996
OCT-NP/CTAB	1.25	1.15	0.98	0.987	0.9968	0.9937

The reflectivity is then calculated using the optical matrix method (Winston, 1970) and compared to the experimental data. The routine is iterated until reaching a leastsquared minimization. The adsorbed amount G, expressed in mg.m ^{2}, can be calculated using equation 3.2, where t is the fitted layer thickness (determined from the fitting routine) and d the density expressed in g.m ^{3}.

$$G_i = tf_i d10^{7} \quad (3.2)$$

Scattering length density values for all components used in the study are shown in Table 3.3. The two nanoparticles (MEEA-NP and OCT-NP) were studied independently in the presence of both CTAB and SDS surfactants at Critical micelles concentration (CMC). In all cases both the oil and the aqueous phase were contrast matched to silicon (see Figure 3.1) and each system was characterized at 2 different surfactant contrasts: (A) a mixture of deuterated and hydrogenated (non-deuterated) surfactant to match the scattering length density of silicon and (B) just the deuterated surfactant.

The contrast schemes are depicted in Figure 3.1. Knowing the NPs-surfactant solution density from pycnometer measurements (see Table 3.2) and the scattering length density of the NPs from SANS measurements (4.8→10 ^{6} Å^{2}) (Al-Shatty, Alexander, and Barron, 2022), contrast (A) enables us to calculate the adsorbed amounts of NPs at the interface. In comparison contrast (B) shows an increase in scattering intensity due to the presence of deuterated surfactant: the more the increase in signal, the higher the amount of surfactant at the interface. In both cases of OCT-NP, more increase in scattering was observed with contrast (B), indicating a larger amount of adsorbed surfactant compared to MEEA-NP. In all cases both contrasts were co-fitted to a single model.

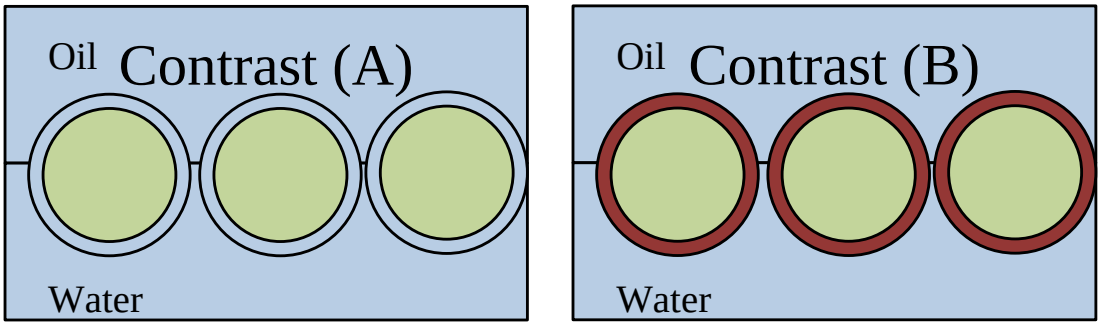

FIGURE 3.1: Contrast scheme used in the experiment. In all cases the oil and the water are both matched to silicon. In Contrast (A) a mixture of deuterated and hydrogenatedsurfactant with the same scattering length density of silicon is used. In Contrast (B) the surfactant used is chain deuterated.

TABLE 3.3: Values for scattering length density *r* for all components used in the study.

Material	*r*\→10 ^{6} Å^{2}
Silicon	2.07
H_2O	-0.56
D_2O	6.35
h-SDS	0.34

131*Recovery Study.*

d-SDS	5.72
h-CTAB	-0.35
d-CTAB	6.24
MEEA-NP	4.80
OCT-NP	4.80

3.2.3 Nanoparticle and surfactant characterization

Small Angle Neutron Scattering (SANS) measurements were carried out on Larmor at ISIS, Didcot (LARMOR, 2020), UK. Larmor is a fixed-sample detector instrument that use neutron with wavelengths 8 Å; and two samples of placement detector (1.2 and 8 m) to provide a Q range of 0.002 – 0.4 Å. All samples were measured in 2 mm path-length rectangular quartz cells in D_2O. The raw SANS data were normalized by subtracting the scattering of the empty 2 mm cell and a D_2O (scattering length density, Þ = 6.33 x 10^{6} $Å^{2}$) as a solvent background at 25 C. Each sample solution was prepared first making surfactant solution at CMC 0.9 mM (0.32 g L^{1}) and 2.8 mM (2.36 g L^{1} for CTAB and SDS, respectively using 10 mL D_2O (taking into account the density of heavy water) by stirring for 24 h to reach equilibrium. Then 0.5 wt.% of each of the nanoparticle added into surfactant solution and left stirring for anther 24 hour to create a homogenous solution. The solutions transferred into 2 mm rectangular quartz cell cuvettes with lid and placed into SANS chamber where measurements were carried out. Data reduction used the Mantid data analysis package (Arnold et al., 2014) program and fitting of the SANS was carried out using SASVIEW program (SASVIEW, 2021). Zeta potentials were used to determine the charge of the tested system in dispersed solutions. For charge measurements, (0.5 wt.%) concentration of each NPs sample was dissolved in 10 mL of deionized water

or isopropanol (considering the density, in the case of hydrophobic OCT-NPs) and left magnetically stirred for 24 hours to create homogenous fluid. For charge of surfactants (at CMC) of each surfactant CTAB and SDS, samples were dissolved in 20 ml of deionized water and left for 24 h to reach equilibrium. Samples of the NPs (0.5 wt.%) were then weighed and added onto 10 mL of the surfactant solutions and left for another 24 hours to create a homogenous suspension. The analysis was performed using a Ztasizer Nano Zs equipped with a He-Ne laser operating at a wavelength of 633 nm, at 20 C with 120 s equilibration time and 173 scattering angles. Data processing was performed by the Zetasizer software. The data was average of 5 measurements. Surface tension (SFT) and interfacial tension (IFT) on hexadecane oil has been measured by a collection of time dependent method using a Drop Shape Analyzer (Krüss) at ambient condition. A disposable plastic syringe was filled with NPs/surfactant solution, placed in the chamber, and loaded gently. All the SFT and IFT were an average of three repeated measurements. The IFT values between the NPs/surfactant solution and hexadecane oil were measured using same method but the filled syringe immersed into hexadecane oil phase. For both SFT and IFT measurements, the syringe was calibrated before each test, and then analyzed with ADVANCE software. The IFT value was obtained by fitting the Young Laplace equation to the contour profile of a 4.0 μL droplets.

3.2.4 Fluid's formulation, reservoir rock cleaning and modification

Nanoparticle's surfactant mixtures (MEEA-NP and OCT-NP with CTAB and SDS) were formulated by preparing a surfactant solution at CMC 0.9 mM (0.32 g L^{1}) and 2.8 mM (2.36 g L^{1}) for CTAB and SDS, respectively by stirring for 24 h to reach equilibrium. Following that, NPs powder (0.5 wt.%) was added to each of the surfactant solutions and left with a stirrer for 24 h at 25 C to create a homogeneous fluid (Figure 3.2).

Brine solution was made at 20 wt.% NaCl in DI water. The reservoir rocks were cleaned via Soxhlet extraction using toluene for two weeks to remove all organic compounds. The rock samples then dried at 60 C in air. The samples were further cleaned by DI water to remove salt twice daily, and at each time tested for the presence of salts with $AgNO_3$. After removing all ions/salts from reservoir rock, it is then dried with air oven at 60 C for 7 h.

3.2.5 Core flooding experiment

Figure 2.1 (Chapter 2) shows a schematic representation of the core flooding experiments setup (Al-Shatty, Alexander, and Barron, 2022). The aim of the core flooding tests was to evaluate the capability of the functionalized alumina nanoparticles as potential agents of enhancing oil recovery in reservoir rocks after flooding with high salinity brine solution. At the beginning of each test, a core was fully saturated with brine solution (20 wt.% NaCl) in a close high-pressure stainless-steel cylinder at 1500 psi for 2 days. The core flooding system is characterized with an oven for adjusting the temperature and three piston cylinders for accommodating the injection fluids. Additionally, a core holder was used to enable the system to perform different injection scheme. The first accumulator cylinder was filled with brine, while the second and third was used for oil and testing nanofluids, respectively. Each core sample was cleaned after every use by Soxhlet extraction (refer to section: Fluid's Formulation, Reservoir Rock Cleaning and Modification). A series of core-flooding experiment were performed to evaluate the effect of the functionalized alumina (MEEA-NP, and OCT-NP) with surface-active agent (either CTAB or SDS) present on flooding performance. The system was pressurized to 1500 psi, supported with 100 psi as a backpressure. The procedure for oil flooding test includes air

evacuation, initial saturation of the core with brine (20 wt.% NaCl), and then oil flooding until the water saturation was reached (Gbadamosi et al., 2019; Bayat et al., 2014). Air compressor pump was used for pumping the injections fluids from accumulator through the core flooding system. Medium oil was injected at a flow rate of 0.3 mL/min. The system was then aged for 2 weeks to establish equilibrium and attain uniformity. Subsequently, brine injection was continued until the oil amount was 0.05 mL. Afterward, the test/synthesized nanofluid was injected at a flow of 0.3 mL.min ^{1} to recover remaining oil.

3.3 RESULTS AND DISCUSSION

3.3.1 Reflectivity profiles

The reflectivity profiles measured for the NP/SDS systems were initially fitted to a single layer model. The fitting parameters for this were the layer thickness, the volume fractions of NP and SDS, and 2 (n layers +1) interlayer roughness. Reflectivity profiles and best fits are shown in Figure 3.2-a for MEEA-NP/SDS and Figure 3.2-b for OCT-NP/SDS. The single layer model provides an adequate fit, but the layer thickness is smaller than expected for the NPs. Thus, the fitted thickness was ⇠ 48.5 Å and ⇠ 38.5 Å for MEEA-NP and OCT-NP, respectively. This is different to the expected particle size of around 42 Å and 400 Å for polar and equatorial radius, respectively, for both NPs system (Al-Shatty, Alexander, and Barron, 2022). This discrepancy should not come as a surprise as we are attempting to represent a layer of ellipsoidal objects as a uniform slab, which is not the ideal case. In the event of a well-organized layer there should be a gradient of material where the densest part is at the center.

In order to represent the interface with a more realistic model, we have assumed an elliptical NP (with size as determined by SANS, with a core of 42 Å ⇥ 400 Å ⇥ 400 Å) (Al-Shatty, Alexander, and Barron, 2022) covered with a homogeneous layer of surfactant with a thickness of 20 Å (i.e., the shell) corresponding to a fully extended surfactant molecule. Since the shell may not be fully composed of surfactant, we have introduced a parameter called surfactant coverage to simulate the amount of surfactant on the NP surface (0 = no surfactant, 1 = full coverage). The NP/surfactant complex was then sliced into 10 slices of equal thickness, whereby the thickness d was a fitting parameter. The volume fraction of both core and shell are thus geometrically constrained. The coverage of the NP-surfactant complexes was then fitted introducing a new fitting parameter: the packing of particles at the interface. Assuming a well-organized layer of circles in a plane, the maximum packing achievable is ⇠ 0.906 (or slightly higher because of elliptical nature of the NPs and possibly staggering of the NPs). With this geometric model, the fitting parameters included: the thickness of each slice; the surfactant coverage in crown; the sphere packing. In order to simulate a smooth transition between each layer, the interlayer roughness was fixed as half of the fitted layer thickness.

Applying this model to MEEA-NP and OCT-NP complexes with SDS, the quality of the fit was not affected. The best fits are shown in Figure 3.2a and b for MEEANP/SDS and OCT-NP/SDS, respectively. The overall thickness increases respectively to 112.8 ±⇠ 17 Å and 63.2 ±⇠11 Å, in both case by a factor 2.3-1.6. The layer thickness is now in line with a monolayer of complexes adsorbed at the interface: these disk-like complexes adopt an almost conformation upon adsorption at the oil/water interface. The thicker interface observed for MEEA-NP/SDS

complexes could be an indication of slight staggering, however this would not be because of increased surface packing (within error for the two systems). Alternative explanations for the observed staggering could be because of the disk-like shape of these particles, the surfactant distribution across the interface appears to be somewhat bimodal (Figure 3.3-a and b), where the top and bottom parts of the interface are surfactant-rich and most of the NP resides in the middle part. We have simulated the adsorption of near-spherical particles coated with an analogous surfactant shell, where the surfactant distribution is more similar to that of the NP (see Figure 3.5 a and b, Figure 3.6, 3.7, and Figure 3.8). This may well be the case in our situation as the role of the surfactant if a dispersant, therefore the formation of smaller complexes is to be expected in presence of surfactant. It must be stressed that in both NP-SDS systems the adsorbed amount of the two components is hardly affected by the shape of the particles, hence the quantitative interpretation is independent on the choice of model used (Table 3.3.). In addition, this could very well be for an additional reason: the OCT-NP is hydrophobic, it is more likely in order to force these NPs to disperse in aqueous solution, the surfactant cover small particles before agglomerations happened.

(a)

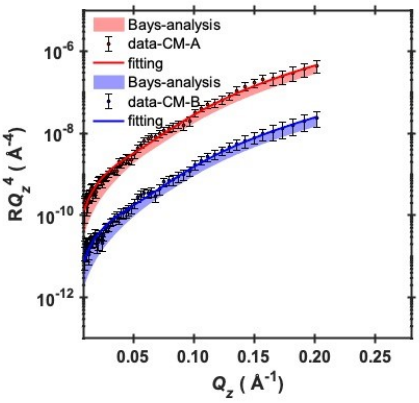

(b)

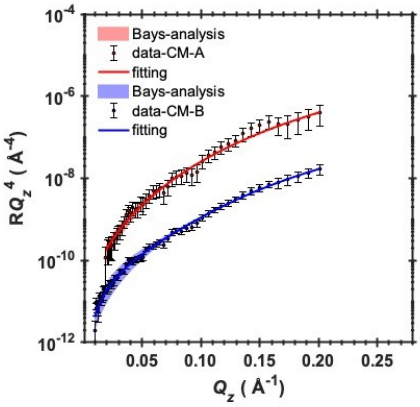

FIGURE 3.2: Data and best line fits for (a) the MEEA-NP/SDS and (b) the OCT-NP/SDS system systems using a single layer model. The shaded areas correspond to the 95% confidence interval as determined by Bayesian analysis. Contrast (A) is shown on top, Contrast (B) below. Profiles are offset to visualise the quality of the fit. Because of the low signal measured, data for Contrast (A) contains a few points with zero counts. As Rascal has difficulties simulating data in this situation, the data at Q < 0.02 Å ^{1} was truncated. The fit describing the whole Q profiles is satisfactory and is shown in Figure 3.3.

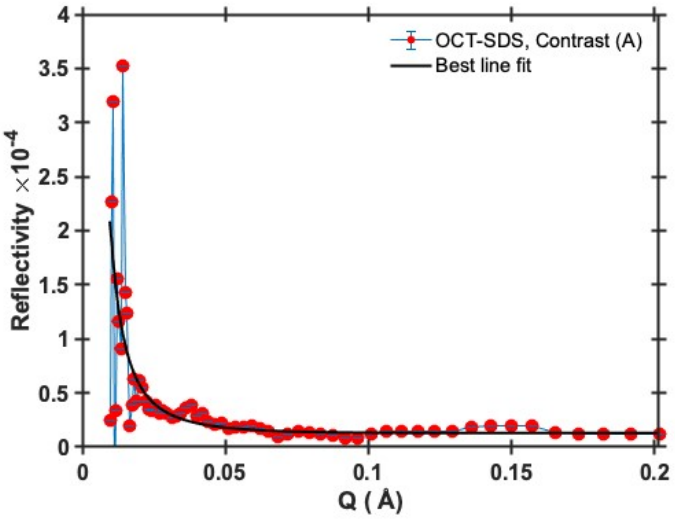

FIGURE 3.3: Reflectivity profile and best fit for Contrast (A) for OCT-NP/SDS showing the full Q range.

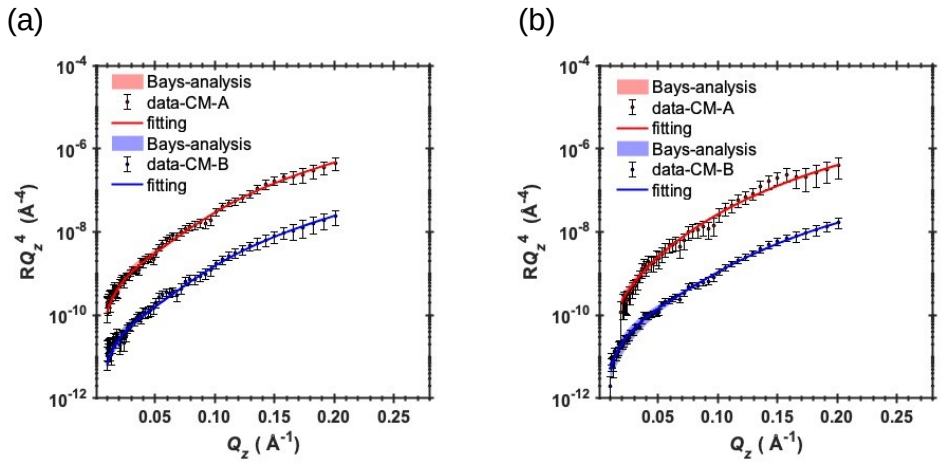

FIGURE 3.4: Data and best line fits for the (a) MEEA-NP/SDS and (b) OCT-NP/SDS systems using the geometric model. The shaded areas correspond to the 95% confidence

interval as determined by Bayesian analysis. Contrast (A) is shown in red and contrast (B) in blue. Profiles are offset to visualize the quality of the fit. Show a and b.

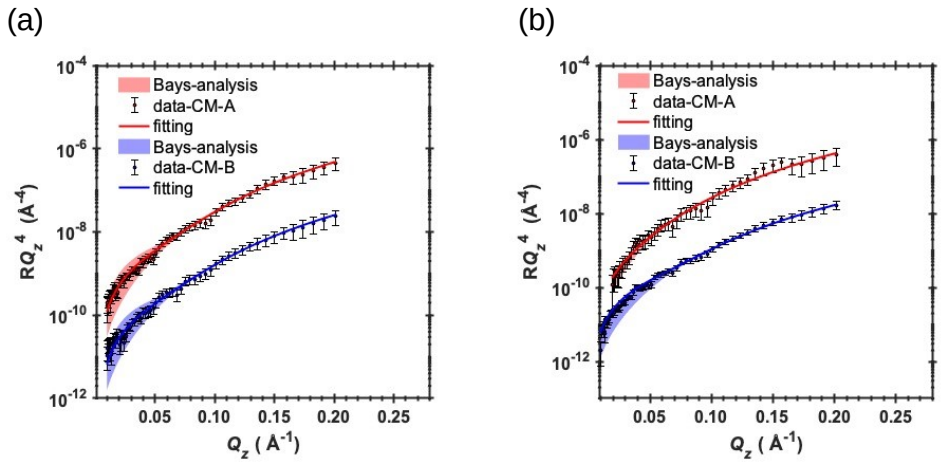

FIGURE 3.5: Data and best line fits for the (a) MEEA-NP/SDS and (b) OCT-NP/SDS systems using the near-sphere geometric model. The shaded areas correspond to the 95% confidence interval as determined by Bayesian analysis. Contrast (A) is shown in red and contrast (B) in blue.

TABLE 3.4: Adsorbed amount for NPs and surfactants in the SDS (near-spherical and Ellipsoidal) systems studied. Surfactant and NPs are shown separately for each system. In all cases the total optimum adsorbed amount is shown together with the 95% confidence interval in parentheses.

	Adsorbed amount, G (mg.m ^{2}) Layer	
	Nanoparticles	surfactant
MEEA-NP/SDS (near sphere)	0.732 (0.687,0.792)	0.033 (0.003,0.079)
MEEA-NP/SDS (Ellipsoidal)	0.755 (0.676,0.852)	0.035 (0.0026,0.088)
OCT-NP/SDS (near sphere)	0.404 (0.344,0.477)	0.193 (0.119,0.308)
OCT-NP/SDS (Ellipsoidal)	0.416 (0.360,0.495)	0.154 (0.097,0.247)

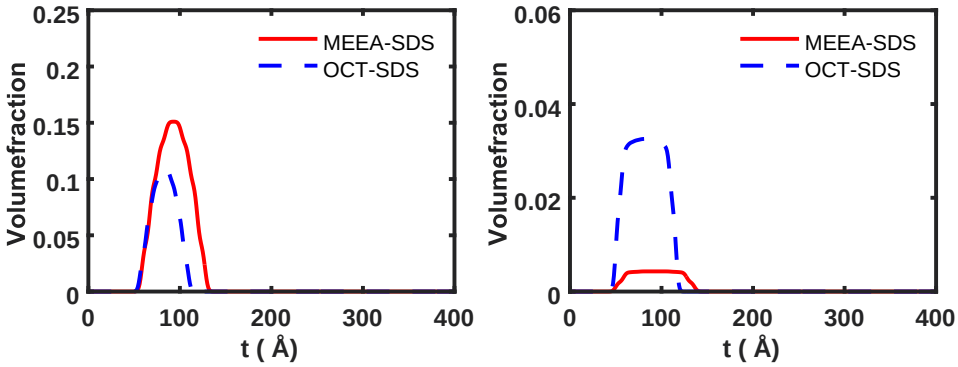

FIGURE 3.6: The distribution of NP (a) and surfactant (b) across the interface for both systems for the NP/SDS system using near-spherical particles model. The scaling for the NP and surfactants is different to facilitate visualizing the higher amount of adsorbed NP compared to the surfactant.

The adsorbed amount for both NPs and SDS is shown in Table 3.6 and detailed layer-by-layer calculations are shown in Tables (3.4, and 3.6). Of the two NPs, MEEANP shows a higher adsorbed amount at the interface compared to OCT-NP: ⇠ 0.76 mg.m ^{2} and ⇠0.42 mg.m ^{2}, respectively. What is more interesting is the trend of surfactant adsorbed in terms of amount. For example, MEEA-NP requiring a little surfactant adsorption to become surface active, on the other hand, OCT-NP/SDS mixture adsorbed at the interface present a surfactant-rich crown, showing that much more surfactant is required to make the OCT-NP surface active. We have investigated the possibility of free surfactant co-adsorption at the interface. This can be easily modelled by introducing additional fitting parameters, but the increase in quality fit does not justify the use of an increasingly complex model. At this stage we may not be able to exclude the presence of free surfactant at the oil/water interface, and this experiment does not show any clear evidence of its presence.

(a) (b)

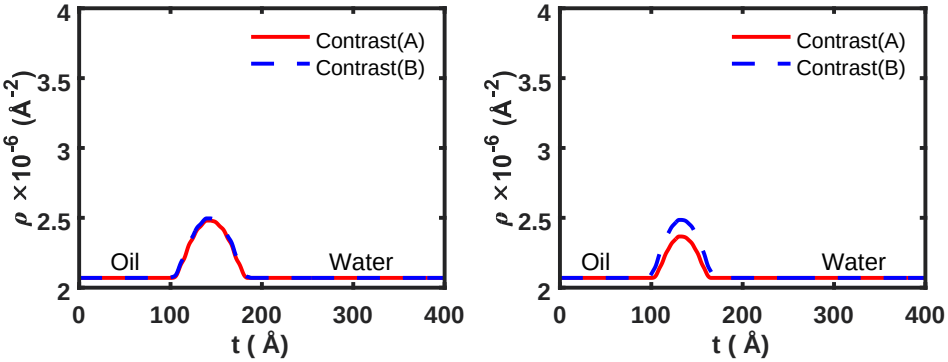

FIGURE 3.7: The Scattering length density profiles for (a) MEEA-NP/SDS, (b) OCTNP/SDS using near-spherical particles model. Contrast (A), with CMSi surfactant, is shown in red while Contrast (B), with d-surfactant, is shown in blue. Note that in all cases Contrast (A) has a lower signal compared to Contrast (B).

TABLE 3.5: The fitting parameters for MEEA-NP and OCT-NP in SDS surfactant system under study. Each parameter shows the associated best fit parameter next to it, followed by the 95% confidence interval in brackets. Where L refer to layer.

Properties of NR with SDS	MEEA-NP	OCT-NPS
Substrate Roughness	8.08 (1.31, 12.84)	7.37 (1.4383, 12.72)
Thickness L1	48.37 (37.14, 59.69)	38.63(27.5, 47.93)
Vol-NP L1	0.15(0.15, 0.19)	0.11(0.085, 0.157)
Vol-SDS L1	0.007 (0.0008, 0.013)	0.044(0.032, 0.06)
Roughness L1	7.63 (0.17, 12.86)	6.93 (0.51, 12.68)

TABLE 3.6: Shows the volume fraction of NP and SDS in each slice of the NP-SDS complex.

Slices/n	Vol-NP$_{Ln}$	Vol-SDS$_{Ln}$
1	0	0.1867
2	0.0386	0.4681
3	0.4063	0.3404
4	0.7226	0.1841

5	0.8807	0.106
6	0.8807	0.106
7	0.7226	0.1841
8	0.4063	0.3404
9	0.0386	0.4681
10	0	0.1867

TABLE 3.7: Adsorbed amount for NPs and surfactants in the 4 systems studied. Surfactant and NPs are shown separately for each system. In all cases the total optimum adsorbed amount is shown together with the 95% confidence interval in parentheses.

	Adsorbed amount, G (mg.m ^{2}) Layer	
	Nanoparticles	surfactant
MEEA-NP/SDS	0.755(0.676,0.852)	0.035(0.0026,0.088)
OCT-NP/SDS	0.416(0.360,0.495)	0.154(0.097,0.247)
MEEA-NP/CTAB	5.850(5.251,6.375)	0.384(0.110,0.728)
OCT-NP/CTAB	6.207(5.605,6.863)	0.674(0.512,0.958)

The single layer model used to describe the NP-SDS systems fails to describe the interface in presence of NP-CTAB. An example of the poor 1-layer fit is shown in Figure 3.9-a. The geometric model also failed to fit the reflectivity profiles; this is proof that the adsorption of NPs in presence of CTAB leads to a more complex interface that cannot be modelled simply in the same way as with the SDS. To overcome the bad fitting, a step to gradually increase the complexity was taken as an approach, whilst maintaining to a minimum number of fitting parameters. Initially, a second layer was added to the model to increase its complexity. Fitting parameters included: the 2layer thicknesses, the volume fractions of NP and CTAB in each layer and 3 interlayer

roughness's. Again, the best model could not fit the experimental data (see Figure 3.9b), therefore a further in the model complexity was required. A three-layer model was found to adequately describe the oil/water interface in presence of MEEA-NP/CTAB. The fit quality is slightly inferior for the OCT-NP/CTAB; an attempt was made to increase the complexity of the model by adding a fourth layer, but with little effect on the fitting quality. Another approach taken was to interduce a free surfactant layer in different locations across the interface, however, no noticeable improvement in the quality of the fitting was observed. In summary, the three-layer model presented here is believed to be the best fit for the collected data. The data and best fits for the three-layer model are shown in Figure 3.10.

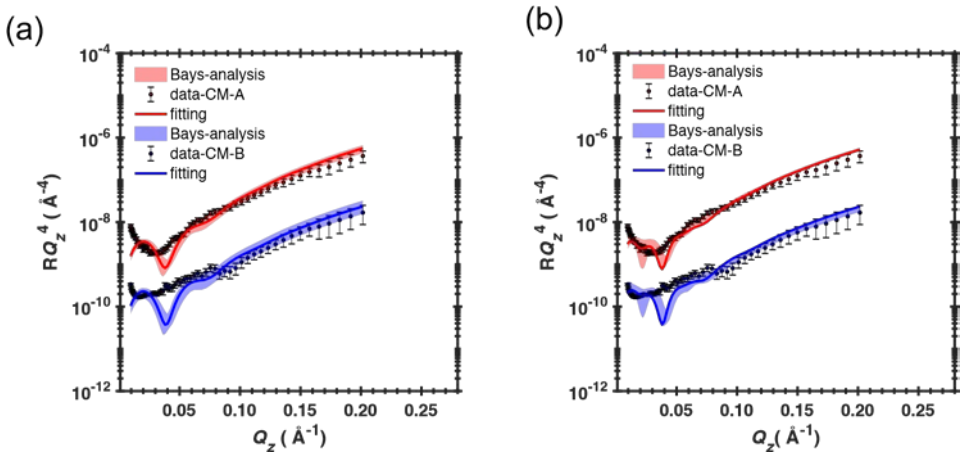

FIGURE 3.8: Data and best line fits for the (a) OCT-NP/CTAB system using a 1-layer model in which the fit quality was extremely poor and thus no Bayesian analysis was performed, and (b data and best line fits for the OCT-NP/CTAB system adopting a 2-layer model. Again, the fit is far from satisfactory and increasing complexity was required to adequately model the interface.

In both systems the interface could be modelled with a monolayer of relatively good coverage (around 45% in both cases) followed by a much thicker secondary layer with around 25% coverage. A thick diffuse layer, with coverage between 3% and 6%, was then observed on the aqueous side of the interface. The roughness between layer 2 and layer 3 is very large (however within less than $\frac{1}{2}$ of the layer thickness)

indicating a gradual transition between the secondary adsorption layer and the diffuse region.

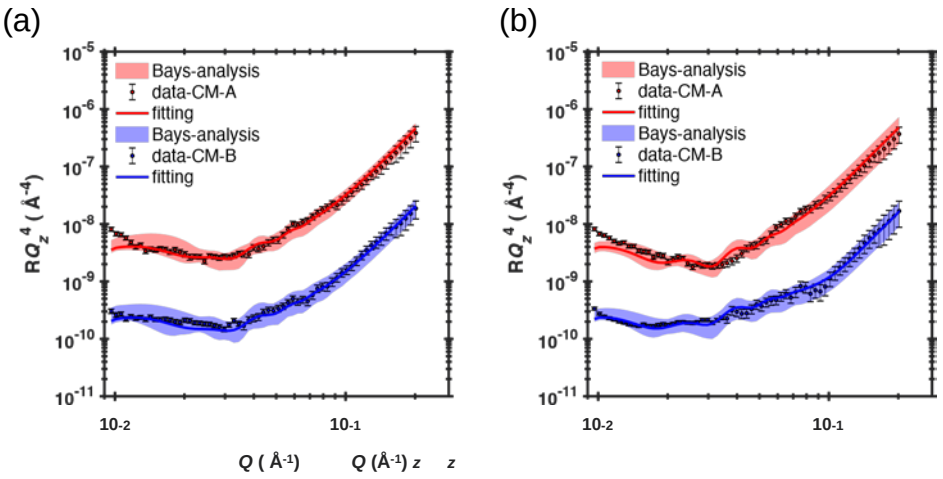

FIGURE 3.9: Data and best line fits using 3-layer model for (a) the MEEA-NP/CTAB system and (b) the OCT-NP/CTAB system. Although the fit for Contrast (A) is the worst of all reported here, large error bars allow to describe the main features of the reflectivity curve.

The thickness of the first layer, which represents the most ordered region within the interface, is around 33 ± 9 Å. The thickness of this region is smaller compared to a single NP-CTAB complex, however the same argument used for the NP-SDS complexes apply here: we are attempting to represent a layer composed of ellipsoidal objects using a single slab. Therefore, one would expect the real thickness of this region to be in line with what reported for the NP-SDS.The thickness of the secondary adsorption layer and the diffuse region (third layer) is significantly thicker than the primary monolayer: for MEEA-NP/CTAB t= 159 ± 11 Å and 177 ± 16 Å, respectively, similarly for OCT-NP/CTAB t= 175 ± 6 Å and 180 ± 13 Å. This shows that the overall thickness of the interface is similar, and it is much broader with CTAB compared to SDS.

TABLE 3.8: Layer-by-layer detailed adsorbed amount G for the MEEA/CTAB system. In all cases the optimum adsorbed amount is shown together with the 95% confidence interval in parentheses.

	Adsorbed amount, G (mg.m ^{2}) Layer	
	MEEA-NP	CTAB
Primary layer	1.295(1.105,1.478)	0.118(0.062,0.170)
Secondary layer	3.981(4.129,4.477)	0.177(0.052,0.314)
Diffuse layer	0.574(0.346,0.784)	0.090(0.000,0.274)

TABLE 3.9: Layer-by-layer detailed adsorbed amount G for the OCT-NP/CTAB system. In all cases the optimum adsorbed amount is shown together with the 95% confidence interval in parentheses.

	Adsorbed amount, G (mg.m ^{2}) Layer	
	OCT-NP	CTAB
Primary layer	1.197 (1.027,1.422)	0.333 (0.224,0.456)
Secondary layer	4.152 (3.957,4.328)	0.177 (0.141,0.265)
Diffuse layer	0.858 (0.621,1.114)	0.164 (0.146,0.237)

The detailed layer by layer fitted data are shown in Tables (3.3 and 3.4) for the both NPs/CTAB complexes. The adsorbed amount of NP in the primary layer for MEEA-NP and OCT-NP is within error; however, this region contains considerably more CTAB with OCT-NP (7-13%) compared to MEEA-NP (2-5%). This is in comparison with what was observed for the NP-SDS complexes, where OCT-NP at the interface was associated to more surfactant molecules compared to MEEA-NP (Table 3.6). The amounts of NPs in the secondary layer is less compared to the primary layer, however the decrease in amount of

surfactant between the two regions is much more pronounced, dropping to 0-2%. The same was observed in the diffuse region, where the amount of surfactant dropped to less than 1.5% in both cases. Overall, the adsorbed amounts of NPs at the interface are 5.85 ±0.58 $mg.m^{2}$ for MEEA-NP and 6.21 ±0.62 $mg.m^{2}$ for OCT-NP. The distribution of NPs across the interface is remarkably similar between the two systems, with most of the material (⇠67%) contained in the secondary adsorption layer. This is because, despite showing a smaller volume fraction compared to the first layer, it is considerably thicker.

The amount of surfactant at the interface differs greatly between the two systems, with OCT-NP/CTAB showing more surfactant at the interface compared to MEEANP/CTAB. This can also be visually seen from the increase in scattering between contrast (A) and contrast (B), which is much more pronounced for MEEA-NP and OCT-NP. It is noteworthy that not only the amount of surfactant differs between the two systems but also its distribution across the interface. The amount of both NP and CTAB found in the secondary layer is fairly similar between the two systems, therefore it can be inferred that the structure of these two regions is very similar in the two systems. In the case of OCT-NP/CTAB there is however a considerable amount of surfactant in the first layer, 3 times higher than the MEEA-NP/CTAB system.

The difference in CTAB adsorbed amount in the primary layer is the most striking difference between the two systems and is in analogy to with what reported for the NP-SDS systems. Similarly, to OCT-NP/SDS, the adsorbed amount ratio of NP to surfactant is around 3:1. The amounts of NPs and SDS in solution is 5.00 and 2.50 $mg.mL^{1}$, respectively, and the ratio 3:1 is not too different from the stoichiometric

ratio in solution. However, the amount of CTAB is in solution is considerably lower: there is only 0.33 mg.mL ^{1} as opposed to 5.00 mg.mL ^{1} of NPs when preparing the solution, very far from the 3:1 NP to surfactant found in the primary monolayer. There are several possible explanations for this discrepancy:

First, surfactants preferentially adsorb to some NPs. This could be because of size distribution: smaller NPs have a higher surface-to-volume ratio, adsorb more surfactant molecules, and become more surface active, hence a higher fraction of surfactant at the interface. This could also be caused by differences in NP's coating, causing some NPs to have a higher affinity to surfactant than others.

Second, surfactants are not effective at dispersing the NPs. Large aggregates may be present in solution and the surfactant may not be ready to separate the individual NPs effectively. In this case the free NPs have access to a small fraction of surfactant and become readily surface active, reaching the interface first, forming the primary monolayer on their own resulting in a higher NP to surfactant ratio. The larger aggregates are characterized by a slower Brownian motion and would reach the interface after the smaller aggregates; these are surfactant-rich complexes and would therefor form the secondary adsorption layer. This would also explain why the secondary layer forms even when the primary layer is far from full coverage: these larger aggregates would act as a steric barrier for other NPs in solution.

Third, NP-Surfactant complexes adsorb at the interface together with free surfactant. This is proving difficult to verify as the fits are inconclusive on the matter. The scattering length density and volume fraction profiles are shown in Figure 3.11 and

3.12, respectively.

3.3.2 SANS measurements

SANS data were collected for 0.5 wt.% nanoparticles (MEEA-NPs, and OCT-NPs) which dispersed in surfactant solution (CTAB and SDS) at CMC. The SANS scattering patterns are shown in Figure 3.13. As can be seen from the scattering patterns, the system appears to be bimodal with higher Q range corresponds to the scattering of the surfactants and lower Q range to the NPs. Due to the complexity of the scattering data, we fit the data with the power-law to understand the system. The power low shows both nanoparticles with both surfactants have Q slop of around 2.1-2.5 at lower Q which indicate the scattering from 2D subject such as plate or ellipsoidal (Al-Shatty, Alexander, and Barron, 2022). There is one possible explanation for this bimodal system, and this can be due to NPs being coated with both unimeric and surfactant micelles. The data at high Q region is showing similar shape to the surfactants micelles (Hammouda, 2013), which could be due to scattering from micelles around the NPs.

However, the data from the lower Q region has pattern similar to nanoparticles (AlShatty, Alexander, and Barron, 2022) which indicate that surfactants have coated NPs as unimers rather than micelles.

TABLE 3.10: The fitting parameters for MEEA-NP and OCT-NP in CTAB surfactant system under study. Each parameter shows the associated best fit parameter next to it, followed by the 95% confidence interval in brackets. Where L refer to layer.

Properties of NR with CTAB	MEEA-NP	OCT-NPS
Substrate Roughness	6.23 (2.35, 23.27)	7.147 (1.46, 12.62)
Thickness L1	33.01(25.51, 4.40)	33.67 (25.49, 43.91)
Thickness L2	158.94 (147.38, 169, 05)	174.92 (157.54, 189.29)

148*Recovery Study.*

Thickness L3	177.69 (161.16, 193.38)	180.74 (167.18, 193.77)
Vol-NP L1	0.396 (0.34, 0.45)	0.35 (0.302, 0.42)
Vol-NP L2	0.25 (0.24, 0.26)	0.24 (0.22, 0.25)
Vol-NP L3	0.0312 (0.019, 0.26)	0.047 (0.034, 0.061)
Vol-CTAB L1	0.0364(0.019, 0.052)	0.0979 (0.067, 0.13)
Vol-CTAB L2	0.0108 (0.003, 0.018)	0.0006 (0.00, 0.003)
Vol-CTAB L3	0.005 (0.0001, 0.015)	0.009 (0.008, 0.012)
Roughness L1	6.735 (0.520, 12.7)	7.22(0.53061, 12.78)
Roughness L2	72.195 (65.795, 74.893)	72.19 (65.60, 74.91)
Roughness L3	18.65 (2.45, 28.24)	21.46 (5.60, 31.39)

3.3.3 IFT, SFT and oil recovery

The pendent drop method was performed in order to investigate the effect of nanoparticles in combination with surfactants (SDS, and CTAB) on the IFT values. Table 3.5, and Figure 3.14. show the static and dynamic measurement between NP with SDS and CTAB in n-hexadecane. It shows that using dispersed NP in surfactant solutions leads to significant decrease in IFT. The dynamic measurements were conducted on NP in surfactant solution over 120 s in n-hexadecane and are shown in (Figure 3.14). As can be seen, the IFT quite stable with time. Our previous research showed that both NPs

are able to reduce IFT of hexadecane from 51 mN/m up to 40.7 and 45.1 mN/m for OCT-NP, and MEEA-NP, respectively (Al-Shatty et al., 2017). By comparing the IFT reduction of NPs alone and with surfactant addition shown in Table 3.11, It can be observed that there is significant reduction of IFT of hexadecane oil due to the presence of surfactants, which indicate the interaction between the surfactant and NPs increase the reduction of the IFT (Rana et al., 2012). In order to find the charge of the tested system and confirm the NPs/Surfactant interactions, Zeta potential has been used. It was found that unmodified alumina NPs has a positive charge, however, it altered to negative after addition of SDS solution and remain positive with CTAB solution. In addition, the zeta potential result for both system is between ± 30 to ± 50, which indicate a stable dispersed system (Ouikhalfan et al., 2019). These results are in line with direct visual observation result which shows dispersed solutions up to one day (see Figure 3.15).

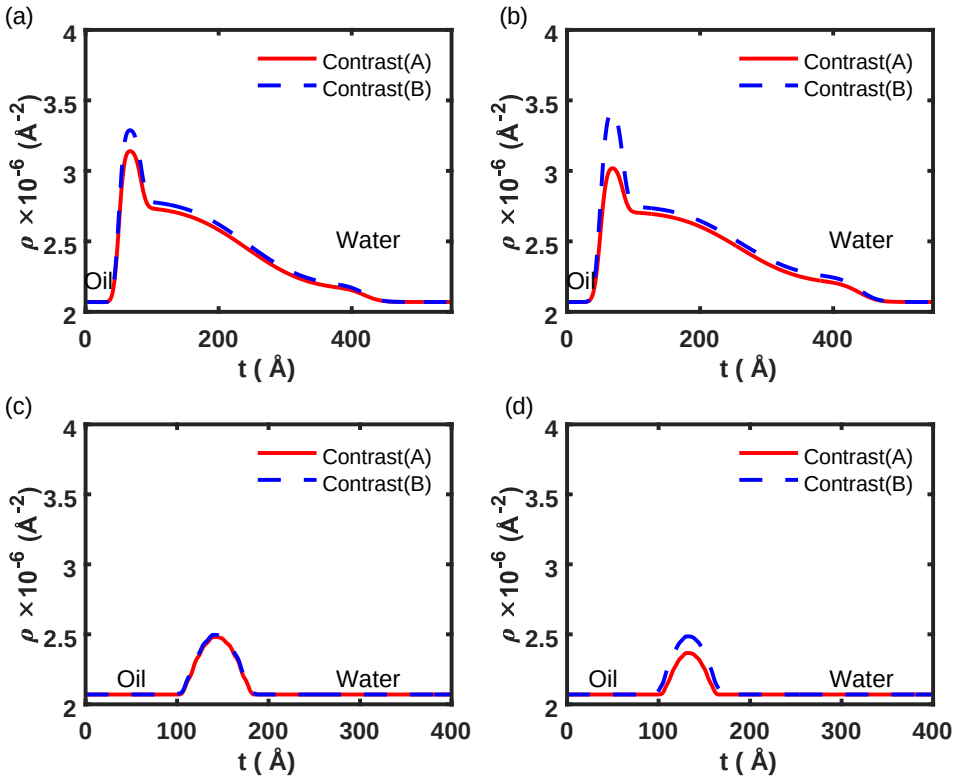

FIGURE 3.10: The Scattering length density profiles for all samples measured in the experiment. Contrast (A), with CMSi surfactant, is shown in red while Contrast (B), with d-surfactant, is shown in blue. Note that in all cases Contrast (A) has a lower signal compared to Contrast (B).(a) MEEA-NP/CTAB, (b) OCT-NP/CTAB, (c) MEEA-NP/SDS, and (d) OCT-NP/SDS.

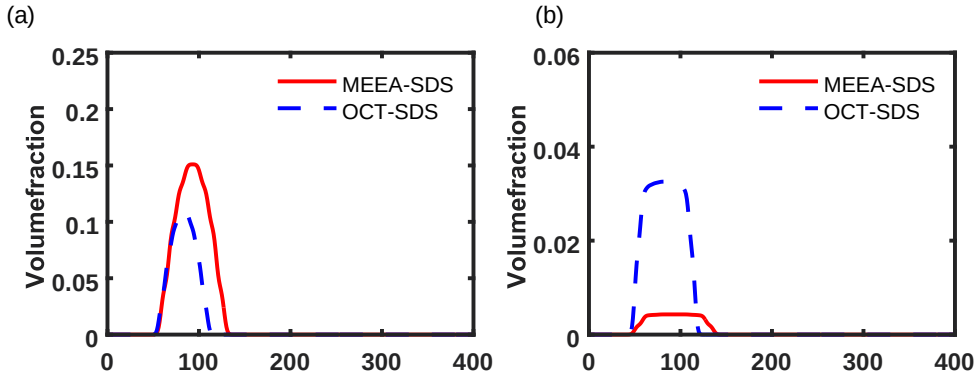

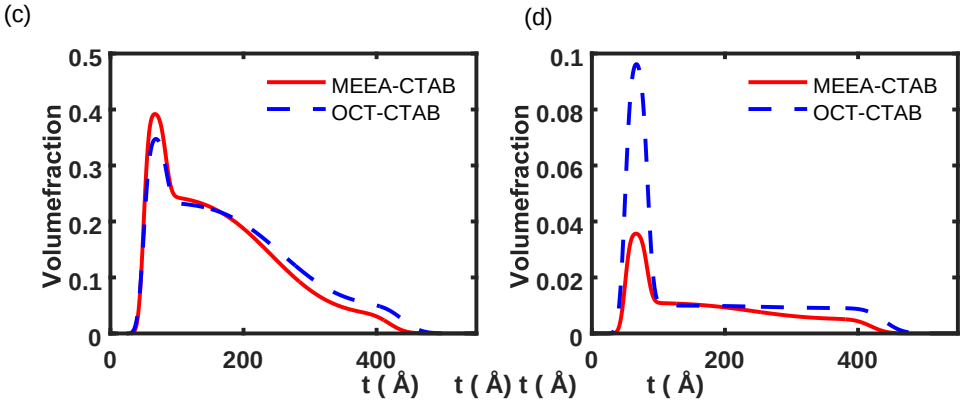

FIGURE 3.11: The distribution of NP (a and c) and surfactant (b and d) across the interface for both systems for the NP/SDS systems (a and b) and the NP/CTAB systems (c and d). The scaling for the NP and surfactants is different to facilitate visualizing the higher amount of adsorbed NP compared to the surfactant. a-top-left: *f* of NP; b-top-right: *f* of SDS; c-bottom-left: *f*of NP; d-bottom-right: *f* of CTAB. This plot has changed.

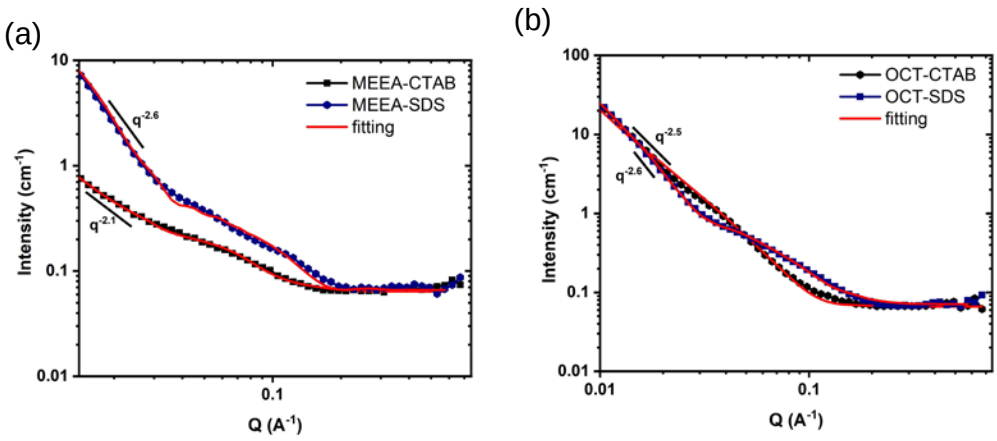

FIGURE 3.12: SANS scattering patterns from 0.5 wt./vol% of (a) MEEA-NPs and (b) OCT-NPs at CMC of surfactant solution (CTAB, and SDS) at 25 C, in D_2O.

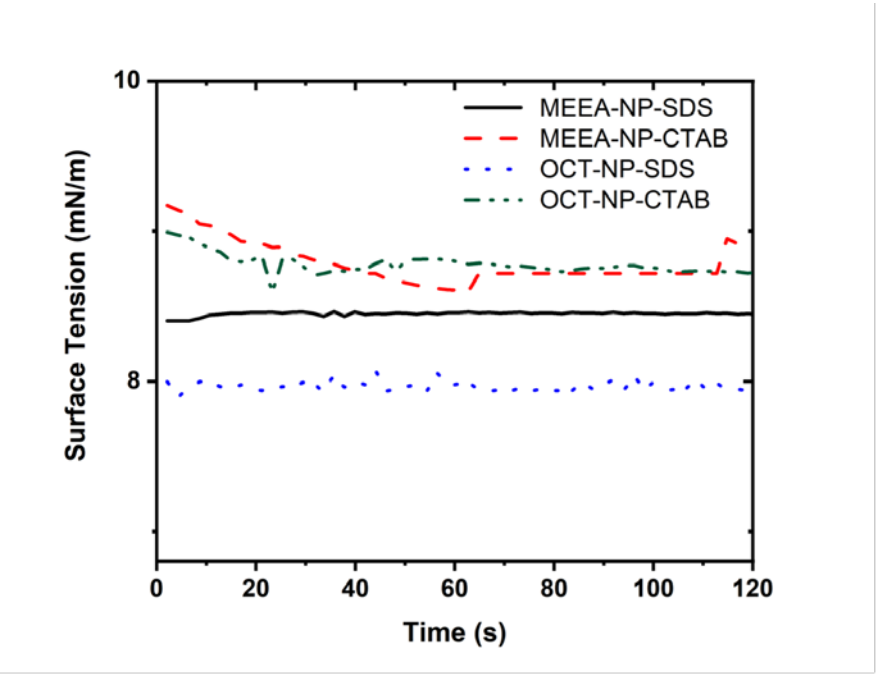

FIGURE 3.13: Dynamic IFT of MEEA-NP and OCT-NP in SDS and CTAB surfactant in n-hexadecane at 120 s.

TABLE 3.11: Interfacial tension, surface tension, and Zeta potential of nanoparticles with CTAB or SDS surfactant, the data all within ± 0.5 error at 20 C.

Materials	IFT (mN/m)	SFT (mN/m)	Zeta potential (mV)
Hexadecane	50.52	-	-
CTAB	5.27	36	+53
SDS	8.8	34	-31
Unmodified alumina	41.3	-	39.6
MEEA-NP/SDS	8.9	33.40	-34.2
MEEA-NP/CTAB	9.1	41.53	35.8
OCT-NP/SDS	7.9	34.33	-34
OCT-NP/CTAB	8.8	40.87	34.9

Oil flooding experiment of modified alumina nanofluid with surfactants (CTAB, and SDS) was conducted in reservoir rocks at 20 C. The nanofluids tests was based upon previous reported method (Al-Shatty, Alexander, and Barron, 2022). Brine was injected first until the amount of oil displacement was 0.05 ml. This was subsequently followed by testing nanofluids: CTAB, SDS, MEEA-NP/CTAB, MEEA-NP/SDS, OCT-NP/CTAB, and OCT-NP/SDS. The testing parameters, conditions such as pressure, flow rate, temperature, salinity, and pore volume injection remained the same for all core tests.

Figure 3.14 shows the oil displacement from the injected NPs with CTAB surfactant (a), and with SDS surfactant (b). The recovery from NPs dispersed in CTAB solution shows higher percentage than from SDS solution. Interestingly, the recovery from the hydrophobic NPs (OCT-NP) in both systems showed higher recovery than from hydrophilic NPs (MEEA-NP). This result is in agreement with our previous research where OCT-NPs showed more effectiveness in oil displacement that MEEA-NPs29. The highest oil recovery was from injected OCT-NP/CTAB which is around 4% more than injected surfactant alone as well as the MEEA-NP/surfactants complexes. These results indicate that, NPs/surfactants complexes can be promising candidates for EOR application.

(a)

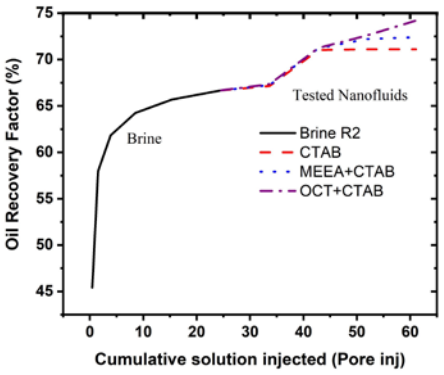

(b)

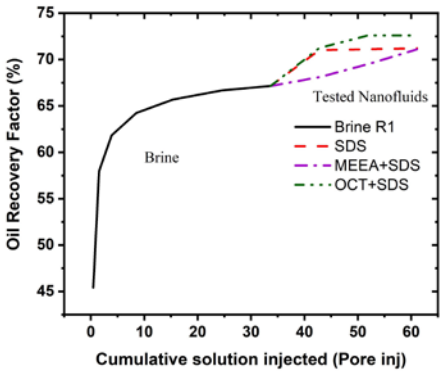

FIGURE 3.14: Oil recovery factor in brine solution using sandstone reservoirs rocks for MEEA-NP and OCT-NP mixing with (a) CTAB surfactant and (b) SDS surfactant. Show a and b in the graph.

FIGURE 3.15: Nanoparticle's surfactant mixtures: a) OCT-NP in SDS surfactant, b) OCT-NP in CTAB surfactant, c) MEEA-NP in SDS surfactant, and d) MEEA-NP in CTAB surfactant.

3.4 Conclusions

The use of neutron reflectometry has been uniquely applied to obtain information on the behavior of NPs at oil/water interface. While column tests ordinarily used by researchers (Mitzel et al., 2016) for the examination of NPs supply information on the dynamic moving behavior, NR technique provide information on the equilibrium structure and interaction of NPs aggregated and/or deposits at the interface. In this regard, NR is unique compared to other techniques due to its ability to supply information on the distribution of the particles near interface. In addition, NR provides previously unobtainable information about the interaction between the NPs and surfactants, including the surfactant coverage NPs and their prospective volume fractions. Thus, the introduction of NR as new technique to study particles interaction with surfactant at interface will advance our current understanding of the mechanisms behind the surface and interaction of NPs with surfactants in natural and engineered environmental systems. The NR data indicated more interaction between NPs and SDS (1:3 ratio), however, the interaction was much smaller (1:15) for NPs with CTAB, with many layers (complex system) at the interface. On the other hand, the adsorb amount of OCT-NP/CTAB complexes showed more affinity to the oil/water interface compared to the NPs/SDS system and this has led to a high oil displacement. The IFT data for NPs alone from our previous published paper (Al-Shatty et al., 2017), showed IFT of around 40 to 45 mN/m, however, IFT reduction was significantly improved by in the presence of NPs/Surfactant complexes (⇠ 8-9 mN/m). This shows that presence of surfactant and its interaction with NPs significantly improve the surface activity of the NPs, which lead to the reduction of IFT compared to the NPs alone. Oil recovery data showed an increase of around 4% for both OCT-NPs (hydrophobic) complexes especially with CTAB surfactants compared.

Chapter 4

Eco Friendly Pickering Emulsion Stabilized by Carboxylic Acid Modified Alumina Nanoparticles

4.1 Introduction

Emulsions are applied in various fields such as: paints, cosmetics, coal treatment, pesticides, and foods. In industry, a long term stabilized emulsion is commonly achieved by the addition of organic materials e.g., surface active polymer or surfactant (Sharma et al., 2015). Emulsions which are stabilized by solid particles are known as Pickering emulsions (PES) (Dai et al., 2018b; Feng et al., 2020; Shah et al., 2016). The differences between Pickering and traditional emulsions are that pickering emulsion exhibits chemical and physical stabilization (Frelichowska et al., 2009). PES is stabilized by solid particles adsorption such as: $CaCO_3$ nanoparticles (NPs) (Guo et al., 2021), clay (Lu et al., 2021), silica NPs (Griffith and Daigle, 2018), magnetic particles (Bielas et al., 2020), latex particles (with a positive charge) (Voorn, Ming, and Van Herk, 2006), biopolymer-based particles, and chitosan coated alginate (Dai et al., 2018b). As nontoxic, safe and environmentally friendly inorganic particles, silica is used in different applications. A clear interaction between surfactant and silica has been found and explained in detail in literature.

The key factor in the stabilized emulsion is the long term stability; it resistance

to the reverse phase. Long term stability can be increased by the addition of homogenously dispersed NPs in a continuous phase. However, it is difficult to form a consistent PES because the system is not easily adsorbed into the interface. Previous studies reported stabilized emulsion by surface modification using NPs and surfactants such as: chitosan by polystyrene (Zhang, Zhou, and Yang, 2015), propionic acid for alumina NPs, and Cetrimonium bromide (CTAB) for silica (Torres et al., 2007). PES stabilized by NPs can form a network or film between oil droplet interfaces. One of the main advantages of PES, it that can provide a barrier against coalescence and provides a tremendous steric stabilization to Oil/Water (O/W) droplets (Torres et al., 2007).

Over the last few years, there is a growing interest in PES of both types: O/W and W/O stabilized by nanoparticles with surfactant or polymer combination. O/W PES have been achieved by using chitosan and polystyrene composite particles. Meanwhile, (Zou et al., 2015) and his co-authors were successful in fabrication of PES gels using high oil volume fraction and a novel zein-tannic acid. They explained that stable PES gels formed because the oil droplets are close to each other and the stable PES form a continuous network due to cross-linking of protein particles and oil droplets. In addition, silica particles have been used in long term emulsion stabilization in crude oil/seawater emulsions which were modified with rhamnolipid.

In a previous study, we demonstrated changing surface wettability of alumina by functionalizing with a carboxylic acids. The hydrophilic NPs were functionalized with 2-(2-methoxyethoxy)- etho-xy]acetic acid (MEEA) and the hydrophobic NPs with octanoic acid (OCT). Herein, we sought to identify functionalized alumina NPs that are nontoxic, safe, and eco-friendly. This chapter focuses on the use of modified alumina NPs with carboxylic acids and with and without surfactants to synergistically

stabilize O/W and W/O emulsions. It also examines the influence of the NPs concentrations, oil properties and type of the surfactants on PES stability properties, phase behaviour, and size of emulsions. The latter was examined by direct visual observation (phase behaviour), dynamic light scattering, and optical microscopy (for measuring size of the emulsions).

4.2 Materials and methods

4.2.1 Materials

Aluminium oxide nanoparticles (13 nm, 99.8%), 2-(2-methoxyethoxy)- etho-xy]acetic acid (MEEA, Scheme 2.2a), octanoic acid (OCT, Scheme 2.2b), decane, hexadecane, toluene, Sodium chloride (NaCl) all were purchased from Sigma Aldrich (United Kingdom) and used as received without further purification. Three surfactant have been chosen in this research: low surface energy of the anionic surfactant (iC18S(FO180, LSES) (for chemical structure, as seen in Scheme 2.1) has been synthesized as per previous methods (Kiani et al., 2019; Al-Shatty et al., 2017), dodecyl sulphate (SDS, Scheme 4.1 a), and Cetrimonium bromide (CTAB, Figure 4.1 Sodium .b).

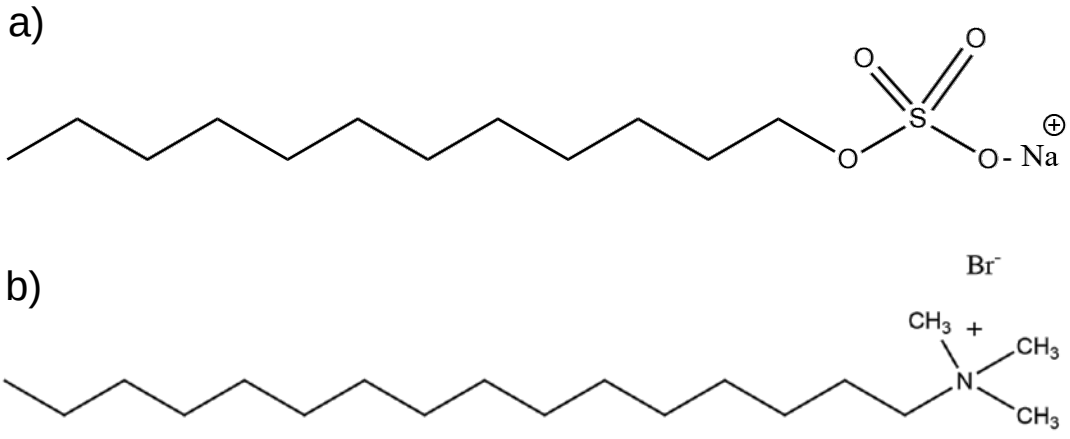

SCHEME 4.1: Chemical structure of Sodium dodecyl sulphate (SDS) (a), and Cetrimonium bromide (CTAB) (b).

4.3 Synthesis

4.3.1 Modified alumina nanoparticles by carboxylic acid

The modified procedure is based on a method reported in literatures by (Maghzi et al., 2012; Al-Shatty et al., 2017), with a slight modification. An a mount of 10 g of aluminium oxide nanoparticles (13 nm) were refluxed overnight in toluene (300 ml) with the 10 mM of carboxylic acid (2-2-(2-Methoxyethoxy) ethoxyacetic acid, and Octanoic acid). After the nanoparticles were refluxed, the mixture was centrifuged for (30 min at a velocity of 5500 rpm). The supernatant was collected and washed three times with 2-propoanal (3x45 mL) and twice with ethanol (2x 45 mL) to remove the unreacted carboxylic acid. The white powder (NPs) was recovered after drying overnight at temperature of 80 C on an oven. The functionalised NPs of mass 8.5 and 9 g was obtained.

4.3.2 Preparation of pickering emulsion

For hydrophilic nanoparticles (unmodified alumina, modified alumina with MEEA (MEEA-NPs)) (w/o) emulsion, (hexadecane and decane were chosen as an oil phase). Emulsions were prepared by initial dispersing (0.3 and 0.5 wt.%) of nanoparticles in water or with an aqueous solution made of 1 wt.% of NaCl. Five different water-oil ratios were used as follow: 90:10, 75:25, 50:50, 25:75, and 10:90. The emulsions were then made using a probe sonicator (Cole Palmer Ultrasonic Processor) for 4 minutes at 30 % amplitude. The resulting emulsions and the phase ratios were examined directly after the following time intervals: 5 min, 1 hour, 1 day, 1 week, and a month.

In terms of hydrophobic nanoparticles (modified alumina with OCT (OCT-NPs)) the O/W emulsion was prepared by initial dispersion (0.3 and 0.5 wt.%) of NPs in oil (hexadecane and decane are chosen as an oil phase) or with an oily solution made

with 1 wt.% of NaCl. Five different water-oil ratios were used as follow: 90:10, 75:25, 50:50, 25:75, and 10:90. The emulsions were then made using a probe sonicator (Cole Palmer Ultrasonic Processor) for 4 minutes at 30 % amplitude. The resulting emulsions and the phase ratios were examined directly after the following time intervals: 5 min, 1 hour, 1 day, 1 week, and a month.

In terms of nanoparticle-surfactant emulsions, three surfactants were chosen in this research (LSES, CTAB, and SDS). First, a surfactant solution was prepared at CMC (1.2 mM (1.003 g/L), 0.9 mM (0.32 g/L), and 2.8 mM (2.36 g/L)) for each surfactant, respectively, then (0.3 and 0.5 wt.%) of NPs added to each of the surfactant solutions. For each type of emulsion (surfactant alone and with NPs), five different water: oil ratios were used (10:90, 25:75, 50:50, and 90:10). The emulsions were then made using a probe sonicator (Cole Palmer Ultrasonic Processor) for 4 min at 30% amplitude. The resulting emulsions and the phase ratios were examined after 5 minutes, one hour, one day, one week, and a month.

4.3.3 Optical microscopy

The microstructure of unmodified alumina NPs and modified alumina with MEEANPs and OCT-NPs with and without surfactants synergistic stabilized PES were observed by optical microscopy. The VHX digital microscope equipped with KEYENCE imaging camera was used to conduct the analysis. The average droplet size of prepared emulsions was measured directly in the intervals of: 1 hour, 1 week, and 1 month; by taking one droplet of emulsion phase and placing it on a glass microscope slide (20x5 cm^2). The emulsion is then sandwiched with another slide on top before being placed underneath the optical microscope camera for analysis.

4.3.4 Dynamic light scattering (DLS)

Dynamic light scattering techniques were employed to determine the PES size in dispersed solutions. For estimating emulsion size of each system, 1 ml of each sample was placed in a disposable cell with a lid and placed in the equipment chamber. The analysis was performed using a Ztasizer Nano Zs equipped with a He-Ne laser, operating at a wavelength of 633 nm, (at 20 C) with 120 s equilibration time and 173 scattering angles. Data processing was performed by the Zetasizer software. The data was taken in triplicate and averaged (mean). The average droplet size of the prepared emulsions was measured directly in the intervals of: 1 hour, 1 week, and 1 month.

4.4 Results and discussions

4.4.1 Pickering emulsion phase

The influence of the unfunctionalized alumina and functionalized alumina with carboxylic acid (MEEA-NPs and OCT-NPs) and inclusive system on the particle size distribution of O/W emulsions stabilization were studied. Two types of modified alumina were dispersed in DI-Water or oil (depending on hydrophilicity) with and without salt (1 wt.% of NaCl dissolved in DI-Water). This was followed by the addition of oil (here decane and hexadecane used as an oil simulant before emulsification) in various fractions ranging from 10 to 90% water to oil ratio. The emulsion stabilization and phase change (via direct visual observation) were timed at these intervals: directly, one hour, a day, one week, and after one month. Tables 4.1 to 4.6.
show the result of the phase emulsion at focusing ratios (50:50, 25:75, and 90:10).

Direct observation are summarised below:

1. For emulsion made from unmodified alumina (un-Al_2O_3-NPs) at 0.3 wt.% without salt in decane: the emulsion displaced phase III in almost at all tested

ratios and stabilized for up to one month with a reduction in emulsion phase with time. In contrast, the presence of NaCl reduced the emulsion stability; all testing ratios showed a complete separation after one day. Increasing NPs concentrations did not improve emulsion stability. Emulsion made of the same system but in hexadecane show phase IV at all ratios studied. The emulsion followed the same trend except emulsion made of 10:90 oil:water ratio, which it showed a complete separation after an hour. Similar to the behaviour of the emulsion in decane the addition of NaCl reduced the emulsion stability.

2. For emulsion made from 0.3 wt.% of MEEA-NPs in decane without salt: the emulsion displaced three-phase emulsion (type-III) across all tested times, where at 25:75, and 10:90 excess water (type-II) were formed for all tested times. In comparison with higher concentration (0.5 wt.%), the emulsions formed excess water for all ratios and at all tested times, except at 50:50 ratio, where the emulsion phase transferred to (three phase- type III) after a week. On the other hand, OCT-NP behaves the same, in both concentrations (0.3, and 0.5 wt.%): excess water (type-II) at all cases and changed to three-phase (type-III) after 1 day for both 25:75 and 10:90 ratios. In both systems (MEEA-NPs and OCT-NPs), adding NaCl reduced emulsion stability.

   For the emulsion made of the same NPs (MEEA-NPs and OCT-NPs), at 0.3 and 0.5 wt.% but in hexadecane, the phase behaviour was the same as the emulsion in the decane system.

3. For emulsions made of surfactants (LSES, SDS, and CTAB) without salt: the emulsions show phase IV and remain stable for up to one week. The phase changed after one month to phase II, III, and IV, for LSES, CTAB, and SDS, respectively. The addition of NaCl to the surfactants systems showed a phase change from one phase IV to two phase I (excess oil), whereas emulsion from

SDS surfactant was slightly affected by salt addition. Interestingly, the presence of salt on the emulsion made of LSES showed a complete separation after one day. This reflects on the combination of NaCl and LSES may result in work as a de-emulsifier. Further investigation is recommanded with lower NaCl concentration, different salt, and emulsifier test to understand the mechanism and confirm the de-emulsifier behaviour.

4. For emulsions made of unmodified alumina (un-Al_2O_3-NPs) with three tested surfactants (LSES, SDS, and CTAB) in both decane and hexadecane: the emulsions phase display IV phase at all tested ratios and remain stable up to one week, then followed by phase II (excess water). Adding salt reduced the emulsion stabilization, especially with LSES, it showed a complete phase separation after one hour.

5. For emulsions made of MEEA-NP with LSES, SDS, and CTAB in decane and hexadecane: the emulsion phase displayed IV phase at all tested ratio and remained stable for up to one week, then followed by phase II (excess water). Adding salt reduce the emulsion stabilization, especially with LSES. It shows a complete phase separation after one hour.

6. For emulsion made of OCT-NP with LSES, SDS, and CTAB in decane and hexadecane: the emulsion phase display the IV phase at all tested ratio and remain stable up to one month, one exception was with 10:90 ratio, phase changed to II (excess water). Adding salt reduce the emulsion stabilization, especially with LSES. Emulsion made of NPs/LESE in present of salt show a complete phase separation after one hour. These results are linked to the wettability result of NPs which shows that hydrophobicity has a positive effect on emulsion stabilization. Increased NPs concentration and hydrophobicity, lead to increase emulsion stability.

4.4.2 Microstructure of NPs and surfactant emulsion

Figures 4.1, 4.2, and 4.3 show a photograph and size distribution of emulsions made from surfactants in hexadecane LSES, CTAB and SDS, respectively at (O/W) ratios 50:50, 25:75, and 10:90 after an hour (a, b, c) and a day (d, e, f). Figure 4.3 shows a photograph and size distribution of emulsions stabilized by 0.3 wt.% of OCT-NP at (50:50 (a), 25:75 (b), and 10:90 (c)) in hexadcane with after a day with LSES, SDS, and CTAB without salt. In the presence of salt, the size distribution shifted toward smaller droplet sizes when the NPs concentration increased. In other words, at increased NPs concentration the droplet size distribution of emulsion attained a narrower range. The small size of the emulsion exhibits longer stability of emulsion (Zhao et al., 2018). OCT-NP is actually a hydrophobic NPs, and it can act as a surface-active agent. From NR data (chapter three), that data shows that particle of OCT-NP/SDS is smaller, which indicates that surfactant covers the OCT-NP and form a bimodal system before the aggregation occur. SDS surfactant might form micelles and accordingly causes interfacial NPs displacement, leading to decreasing in emulsion droplet size, and enhancing the physical stability of OCT-NP/SDS based emulsions.

Figure 4.4 shows a photograph and size distribution of emulsions stabilized by 0.3 wt.% of MEEA-NP at (50:50 (a), 25:75 (b), and 10:90 (c)) in hexadcane with after a day with LSES, SDS, and CTAB without salt. The DLS measurements were performed at various time points (1 hour, 1 day, 1 week, and 1 month) to monitor any changes in the emulsion's particle size. DLS data confirmed the generation of emulsions from all tested materials. The nano and microemulsion particles all showed a larger diameter relative to the corresponding NPs. The results from DLS measurement showed decreasing in particles size after 1 day and increasing after 1 week. However, the particles size of emulsion made of hydrophilic NPs has high size than the particles size of emulsion made of hydrophobic NPs (OCT-NP), increasing hydrophobicity,

decreases emulsion particle size. This suggests that the NPs were effectively encapsulated with a surfactant, and the emulsion were stable. The particle size from the NPs was further examined by optical microscopy.

TABLE 4.1: Microemulsion phase behaviour stability of un and modified alumina NP with carboxylic acid, and surfactant with and without salt in decane with time.

Sample	o: w r	A-Emulsion					B-Emulsion				
		5m	h	d	w	m	5m	h	d	w	m
0.3 wt.% Al_2O_3	50:50	III	III	III	III	III	I	III	X	X	X
	25:75	III	III	III	II	II	III	III	X	X	X
	10:90	II	II	II	II	II	IV	IV	IV	II	II
0.5 wt.% Al_2O_3	50:50	III	X	X	X	X	I	III	X	X	X
	25:75	I	X	X	X	X	III	III	X	X	X
	10:90	I	II	II	II	II	IV	II	II	X	X
0.3 wt.% MEEA-NP	50:50	III	III	III	III	III	III	III	III	III	X
	25:75	II	II	II	II	II	II	II	II	II	II
	10:90	IV	II	II	II	II	II	II	II	II	II
0.5 wt.% MEEA-NP	50:50	IV	IV	II	II	III	III	II	III	III	III
	25:75	IV	IV	II	II	II	II	II	II	II	II
	10:90	IV	IV	II	II	II	IV	III	IV	II	II
CMC LSES	50:50	IV	IV	IV	II	II	IV	I	X	X	X
	25:75	IV	IV	IV	II	II	IV	I	X	X	X
	10:90	IV	IV	IV	II	II	IV	I	X	X	X

CMC SDS	50:50	IV	IV	IV	II	II	IV	IV	IV	II	III
	25:75	IV	IV	IV	II	II	IV	IV	IV	II	II
	10:90	IV	IV	IV	II	II	IV	IV	IV	II	II
CMC CTAB	50:50	I	I	I	III	III	I	I	III	X	X
	25:75	I	I	I	II	II	I	I	III	X	X
	10:90	IV	IV	IV	II	II	IV	IV	II	X	X

Type I = excess-oil; type II = excess-water; type III = three-phase emulsion; type IV = one-phase; x = full separation. A = without salt, B = with 1 wt.% of NaCl.

TABLE 4.2: Microemulsion phase behaviour stability of un-modified alumina NP with and without (salt and surfactant) in decane with time.

Sample	o:	A-Emulsion					B-Emulsion				
	w r	5m	h	d	w	m	5m	h	d	w	m
0.3 wt.% Al_2O_3 with SDS	50:50	IV	IV	IV	III	III	IV	IV	IV	II	II
	25:75	IV	IV	IV	II	II	IV	IV	IV	II	II
	10:90	IV	IV	IV	II	II	IV	IV	IV	II	II
0.3 wt.%Al_2O_3 with CTAB	50:50	IV	IV	IV	II	II	IV	IV	III	III	III
	25:75	IV	IV	IV	II	II	IV	IV	II	II	II
	10:90	IV	IV	IV	II	II	IV	IV	II	II	II
0.3 wt.% Al_2O_3 with LSES	50:50	IV	IV	IV	III	III	III	X	II	II	II
	25:75	IV	IV	IV	II	II	I	X	X	X	X
	10:90	IV	IV	IV	II	II	IV	X	X	X	X
0.5 wt.% Al_2O_3 with SDS	50:50	IV	IV	IV	III	III	IV	IV	IV	II	II
	25:75	IV	IV	IV	II	II	IV	IV	IV	II	II
	10:90	IV	IV	IV	II	II	IV	IV	IV	II	II

0.5 wt.% Al_2O_3 with CTAB	50:50	IV	IV	IV	II	II	IV	IV	II	III	III
	25:75	IV	IV	IV	II	II	IV	IV	II	II	II
	10:90	IV	IV	IV	II	II	IV	IV	II	II	II
0.5 wt.% Al_2O_3 with LESE	50:50	I	I	III	X	X	III	X	X	X	X
	25:75	IV	IV	II	II	II	II	X	X	X	X
	10:90	IV	IV	II	II	II	IV	X	X	X	X

Type I = excess-oil; type II = excess-water; type III = three-phase emulsion; type IV = one-phase; x = full separation. A = without salt, B = with 1 wt.% of NaCl.

TABLE 4.3: Microemulsion phase behaviour stability of modified alumina NP with and without (salt and surfactant) in decane with time.

Sample	o: w r	A-Emulsion					B-Emulsion				
		5m	h	d	w	m	5m	h	d	w	m
0.3 wt.% MEEA-NP with SDS	50:50	I	I	I	III	III	I	I	I	III	III
	25:75	IV	IV	IV	II	II	I	I	I	III	III
	10:90	IV	IV	IV	II	II	IV	IV	IV	II	II
0.3 wt.% MEEA-NP with CTAB	50:50	IV	IV	IV	II	II	IV	IV	IV	II	II
	25:75	IV	IV	IV	II	II	IV	IV	II	II	II
	10:90	IV	IV	IV	II	II	IV	IV	IV	II	II
0.3 wt.% MEEA-NP with LSES	50:50	I	I	III	III	III	III	X	X	X	X
	25:75	I	I	III	III	III	III	X	X	X	X
	10:90	IV	IV	IV	II	II	IV	X	X	X	X
0.5 wt.% MEEA-NP with SDS	50:50	I	I	I	III	III	I	I	I	III	III
	25:75	IV	I	I	II	II	I	I	I	II	II
	10:90	IV	IV	IV	IV	II	IV	IV	IV	IV	II
0.5 wt.% MEEA-NP	50:50	IV	IV	IV	II	II	IV	IV	II	II	II

with CTAB	25:75	IV	IV	IV	II	II	IV	IV	II	II	II
	10:90	IV	IV	IV	II	II	IV	IV	IV	IV	II
0.5 wt.% MEEA-NP	50:50	I	III	III	III	X	I	I	X	X	X
with LSES	25:75	I	I	III	III	X	I	I	I	III	X
	10:90	IV	IV	IV	II	X	IV	IV	IV	IV	X
0.3 wt.% OCT-NP	50:50	I	I	I	III	III	I	I	I	III	III
with SDS	25:75	IV	IV	I	II	II	I	I	I	III	II
	10:90	IV	IV	IV	II	II	IV	IV	IV	II	II
0.3 wt.% OCT-NP	50:50	IV	IV	IV	II	II	IV	II	II	II	II

Table 4.3 continued from previous page

Sample	o: w r	A-Emulsion					B-Emulsion				
		5m	h	d	w	m	5m	h	d	w	m
with CTAB	25:75	IV	IV	IV	II	II	II	II	II	II	II
	10:90	IV	IV	IV	II	II	IV	IV	II	II	II
0.3 wt.% OCT-NP	50:50	I	I	III	X	X	X	X	X	X	X
with LSES	25:75	I	I	III	X	X	X	X	X	X	X
	10:90	IV	V	II	X	X	X	X	X	X	X
0.5 wt.% OCT-NP	50:50	IV	IV	IV	II	II	I	I	III	III	III
with SDS	25:75	IV	IV	I	III	II	IV	I	III	III	II
	10:90	IV	IV	IV	II	II	IV	IV	IV	IV	II
0.5 wt.% OCT-NP	50:50	IV	IV	II	II	I	III	I	I	II	II
with CTAB	25:75	IV	IV	II	II	I	IV	IV	IV	II	II
	10:90	IV	IV	IV	II	IV	IV	II	II	II	II
0.5 wt.% OCT-NP	50:50	III	X	X	X	X	X	X	X	X	X
with LSES	25:75	I	X	X	X	X	X	X	X	X	X

	10:90	I	X	X	X	X	X	X	X	X	X

Type I = excess-oil; type II = excess-water; type III = three-phase emulsion; type IV = one-phase; x = full separation. A = without salt, B = with 1 wt.% of NaCl.

TABLE 4.4: Microemulsion phase behaviour stability of un and modified alumina NP with carboxylic acid, surfactant with and without salt in hexadecane with time.

Sample	o: w ratio	A-Emulsion					B-Emulsion				
		5m	h	d	w	m	5m	h	d	w	m
0.3 wt.% Al_2O_3	50:50	IV	IV	III	X	X	III	III	III	III	III
	25:75	IV	IV	II	II	II	II	II	II	II	II
	10:90	IV	X	X	X	X	II	II	II	II	II

Table 4.4 continued from previous page

Sample	o: w ratio	A-Emulsion					B-Emulsion				
		5m	h	d	w	m	5m	h	d	w	m
0.5 wt.% Al_2O_3	50:50	IV	IV	II	II	II	IV	II	II	II	II
	25:75	IV	IV	II	II	II	II	II	II	II	III
	10:90	IV	IV	II	II	II	II	II	II	II	II
0.3 wt.% MEEA-NP	50:50	III	III	X	X	X	III	III	III	III	III
	25:75	II	II	II	II	II	II	II	II	II	II
	10:90	II	II	II	II	II	II	II	II	II	II
0.5 wt.% MEEA-NP	50:50	III	III	III	III	III	III	III	II	III	III
	25:75	II	II	II	II	II	II	II	III	II	II
	10:90	II	II	II	II	II	II	II	II	II	II

CMC LSES	50:50	IV	IV	IV	IV	II	I	X	X	X	X
	25:75	IV	IV	IV	IV	II	I	X	X	X	X
	10:90	IV	IV	IV	IV	IV	IV	X	X	X	X
CMC SDS	50:50	IV	IV	IV	IV	IV	IV	IV	IV	III	III
	25:75	IV	IV	IV	IV	IV	IV	IV	IV	IV	II
	10:90	IV	IV	IV	IV	IV	IV	IV	IV	IV	II
CMC CTAB	50:50	IV	IV	IV	IV	III	I	I	I	X	X
	25:75	IV	IV	IV	IV	II	I	I	I	X	X
	10:90	IV	IV	IV	IV	II	IV	IV	IV	X	X

Type I = excess-oil; type II = excess-water; type III = three-phase emulsion; type IV = one-phase; x = full separation. A = without salt, B = with 1 wt.% of NaCl.

TABLE 4.5: Microemulsion phase behaviour stability of un-modified alumina NP with and without (salt and surfactant) in hexadecane with time.

Sample	o: w ratio	A-Emulsion					B-Emulsion				
		5m	h	d	w	m	5m	h	d	w	m
0.3 wt.% Al_2O_3 with SDS	50:50	IV	IV	IV	IV	IV	IV	IV	IV	IV	II
	25:75	IV	IV	IV	IV	IV	IV	IV	IV	IV	II
	10:90	IV	IV	IV	IV	IV	IV	IV	IV	IV	IV
0.3 wt.%Al_2O_3 with CTAB	50:50	IV	IV	IV	IV	II	IV	IV	II	II	II
	25:75	IV	IV	IV	IV	II	IV	IV	II	II	II
	10:90	IV	IV	IV	IV	II	IV	IV	IV	II	II
0.3 wt.%Al_2O_3 with LSES	50:50	IV	IV	IV	IV	III	IV	I	X	X	X
	25:75	IV	IV	IV	IV	II	IV	IV	X	X	X
	10:90	IV	IV	IV	IV	II	IV	X	X	X	X

0.5 wt.% Al_2O_3 with SDS	50:50	IV	IV	IV	IV	IV	IV	IV	IV	IV	II
	25:75	IV	IV	IV	IV	IV	IV	IV	IV	IV	II
	10:90	IV	IV	IV	IV	IV	IV	IV	IV	IV	II
0.5 wt.% Al_2O_3 with CTAB	50:50	IV	IV	IV	IV	II	IV	IV	II	II	II
	25:75	IV	IV	IV	IV	II	IV	IV	IV	II	II
	10:90	IV	IV	IV	IV	II	IV	IV	IV	IV	II
0.5 wt.% Al_2O_3 with LESE	50:50	IV	IV	IV	IV	III	I	IV	X	X	X
	25:75	IV	IV	IV	IV	II	IV	I	X	X	X
	10:90	IV	IV	IV	IV	II	IV	IV	X	X	X

Type I = excess-oil; type II = excess-water; type III = three-phase emulsion; type IV = one-phase; x = full separation. A = without salt, B = with 1 wt.% of NaCl.

TABLE 4.6: Microemulsion phase behaviour stability of modified alumina NP with and without (salt and surfactant) in hexadecane with time.

Sample	o: w ratio	A-Emulsion					B-Emulsion				
		5m	h	d	w	m	5m	h	d	w	m
0.3 wt.% MEEA-NP with SDS	50:50	IV	I	I	I	III	I	I	I	III	III
	25:75	IV	IV	IV	IV	I	I	I	I	I	II
	10:90	IV	IV	IV	IV	II	IV	IV	IV	IV	II
0.3 wt.% MEEA-NP with CTAB	50:50	IV	IV	IV	II	II	IV	IV	II	II	II
	25:75	IV	IV	IV	IV	II	IV	IV	II	II	II
	10:90	IV	IV	IV	IV	II	IV	IV	IV	IV	II
0.3 wt.% MEEA-NP with LSES	50:50	I	I	I	III	III	I	I	X	X	X
	25:75	IV	IV	IV	II	II	I	I	X	X	X
	10:90	IV	IV	IV	II	II	IV	IV	X	X	X
0.5 wt.% MEEA-NP	50:50	IV	I	I	I	III	I	I	I	III	III

with SDS	25:75	IV	IV	IV	IV	III	IV	IV	IV	I	II
	10:90	IV	IV	IV	IV	II	IV	IV	IV	IV	II
0.5 wt.% MEEA-NP	50:50	IV	IV	IV	II	II	IV	IV	II	II	II
with CTAB	25:75	IV	IV	IV	IV	II	IV	IV	II	II	II
	10:90	IV	IV	IV	IV	II	IV	IV	IV	IV	II
0.5 wt.% MEEA-NP	50:50	I	I	I	III	III	I	I	X	X	X
with LSES	25:75	I	I	I	III	III	I	I	X	X	X
	10:90	IV	IV	IV	II	II	IV	IV	X	X	X
0.3 wt.% OCT-NP	50:50	IV	IV	IV	IV	III	IV	IV	I	III	III
with SDS	25:75	IV	IV	IV	IV	III	IV	IV	IV	IV	II
	10:90	IV	IV	IV	IV	II	IV	IV	IV	IV	II
0.3 wt.% OCT-NP	50:50	IV	IV	IV	IV	II	IV	IV	IV	II	II

Table 4.6 continued from previous page

Sample	o: w ratio	A-Emulsion					B-Emulsion				
		5m	h	d	w	m	5m	h	d	w	m
with CTAB	25:75	IV	IV	IV	IV	II	IV	IV	IV	II	II
	10:90	IV	IV	IV	IV	II	IV	IV	IV	II	II
0.3 wt.% OCT-NP	50:50	I	I	III	III	III	I	I	III	X	X
with LSES	25:75	IV	IV	IV	II	II	I	I	III	X	X
	10:90	IV	IV	IV	II	II	IV	IV	II	X	X
0.5 wt.% OCT-NP	50:50	IV	IV	IV	IV	III	I	I	I	I	III
with SDS	25:75	IV	IV	IV	IV	III	IV	IV	IV	IV	II
	10:90	IV	IV	IV	IV	IV	IV	IV	IV	IV	II
0.5 wt.% OCT-NP	50:50	IV	IV	IV	IV	IV	II	III	III	III	III
with CTAB	25:75	IV	IV	IV	IV	IV	II	IV	II	II	II

	10:90	IV	IV	IV	IV	IV	II	IV	IV	IV	II
0.5 wt.% OCT-NP	50:50	I	I	I	III	III	I	I	III	X	X
	25:75	IV	IV	IV	II	II	IV	I	II	X	X
with LSES	10:90	IV	IV	IV	II	II	IV	IV	II	X	X

Type I = excess-oil; type II = excess-water; type III = three-phase emulsion; type IV = one-phase; x = full separation. A = without salt, B = with 1 wt.% of NaCl.

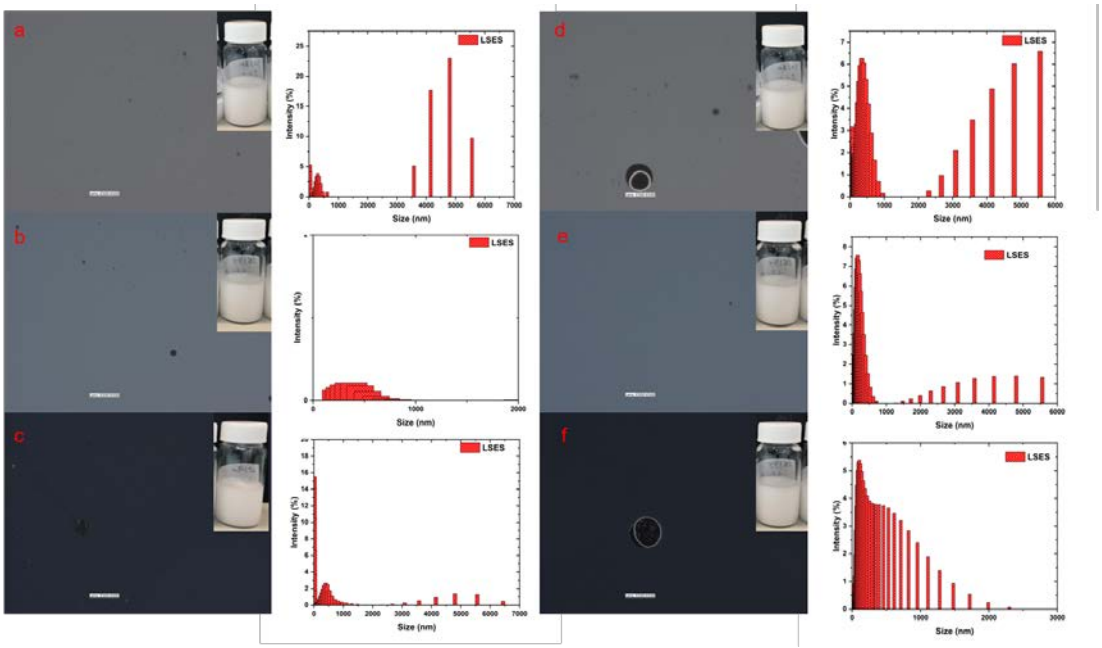

FIGURE 4.1: Optical microscopic images of LSES surfactants at CMC stabilised O/W emulsions in hexadecnae: (a) at 50:50 ratio after an hour, (b) at 25:75 ratio, (c) at 10:90 ratio, (d) at 50:50 ratio after a day, (e) 25:75 ratio after a day, and (f) 10:90 after a day.

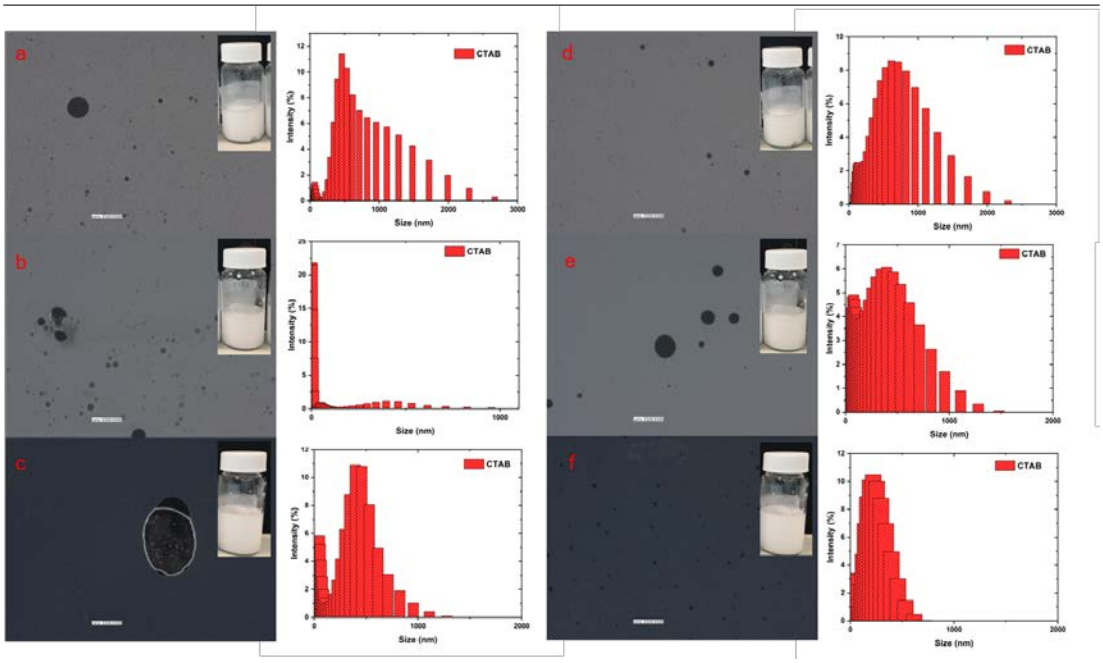

FIGURE 4.2: Optical microscopic images of CTAB surfactants at CMC stabilised O/W emulsions in hexadecnae: (a) at 50:50 ratio after an hour, (b) at 25:75 ratio, (c) at 10:90 ratio, (d) at 50:50 ratio after a day, (e) 25:75 ratio after a day, and (f) 10:90 after a day.

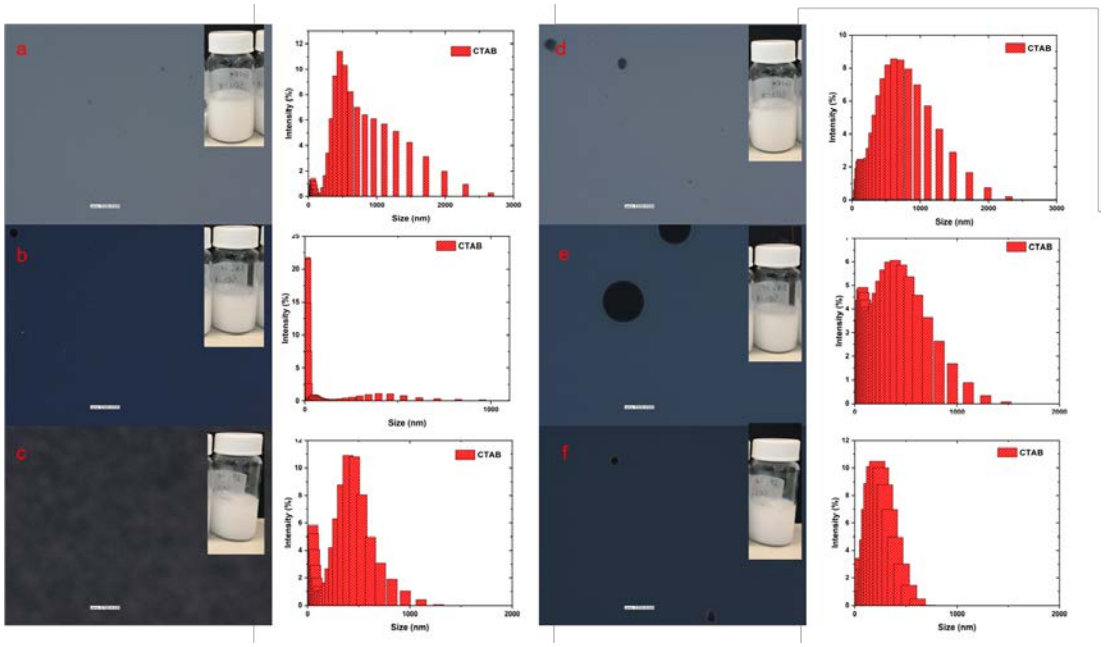

FIGURE 4.3: Optical microscopic images of SDS surfactants at CMC stabilised O/W emulsions in hexadecnae: (a) at 50:50 ratio after an hour, (b) at 25:75 ratio, (c) at 10:90 ratio, (d) at 50:50 ratio after a day, (e) 25:75 ratio after a day, and (f) 10:90 after a day.

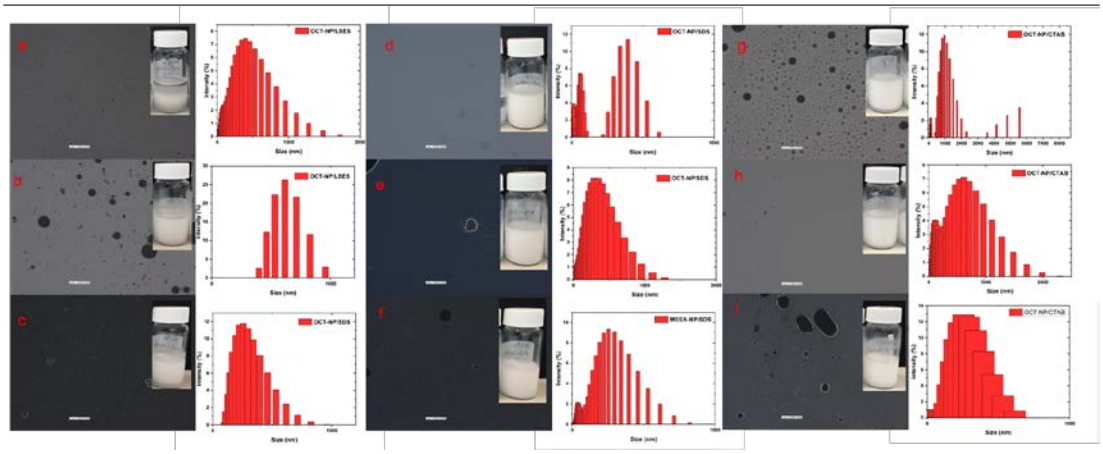

FIGURE 4.4: Optical microscopic images of stabilised O/W emulsions made of 0.3 wt.% OCT-NP without salt in hexadecnae after a day with: (a) LSES at 50:50 ratio, (b) LSES at 25:75 ratio, (c) LSES at 10:90 ratio, (d) SDS at 50:50 ratio, (e) SDS at 25:75 ratio, (f) SDS at 10:90, (g) CTAB at 50:50 ratio, (h) CTAB at 25:75 ratio, and (i) CTAB at 10:90 ratio.

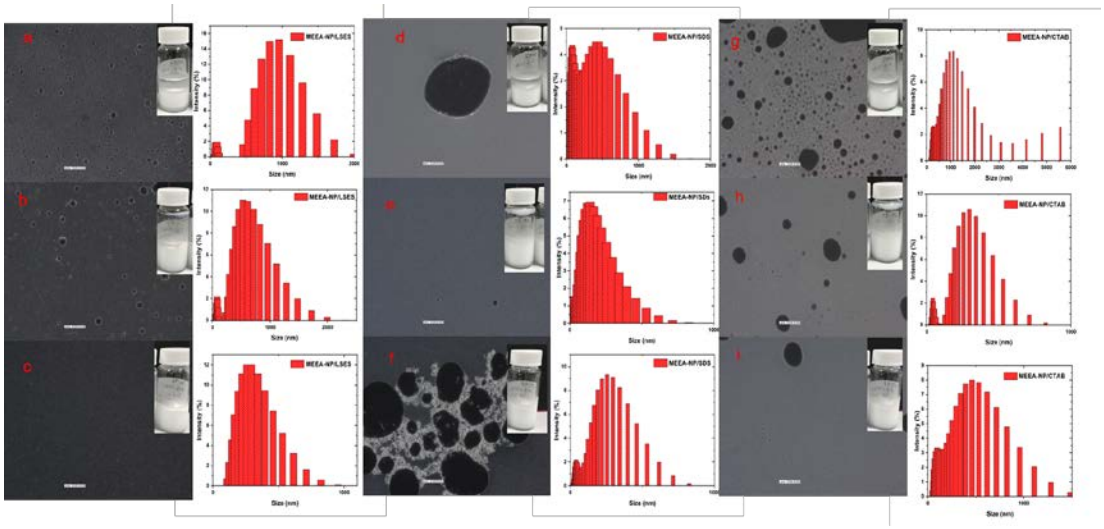

FIGURE 4.5: Optical microscopic images of stabilised O/W emulsions made of 0.3 wt.% MEEA-NP without salt in hexadecnae after a day with: (a) LSES at 50:50 ratio, (b) LSES at 25:75 ratio, (c) LSES at 10:90 ratio, (d) SDS at 50:50 ratio, (e) SDS at 25:75 ratio, (f) SDS at 10:90, (g) CTAB at 50:50 ratio, (h) CTAB at 25:75 ratio, and (i) CTAB at 10:90 ratio.

4.5 Conclusions

Unmodified alumina nanoparticles and alumina modified with carboxylic acid were investigated as emulsion stabilizers with and without surfactants (LSES, SDS, and CTAB). The influence of the salt addition on the emulsion's stability was also studied.

The studies presented in this chapter demonstrated that O/W Pickering emulsions were formed by hydrophilic and hydrophobic modified alumina NPs and can be stabilized for up to one week. PES synergistically stabilized by modified alumina NPs produced small oil droplets which increased emulsion stability (from 1963 nm size for unmodified alumina, to 403, and 503 nm for MEEA-NP and OCT-NP, respectively). Emulsion size of NPs with present of surfactants: 461.9, 423, and 1334 for 0.3 wt.% OCT-NP with CTAB, SDS, and LSES, respectively, and 3826, 734, and 1144, for 0.3 wt.% MEEA-NP with CTAB, SDS, and LSES, respectively. Increasing NPs concentration improves the stability of PES by enhancing the rigidity of the emulsion network structure. Meanwhile, with the addition of surfactant, both the stability and viscoelastic of the PES were increased, and the droplet size was decreased to (409.2, 380, and 643.6 for 0.5 wt.%OCT-NP with CTAB, SDS, and LSES, respectively, and 2443, 465.7, and 1004, for 0.5 wt.% MEEA-NP with CTAB, SDS, and LSES, respectively.). However, salt addition in all emulsion systems shows a negative effect due to screening effects, which is in line with the previous study.

Direct visual observation of emulsion made of OCT-NP with any of the surfactants showed higher stability than MEEA-NP with surfactants, which was attributed to the stronger interaction between hydrophobic part of functional group and oil and bridging effect of hydrophobicity. Increase OCT-NP concentration from 0.3 to 0.5 wt.%, increase the emulsion stability. In comparison, adding salt to emulsion made of LSES surfactant shows a complete phase separation occurred which may lead to a new insight for LSES surfactant. It may indicate that LSES surfactant works as a de-emulsifier in the salt present.

Additional work would be required to investigate whether the LSES works as a de-emulsifier in present of salt. Direct visual observation indicates that the separation

occurs after an hour, and the interface between oil and water is weak. However, further studies would be required to investigate the mechanism of NaCl and LSES surfactants.

From an industrial standpoint, long term emulsion stabilization and de-emulsifiers are both required. For example, oil spilling in water, it is time and cost-effective. Applying de-emulsifier which is effective after one hour may have a big impact for the oil industry. Furthermore, it's possible that the oil and water could be separated with a simple filter. In addition, the surfactant and carboxylic acid could be recovered from the water and used in further processing.

To better understand the underlying mechanism of modified alumina and surfactant synergistic stabilized PES, Figure 4.6. shows a schematic illustration to explain the mechanism of PES. The combination of hydrophobic NPs of modified alumina and low surface energy surfactant can be a promising dispersant and emulsifier.

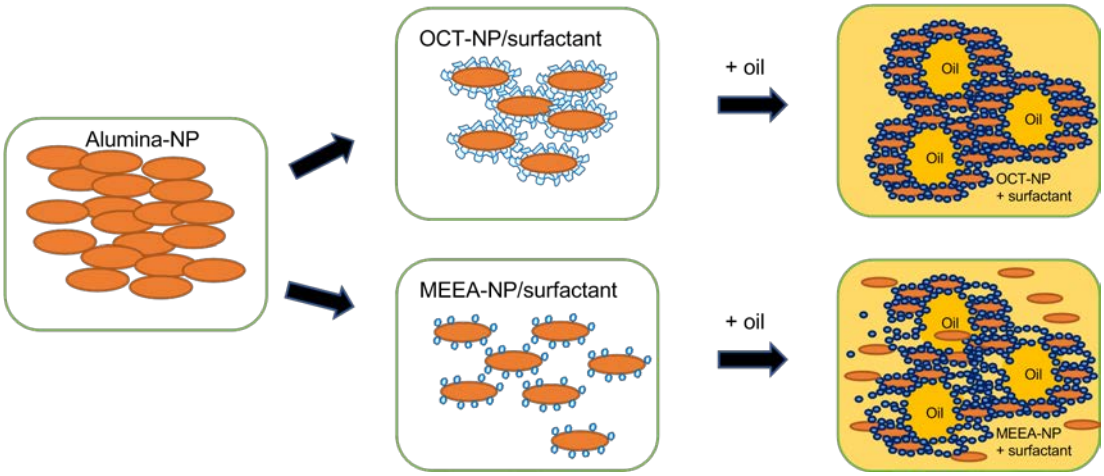

FIGURE 4.6: Schematic of stability mechanism of Pickering emulsion using modified alumina NPs with surfactants.

Chapter 5

Novel Core-Shell Polymeric Surfactants, Part 1: Synthesis and Characterisation

Portions of this chapter have been submitted as a paper: Al-Shatty, W., Hill, D. A., Roher, S. E., Alexander, S., & Barron, A. R. Novel Core-Shell Polymeric Surfactants, Part 1: Synthesis and Characterisation. Submitted to Rsc *J. Colloid Interface Sci.*.

5.1 Introduction

Amphiphilic graft copolymers (AGCs) have been studied for their complex and fascinating chemical properties with vast applications in the medical (Zhang et al., 2012; Zhang et al., 2013; Bontempo and Maynard, 2005; Sigen et al., 2017) and oil industry (Fu et al., 2010; Holmberg, Piculell, and Nydén, 2002; Holmberg et al., 1999; Saha et al., 2020; Wu et al., 2020). In the biomedical field they are prized for their cosmetic attributes and their ability to act as drug carriers or carriers of actives substances due to their low toxicity, biocompatibility and biodegradability (Yang, Cui, and Song, 2020; Kripotou et al., 2016). These polymers are also able to act as surfactants for oil recovery applications (Williams, 2008; Raffa, Broekhuis, and Picchioni, 2016). Other industries have exploited other properties of AGCs that allows them to be used as wetting agents, foaming agents, or plastic modifiers (Garcia et al., 2018).

AGCs are polymers with molecular structures bearing both hydrophobic and hydrophilic moieties. with unique properties that can be synthesized through chemical reactions between suitable functional groups (Garcia et al., 2018). As a

result, stable aggregates can be formed in the presence of selective solvents (e.g., water). These aggregates are principally micellar core-shell structure that form in aqueous solutions and are particularly useful in drug delivery applications (Teulère et al., 2020; Yan et al., 2009; Zehm et al., 2010) and oil separation (Venault et al., 2020; Xie et al., 2017). "Crew-cut" micelle with hydrophobic polymer blocks and hydrophilic chains (such as polyisoprene backbone grafted with Pluronics) have been used to encapsulate drugs and act as stabilizer in both water oil emulsion and soft elastomeric materials (Garcia et al., 2018; Yu, Zhang, and Eisenberg, 1996; Alexander et al., 2014).

One of the most promising polymer blocks to be used for micelle formation is polyethylene glycol (PEG); however, because of its hydrophilicity, it requires reaction with hydrophobic polymers in order to form surface-active materials, capable of forming micelles in solutions or to act as drug carriers with the proper hydrophilic and hydrophobic balance. PEG and its derivatives have been proven useful in forming self-assembly products in biomedical applications and cosmetic industries (Chen, 2014). It has been widely observed in that PEG based materials such as poly (ethylene glycol) methyl ether methacrylate and poly(ethylene glycol) methyl ether acrylate can be used to prepare branched co-polymers for self-assembly in protein conjugation and drug delivery (Zhang et al., 2012; Zhang et al., 2013; Bontempo and Maynard, 2005; Sigen et al., 2017; Odrobinska and Neugebauer,´ 2020). In the cosmetic industry, PEG has been used as a surface active modifier for oil separation and as a stabilizer for water oil emulsions (Fu et al., 2010; Venault et al., 2020; Xie et al., 2017; Neugebauer et al., 2006). A family of AGCs which combine polyisoprene (PIP) backbone with PEG side chains have been developed using the grafting onto method for biomedical and food industry (Cosgrove et al., 2012).

Because of its low toxicity and biocompatibility, we have selected PEG as a grafting agent to modify the chemical structures of two hydrophobic backbones: poly(maleic anhydride-*alt*-1-octadecene) and poly (isobutylene-*alt*-maleic

anhydride). These polymers possess alternating maleic anhydride groups, which act as anchor points for reacting with PEG side chains, leads to creating amphiphilic graft copolymers suitable for use in oil recovery and drug delivery applications.

In a previous study, it was shown that reacting side chains, containing two primary hydroxyl groups at either end of their chains, with functionalized backbone would result in cross-linking and formation of gel networks, unless a large excess of the side chain is used (Alexander et al., 2014). In order to minimize this side reaction, methyl terminated PEGs (having only one hydroxyl group) with different molecular weights (Mn = 550, 2000, and 5000) was selected in order to investigate the effect of chain length on the wettability of the grafted copolymers, the critical micelle concentration, and their aggregation structure. The synthesis was carried out by a "grafting onto" technique through esterification reactions taking place between the terminal hydroxyl groups of the PEG and anhydride groups present on the hydrophobic backbones.

Characterization of the copolymers was performed spectroscopically using ^{1}H NMR and Fourier transform infrared (FTIR) spectroscopy and thermally using Thermogravimetric Analysis (TGA). Analysis of the size and aggregation structures were studied using small angle neutron and X-ray (SANS and SAXS) techniques.

5.2 Materials and methods

5.2.1 Materials

The chemical structures of poly(ethylene glycol) methyl ether (PEG), poly(maleic anhydride-*alt*-1-octadecane) (Octa), and poly (isobutylene-*alt*-maleic anhydride) (IB) are shown in Figure 4.1. All of the chemicals were purchased from Merck Life Sciences and used without further purification. Deionized water (resistivity = 18.2 MW cm, Millipore) was used to prepare solutions for the experiments. Heavy water (D_2O was used as a solvent for SANS measurement and was provided by ISIS neutron facility.

5.2.2 Synthesis of graft copolymers derived from PEG and poly(maleic anhydride-*alt*-1-octadecane) (Octa-*g*-PEG).

Poly (maleic anhydride-*alt*-1-octadecane) (Octa) (1.0 g, 2.8 mmol, 1 mol. equiv., Mn ⇠ 30,000 to 50,000 gmol ^{1}) was heated to reflux in toluene (150 ml) in the presence of PEG (2.9, 10.6, 26.5 g, 1.5 mol. equiv. of the backbone, Mn = 550, 2000 or 5000 g.mol ^{1}, respectively) under magnetic stirring. The mixture was heated to reflux a three-neck round-bottom flask equipped with a DeanStark head for 24 hours during which time water was observed to condense inside the Dean-Stark head, indicating that the esterification reaction was taking place (Figure 5.1). Once the reaction time had elapsed, the mixture allowed to cool in air until it reached room temperature. Following this, the majority of the toluene was evaporated in vascuo, leaving about 15 mL in the reaction flask and the residual mixture was then poured into deionized water in order to precipitate the copolymer product. The product was then placed inside a dialysis tubing cellulose membrane (Mw cut off 14000) to remove unreacted PEG and submerged in deionized water for 4 days. The deionized water was changed twice daily. The purified copolymer was then dried using rotary evaporator at 50 C and dried under vacuum.

5.2.3 Synthesis of graft copolymers derived from poly (isobutylene-*alt*-maleic anhydride) (IB-*g*-PEG).

IB-*g*-PEG was synthesized and purified in a similar manner to Octa-*g*-PEG: Poly (isobutylene-*alt*-maleic anhydride) (IB) (1.0 g, 6.4 mmol, 1 mol. equiv. Mn ⇠ 6000 g.mol ^{1}) was refluxed with PEG (5.35, 19.48, 48.76 g, 1.5 mol. equiv., Mn = 550, 2000 or 5000 gmol ^{1}, respectively) in a mixture of toluene and dimethylformamide (IB was dissolved in 40 mL of DMF for 1 h and then 80 mL of toluene was added to the mixture), for 24 hours under magnetic stirring.

5.3 Characterization

^{1}H NMR spectra were recorded using a 500 MHz Bruker Avance NMR spectrometer. Spectra were recorded in $CDCl_3$ (unless otherwise stated). The sample concentration was 2 wt/vol%. Spectra were analyzed using MestReNova. IR spectra were recorded in transmittance mode using a Perkin-Elmer Spectrum 100 attenuated total reflection (ATR) IR spectrometer between 650-4000 cm ^{1}. Sixteen scans were recorded during each measurement. TGA experiments were conducted on a TA Instrument, SDT Q600. The samples were run in an open alumina crucible under continuous argon flow. The heating profile was equilibrated at 25 C and then ramped at 10 C/min to 600 C.

SANS measurements were carried out on the Larmor instrument at ISIS, Didcot, UK (LARMOR, 2020). Larmor is a fixed-sample detector instrument that use neutron with wavelengths between 0.9 - 13.0 Å to provide a Q-range of 0.003-0.7 Å. All samples were measured in 2 mm path-length rectangular quartz cells in D_2O. The raw SANS data were normalized by subtracting the scattering of the empty 2 mm cell and a D_2O as a solvent background. The measurements were carried out at 25 C. The SAXS measurement were carried out on the Nanostar SAXS equipment from Bruker at Liverpool university. This equipment has a liquid Gallium anode-based x-ray source. A circular x-ray beam of 500 μm diameter is obtained. The X-ray have a wavelength of 1.342 Å. The sample to detector distance was set up to 107 cm, AgBh used a calibrant. Each sample were measured 1200 s each, background was subtracted properly after transmission calculation. Background is water in all cases except for (Octa, and IB) backbones which toluene and DMF was used, respectively. The SANS data reduction was carried out using Mantid program (Arnold et al., 2014), and fitting of the SANS and SAXS data were carried out using SasView program (SASVIEW, 2021). The data were fitted using an Ellipsoidal Core-Shell model.

Surface tension (*g*) measurements were carried out through diluting (3 to 4.5 wt.%) aqueous stock solutions of the grafted polymers. Measurements were carried out using a DSA25 Drop Shape Analyser (Krüss) using the pendant drop method at ambient conditions. The *g* was obtained by fitting the Young Laplace equation to the contour profile of a 4.5 μL droplets. Presented values were taken 100-130 s after the droplets were dispensed and are the average of three measurements.

Contact angle measurements were performed a DSA25 Drop Shape Analyzer (Krüss) using the sessile drop method. Deionized water droplets (4.5 μL) were placed on the surfaces. Values presented are the average of three measurements, carried out at three different positions on the new coating surfaces. Glass microscope slides were used as substrates to investigate the wettability of the copolymer films. Copolymer films were spray-coated onto the substrate from 2 wt.% aqueous suspensions using an artist's spray gun and hydrocarbon airbrush propellant. Three layers of coating were sprayed onto the substrates to ensure all areas of the surface were covered. The morphology of selected substrates was examined using atomic force microscopy and noncontact cantilevers (RTESP, AFM). Images for each thin polymer coated sample were obtained using intermittent contact mode, at a scan rate of 0.6-1 HZ and an image resolution of 512x512 pixels, (10x10) μm^2 size. The captured imaged for testing films were analyzed using Gwyddion off line processing software to define the surface roughness from the AFM scans.

Sample preparation for the UV-vis measurement was carried out by making (3 to 4.5 wt.%) stock solution of grafted polymers in deionized water, then a series of concentrations were made up by dilution of the stock solution. 0.90 mM of the hydrophobic dye azobenzene was added to the diluted samples. The samples were left on the stirrer plate for 24 hours. The measurements were repeated twice with new prepared solutions.

5.4 Results and discussions

5.4.1 Characterization

Grafting of PEG onto the hydrophobic backbones was achieved through ring opening reactions taking place between the terminal OH groups of the PEG molecules and the cyclic anhydride functionality present in Octa and IB backbone (Scheme 5.1). Reactions were conducted with Dean-Stark apparatus in order to collect the water generated in the condensation reactions.

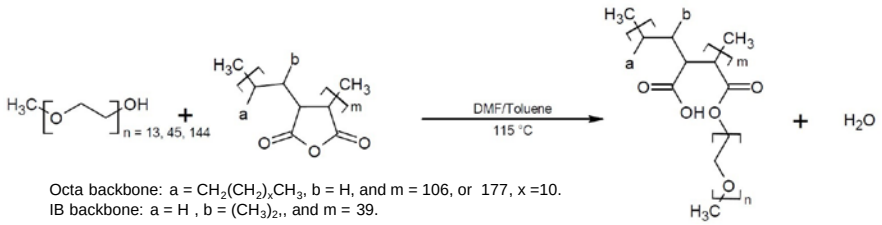

SCHEME 5.1: Synthetic route, "graft onto" polymerization between poly (ethylene glycol) methyl ether and poly (maleic anhydride-*alt*-1-octadecane)/ poly (isobutylene-*alt*maleic anhydride) backbone.

The products as well as the starting materials were analyzed by FTIR in order to confirm the chemical reaction occurrence. The data are shown in Figure 5.1a, b, and c for grafted PEG (Mn= 550, 2000, 5000, respectively) onto IB (left) and Octa backbones (right). Analysis of PEG shows a strong band at about 2860 cm ^{1} ascribed to the C-H stretches of the CH_2 groups and a band at 1460 cm ^{1} ascribed to CH_2 scissoring. Strong bands attributed to C-O-C stretching of the ether groups were also observed between 1070-1100 cm ^{1} and CH_2 rocking bands at 1250 cm ^{1} (Sun, Yang, and Yao, 2020). By comparison the hydrophobic backbone, Octa, showed intense C-H asymmetric and symmetric stretching bands at 2921 and 2852 cm ^{1}, respectively and C=O stretching bands of the cyclic anhydride functional groups and the ring opened carboxylic acid at 1777 and 1711 cm ^{1}, respectively (Rotko et al., 2019). Similarly, IB also showed an intense band at about 1770 cm ^{1} ascribed to C=O stretching of the maleic anhydride; however, weaker C-H stretching bands were

observed due to the absence of the longer alkyl side groups present in Octa. Reaction of the lactone groups of IB was confirmed by the absence of the anhydride C=O stretch at 1770 cm^{-1} and the appearance of weaker C=O stretching bands between 1710 and 1720 cm^{-1} ascribed to the newly created ester groups. In addition, C-H stretching and bending vibrations, and C-O stretching bands, from the ether groups present in PEG were also observed in the IR spectrum, confirming that grafting had occurred.

Similar observations were present in the IR spectrum of Octa after exposing the polymer to the reaction conditions, where the presence of grafted PEG was confirmed by the appearance of strong C-O stretching along with the absence of the anhydride C=O stretch at 1777 cm^{-1}. Furthermore, one broad band was observed in the C-H stretching region 2893 cm^{-1} of the grafted Octa copolymer, similar to that in the spectra of the as received PEG, providing further evidence that grafting had occurred. In addition, the IR spectra of the grafted PEG_{550} onto IB or Octa backbones (Figure 5.1a,) show a small peak related to maleic anhydride C=O stretching, that indicate some of the maleic anhydride are not reacted. This is consistent with the calculated total number of PEG in the grafted sample, which is less than the available grafted points for the backbone. In order to further proof that grafting reaction has occurred, both the backbones and the PEG chains were physically mixed (method 2-AppendixA) and the IR spectra (Figure 5.2) were compared to the chemically mixed data. The data show that mix material has both the C-H stretching 2878 cm^{-1} and C=O stretching bands for cyclic anhydride functional groups which indicate that no maleic anhydride ring opening and therefore no chemical reaction has occurred upon mixing PEG and hydrophobic backbones.

The grafted samples were also characterized using ^{1}H NMR to confirm the presence of both PEG and the backbones in the products and estimate the total number of PEG chains per backbone (free and grafted). The ^{1}H NMR spectra of as received Octa or IB shows peaks ascribed to the aliphatic C-H protons at around 1-1.5

ppm. The proton peaks associated to PEG ($–CH_2CH_2–O$) appears at around 3.6 ppm. Following grafting, in all the ^1H NMR spectra of products, both peaks related to the backbone and the PEG chains can be observed (Figures 5.3 to 5.8).

Octa has alternating C_{18} chains with the average molecular weights of between 30 to 50 KDa, hence it has around 106 to 177 grafting points (from alternating maleic anhydride groups). However, the average number of molecular weights of IB is 6 KDa, hence has around 39 grafting points. From the estimated grafting points and the ^1H NMR integrals (all calculations are shown in the Appendix), we can calculate the total number of the PEG in the product (either grafted or free). Table 5.1 shows the calculated total number of PEG chains in various products. According to the NMR data IB-*g*-PEG_{550} shows 13 number of PEG in the product out of possible 39, which indicates that, some of the maleic anhydride groups are not reacted (in line with IR data). In comparison grafted PEG 2000, and 5000, has 31, and 40, number of PEG, respectively. The results indicate that possibly nearly all of the malic anhydride groups are reacted in the case of grafted PEG_{5000}, in agreement with the IR data (Figure 5.1b). The same trend is also observed for Octa-*g*PEG, with possibly all the grafting points reacted or targeted for PEG_{2000} and PEG_{5000}.

The thermal stability of the polymers was also studied using TGA. It was observed that some of the copolymer samples contained residual water, as evidenced from weight losses below 100 C. As is shown in the TGA data (Figure 5.9), maximum thermal degradation of PEG_{2000} and PEG_{5000} was observed to occur at about 420 C, whereas degradation of the shorter chain PEG_{550} was observed to occur at approximately 300 C. Degradation of the pure Octa and IB backbone shown two peaks at 280 C (which is related to maleic anhydride group (Bettahar et al., 2021; Martínez, Uribe, and Olea, 2005; Kumar et al., 2016)) and 400 C (for the rest of the hydrocarbon polymer backbones). The first peak (280 C) disappeared or reduced in the thermal degradation of the grafted PEG onto IB and Octa backbones, that

indicates the ring opening and the reaction has occurred between the PEG and backbones.

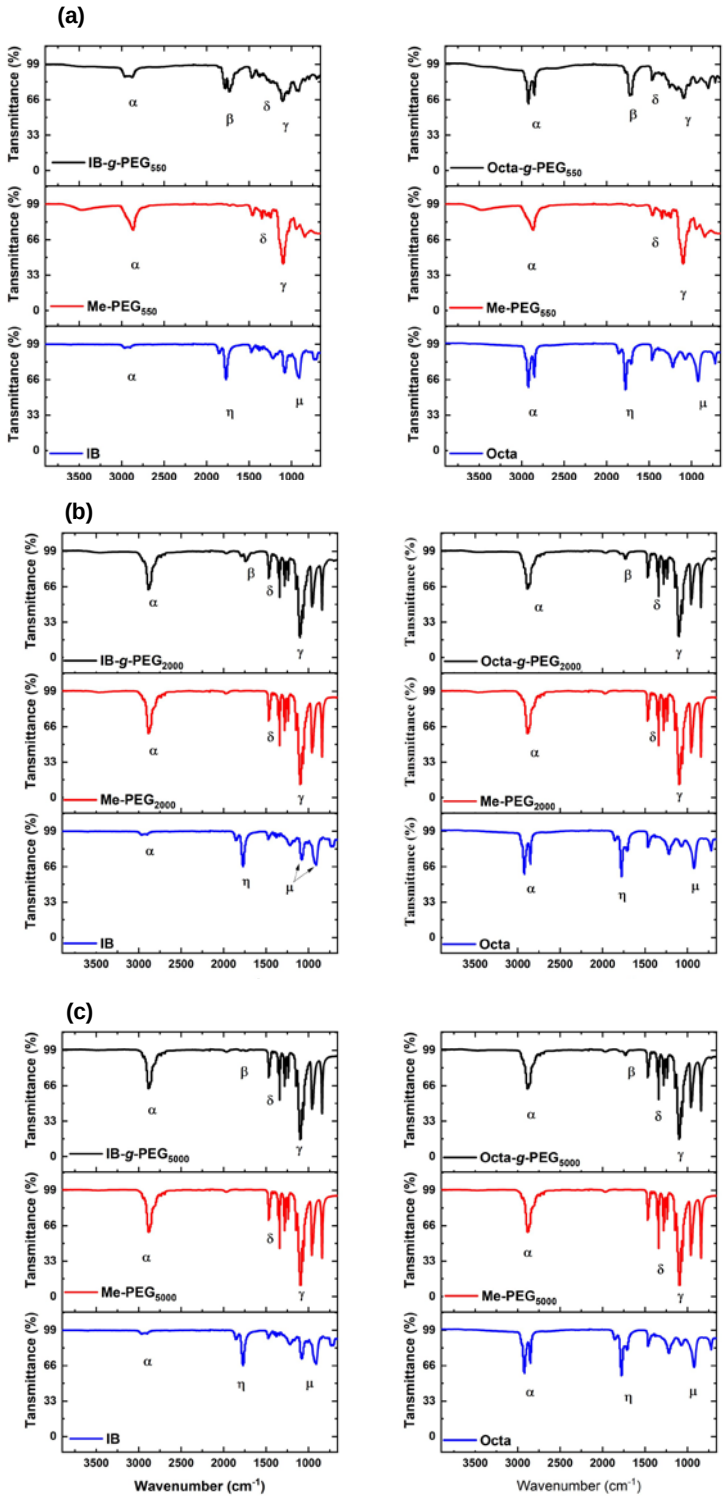

FIGURE 5.1: FTIR spectra of backbone, un-grafted PEG at Mn (2000), and grafted PEG onto (a) IB and (b) Octa backbone. *a* = C-H stretching, *s* = C-H bending, *g*= C-O-H stretching, *μ*= asymmetrical C-H, *h*= C-O-C anhydride, *b* = -C=O ester bending.

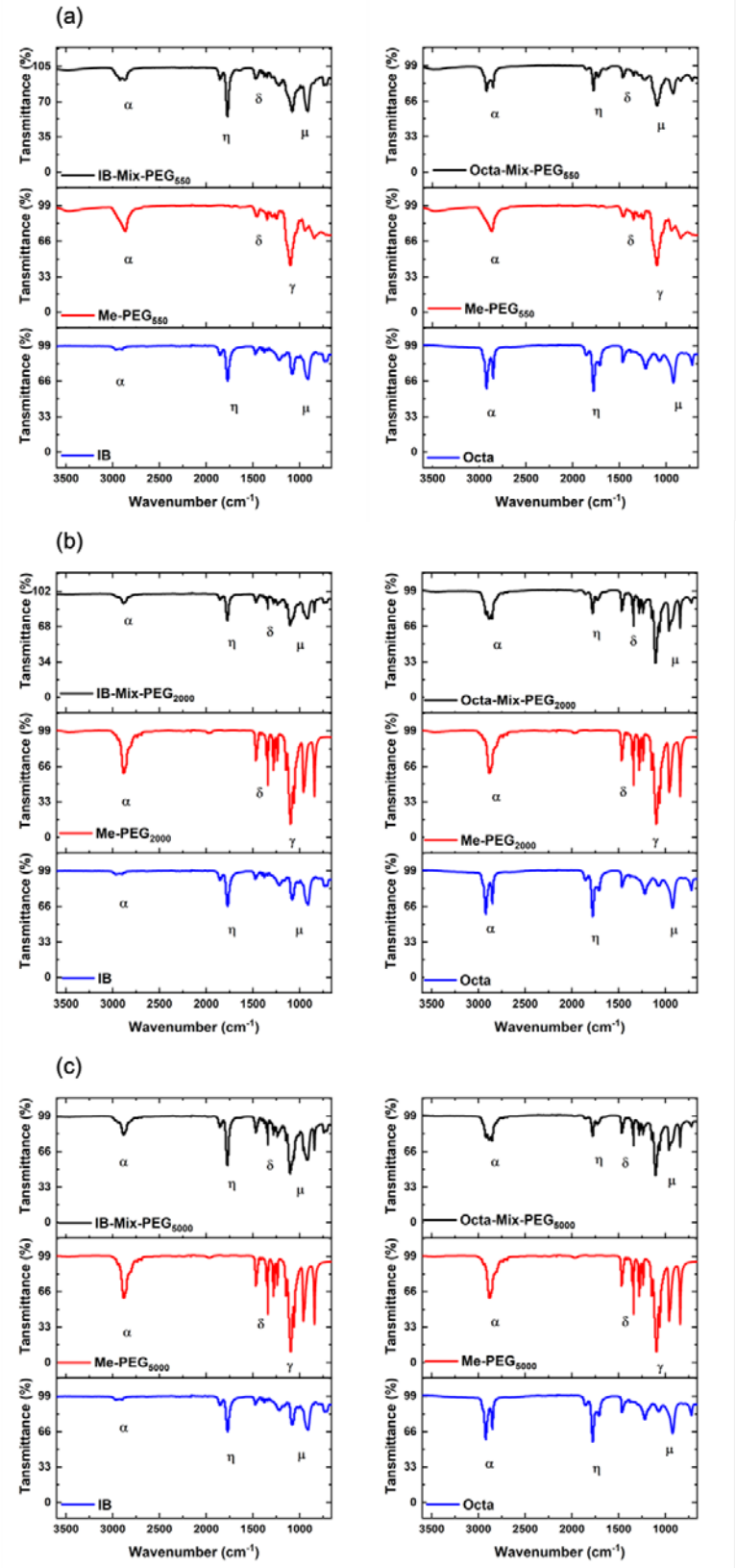

FIGURE 5.2: FTIR spectra of backbone, un-grafted PEG at Mn (550 (a), 2000 (b), and 5000 (c)), and Mix PEG with IB (left), Octa backbone (right). *α*= C-H stretching, *s*= C-H bending, *μ*= asymmetrical C-H, *h*= C-O-C anhydride.

TABLE 5.1: List of the AGCs and the total number of grafted PEG per backbone.

Co-polymer	Total number of PEG	Co-polymer	Total number of PEG
Octa-*g*-PEG_{550}	21 or 35	IB-*g*-PEG_{550}	13
Octa-*g*-PEG_{2000}	101 or 169	IB-*g*-PEG_{2000}	31
Octa-*g*-PEG_{5000}	110 or 183	IB-*g*-PEG_{5000}	40

The degradation of the grafted co-polymers was observed to occur at temperatures ranging between about 350-400 C. The TGA data related to grafted PEG_{550} onto IB or Octa backbone show a small weight loss at area around 280 C, which is related to maleic anhydrite decomposition. These results are in line with ^{1}H NMR and FTIR results at which shows the presence of unreacted maleic anhydride in the backbone. In addition, the TGA data were compared to TGA data of physical mix between of PEGs and the backbones (Figure 5.10). The preparation of the physical mixture and the TGA data are provided in the appendix. The thermal degradations of the mix materials show apparent difference to the chemical mixtures. For example, for the chemical mixture the weight loss starts at around 350 and peaks at around 400 C, whereas for the physical mixture the weight loss starts at around 200 C and there is a clear weight loss at around 280 C which is referred to maleic anhydride groups. These results confirm the occurrence of the esterification reaction between the PEG and the backbones.

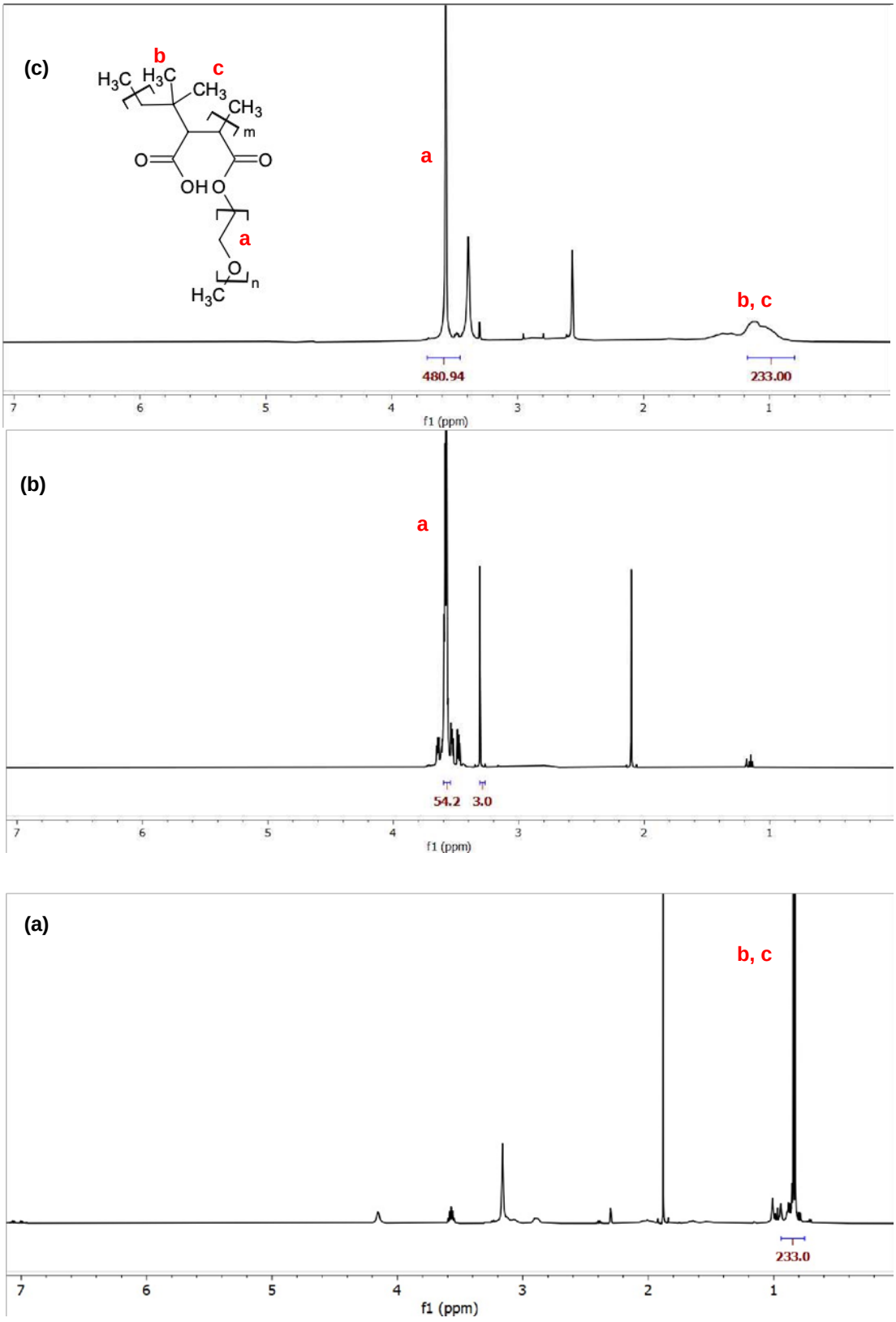

FIGURE 5.3: ^{1}H NMR of starting materials backbone (a), PEG (b) and the grafted backbone IB-*g*-PEG$_{550}$.

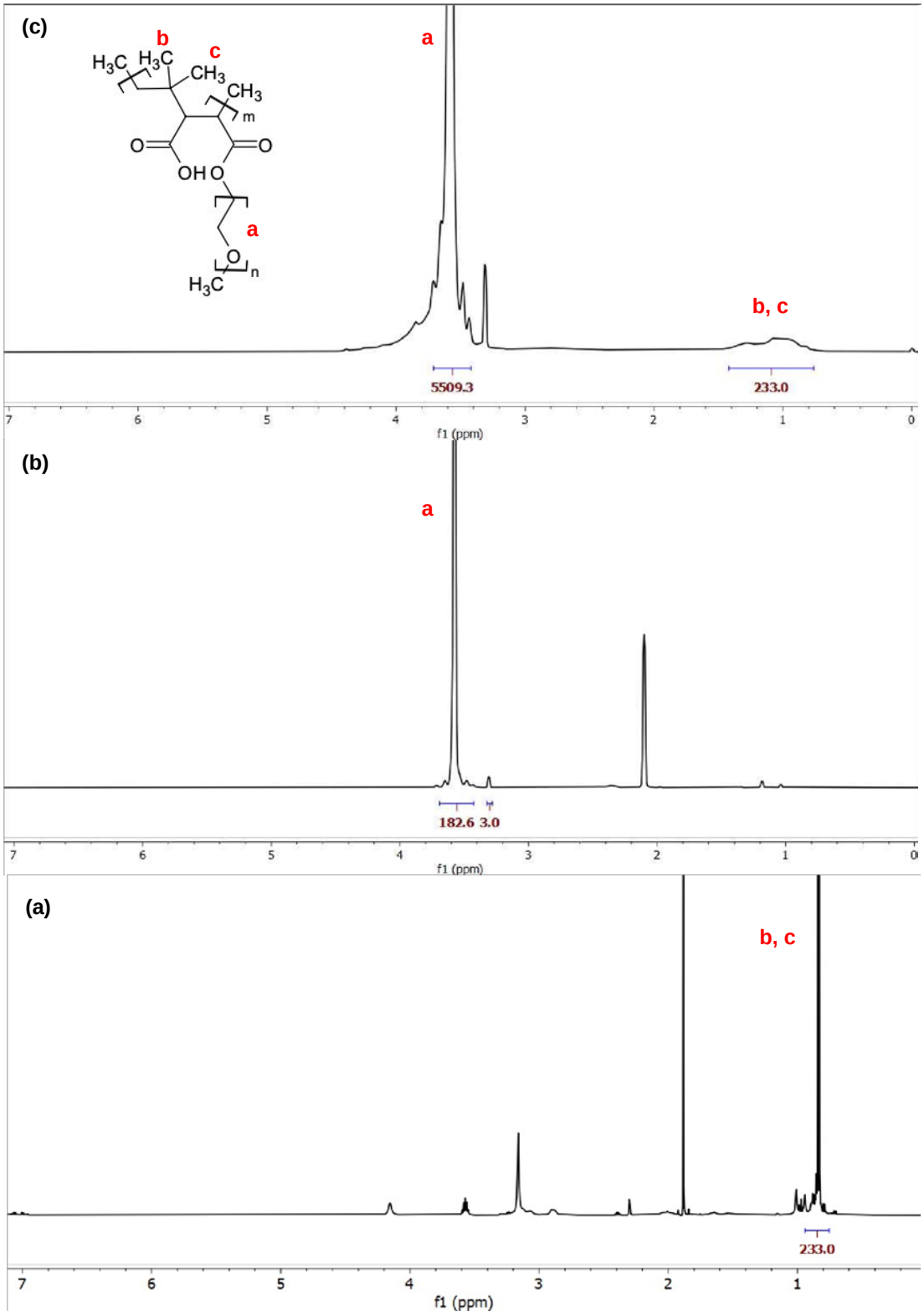

FIGURE 5.4: ^{1}H NMR of (a) starting materials backbone PEG and (b) the grafted backbone IB-*g*-PEG_{2000} (c).

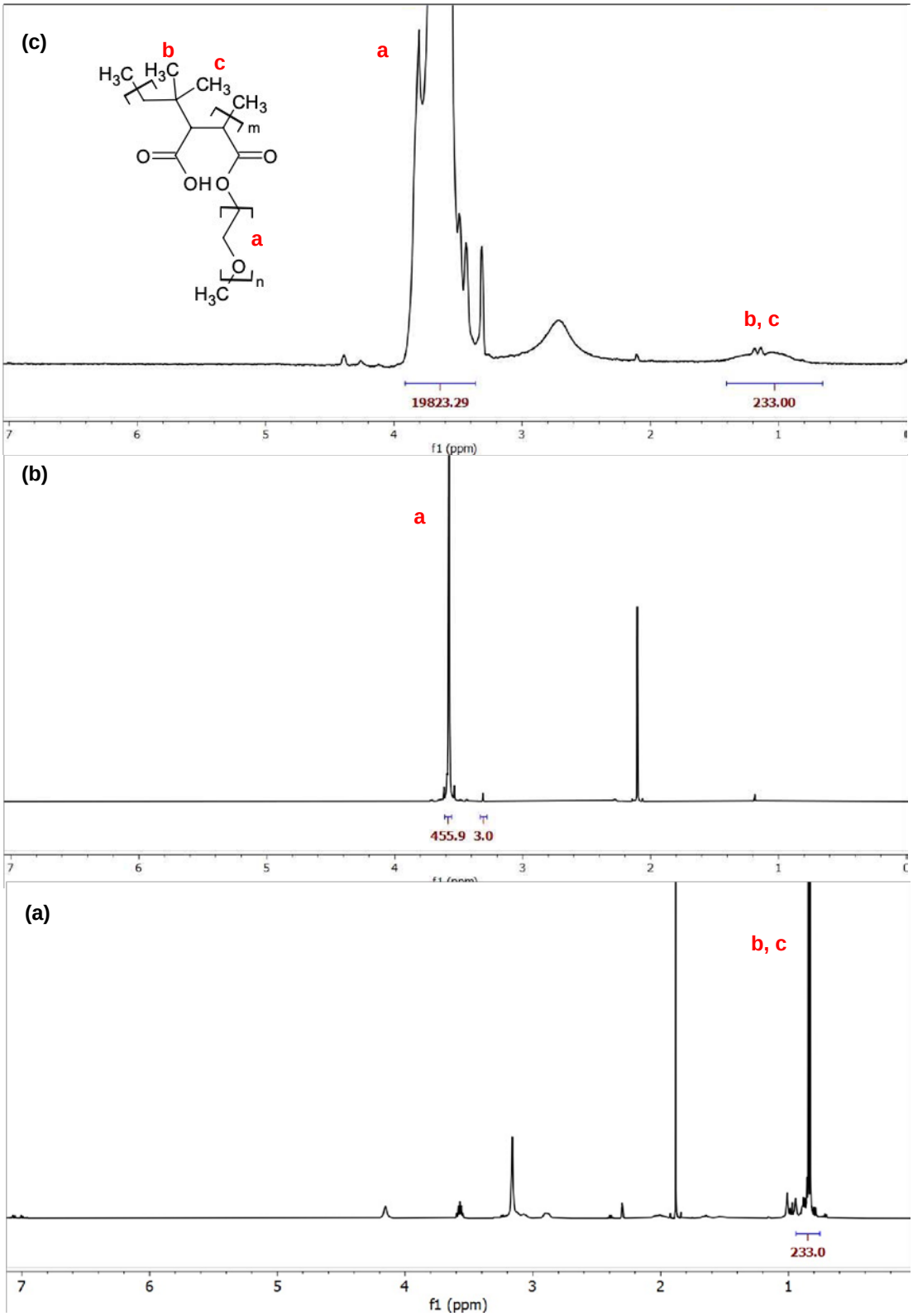

FIGURE 5.5: ^{1}H NMR of starting materials backbone (a), PEG (b) and the grafted backbone IB-*g*-PEG_{5000}.

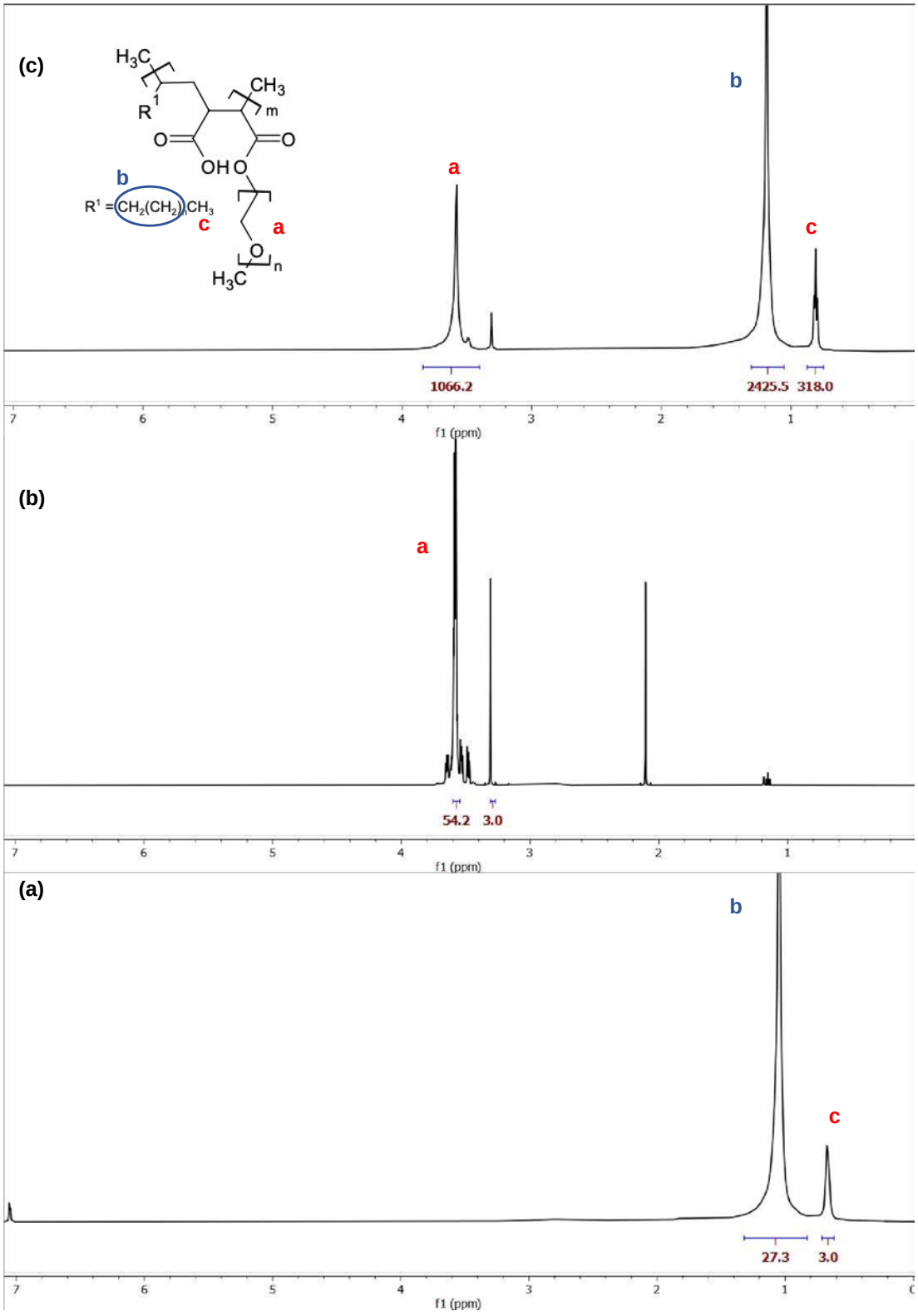

FIGURE 5.6: ^{1}H NMR of starting materials backbone (a), PEG (b) and the grafted backbone Octa-*g*-PEG$_{550}$.

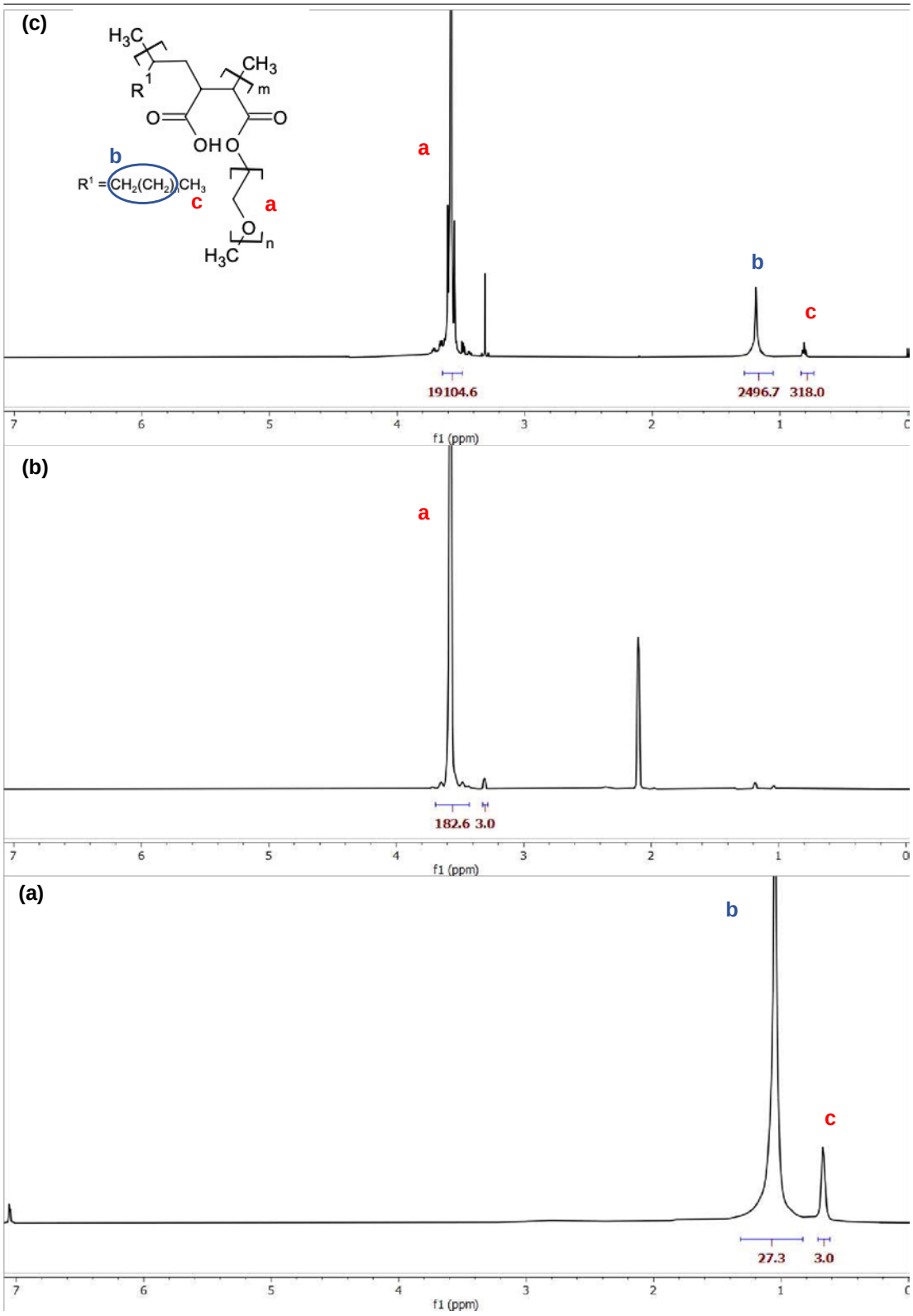

FIGURE 5.7: ^{1}H NMR of (a) starting materials backbone PEG and (b) the grafted backbone Octa-*g*-PEG$_{2000}$ (c).

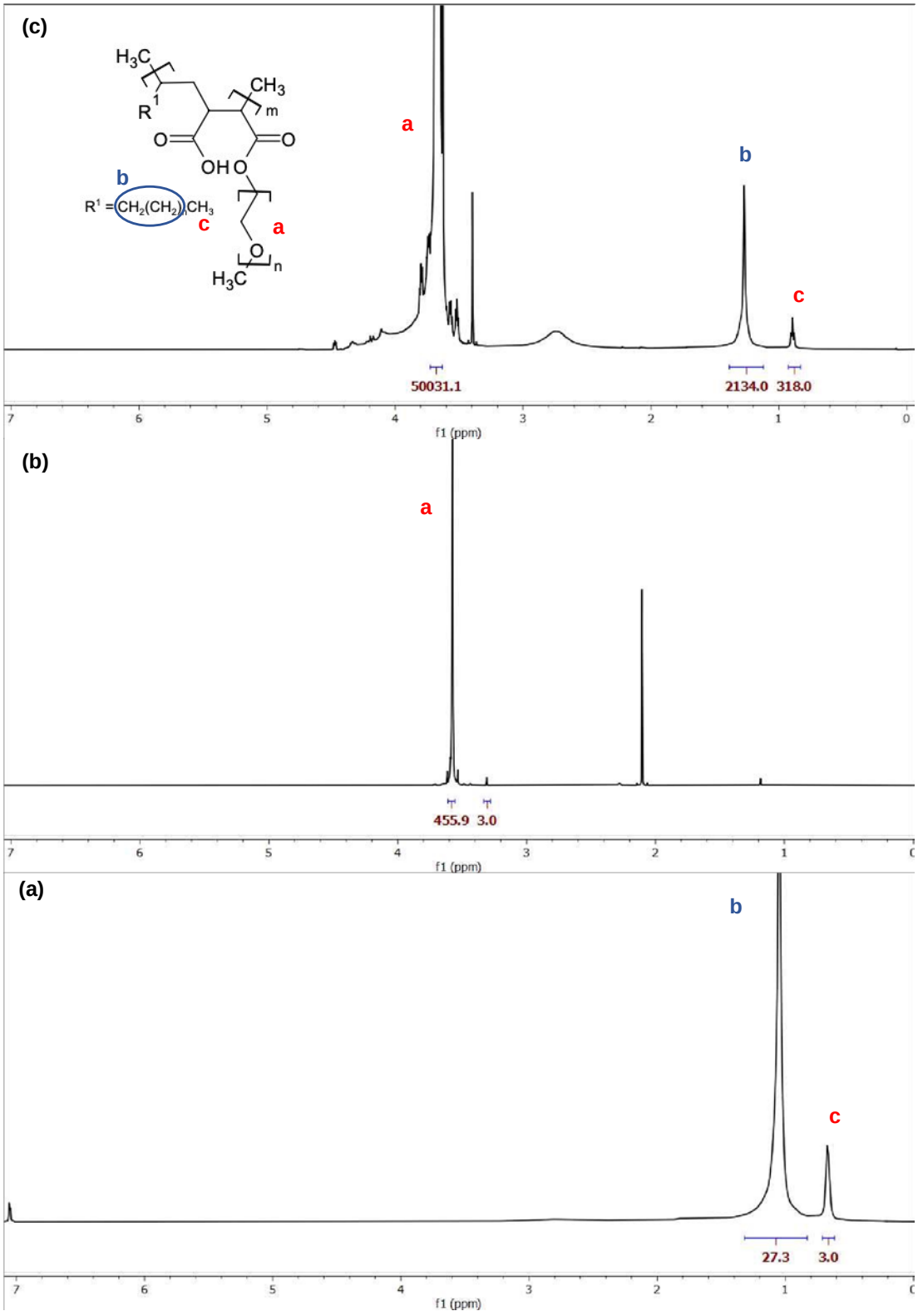

FIGURE 5.8: ^{1}H NMR of starting materials backbone (a), PEG (b) and the grafted backbone Octa-*g*-PEG$_{5000}$.

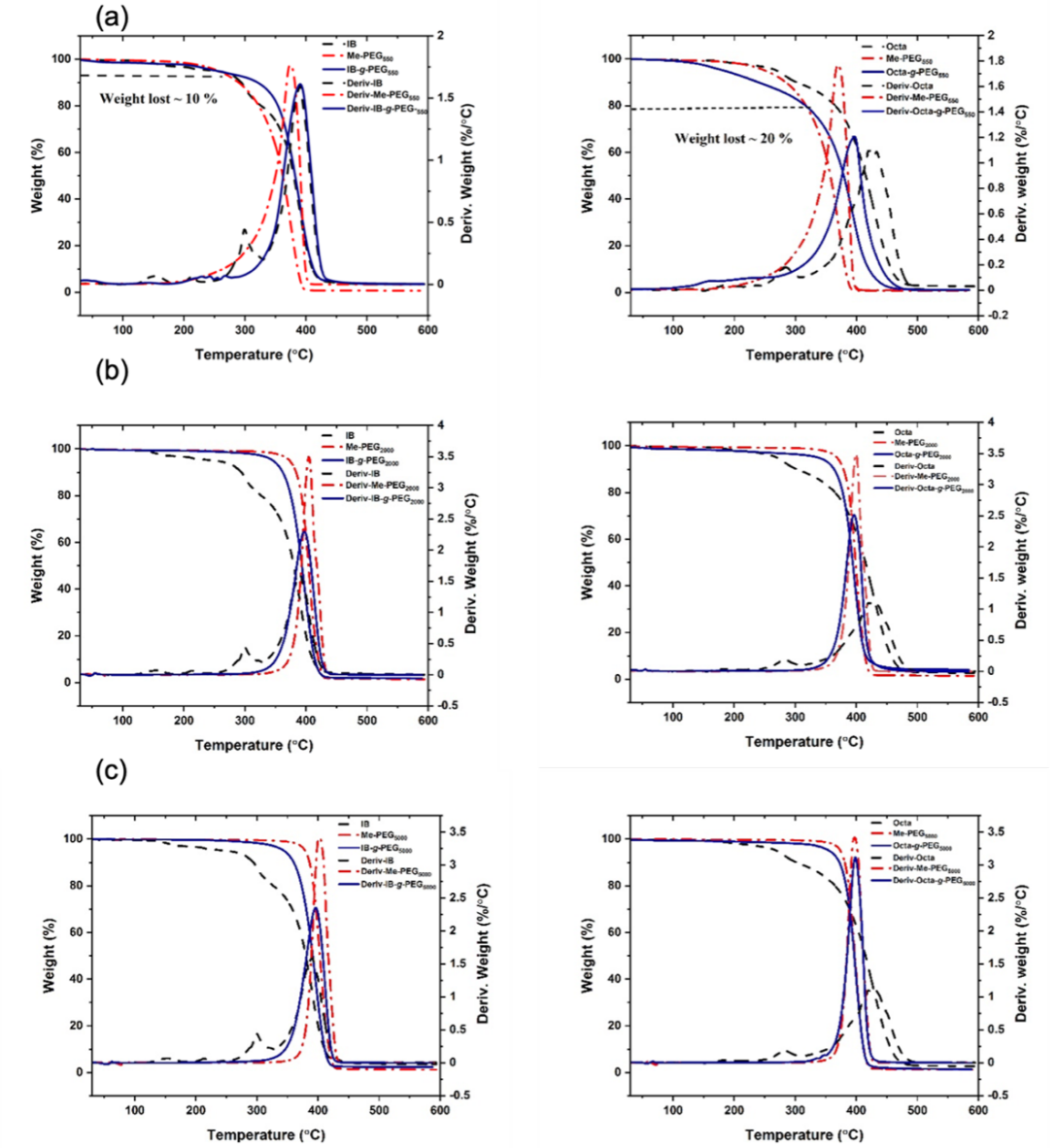

FIGURE 5.9: TGA and associated derivative curves (for grafted PEG (Mn 550 (a), 2000 (b), and 5000 (c)) onto IB (left) and Octa backbone (right).

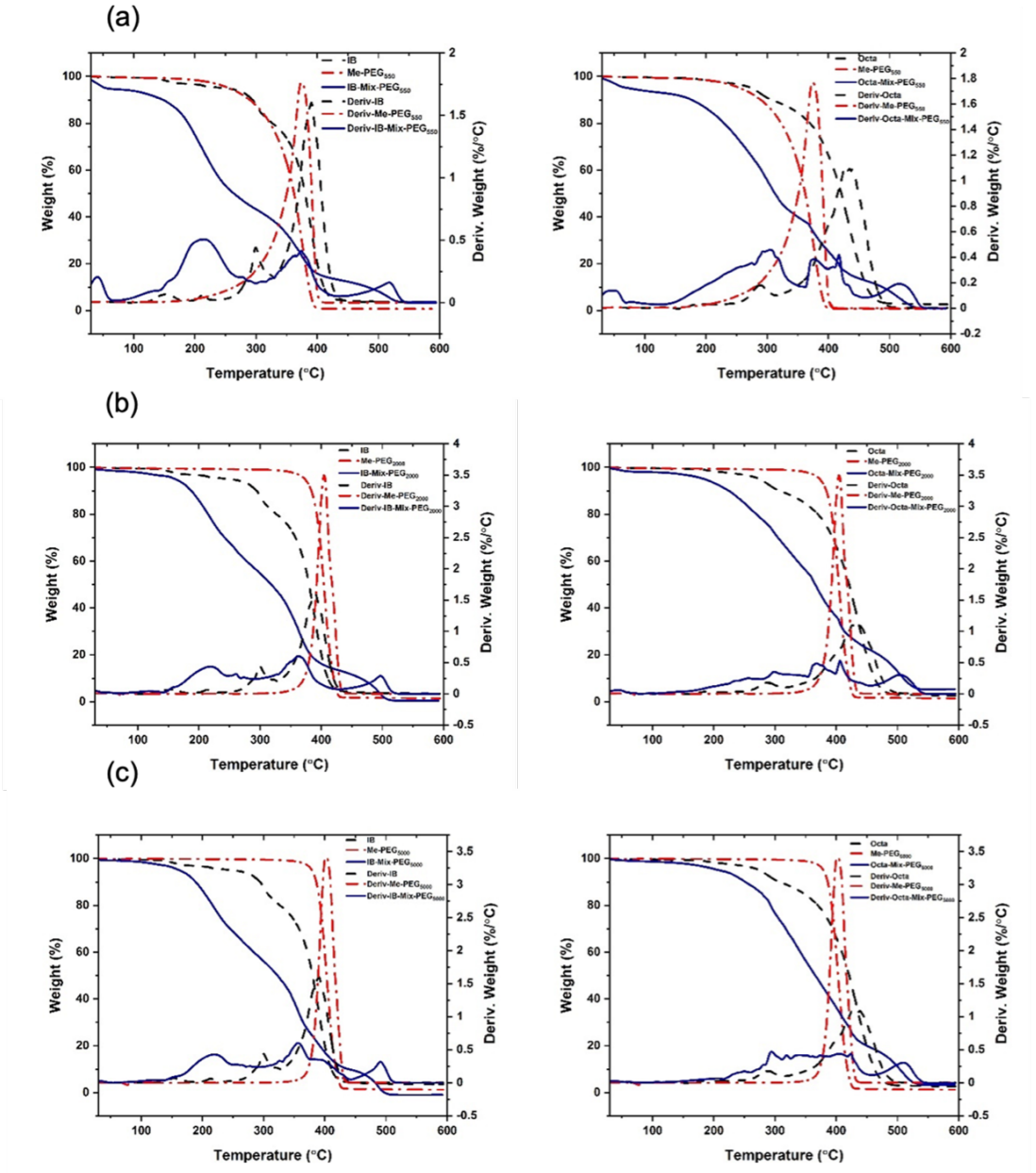

FIGURE 5.10: TGA and associated derivative curves (for mixing PEG (Mn 550 (a), 2000 (b), and 5000 (c)) with IB (left) and Octa (right) backbone, method 2).

5.4.2 Water contact angle (WCA) measurements

Both backbones are hydrophobic in nature due to their high carbon numbers. However, their alternating grafting point positions (maleic anhydride) can be functionalized using hydrophilic graft chains (such as PEG) to obtain highly aqueous soluble amphiphilic copolymers. The higher the number of the grafting point

(functional groups), the more hydrophilic polymers can be achieved. WCA measurements were used to study the wettability of the as received polymers and graft copolymer films. To investigate this, the polymers were sprayed onto glass microscope slides from aqueous suspensions. Spraying the as received PEG onto glass microscope slides was observed to create a hydrophilic coating (as expected) on glass and create surfaces that display contact angles ranging between (10 - 20) (The WCA images of the starting materials and products are shown in the appendix, Figure 5.11). Copolymer films created using PEG grafted onto the Octa backbone were observed to display lower contact angles than that of films generated using the as received Octa (WCA ⇠ 89) and were observed to correlate with the molecular weight (or chain length) of the grafted PEG. Whereas, for the IB/ PEG copolymer films the hydrophilicity was observed to be similar to that of the as received PEG films and did not appear to depend on the molecular weight of the grafted PEG. This is because the IB backbone has relatively low molecular weight and after a certain number of grafts the molecular weight of hydrophilic segments exceed the hydrophobic backbone and the wettability of the product corresponds purely to that of the graft chains. These results parallel with the total number of PEGs obtained by ^{1}H NMR (Table 5.1). The total number of grafted PEG into IB backbone does not show an immense change with M_W of the PEG, hence similar product wettability (18 to 15). Whereas, the number of grafted PEG into Octa backbone shows a large increase from 20 to 100 for PEG 550 and 2000, respectively, which in turn result in reducing of contact angle from 67 to 29 .

The results were compared to contact angle results of thin film made from spray coated of physical mix between PEGs the backbones solution. The WCAs of the chemical and physical reactions are plotted as a bar chart in Figure 5.13. In physical reaction, the WCA is reduce from 89 to 82 for Octa backbone and from 117 to ⇠ 55 for IB backbone and remain relatively comparable without any effect from increasing M_W of PEG, specifically for Octa backbones. These results also indicate

that the reaction had occurred between the terminal OH groups of the PEG molecules and the cyclic anhydride functionality present in Octa or IB backbone. Similarly, these results specify that the molecular weight of PEG and therefore the ratio of hydrophobic to hydrophilic components have profound effect on the wettability of the polymer and designing a desirable hydrophilicity for specific applications.

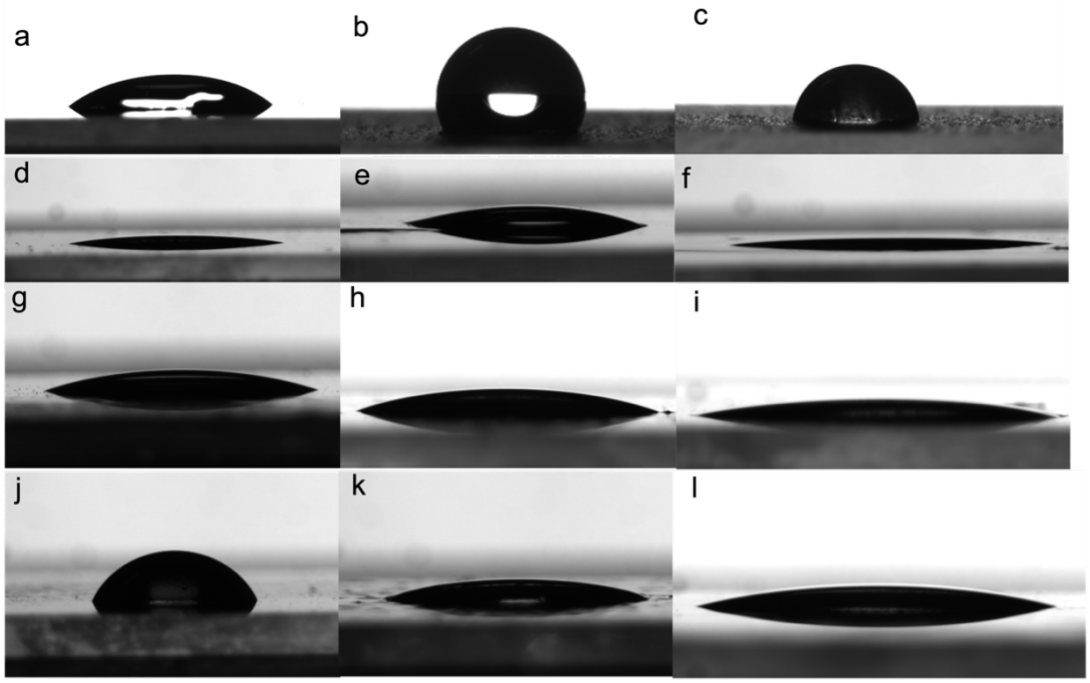

FIGURE 5.11: Water contact angle of deionized water on, (a) as received microscopic glass, (b, and c) after spray coated with three layers of Octa and IB backbone, respectively, (d, e, and f) after spray coated with three layers of PEG Mn: 550, 2000, and 5000, respectively, (g, h, and i) after spray coated with three layers of grafted PEG into IB backbone [IB-*g*-PEG_{550}, IB-*g*-PEG_{2000} , and IB-*g*-PEG_{5000}], respectively, (j, k, I) after spray coated with three layers of grafted PEG into Octa backbone, [Octa-*g*-PEG_{550}, Octa-*g*-PEG_{2000} , and Octa-*g*-PEG_{5000}], respectively.

In addition, the coated surfaces have been analyzed by AFM to determine the surface roughness. The AFM 3D scan images of the polymer coated film are shown in (Figure 5.14). The surface roughness values follow the same trend with contact angle and the results in (Table 5.2) illustrates that generally the rougher the surface the higher contact angle for grafted PEG into IB backbone and Octa backbone. For both grafted PEG onto backbones, the file roughness decreases with the PEG length chain and a number of grafts, which mean the polymer become organised into smother

film. This result indicates that the chemical treatment of a surface (grafted backbone) has a key role for defining the wetting properties of the coated surface.

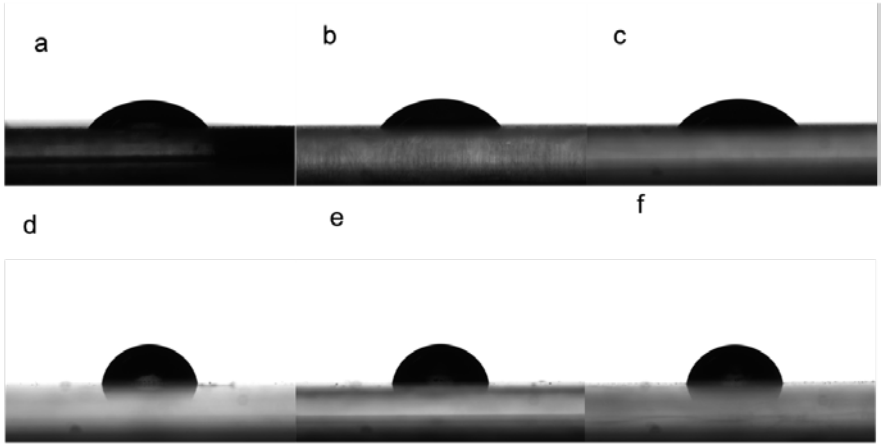

FIGURE 5.12: Water contact angle of deionized water on, (a, b and c) after spray coated with three layers of mix PEG with IB backbone using (THF as a solvent) Mn:550, 2000, and 5000, respectively, (d, e, and f) after spray coated with three layers of mix PEG with Octa backbone using (THF as a solvent) , Mn:550, 2000, and 5000, respectively.

TABLE 5.2: List of the AGCs and the total number of grafted PEG per backbone.

Grafted polymer	Ra/nm	Rq/nm	Rt/nm
IB-*g*-PEG$_{550}$	127.55	106.55	664.21
IB-*g*-PEG$_{2000}$	43.3	53.8	323.2
IB-*g*-PEG$_{5000}$	12.4	9.8	86.3
Octa-*g*-PEG$_{550}$	290.8	213.7	43.41
Octa-*g*-PEG$_{2000}$	5.56	6.97	78.9
Octa-*g*-PEG$_{5000}$	34.7	26.6	264.0

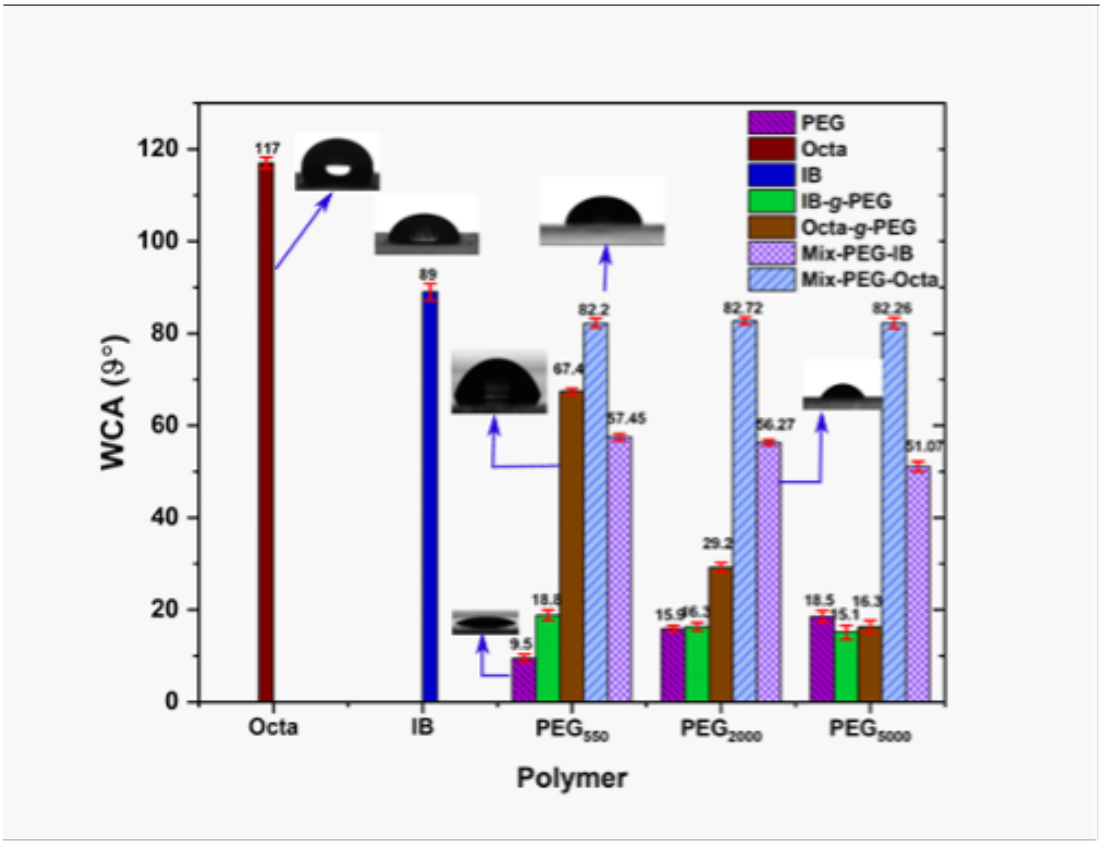

FIGURE 5.13: Bar plot of water contact angle on glass spray coated with 2 wt.% ungrafted PEGs, pure backbones, grafted PEGs onto (IB and Octa) backbones, and mix solution as a function of various backbones and PEG Mw.

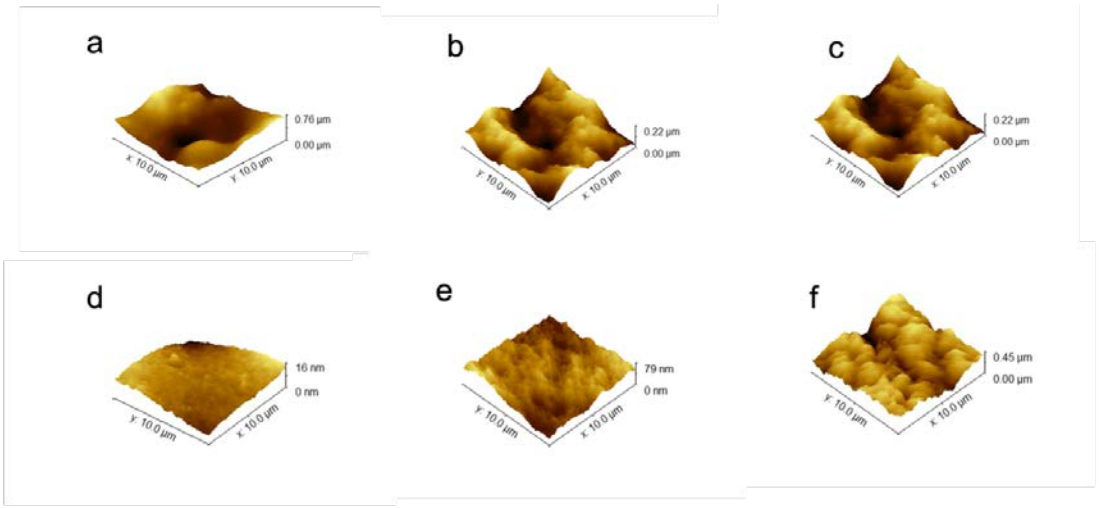

FIGURE 5.14: AFM images of polymer films spray coated onto a microscope slide of grafted PEG Mn a) 550 b) 2000, and c) 5000 onto IB backbone, and d) 550, e) 2000, and e) 5000 onto Octa backbone.

5.4.3 Surface tension

In order to determine whether the grafted co-polymers have surface-active properties and obtain their critical micelle concentration (CMC), surface tension (SFT) of each of the grafted copolymer solutions at different concentrations was studied. Using the surface tension method relies on the observation that increasing the surfactant concentration leads to a decrease in surface tension up to a break point (CMC), as is shown in Figure 5.15. The grafted PEG with the longer PEG chains (2000 and 5000) has a lowest SFT when compared to the grafted co-polymers with the PEG (550) substituent. These findings are comparable to previous studies that describe the effect of poly(ethylene oxide) (PDMS-*g*-PEO) on SFT of polydimethylsiloxane (Chung and Lim, 2009). The findings indicate that increase in PEG molecular weight in PDMS-g-PEO lead to decrease in surface tension. Here in, for both series of grafted PEG onto IB and Octa backbones, increasing PEG chain length led to decreasing surface tension due to increase in hydrophilic to hydrophobic ratio, in line with ^{1}H NMR and wettability data. Although these polymers are not reducing the surface tension of water significantly, however, still can be considered as polymeric surfactants as they are cable of reducing the surface tension of water by at least 30 mN/m. The reduction of water SFT by these grafted polymers is in line with literature data (Gupta et al., 2020; Anghel et al., 2007; Wu et al., 2018; Slastanova et al., 2020). For example, research done by Gupta and his co-authors, they synthesised a series of an amphiphilic polyhydromethysilicoxane backbone grafted by PEG (n= 3 or 11). Their findings were, the limiting SFT at CMC was ⇠40 mN/m for grafted PEG 11 and ⇠ 30 mN/m for PEG (3), respectively.

CMC were also established from using the SFT technique from Figure 5.15 a and b, which are taken as the intersection of two straight lines of SFT at low and high concentrations. For these polymeric surfactants, the CMC was observed to be ⇠ 1.7 to 3 wt.% (shown in Table 5.2), and are comparable to the CMC of polymeric

surfactants present in the literature (Chung and Lim, 2009; Szutkowski et al., 2018).

As can be seen from the data in Table 5.3, the CMC of the grafted PEG onto both backbones stay constant (within the experimental errors) with the PEG molecular weight. The formation of micelles depends mainly on hydrophobic/ hydrophilic balance, and CMC decreases with the alkyl chain length of a surfactant. However, these results show that after reaching a threshold of hydrophilicity, the CMC/hydrophobicity relation become weaker, and CMC remains mainly constant. The CMC of grafted PEGs onto IB backbones are slightly higher than the grafted PEGs onto Octa backbones, which is due to the higher hydrophilic to the hydrophobic ratio for IB grafted backbones, and that is in line with WCA (wettability) data. In summary, the CMC obtain using both techniques are similar and within experimental errors.

The CMC data were also confirmed using dye solubilization method via UV-vis spectroscopy. The plot of the absorption spectrum of the azobenzene dye (wavelength = 320 nm) versus grafted PEG polymers concentration at 25 C are shown in the Figure 5.15 c and d. As the grafted polymers concentrations increase but below the CMC value, the dye molecules absorbance stays constant (or increase gradually). This is related to limited solubility of the azobenzene molecules in water. However, above the CMC, the rise in the absorbance is sharp, due to solubility of the hydrophobic dye molecule within the hydrophobic core, and that confirms the micelles formation. The data are shown in Table 5.2 and are generally in good agreement with the surface tension data. These data indicate that, these grafted polymers are useful for encapsulations and drug delivery due to their ability to solubilize hydrophobic dyes within their hydrophobic core.

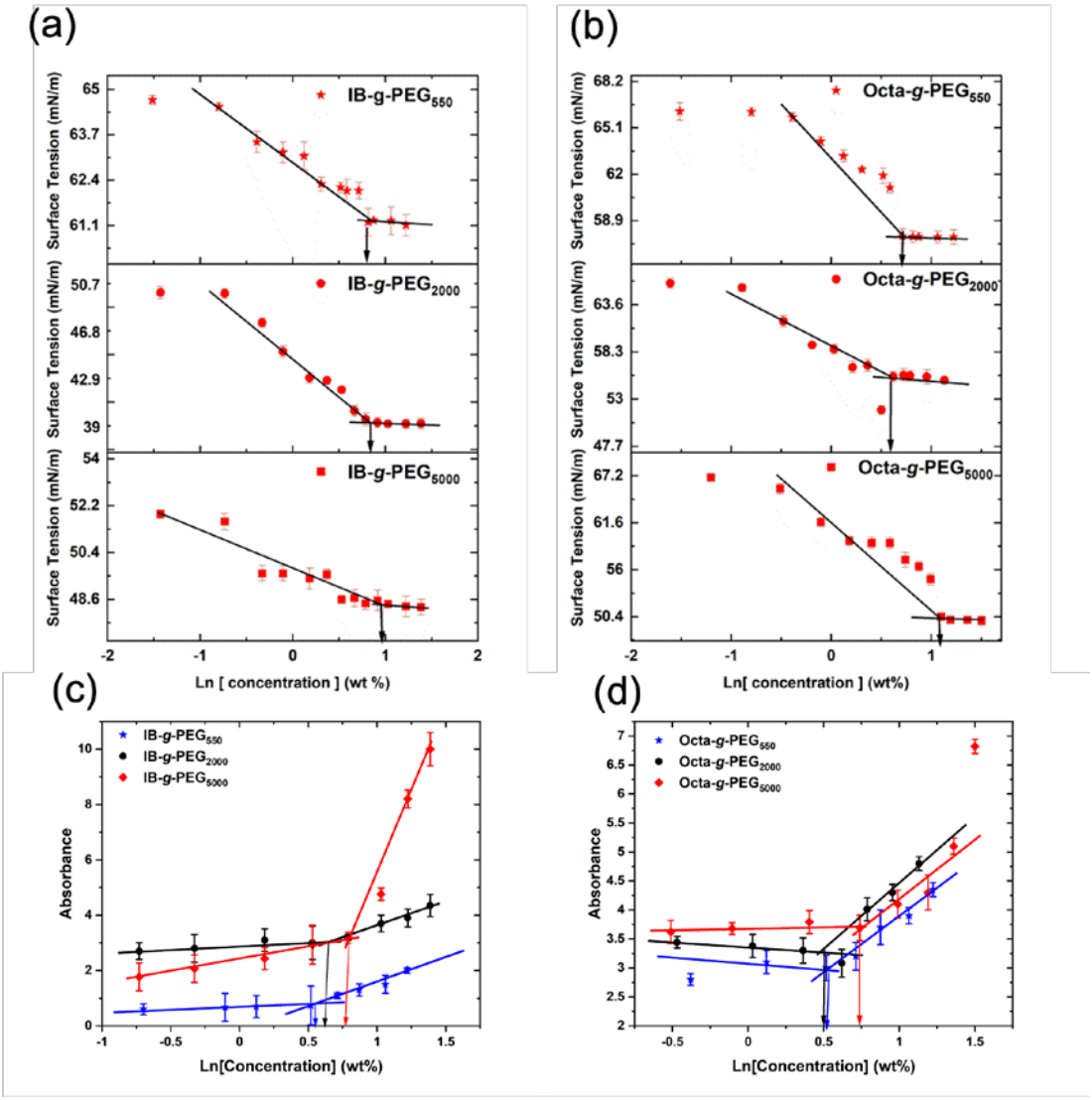

FIGURE 5.15: Surface tension behavior of various grafted PEGs onto IB and Octa backbone, IB-*g*-PEG_{550}, IB-*g*-PEG_{2000} and IB-*g*-PEG_{5000} (a), and Octa-*g*-PEG_{550}, Octa-*g*PEG_{2000} and Octa-*g*-PEG_{5000} (b), respectively. a plot of the UV absorbance of Azobenzene (0.9 mM) at wavelength 320 nm versus the concentration for grafted PEG onto IB samples (c), and grafted Octa samples (d) at 25 C. Each experimental point was repeated twice.

TABLE 5.3: List of the AGCs and the total number of grafted PEG per backbone.

	CMC wt.%	
	SFT	UV
IB-*g*-PEG_{550}	1.8±0.4	1.68±0.5
IB-*g*-PEG_{2000}	1.91±0.43	1.7±0.3
IB-*g*-PEG_{5000}	2.75±0.15	2.1±0.2

Sample		
Octa-*g*-PEG$_{550}$	2.2±0.4	1.68±0.51
Octa-*g*-PEG$_{2000}$	2.5±0.4	1.85±0.4
Octa-*g*-PEG$_{5000}$	2.82±0.3	2.2±0.6

5.4.4 Aggregation structures

SANS and SAXS data were collected for the grafted polymers at fix concentration of 2 wt.%. The SANS scattering patterns are shown in Figure 5.16 and Table 5.4. The scattering data were fitted with an Eillipsoild core shell model with parameters such as (Radius-equat-core (Equatorial radius of core (Å)), Thick shell (thickness of shell at equator (Å)), Radius of the polar core (⇥-core ⇥ radius-equat-core), and thick of the polar core (⇥-polar shell ⇥ thick-shell). As can be seen from the results shown in Table 4.4, the radius equatorial of the core is reduce (from ⇠ 500 *to* ⇠ 135Å) by increasing of the M_W of the PEG (in consistent with photographs of the solutions (Figure 5.17) which show much more transparent solutions for higher M_W of PEGs). This is due to the increased number of the grafted PEG onto the hydrophobic backbone as well as chain length of the PEG which results in the formation of more stable and welldefined aggregates. In comparison the shell thickness increases by increasing the chain length of PEG, as can be expected. In order for better understanding of the aggregation structure of grafted polymers, SAXS measurement of 1 wt.% polymeric solutions in aqueous solution were also carried out. The results are shown in (Figures 5.18 and Table 5.5). Similar to SANS data, the SAXS patterns were fitted using the Ellipsoid core shell model, and the fitted data are in good agreement with SANS results. The fitting results shows the core radius of the polymeric solution is larger for the lower M_W of grafted PEGs. For grafted PEG$_{550}$ onto

Octa, Bragg peak was observed in the scattering pattern which means crystalline order, and the data could not be fitted to the ellipsoidal model.

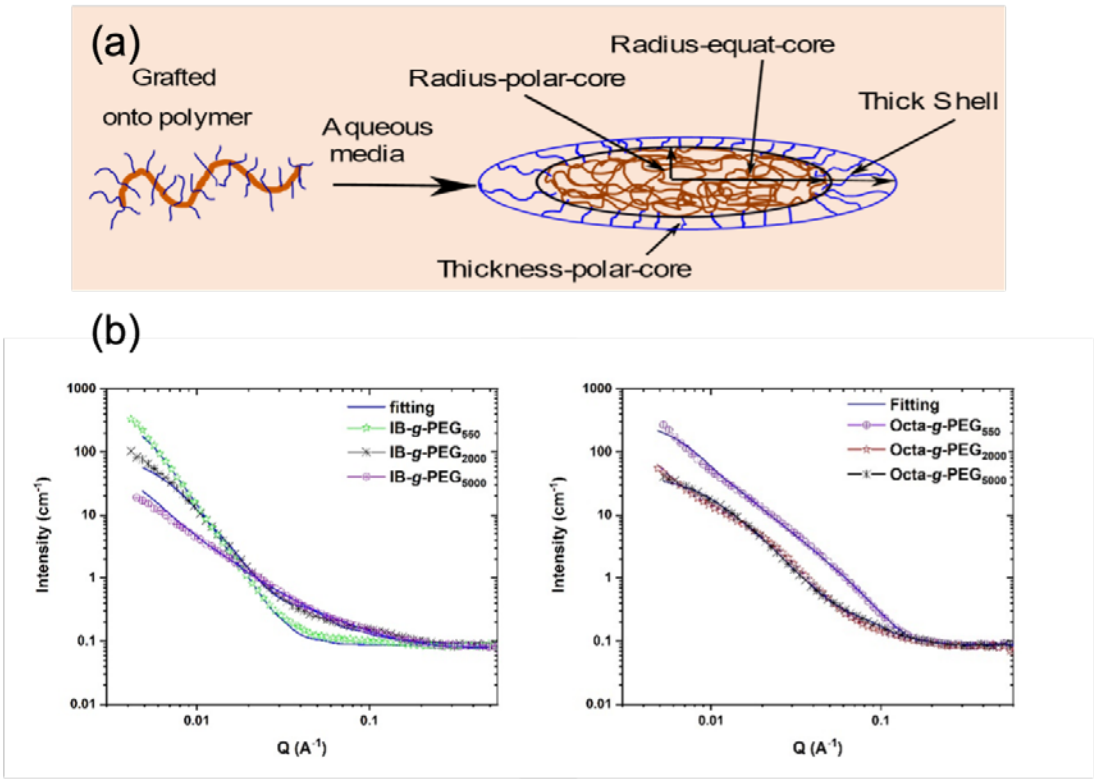

FIGURE 5.16: (a) The experimental schematic showing the reaction between PEG and IB or Octa backbone and showing the aggregation structure (ellipsoidal core shell) of the grafted polymers in solutions. (b) Scattering patterns from 2 wt./v % of Grafted polymers: IB-*g*-PEG$_{550}$, IB-*g*-PEG$_{2000}$ and IB-*g*-PEG$_{5000}$ (left), and Octa-*g*-PEG$_{550}$, Octa-*g*PEG$_{2000}$ and Octa-*g*-PEG$_{5000}$ (right), respectively at 25 C, in D_2O. Solid lines are fits to the Ellipsoid Core Shell model.

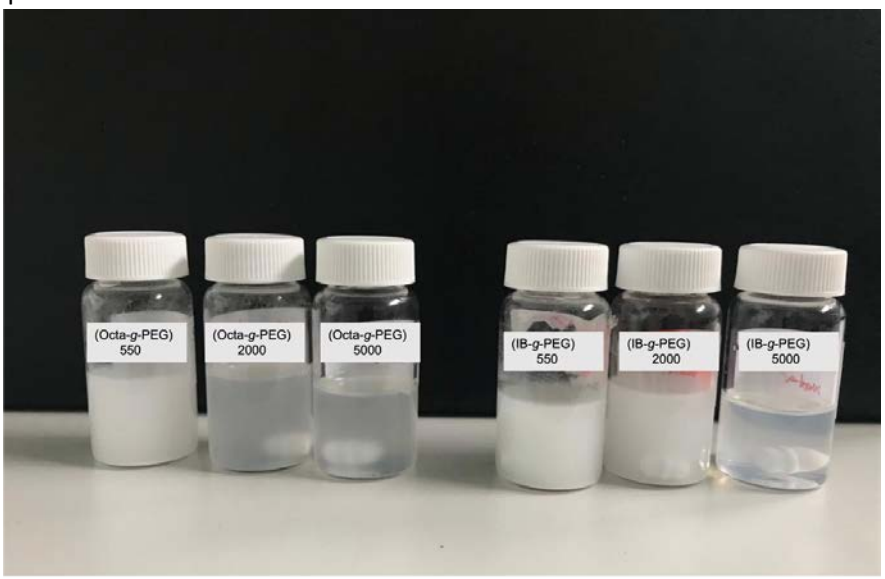

FIGURE 5.17: a photograph of the 2 wt.% of the grafted co-polymer onto Octa (left) and IB (right) backbone at (Mn: 550, 2000, and 5000), respectively, for SANS measurement.

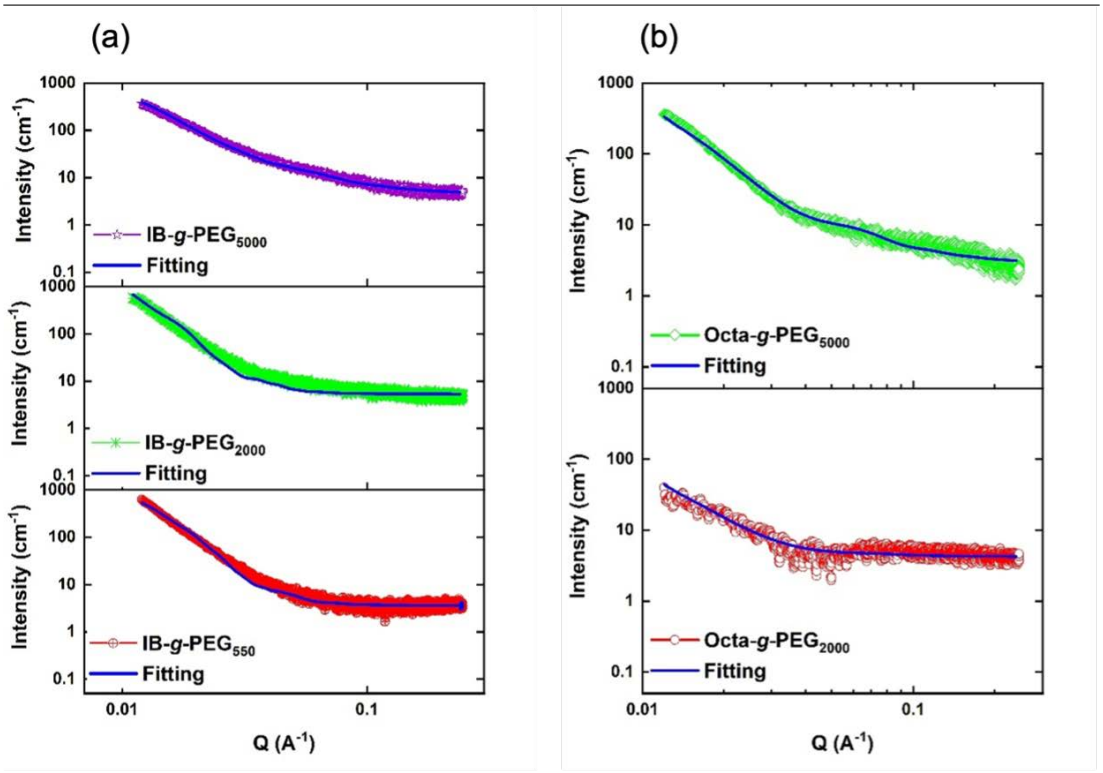

FIGURE 5.18: SAXS from 3 mM of grafted PEG Mn (550, 2000, and 5000) onto IB backbone (a), and Octa backbone (b) in H_2O, at 25 C. Solid lines are fits to the Ellipsoid Core Shell model.

TABLE 5.4: Fitting Parameters obtained using the Ellipsoid core shell model of SANS measurement in D_2O solutions at 25 C.

Sample	Radius equat. core (Å)	Radius of polar core (Å)	Thickness (eq.) shell(Å)	Thickness (polar.) shell(Å)
IB-*g*-PEG550	506.2±1.7	101	160±2.3	14
IB-*g*-PEG2000	346.1±1.7	10	211.9±1.9	45
IB-*g*-PEG5000	135.1±4.4	11	220±1.2	147
Octa-*g*-PEG550	545.4±0.8	201	180.7±0.1	18
Octa-*g*-PEG2000	155.7±1.4	14	203.1±2.3	60
Octa-*g*-PEG5000	154.7±1.4	25	206.6±2.3	180

TABLE 5.5: Fitting Parameters Obtained using the Eillipsoild core shell model of SAXS measurement in H_2O solutions at 25 C.

Sample	Radius equat. core (Å)	Radius of polar core (Å)	Thickness (eq.) shell(Å)	Thickness (polar.) shell(Å)
IB-*g*-PEG$_{550}$	484.27±6.31	72	169.6±2.45	20
IB-*g*-PEG$_{2000}$	361.83±3.25	12	241.6±7.3	12.6
IB-*g*-PEG$_{5000}$	212.92±4.46	10	338.5±1.23	135
Octa-*g*-PEG$_{550}$	-	-	-	-
Octa-*g*-PEG$_{2000}$	151.84±1.17	15	200±2.05	53
Octa-*g*-PEG$_{5000}$	158.98±2.18	25	215.5±1.3	193

5.5 Conclusions

Although the synthesis of amphiphilic graft copolymers (AGCs) has been examined previously (Bontempo and Maynard, 2005; Wu et al., 2020; Alexander et al., 2014), in this work, we investigate the fundamental structural-property relationship of novel families of AGCs using various PEG chain lengths. The reaction occurred through a condensation reaction, taking place between the terminal OH groups of the PEG molecules and the alternating cyclic anhydride functionality present in Octa or IB backbone (grafting onto). The synthesis was confirmed by FTIR, NMR, and contact angle measurements and the results concluded that the higher the number of the functional groups on the backbones, and the PEG chain lengths, the higher the hydrophilicity of the polymer films. The surface activities of the grafted copolymers were also established by surface tension and UV techniques. The data indicated that these polymers are capable to reduce the surface tension of water by at least 30 mN/m and forming micelles in water at around 1.7 to 3 wt.% depending on the molecular weight of the backbone and the grafted chains. The aggregation structures of the AGCs were studied in aqueous solutions using SANS and SAXS. These polymers with varying hydrophobic to hydrophilic balances were directly soluble in aqueous media due to the high number of grafts available in their structure and the fitted data signified ellipsoidal core-shell micelles composed of hydrophobic cores and hydrophilic grafted shells. Our research indicates that it is possible to tailor the wettability and applicability of hydrophobic polymers bearing functional groups through grafting with different PEG chain lengths. These AGCs are a great candidate in applications such as encapsulation of hydrophobic materials: drugs (Zhang et al., 2012; Zhang et al., 2013) and perfumes (Mamusa et al., 2020) (based on the UV results which showed encapsulation of hydrophobic dyes), oil recovery (Williams, 2008; Raffa, Broekhuis, and Picchioni, 2016) and cosmetics due to their core-shell aggregation structure, and their surface activity nature.

Chapter 6

Novel Core-Shell Polymeric Surfactants, Part 2: New Candidates for Enhance Oil Recovery and Emulsifiers Applications.

6.1 Introduction

Amphiphilic polymers have been utilized for several decades to either control the mobility of injection water in enhanced oil recovery (Raffa, Broekhuis, and Picchioni, 2016; Raffa and Picchioni, 2021) or increase emulsion stabilization (Saha et al., 2020; Wu et al., 2020). The usage of amphiphilic polymers is attractive due to their ability to increase water viscosity (Du et al., 2018). Increasing the injected water viscosity by the use of these polymers would lead to a decrease in mobility (M) ratio between water and oil; and rock permeability (Ahmed, 2018) (expressed in equation 6.1). As these two factors decreases, oil recovery is improved. The role and mechanism of mobility control in enhanced oil recovery has been detailed extensively in literature (Wang and Dong, 2009; Samanta et al., 2013; Farajzadeh, Wassing, and Lake, 2019). Equation 6.1., describes the mechanism to modulate mobility within oil displacement system:

$$M = \frac{l_w}{l_o} = \frac{K_w/h_w}{K_o/h_o} = \frac{K_w h_w}{K_o h_o} \quad (6.1)$$

where M refer to end point mobility ratio (Zhang and Seright, 2014; Koh, Lee, and Pope, 2018; Raffa and Picchioni, 2021), *l* = mobility, k = permeabilities, *h* = viscosity; w,o = subscripts denoting water and oil, respectively.

The most used polymer in oil recovery is partially hydrolysed polyacrylamide due to its high solubility in water. The fact that it is a polyelectrolyte with negative charges (COO^-) on the carboxylate groups also makes it an attractive candidate (Kamal et al., 2015; Raffa and Druetta, 2019). The carboxylate group is highly sensitive to ion composition, salinity, concentration, and pH. However, a drawback with this polymer is that it has a poor stability and viscosity characteristics above a certain temperature threshold level of 99 C depending on salinity (Oliveira et al., 2019).

The advantage of using polymeric surfactant for Enhanced Oil Recovery (EOR) applications is to combine the positive effect of surfactants and polymers in one material (Raffa et al., 2015). The benefits include are chromatographic separation in the porous media, avoiding unwanted interactions between chemicals, and loss of the surfactant by selective adsorption on the reservoir rock or in the oil (Sheng, 2010).

Polymers are soluble in water but contain hydrophobic substitutions which has also been examined for EOR flooding experiments (Cao et al., 2019; Li et al., 2020). The hydrophobic part in these polymers improve the rheology and alter surface interaction behaviour. However, the emulsification and surface activity properties have been given little attention in experimental studies, which means their role in the oil recovery applications remains mainly theoretical (Taylor and Nasr-El-Din, 1998).

Amphiphilic polymers/grafted polymers with core shell structure are a logical choice, since they are actually employed for the same purpose as solution

thickenings. Amphiphilic polymers with hydrophobic core have been evaluated as polymeric surfactants for EOR applications. For example, the polymers were prepared by free radical co-polymerization of acrylamide with styrene, N-benzylacrylamide, N-Phenylacrylamide, N-Phenethylacrylamide (Raffa, Broekhuis, and Picchioni, 2016). All polymers in the previous system showed good interface activities in water and brine, and proved to be good solution thickener, rendering them promising for the proposed applications. The use of amphiphilic polymers in the preparations of surface-active polymers has recently experienced a great interest. These polymer systems are salt tolerant, water soluble, and in some cases, they can be thermo responsive due to ability of controlling radical polymerization methods. The core shell shape is desirable conformation for oil displacement, micelles which help reduce in the interfacial tension (IFT) and improve oil displacement.

A novel series of amphiphilic grafted polymers have been recently synthesized [see Chapter 5]. These grafted polymers showed ability to form micelles and reduce interfacial tension of pure water up to 30 mN/m which makes them excellent candidates as a polymeric surfactant and promising for EOR recovery applications. They possess lower molecular weight, which could be favourable in reducing adsorption on the reservoir rocks.

This study will investigate: 1) the effect of salt concentration (NaCl) and seawater on the surface tension (SFT), critical micelles concentration (CMC) of grafted polymers and studying the effect of interfacial tension (IFT) between polymer and of various oils (hexadecane, decane, hexane, and flooding oil). 2) The grafted polymers ability to displace oil for EOR applications and stabilizes emulsions. Small angle x-ray scattering was used to investigate the structure of the polymeric surfactant in

presence of salts. The analysis of surface tension and interfacial tension were performed by pendant drop method.

6.2 Materials and methods

6.2.1 Materials

The starter polymer material used was poly (ethylene glycol) methyl ether (PEG) with three Mn: 550, 2000 and 5000. These polymers were synthesized by grafting them onto two hydrophobic backbones namely: poly (maleic anhydride-*alt*-1-octadecane) (Octa), and poly (isobutylene-*alt*-maleic anhydride) (IB). The synthesis was conducted via the grafted onto method (Scheme 6.1), details refer to chapter five. The products were named after their respective backbone as follow: IB-*g*-$PEG_{550,2000,5000}$ and Octa-*g*- $PEG_{550,2000,5000}$. The same batch of samples that were already characterized in the synthesis chapter five was used in this study.

The saline solution (seawater) used in this study contained the following compounds (NaCl, $MgCl_2$, Na_2SO_4, $CaCl_2$, KCl, $NaHCO_3$, KBr, Boric acid (H_3BO_4), $SrCl_2$ and NaF (Table 6.1. has information about their amounts).

All chemicals were purchased from Sigma Aldrich and used as received. Deionized water (resistivity = 18.2 MW.cm, Millipore) was used to prepare solutions for the experiments.

TABLE 6.1: List of the amount of salt that used to prepare seawater.

Materials	Amount g/L
NaCl	24.53
$MgCl_2$	5.20

Na_2SO_4	4.09
$CaCl_2$	1.16
KCl	0.695
$NaHCO_3$	0.201
KBr	0.101
Boric acid	0.027
$SrCl_2$	0.025
NaF	0.003

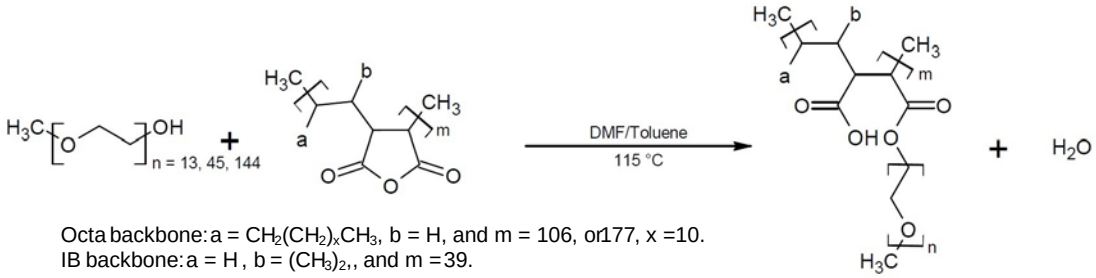

Octa backbone: a = $CH_2(CH_2)_xCH_3$, b = H, and m = 106, or177, x =10.
IB backbone: a = H , b = $(CH_3)_2$,, and m =39.

SCHEME 6.1: Synthetic route, "graft onto" polymerization between poly (ethylene glycol) methyl ether and Poly (maleic anhydride-*alt*-1-octadecane)/ poly (isobutylene-*alt*maleic anhydride) backbone.

6.2.2 Density and viscosity characterization

Density and viscosity of the oil, brine, and testing polymeric solutions were performed with pycnometer measurements, and constant temperature viscosity (water or oil) bath, respectively, at three temperatures: 10, 20, and 30 C, respectively.

The solutions were prepared by dissolving the amphiphilic polymers in DI-water or in aqueous solution made of 1 wt.% of NaCl. Followed by magnetic stirring for 24 hours before the measurements were taken in order to get equilibrium. All the prepared polymers were dispersible in water without heating or co-solvent.

6.2.3 Rock properties, cleaning preparation and set up

The sandstone cores used for the water flooding experiments was from one of the Basra reservoirs wells. The diameter of the cores was 3.80 cm with length of 5.5 cm. The reference properties of the reservoir rocks such as porosity (*f*), air permeability (Kr), and pore volume (vp) are detailed in Table 6.2.

In the aging experiment, the cores were first cleaned via Soxhlet extraction using toluene until all organic compounds removed (changing toluene twice daily). The rocks samples then dried at 60 C in air oven for 7 h. The samples were further cleaned by DI-water to remove salt remnants twice daily; and at each cleaning interval the presence of salts was tested by adding few drops of aqueous solution made of (1 mM of $AgNO_3$). After removing all ions/salts from reservoir rock, it was then dried with air oven at 60 C for 7 h.

The aim of the core flooding tests was to evaluate the EOR capability of a novel family of amphiphilic polymers (synthesised by the grafted onto method) after flooding with high salinity brine solution. At the beginning of each test, a core was fully saturated with Brine solution (made of 20 wt.% NaCl dissolved in DI-water) in a close high-pressure stainless-steel cylinder at 1500 psi for 2 days (checks were put in place to ensure the pressure remained constant). The core flooding system is comprised of an oven for adjusting temperature, three piston cylinders for accommodating the injection fluids; and core holder to enable the system to perform different injection schemes. The three cylinders were used at temperature 25 C and were filled with: brine, oil and the testing polymeric fluids, respectively. Each core sample was cleaned after every use by Soxhlet extraction, the rock properties (kr, vp, and F) were re-measured, before repeated the prescribed above method was repeated (involving the brine saturation, oil and polymeric fluids).

TABLE 6.2: Reservoir Rocks Properties.

Sample	Depth (m)	Length (cm)	Area (cm^2)	Kr (md)	F(%)	Vp (cm^3)
R1	2806.1	5.48	11.46	968	27	17.79
R2	2807.13	5.5	11.34	1991	27.4	17.09
R3	2809.13	5.61	11.34	1634	27.3	17.3

6.2.4 Fluid's properties and preparation

The properties of the crude oil used in the flooding experiments are listed in the Table 6.3. The brine solution was made up of 20 wt.% of NaCl dissolved in deionized water. Six previously synthesized grafted polymers (amphiphilic polymers) were tested (refer to Chapter 5 for characterization and detailed description). 1 wt.% of each polymeric surfactant was tested with and without salt (1 wt.% NaCl), in order to the investigate the effect of low salinity on grafted polymer properties and their effect on oil displacement. The required amount of grafted polymer was weighed in a glass vial with lid and placed on magnetic stirrer plate at 20 C with DI-water used as a dispersing agent.

6.2.5 Seawater preparation

The required amount of the materials (listed in Table 6.1) was dissolved in a beaker with 1000 ml of deionized water using a magnetic stirrer so that the TDS of the solution is 35000 ppm, the pH of the seawater is 7.8. The density and viscosity properties of the brine and polymeric solution are listed in the Table 6.3.

6.2.6 Microemulsion preparation

Since all the grafted polymers are amphiphilic, the type of emulsion was comprised off water-oil (w/o) emulsion (hexadecane and decane as an oil phase). Emulsions were prepared by initially dispersing 0.5 wt.% of the grafted polymers (IB-*g*$PEG_{550,2000,5000}$ and Octa-*g*- $PEG_{550,2000,5000}$) in water or with aqueous solution made

of 1 wt.% of NaCl dissolved in DI-water. Five different water-oil ratios were used as follows: 90:10, 75:25, 50:50, 25:75, and 10:90. The emulsions were then made using a probe sonicator (Cole Palmer Ultrasonic Processor) for 4 minutes at 30% amplitude. The resulting emulsions and the phase ratios were examined directly after the following time intervals: 5 min, 1 hour, 1 day, 1 week, and 1 month. The emulsions size was measured by two different techniques namely: dynamic light scattering and an optical microscope.

6.2.7 Dynamic light scattering (DLS)

Dynamic light scattering techniques were employed to determine the emulsion size in dispersed solutions. For estimating emulsion size of each system, 1 ml of each sample was placed in a disposable cell with lid and placed in the equipment chamber. The analysis was performed using a Ztasizer Nano Zs equipped with a He-Ne laser, operating at a wavelength of 633 nm, at 20 C with 120 s equilibration time and 173 scattering angles. Data processing was performed by the Zetasizer software. The data obtained was an average of 3 measurements.

6.2.8 Optical microscopy

The microstructure of grafted polymers with and without salt that were emulsion stabilized were observed by an optical microscope. The VHX digital microscope equipped with KEYENCE imaging camera was used to conduct the analysis. The average droplet size of prepared emulsions was measured directly after each time interval: 1 hour, 1 week, and 1 month; by taking one droplet of emulsion phase and placing it on a microscopic glass (20x5 cm^2). The co-polymer is then sandwiched with another glass on top before being placed underneath the optical microscope camera for analysis.

6.3 Synthesis

For synthesis details, please refer to Chapter 5, sections 5.2.2 and 5.2.3.

6.3.1 Surface interface analysis

The collection of time dependent surface tension (SFT) *g*, CMC, and interfacial tension (IFT) on different light and medium oils (hexadecane, decane, toluene, and flooding oil) was performed on a Drop Shape Analyzer (Krüss) using DI-water. The pendant drop method was used to measure the SFT, CMC, and IFT at ambient condition. For each experiment, the disposable plastic syringe was filled with ⇠ 1 ml of grafted polymer solution, placed in the chamber, and loaded gradually. All the measurements were an averaged after three repeats. The IFT values between oil-polymeric solution with different salinities were measured using the following method: whereby a syringe was filled with the tested solution and immersed into the chosen tested oil phase (hexadecane, decane, hexane, and flooding oil). For each sample solution, the syringe was calibrated, and then analysed using ADVANCE software. The dynamic and static IFT measurements are an average of three measurements. The *g* was obtained by fitting the Young Laplace equation to the contour profile of a 4.5 μL droplets.

6.3.2 Small Angle X-ray Scattering (SAXS)

Measurements were carried out on the Nanostar SAXS equipment from Bruker at Liverpool university. This equipment has a liquid Gallium anode-based x-ray source. A circular X-ray beam of ⇠ 500 μm diameter is obtained. The X-ray has a wavelength of 1.342 Å. The sample to detector distance was set up to 107 cm, AgBh was used as a calibrant. Each sample was measured 1200 s, with background subtracted after

transmission calculation. Background solvent was water (1wt.% NaCl) in all cases. The fitting of the SAXS data was carried out using SasView program (SASVIEW, 2021). The data was fitted using an Ellipsoidal Core-Shell model.

6.3.3 Oil displacement experiment

A series of core-flooding experiment were performed to evaluate the behaviour of grafted polymer on flooding performance. The system was pressurized to 1500 psi, supported with 100 psi as a backpressure. The procedure for oil flooding test includes air evacuation, initial saturation of the core with brine (20 wt.% NaCl), and then oil flooding until the water saturation was reached (Gbadamosi et al., 2019; Bayat et al., 2014). Air compressor pump was used for pumping the injections fluids from accumulator through the core flooding system. Medium oil was injected at a flow rate of 0.3 mL/min [Table 6.2 list all oil properties]. The system was then aged for 2 weeks to establish equilibrium and attain uniformity. Subsequently, brine was injected at the same flow rate until breakthrough occurred. Afterward, the test polymeric nanofluids was injected at a flow rate of 0.3 mL/min until the oil amount was 0.05 mL. This was followed by more brine injection to recover the remaining oil.

6.4 Result and discussions

6.4.1 Density and viscosity

The relevant density and viscosity information about the polymeric solutions used in this research are summarized in Table 6.3. They are constituted by a hydrophobic core and hydrophilic shell of PEG. As reported in the [Chapter 5], grafted polymers are known to form an ellipsoidal core shell micellar aggregates in aqoues solution. Due to the PEG nature of the hydrophilic shell, the latter are stretched in DI-solution.

As clearly shown in the table, all grafted polymer increased in apparent viscosities with NaCl addition. This increase is due to the electrostatic shielding effect (Karimi et al., 2016). The exception was with grafted PEG 2000 onto Octa backbone which decreased (which might be due to dispersibility issues).

TABLE 6.3: Density and viscosity for oil and brine, grafted polymers in absent and present of salt.

Injected Fluid	Density (g/cm^3) at C			Viscosity (cp) at C		
	10	20	30	10	20	30
Oil	0.834	0.827	0.819	5.511	4.511	3.497
Brine	1.141	1.136	1.131	1.751	1.460	1.204
Octa-*g*-PEG$_{550}$	0.999	0.9995	0.998	1.25	1.091	0.977
Octa-*g*-PEG$_{2000}$	1	0.9985	0.996	2.01	1.786	1.413
Octa-*g*-PEG$_{5000}$	0.9991	0.9975	0.9947	1.151	1.05	0.896
(Octa-*g*-PEG$_{550}$)NaCl	0.9876	0.9801	0.9714	1.55	1.333	1.71
(Octa-*g*-PEG$_{2000}$)NaCl	1.0014	0.9934	0.9852	1.3	1.145	1.008
(Octa-*g*-PEG$_{5000}$)NaCl	0.9912	0.9754	0.9638	1.311	1.134	0.982
IB-*g*-PEG$_{550}$	0.9931	0.9884	0.9823	1.17	1.05	0.912
IB-*g*-PEG$_{2000}$	1.0002	0.9998	0.9998	1.2	1.054	0.94
IB-*g*-PEG$_{5000}$	0.9972	0.9947	0.9907	1.251	1.083	0.965
(IB-*g*-PEG$_{550}$)NaCl	0.9831	0.9796	0.9785	1.55	1.333	1.71
(IB-*g*-PEG$_{2000}$)NaCl	0.9998	0.9931	0.9855	1.401	1.212	1.017
(IB-*g*-PEG$_{5000}$)NaCl	1.0037	0.9966	0.9888	1.181	1.05	0.864

6.4.2 Effect of salinity on the properties of amphiphilic grafted polymers

An investigation about the effect of salinity on the properties of the amphiphilic grafted polymers was conducted. Two types of saline solutions were investigated namely: seawater solution of variable concentration and the incremental increase/addition of NaCl. The increase in NaCl concentration has a positive effect on the SFT however seawater has more of a reduction effect on SFT.

As previously shown in the [Chapter 5], the grafted polymers from PEG onto IB and Octa backbone were able to reduce SFT of water to approximately 30 mN/m and form micelles. Figure 6.1 and Figure 6.2 shows the effect of the grafted polymer concentration on SFT in 0.5 wt.% of NaCl and seawater solutions. As the results show that increasing salt concentration SFT value were decreased for both grafted polymers due to the charge shielding effect (Wu et al., 2018). The rest of surface tension results at 1 wt.% and seawater are shown in (appendices A, Figures: A.11, and 12).

The measured values are moderate and in line with what is usually observed for polymeric surfactants (Gupta et al., 2020). The SFT values of the co-polymer/brine solutions decrease from (56 mN/m) (in pure water [Chapter 5] to (44 mN/m) as the salt concentrations increased. In general, it was found that the solubility of the grafted polymers has not changed much. The grafted PEG onto IB backbone was cloudier than the grafted PEG onto Octa which means the size of the aggregation particle is bigger in IB system than Octa backbone system, this result is in line with SANS and SAXS [Chapter 5]. Grafted polymers into (IB or Octa) backbone in pure water [Chapter 5] has slightly higher SFT than in brine. It can be expected that the

interaction between polymers and counterions decreases the electrostatic repulsion which consequently leads to a decrease in their SFT value and increases the volume of micelles and promoting aggregation (Ren, 2015).

In enhanced oil recovery applications, lower SFTs are governed by the copolymers at the interfacial sites and those between the fluid-rock. The latter improving the oil sweeping efficiency, whilst in pure brine solution removing oil from reservoir rock is difficult due to the high surface tension of the brine solution.

The effect of salinity and co-polymer-brine solutions on IFT was evaluated using the pendant drop method. Dynamic interfacial tension measurements were conducted with brine droplets over 400 s in n-hexane, decane, hexadecane, and oil (which was also used in the flooding experiment). As can be seen in Table 6.4, adding brine to the polymeric solution decreases the IFT from 51 to ⇠ 10 mN/m. As expected in the case of hexadecane, resulting from the interaction between the hydrogen bond and counterions in the presence of oily polar components (Moeini et al., 2014).

IFT static measurements on polymer solutions in present and absent of brine droplets in oil flooding (which used in water flooding experiment as a model) are illustrated in Figure 6.3. Figure 6.3(left) shows grafted PEG onto IB (top) and Ocat (bottom) backbone without salt, and Figure 6.3 (right) shows the IFT for grafted PEG onto IB (top) and Octa (bottom) backbone with salt. The IFT values are between 3 to 4 mN/m.

Comparing the data in Figure 6.6 with the data in Figure 6.4 showed that the addition of the polymer to the brine solutions resulted in signification reduction in IFT from 51 to 12 mN/m, in case of hexadecane. The reduction in the IFT values was

attributed to the electrical repulsion force decrease between the hydrophobic core, which was also found to lower the micelles sizes. Reducing IFT in reservoir wells should result in the deposition of the polymer on its surface thereby creating a new surface on the wells (Kumar et al., 2016). This new surface mobilizes the remaining oil through the pores, so it can pass through the pores (Maurya, Kushwaha, and Mandal, 2017). It is observed that the grafted polymers can reduce the IFT between two immiscible fluids, through reducing the surface energy and could provide new chemical interactions thereby changing rock wettability.

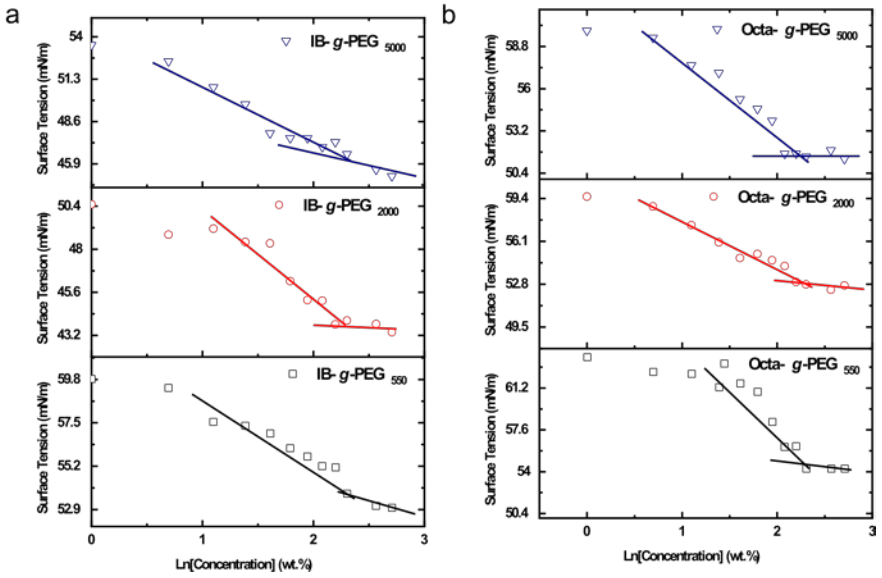

FIGURE 6.1: Surface tension measurements of grafted polymer-brine (0.5 wt% of NaCl solution) droplet in air: (a) grafted PEG onto IB backbone, and (b) grafted PEG onto Octa backbone.

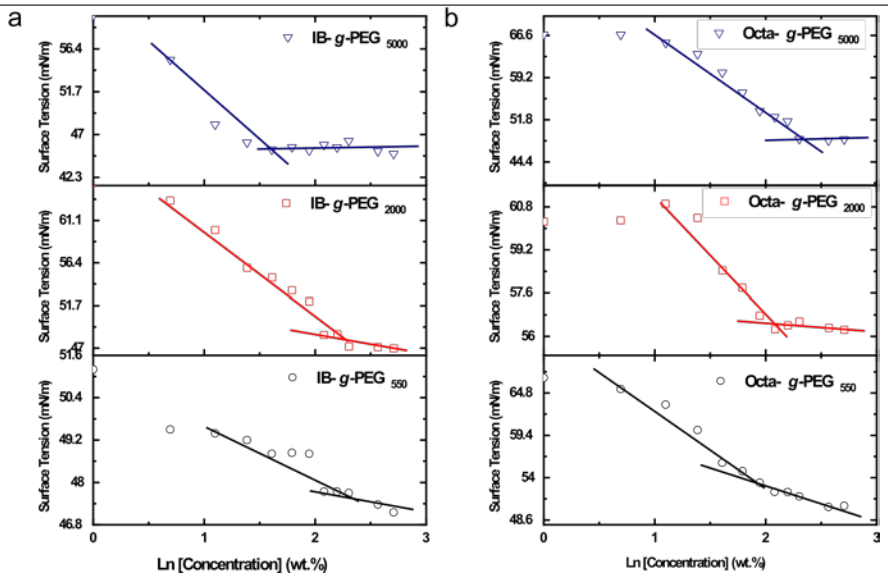

FIGURE 6.2: Surface tension measurements of grafted polymer-brine (diluted seawater solution) droplet in air: (a) grafted PEG onto IB backbone, and (b) grafted PEG onto Octa backbone.

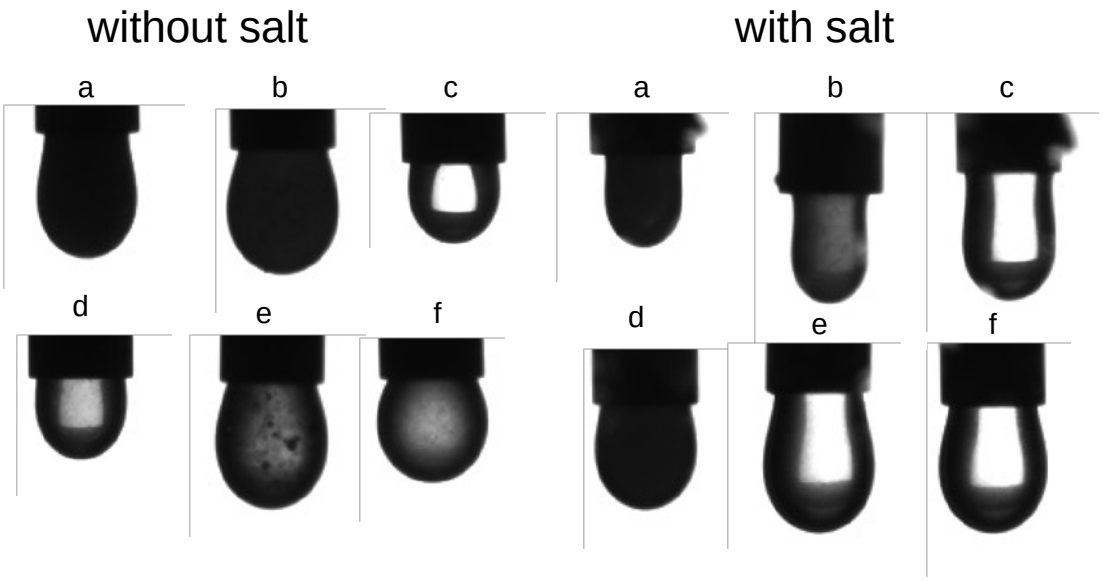

FIGURE 6.3: Static IFT of grafted polymer in oil flooding in present (right) and absent (left) of salt (0.5 wt.% of NaCl): (top) grafted PEG onto IB backbone Mn: 550, 2000 and 5000 (a, b, and c, respectively), (bottom) grafted PEG onto Octa backbone Mn: 550, 2000 and 5000 (d, e, and f, respectively), both at 20 C.

TABLE 6.4: Static IFT of pure oil and grafted polymer-brine droplet in hexane, decane, and hexadecane with and without Salt.

Materials	IFT (mN/m) 20 C			IFT with salt at 20 C		
	Hexane	Decane	Hexad⇤	Hexane	Decane	Hexad⇤
Pure oil	41.8	50.33	53.30	41.8	50.33	53.30
IB-*g*-PEG$_{550}$	23.7	10.3	11.89	16.42	18.1	17
IB-*g*-PEG$_{2000}$	14.30	12.89	13.19	16.32	15.78	14.33
IB-*g*-PEG$_{5000}$	16.40	24.59	25.5	20.47	24.4	20.78
Octa-*g*-PEG$_{550}$	7.6	20.47	21.8	12	20	28
Octa-*g*-PEG$_{2000}$	18.80	19.88	17.8	22	23	23
Octa-*g*-PEG$_{5000}$	19.8	22.5	24.04	17	19	19

where ⇤ refer to Hexadecane oil.

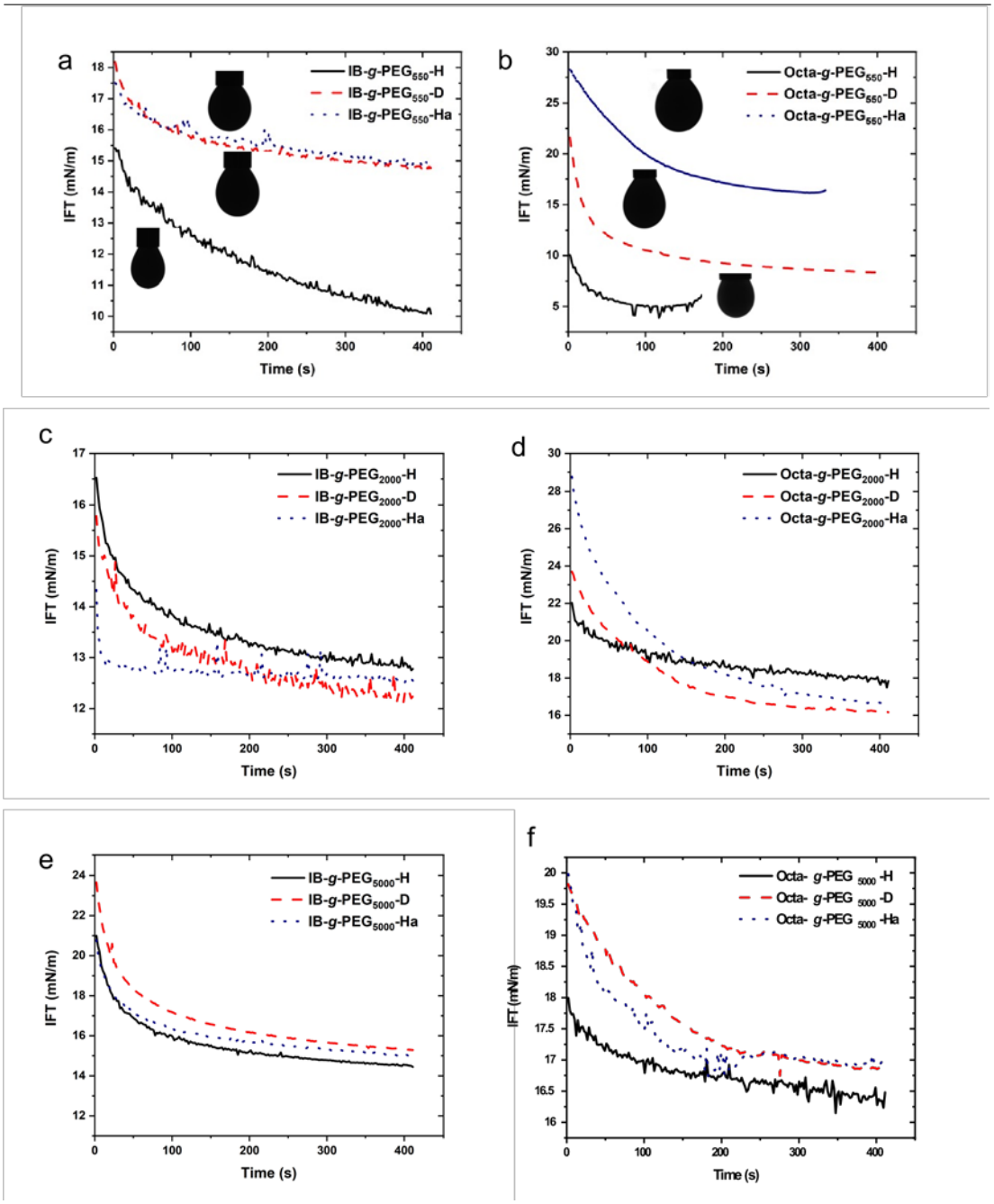

FIGURE 6.4: Dynamic and static IFT measurements of grafted polymer-brine droplet in hexane, decane, and hexadecane: (a) grafted PEG_{550} onto IB, (b) grafted PEG_{550} onto Octa backbone, (c) grafted PEG_{2000} onto IB, (d) grafted PEG_{2000} onto Octa backbone, (e) grafted PEG_{5000} onto IB, and (f) grafted PEG_{5000} onto Octa backbone at 20 C and 0.5 wt% of NaCl solution. Where: H, D, and Ha refer to Hexane, Decane, and Hexadecane, respectively.

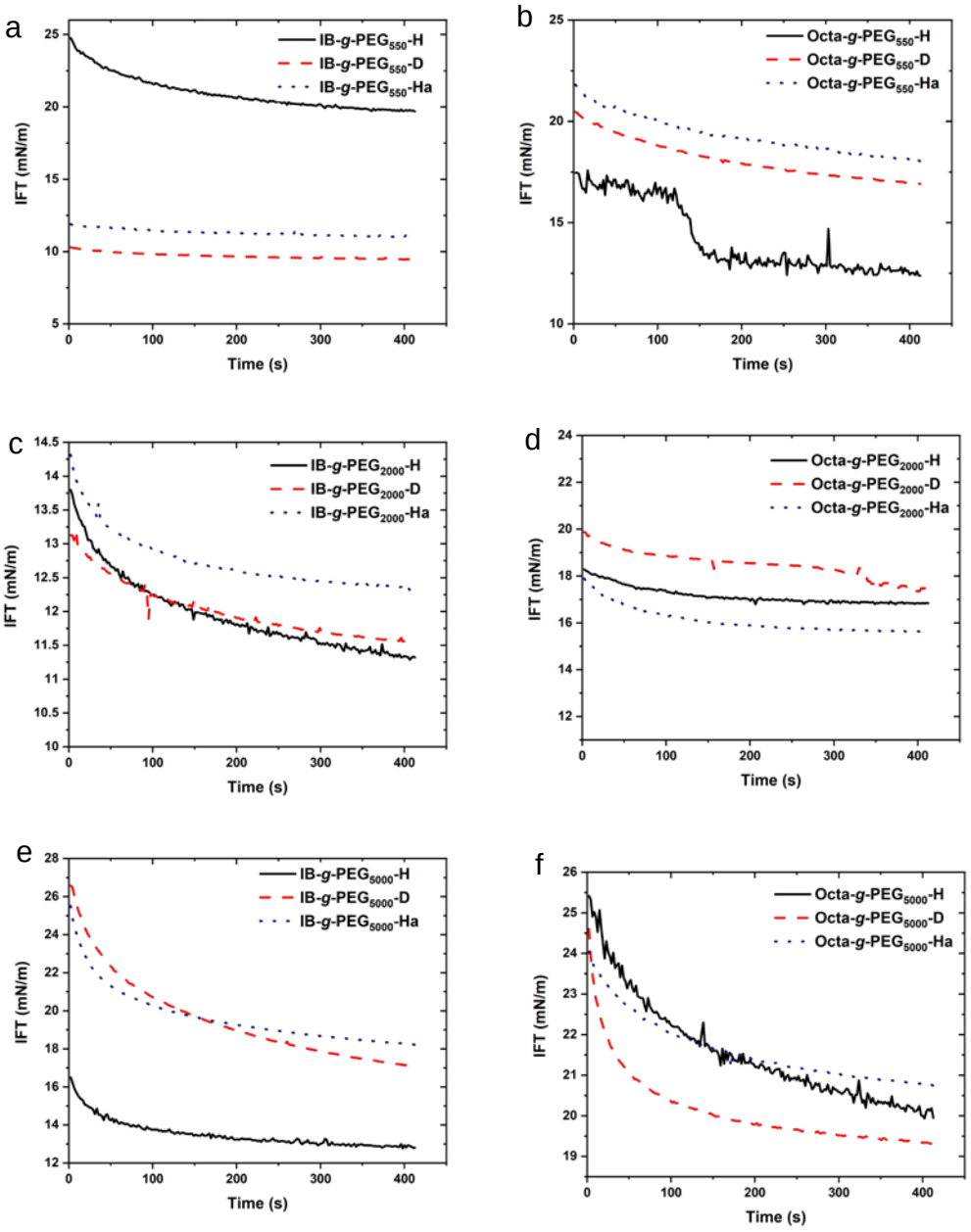

FIGURE 6.5: Dynamic IFT measurements of grafted polymer (without salt)droplet in hexane, decane, and hexadecane: (a) grafted PEG_{550} onto IB, (b) grafted PEG_{550} onto Octa backbone, (c) grafted PEG_{2000} onto IB, (d) grafted PEG_{2000} onto Octa backbone, (e) grafted PEG_{5000} onto IB, and (f) grafted PEG_{5000} onto Octa backbone at 20 C.Where: H, D, and Ha refer to Hexane, Decane, and Hexadecane, respectively.

6.4.3 Small Angle X-ray Scattering (SAXS)

SAXS data was collected for the co-grafted polymers with 1 wt.% of NaCl solution at 2 wt.% above CMC to investigate the effect of NaCl on the polymer shape. The SAXS

scattering patterns are shown in Figure 6.6. The scattering data were fitted with an Ellipsoid core shell model with the following parameters: Radius-equat-core (Equatorial radius of core (Å)), Thick shell (thickness of shell at equator (Å)), Radius of the polar core (⇥-core ⇥ radius-equat-core), and thickness of the polar core (⇥-polar shell ⇥ thick-shell).

As can be seen from the results shown in Table 6.5, the radius equatorial of the core was reduced from ⇠ 530 Å to ⇠ 200 Å by increasing the PEG chain length. The shape of the grafted polymers remained the same regardless of the solution they were immerse in. The radius of their cores increased after NaCl addition, which indicated that the aggregation of the grafted polymers increased. Their shell thickness also changed slightly after NaCl addition. For grafted PEG_{550} and PEG_{2000} onto Octa, Bragg peak was observed in the scattering pattern which means crystalline ordering and therefore, the data could not be fitted to the ellipsoidal model. This observation was in agreement with results obtain without salt. This also indicates that the NaCl does not affect the shape of the polymer but affects the size and aggregation of the system table 6.5.

TABLE 6.5: Fitting Parameters Obtained using the Ellipsoidal core shell model of SAXS measurement in H_2O solutions at 25 C.

Grafted polymer	Radius Equat. core	Radius of polar core (Å)	Thick shell	Thickness (polar.) shell(Å)
IB-*g*-PEG_{550}	527.93±2.9	112.4	235.71±2.3	16.49
IB-*g*-PEG_{2000}	330.78±0.28	69.46	181.94±0.44	13.02
IB-*g*-PEG_{5000}	216.66±3.6	22.74	249.9±4.7	19.99
Octa-*g*-PEG_{550}	-	-	-	-
Octa-*g*-PEG_{2000}	-	-	-	-
Octa-*g*-PEG_{5000}	229.76±0.125	2.29	201.31±0.1	26.81

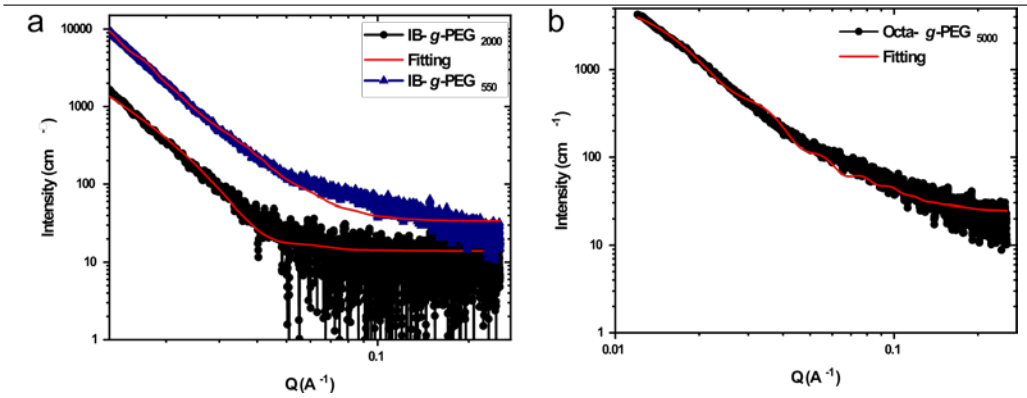

FIGURE 6.6: SAXS from 2 wt.% of grafted PEG Mn (550, 2000, and 5000) onto IB backbone (a), and Octa backbone (b) in H_2O, at 25 C. Solid lines are fits to the Ellipsoid Core Shell model.

6.4.4 Microemulsion

The influence of the grafted polymers and inclusive system on particle size distribution of W/O emulsions stabilization were studied. Six grafted polymers were dispersed in DI-water (with and without 1 wt.% NaCl). This was followed by addition of oil in various fraction ranging from 90-10% of Decane and hexadecane, used as an oil simulant before emulsification. The phase change and emulsion stabilization were timed at these intervals: directly, 1 hour, 1 day, 1 week, and 1 month as listed in tables (6.6 and 6.7), and figures (6.7 and 6.8). The results focused primarily on the ratio (10:90, 25:75, and 50:50). The rest of visual observation results for both grafted polymers are in the appendix A.

1. For emulsion made from grafted PEG onto IB backbone without salt and in decane: the emulsion displayed phase IV (one phase) and remained as phase IV up to 1 day, then phase changed into phase II (excess water) after 1 week. When compared against polymers of the same graft (without salt) but in hexadecane oil, the emulsions followed the same trend except emulsion at 10:90 ratio which displayed phase IV (one phase) for 1 week. This result shows

the effect of the oil on stabilized emulsion which made of the same material, increasing alkane hydrocarbon increase emulsion stability. Further investigate required using heavy oil for more understanding.

2. For emulsion made of grafted PEG onto IB backbone with 1 wt.% NaCl and for all tested ratios and time with both tested oils (decane and hexadecane), the emulsion was formed phase II (excess water) and displayed phase II up to a day. The exception was with emulsion made of grafted PEG_{5000} onto IB at 50:50 ratio, it displayed phase IV and phase changed into phase III (three phase) after 1 week.

3. For emulsions made with grafted PEG onto Octa backbone: the emulsions made of grafted Octa in both oils (decane and hexadecane) with and without NaCl, formed phase IV (one phase) for all three Mn: 550, 2000, and 5000 initially. This was followed by phase separation into phase II (excess oil) which occurred after 1 hour or 1 day.

   For the 10:90 ratio in both oils (decane and hexadecane) without NaCl, the emulsion displayed phase IV (one phase) and stabilized at phase IV at all tested times.

   The one exception was with emulsion made of grafted PEG_{550} onto Octa, the emulsion displayed phase IV and phase changed into phase II which was occurred after one day. The result from PEG_{550} emulsion indicative of increase grafted number of PEG increase emulsion stabilization [Chapter 5].

Summary for emulsion phase behaviour: both grafted polymers are able to stabilize emulsion. The grafted PEG onto IB backbone shows increased stability as hydrocarbon oil increase. The better stabilization occurred from emulsion made of grafted PEG onto Octa backbone at longer chain of grafted PEG (2000 and 5000).

These results linked to the result wettability and number of grafted PEG from ^{1}H NMR and water contact angle (Chapter Five).

The DLS measurement were performed at various time points (1 hour, 1 day, 1 week, and 1 month) to monitor any changes in the particle size. DLS data (tables in the appendix A) confirmed the generation of emulsions from all the six grafted polymers. The nano emulsion particles all showed a larger diameter relative to the corresponding amphiphilic polymers. Based on the results, the particle size decreases after 1 day and an increase after 1 week. However, the particles size decreased as the number of the grafted PEG increases. This suggests that the grafted polymers were effectively encapsulated, and the emulsion were stable. The particle size from the grafted polymers were further examined by optical microscopy, the data of which can be found in appendix.

TABLE 6.6: Microemulsion phase behaviour stability of grafted polymers with and without salt in decane with time.

Sample	O:W ratio	A-Emulsion					B-Emulsion				
		5 min	hour	day	week	month	5 min	hour	day	week	month
IB-*g*-PEG$_{550}$	50:50	IV	IV	IV	II	II	IV	II	II	II	II
	25:75	IV	IV	IV	II	II	IV	II	II	II	II
	10:90	IV	IV	IV	II	II	IV	IV	II	II	II
IB-*g*-PEG$_{2000}$	50:50	IV	IV	IV	II	II	IV	II	II	II	II
	25:75	IV	IV	IV	II	II	IV	II	II	II	II
	10:90	IV	IV	IV	II	II	IV	II	II	II	II
IB-*g*-PEG$_{5000}$	50:50	IV	IV	IV	II	II	IV	IV	II	II	III
	25:75	IV	IV	IV	II	II	IV	IV	II	II	II
	10:90	IV	IV	IV	II	II	IV	IV	IV	II	II
Octa-*g*-PEG$_{550}$	50:50	IV	I	I	I	I	III	III	x	x	x

	25:75	IV	IV	IV	II	II	IV	IV	II	II	II
	10:90	IV	IV	IV	IV	II	IV	IV	II	II	II
Octa-*g*-PEG$_{2000}$	50:50	IV	I	I	I	I	IV	IV	I	I	I
	25:75	IV	IV	IV	II	II	IV	IV	IV	II	II
	10:90	IV	IV	IV	IV	II	IV	IV	IV	IV	II
Octa-*g*-PEG$_{5000}$	50:50	IV	I	I	I	I	IV	I	I	I	I
	25:75	IV	IV	IV	II	II	IV	IV	II	II	II
	10:90	IV	IV	IV	IV	II	IV	IV	IV	II	II

Type I = excess-oil; type II = excess-water; type III = three-phase emulsion; type IV = one-phase; x = full separation. A = without salt, B = with 1 wt.% of NaCl.

TABLE 6.7: Microemulsion phase behaviour stability of grafted polymers with and without salt in hexadecane with time.

Sample	O:W ratio	A-Emulsion					B-Emulsion				
		5 min	hour	day	week	month	5 min	hour	day	week	month
IB-*g*-PEG$_{550}$	50:50	IV	IV	IV	II	II	III	III	III	III	III
	25:75	IV	IV	IV	II	II	II	II	II	III	II
	10:90	IV	IV	IV	IV	II	II	II	II	II	II
IB-*g*-PEG$_{2000}$	50:50	IV	IV	IV	II	II	IV	IV	II	II	II
	25:75	IV	IV	IV	IV	II	IV	IV	II	II	II
	10:90	IV	IV	IV	IV	II	IV	IV	IV	II	II
IB-*g*-PEG$_{5000}$	50:50	IV	IV	IV	III	III	II	II	II	II	III
	25:75	IV	IV	IV	II	II	II	II	II	II	II
	10:90	IV	IV	IV	IV	II	IV	IV	IV	II	II
Octa-*g*-PEG$_{550}$	50:50	IV	IV	IV	IV	IV	IV	II	II	II	II
	25:75	IV	IV	IV	II	II	IV	II	II	II	II

	10:90	IV	IV	IV	IV	II	IV	IV	II	II	II
Octa-*g*-PEG$_{2000}$	50:50	IV	IV	I	I	I	IV	IV	I	I	I
	25:75	IV	IV	IV	II	II	IV	IV	II	II	II
	10:90	IV	IV	IV	IV	II	IV	IV	IV	IV	II
Octa-*g*-PEG$_{5000}$	50:50	IV	IV	I	I	I	IV	IV	II	II	II
	25:75	IV	IV	IV	II	II	IV	IV	II	III	II
	10:90	IV	IV	IV	IV	II	IV	IV	IV	III	II

Type I = excess-oil; type II = excess-water; type III = three-phase emulsion; type IV = one-phase; x = full separation. A = without salt, B = with 1 wt.% of NaCl.

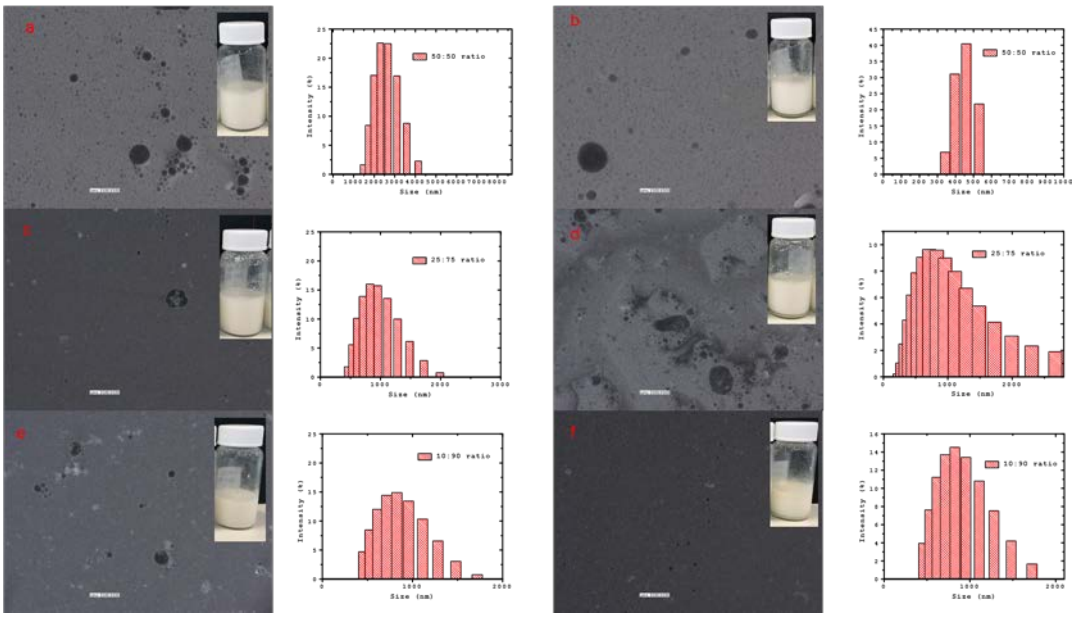

FIGURE 6.7: Optical microscopic images and DLS profile for grafted polymers stabilized W/O emulsions of grafted PEG$_{550}$ onto IB backbone in hexadecane: (a) 50:50 ratio after 1 hour, (b) after 1 day, (c)25:75 ratio after 1 hour, (d) after one day, (e) 10:90 after 1 hour, and (f) after 1 day.

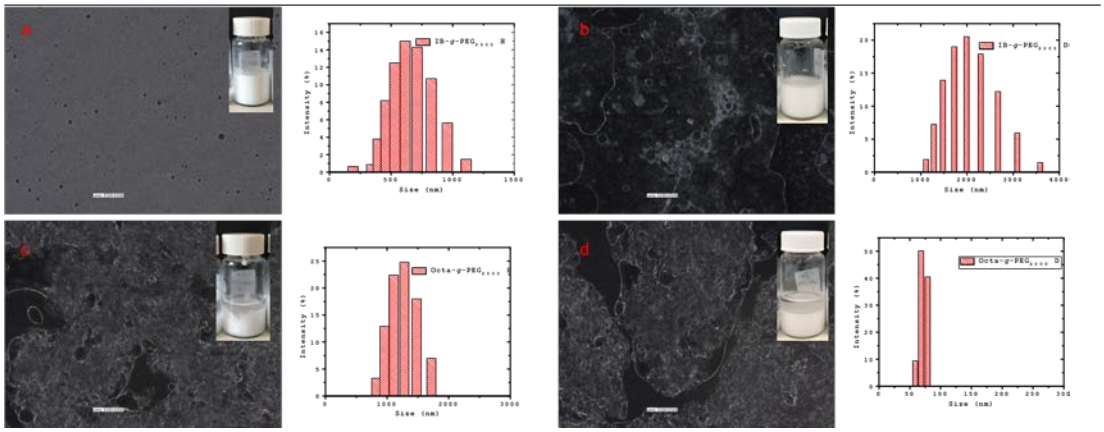

FIGURE 6.8: Optical microscopic images and DLS profile for grafted polymers stabilized W/O emulsions after a day without salt of grafted PEG_{2000} onto IB backbone in hexadecane (a), in decane (b), grafted PEG_{2000} onto Octa becabone in hexadecane (c), and in decane (d).

6.4.5 Oil displacement experiment

The enhanced oil recovery experiment of the grafted polymers was conducted in sandstone reservoir rocks by flooding test. The solution properties and data obtained are summarized in Table 6.2. All experiments were conducted at 25 C.

Prior to polymeric solution flooding, the water flooding (20 wt.% of NaCl dissolved in DI-water) was carried out (as the secondary oil recovery) to generate the residual oil saturated porous media. The polymeric solutions were injected after breakthrough point, then followed by brine solution injection. Figure 6.9. presents the result from the oil displacement test for grafted PEG into Octa backbone at Mn: 550, 200, and 5000 (with and without salt), and only grafted PEG Mn: 2000, and 5000 onto IB backbone. The oil displacement by PEG_{550} onto IB backbone was not included in the test due to the fact that they present higher particle size than the pore space (inside reservoir rock). The oil recovery increased after adding NaCl up to 20%. The highest oil recovery was achieved from the injected polymer 'grafted PEG_{5000} onto IB' with salt. Previous results have showed viscosity of the polymers with salt to be higher than those without, which agrees with observation in the oil recovery test.

The general conclusion of the flooding experiment is that the amount of oil swept seems to be largely determined by the aggregation size, the viscosity of the solution, and interfacial effect. The addition of salt to polymeric fluid increases the oil recovery. The increase wettability increase oil displacement which indicates that hydrophilicity is a key factor to increasing oil recovery.

It is better to do the flooding experiment using a single rock, however the downside is that, it is time consuming with regards to: cleaning, saturating, and preparation (which can take over two months).

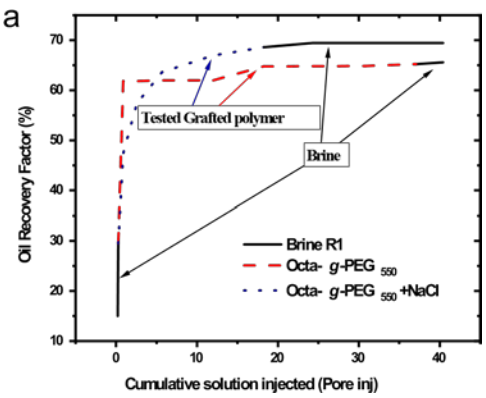

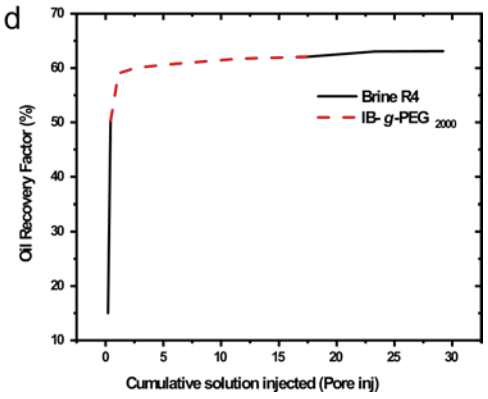

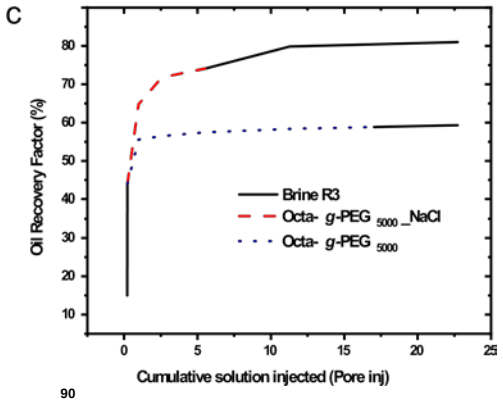

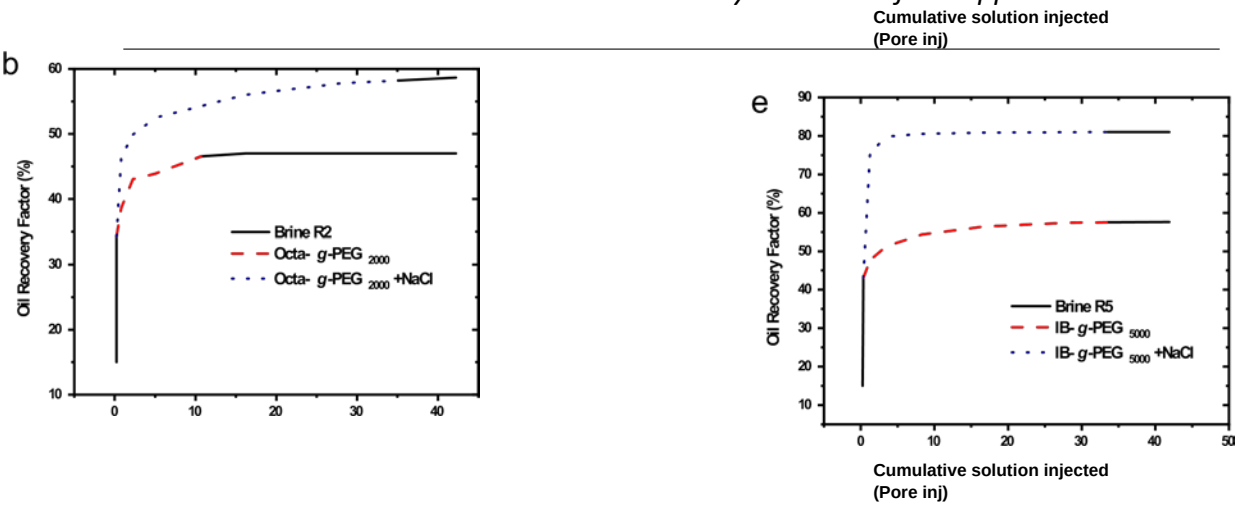

FIGURE 6.9: Plot of the oil displacement for 1 wt.% of grafted polymer with and without salt: (a) grafted PEG_{550} onto Octa backbone, (b) grafted PEG_{2000} onto Octa backbone, (c) grafted PEG_{5000} onto Octa backbone, (d) grafted PEG_{2000} onto IB backbone, and (e) grafted PEG_{5000} onto IB backbone at 20 C and brine (20 wt.% of NaCl).

6.5 Conclusions

In this work, a novel family of amphiphilic polymeric surfactant were prepared with the aim of finding their potential as suitable candidates for oil recovery applications. Two area examined were emulsion stabilization and oil displacement capability.

In terms of emulsion stabilization: the key factors that allowed these amphiphilic polymers to stabilise emulsion effectively were primarily governed by their surface characteristics. Increasing the number of grafted PEG onto the polymer backbone improved the stability of the emulsion by enhancing the rigidity of the network emulsion structure. The results indicated that emulsions stabilized by grafted polymer onto IB backbone had higher stability than grafted polymer onto Octa backbone, which was attributed to the stronger interaction between grafted polymer and oil. Highly stable W/O emulsion were achieved from grafted PEG onto IB backbone in hexadecane at (10:90) ratio. The addition of NaCl to the grafted polymer systems showed a reduction in emulsion stability in all systems. In both oils (hexadecane and decane) the emulsions made of grafted PEG onto IB displayed same phase. The results indicated that the emulsion phase does not effect by oil, whereas

emulsion from grafted PEG onto Octa backbone displayed phase changed from phase (IV) to phase I at 50:50 water/oil ratio only, and remain same in the other ratios.

The novel amphiphilic polymers were surface active and also able to displace oil effectively. Surface tension reduction of 30 mN/m, IFT and CMC shows a significant synergistic effect on fluid-fluid and air-fluid, respectively. The two main factors that controlled oil displacement were aggregation size of the system and hydrophilicity. Polymers with smaller size aggregations and high wettability had a higher oil recovery.

Oil recovery was increased by 20% from injected with grafted PEG_{5000} onto Octa backbone with 1 wt.% NaCl.

The optimal salt concentration required was determined to be 1 wt.% to conduct all experiments. SAXS was effective in determining the micelle conformation by way to statistical fitting of the data. The data fit signified ellipsoidal core-shell micelles composed of hydrophilic grafted shells and hydrophobic backbone cores.

Chapter 7

Conclusions and Future Works

7.1 Conclusions and future works

The work carried out in this thesis shows that the modified alumina nanoparticles by carboxylic acid can be used for improving the oil displacement properties of oil recovery. The size and shape of the native and carboxylic acid functionalized alumina nanoparticles at different concentrations was characterized by DLS and SANS data to provide a theoretical understanding of the interaction between liquid-liquid (oil-nanofluid). The stability of these nanoparticles has been tested with the addition of a novel low surface energy surfactant (LSES). This surfactant shows the ability to stabilize hydrophobic nanoparticles (OCT-NP) at 0.5 wt.% and CMC, up to two hours which is time enough for waterflooding experiment. Our previous research showed that the modified alumina nanoparticles are able to reduce the interfacial tension between oil (hexadecane) and nanofluid from 51 to around 40 mN/m (Al-Shatty et al., 2017). It is possible that these modified nanoparticles are able to increase oil displacement and act as a surface-active agent.

The size of the nanoparticles play a significant role in the oil recovery, it showed that if the particle has high agglomeration it cannot pass through the reservoir rock, while the smaller, non-agglomerated, one does. The research focused on the two main nanoparticles MEEA-NP (hydrophilic NPs) and OCT-NP (hydrophobic NPs). Nanofluids made of 0.5 wt.% of modified alumina injected after brine solution have a positive effect on the oil recovery. Oil recovery has been increased by 8% and 10% from injected with OCT-NP alone and OCT-NP/LSES, respectively. However, only 4%

oil recovery occurred with injection with MEEA-NP/LSES while no improvement was observed with MEEA-NP alone. These results indicate that hydrophobicity has a positive effect on oil recovery and the OCT-NP is the active surface agent herein. To the best of our knowledge, we report herein, for the first time, the use of functionalized alumina NPs as a nanofluid candidate for enhanced oil recovery.

The evaluation of the mechanism of these NPs (MEEA-NP, and OCT-NP) with surfactant complex adsorption at the critical oil/water interface was studied with a high-level technique (Neutron Reflectometry) to give insight on NPs/oil interactions in oil recovery systems. MEEA-NP, and OCT-NP in the presence of two surfactants (CTAB and SDS), were studied at the oil/water interface. A thin oil layer of mixing of deuterated and hydrogenated hexadecane (contrast matching silicon substrate) was spin coated onto a hydrophobic silicon block modified by a layer of trimethylchlorosilane as previously detailed (Campana, 2012). The oil layer was then sandwiched between the silicon layer and the aqueous phase. The samples were allowed to equilibrate for at least 45 minutes prior to measurement. The concentration of the NPs was 0.5 wt.% and surfactant at CMC. In all cases, both the oil and the aqueous phase were contrast matched to silicon. The reflective characterization was at two contrasts: A) a mixture of deuterated and hydrogenated (non-deuterated) surfactant to match the scattering length density of silicon and (B) only the deuterated surfactant. The interface is divided into discrete layers, each characterized by a roughness *s*, thickness t and scattering length density SLD which is a function of layer composition. In terms of SDS system, three models are applied: 1-layer, near-spherical model, and using the actual size of the NPs form SANS data. All models fit the data very well.

The adsorption amount of NPs and surfactants has been calculated using equation 3.1.

The disk-like shape of these particles, the surfactant distribution across the interface appears to be somewhat bimodal, where the top and bottom parts of the interface are surfactant-rich and most of the NPs reside in the middle part. The adsorption of near-spherical particles coated with an analogous surfactant shell, where the surfactant distribution is more similar to that of the NPs. This may well be the case in this situation as the role of the surfactant as a dispersant, therefore the formation of smaller complexes is to be expected in presence of surfactant. It must be stressed that in both NP-SDS systems the adsorbed amount of the two components is hardly affected by the shape of the particles, hence the quantitative interpretation is independent on the choice of model used (see Table 3.4).

As mentioned above, these NPs able to reduce IFT to up to 40 mN/m. Interestingly, the presence of the surfactant in the nanofluid led to a significant reduction in the interfacial tension of hexadecane oil, from 51 mN/m to around 9 mN/m. The surface charge of the system has been studied using zeta potential. The result showed that the native alumina, and modified alumina have a positive charge, however, it changed to negative in the presence of SDS surfactant and remain positive with CTAB addition. The stability of these NPs increased with surfactant presence, as zeta potential results is between (30 to 50), which refer to a stable system.

From SANS data, the power law shows both nanoparticles with both surfactants have Q slope of around 2.1-2.5 at lower Q which indicates the scattering from 2D subjects such as a plate or ellipsoid (Al-Shatty, Alexander, and Barron, 2022). There is one possible explanation for this bimodal system, and this can be due to NPs being coated with both unimeric and surfactant micelles. The data at the high Q region shows a similar shape to the surfactants micelles (Hammouda, 2013), which could be due to scattering from micelles around the NPs. However, the data from the lower Q region has a pattern similar to nanoparticles which indicates that surfactants have coated NPs as unimers rather than micelles.

Injected nanofluid made of 0.5 wt.% of these NPs with CTAB and SDS into a sandstone rock using water flooding experiment showed a positive effect on the oil displacement. The highest oil recovery was from injected OCT-NP/CTAB with 4% more than surfactant alone. This result within line with NR, as the OCT-NP/CTAB showed more affinity toward oil interface than MEEA-NP/CTAB, which is the reason for high recovery.

In a previous published paper (Al-Shatty et al., 2017), the modified alumina with carboxylic acid showed a sign of role of stabilizing emulsion. In order to understand the mechanism, a full study was caried out in this thesis for making emulsion using native and modified alumina (OCT-NP, and MEEA-NP), with and without salt, and three surfactants (SDS, CTAB, and LESE), using hexadecane and decane (as oil phase). The stability of emulsion increased with surfactant presence, however, it decreased with salt addition. Interestingly, LESE surfactant observed a complete emulsion separation after 1 hour with salt addition, it is a good sign that LSES could work as a

demulsifier when salt is present. Future investigation is recommended to understand and confirm the role of salt and LSES.

Two novel families of amphiphilic graft copolymers (AGCs) were successfully synthesized via a 'grafting onto' method. The reaction occurred through a ring opening method, taking place between the terminal OH groups of the PEG molecules and the alternating cyclic anhydride functionality present in Octa or IB backbone. Characterization of the copolymers was performed spectroscopically using ^{1}H NMR, Fourier transform infrared (FTIR) spectroscopy and thermally using Thermogravimetric Analysis (TGA). In terms of NMR data and from estimated grafted point of each backbone, the total number of PEG (grafted or free) in each system can be calculated using (Equation 11, Appendix). The data of IB-*g*-PEG_{550} shows 13 number of PEG in the product out of possible 39, which indicates that, some of the maleic anhydride groups are not reacted. In comparison, grafted PEG 2000, and 5000, has 31, and 40, a number of PEG, respectively. The results indicate that nearly all of the malic anhydride groups are reacted in the case of grafted PEG_{5000}, in agreement with the IR data. The same trend is also observed for Octa-*g*-PEG, with possibly all the grafting points reacted or targeted for PEG_{2000} and PEG_{5000}. Thermally, the decomposition of the maleic anhydride groups occurred around 200 C, however, the rest of the polymer occurred at 400 C.

The result from making a thin film of polymer that deposit onto a glass microscope slide (as a substrate) and by contact angle measurement to measure the hydrophilicity, that showed that the higher number of the grafted PEG the higher the hydrophilicity of the polymer coated substrate. In line with this, AFM analyses

showed that the surface roughness of the coated polymer increased with decreasing the number of grafted PEG. In addition, two techniques were used to establish the surface activity of the grafted copolymers: measuring surface active SFT (to examine surface activity and CMC) using the pendent drop method and UV techniques. The SFT showed that the grafted copolymers are able to reduce the water SFT to 40 mN/m which makes them potential polymeric surfactants. The SFT data indicated that these copolymers formed micelles and having CMC of these copolymers is between (1.7 to 3 wt.%) depending on the molecular weight of the backbone and the grafted chains. Analysis of the size and aggregation structures were studied using small angle neutron and X-ray (SANS and SAXS) techniques. Both techniques indicated that the grafted copolymers have an ellipsoidal core-shell micelles composed of the hydrophilic grafted shells and hydrophobic backbone.

As discussed earlier, these novel synthesised amphiphilic copolymers form core-shell ellipsoidal micelles and reduce the SFT of DI-water within the range of polymeric surfactants. Two potential applications were tested using amphiphilic copolymers: increased oil displacement and stabilizing emulsion. As discussed in section (5.4.1), it is necessary to evaluate aggregation behaviour, the conformational change of the grafted polymers/amphiphilic polymers resulting from the effect of salt/NaCl addition which was investigated by SAXS. It observed that, the salt addition did not change the shape of the amphiphilic copolymers (displayed an ellipsoidal core-shell micelles conformation), however, it changed the size. The oil displacement experiment by amphiphilic copolymers was done by injecting polymeric solution after a breakthrough point. The result indicated two points: the presence of salt (1 wt.% of NaCl) increase the oil recovery by 10 %; and the increasing number of grafted PEG

decreased the IFT between (oil/water) interface which led to ease oil and increase its displacement. In contrast, the copolymers with a higher number of grafted PEG have lower emulsion stability due to the size of the aggregation particle being smaller.

In summary, two points can be addressed from these findings: increasing oil recovery requires high wettability (⇠ 15) and smaller particles (100 to 200 nm); however, increasing emulsion stability requires medium hydrophobicity (between 60 to 90 WCA) and large particles (200 to 300 nm).

As highlighted in section (1.6.1.), it is essential that nanofluids (nanoparticles or polymers) be removed from the reservoir rock after being injected. In chapter five of this thesis, it was observed that traditional cleaning (using the Soxhlet method) using toluene and DI-water removed all the injected materials including nanoparticles, surfactants, and polymers. These results were confirmed by measuring the porosity and air permeability. Furthermore, it could be useful to investigate whether the injected nanofluids that are removed from reservoir rock could be recovered and reused for further processing. In addition to the costs associated with waste materials, it can be hazardous to reservoir rock and also the environment. Despite alumina and PEG polymer consider as non-hazardous materials, investigating the recycling of chemicals that are used in the reservoir should be of high importance to the oil industry. A straightforward approach towards achieving this could be to remove the DI-water from the nanofluid solutions that is used through the evaporation method. The solids (nanoparticles) recovered could be then washed to remove Na and then purified to recover the alumina and carboxylic acid. The purity

of recovered compounds could be studied by surface analytical characterization techniques such as X-ray photoelectron spectroscopy (XPS) and FTIR.

Ahead of any production line trails, it is essential that testing of the nanofluid (polymer, nanoparticles) in different environmental conditions is done before moving to a large scale (industry). In order to cover a wide range of experiments with a considerable time frame, it is worth testing these conditions using the micromodel device (section 1.10.3.). In the context of the work carried out in this thesis, the author carried out some preliminary stages for the fabrication of a 2.5D micromodel. Figure A.1 appendix A, shows (a) the backscattering of SEM image from a piece of a sandstone reservoir rock, (b)100 contrast MATLAB image of the edge of SEM image, (c) The micromodel creation by Autodesk fusion program, and (e) final micromodel mast pattern by Autodesk fusion program. Due to the timeline and loss of access to equipment (plasma laser breakdown) the micromodel fabrication and flooding experiment using the 2.5D micromodel was not possible to complete. However, this can be a great experiment to be carried out in future.

Furthermore, it would be also desirable to investigate whether these amphiphilic copolymers are able to capsulate drag as it is observed from UV results, these copolymer observed ability to disperse hydrophobic dye.

The result of this thesis suggests that modified alumina nanoparticles could be used as a surface-active agent with and without surfactant for oil recovery applications: oil displacement and emulsion stabilization. In addition, it is possible to tailor the wettability and applicability of hydrophobic polymers bearing functional

groups through grafting with different PEG groups. Further work is required to investigate the compatibility of grafted PEG onto alumina nanoparticles to stabilise pickering emulsions. However, the work reported herein does illustrate the amphiphilic grafted polymer and OCT-NP have promising applications as a surface active agent for oil recovery displacement.

Appendix A

NR model description, SANS, SAXS, and NMR description

A.1 Model description

As clearly stated in the chapter three, the model used for describing the data differs substantially between NP-SDS and NP-CTAB systems. The two are discussed separately.

A.1.1 NP-SDS

The interface was initially represented using a 1-layer model characterised by a roughness, bottom roughness, layer thickness (*t*) and hydration (which is dependent of volume fraction of NP, F-NP and volume fraction of SDS, F-SDS). The model was deemed too simple and therefore it was decided to adopt the geometric model. For this geometric model the NP-SDS complexes were divided into 10 slices composed of 2 concentric ellipsoids: the inner ellipsoid represents a NP with dimensions 400 Å.The outer shell has a thickness of 42 Å small axis. The thickness was the same for each of the slices and was allowed to flow in the fitted procedure. The inter-layer roughness was also the same for all layers and allowed to float. Other fitting parameters were the *surfactant coverage* in the shell (0=no surfactant, 1=full coverage) and the sphere packing of complexes at the interface (0=no complexes, 0.909=full packing).

The volume fraction of NPs and SDS in layer n was represented as:

$$f_{NP\,Ln} = Sphere\ \ packing \leftarrow Vol_{NP\,Ln} \qquad \text{(A.1)}$$

$f_{SDS\ Ln} = Spherepacking \leftarrow Surfactantcoverage \leftarrow Vol_{SDS\ Ln}$ (A.2) where VolNPLn and VolCTABLn are the volume fractions of NP and CTAB in each slice n of the complex. These calculated parameters are given in Table 3.6.

A.1.2 NP-CTAB

The interface could be represented using a 3 layer model. Each layer is characterised by a roughness, layer thickness (t) and hydration. For each layer the hydration is calculated from the volume fraction of NP *f* NP and volume fraction of CTAB *f* CTAB. For OCT-NP/CTAB the fitted *f*CTAB for the second layer was much lower than for the third layer. This was deemed unphysical given the distribution of the OCT- NP, therefore *f* CTAB for layer 2 was constrained to be higher than for layer 3.

$$f_{CTAB\ L2} = Incrementalf_{CTAB\ L2} + f_{CTAB\ L3} \quad (A.3)$$

This ensures that the number of fitting parameters does not change between the 2 systems.

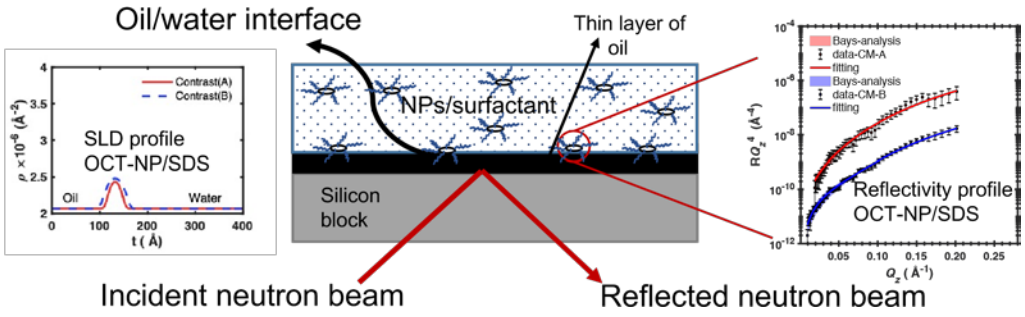

FIGURE A.1: A Schematic representation neutron reflectometry with the interaction between the NPs and surfactants with SLD profile of OCT-NP/SDS.

A.2 SANS and SAXS

A.2.1 Ellipsoidal core shell model

An ellipsoid-core-shell model was used for fitting the date for the grafted polymers aggregates; the overall ellipsoid (grafted polymer micelles) has an inner ellipsoid core (hydrophobic) and an outer ellipsoid shell (hydrophilic). The calculation of intensity of ellipsoid-core-shell-ellipsoid follows the equation below:

$$p(q,a) = scaleVF(q,a)+backgroundp = scaleVF(q,a)+background \quad \text{(A.4)}$$

where:

$$F(q,a) = f(q,radius\_equat\_core,radius\_equat\_core.x\_core,a)+ f(q,radius\_equat\_core+thick\_shell,radius\_equat\_core.x\_core+ thick\_shell.x\_polar\_shell,a). \quad \text{(A.5)}$$

where:

$$f(q,Re,Rp,a) = 3DrV \sin[qr(Reqr,Rp(Re,a,Rp)] ,a\cos)_3 [qr(Re,Rp,a)] \quad \text{(A.6)}$$

and

$$r(R_e,R_p,a) = q[R2_e \sin a2+R2_p \cos 2a] \quad \text{(A.7)}$$

where: *a* is the angle between the axis of the ellipsoid and q , V = (3/4)*p*Re Rp^2 is the volume of the ellipsoid, Rp is the polar radius along the rotational axis of the ellipsoid, Re is the equatorial radius perpendicular to the rotational axis of the ellipsoid and D*r* (contrast) is the scattering length density difference, either (scattering length density for the core–scattering length density for the shell) or (scattering length density for the shell-scattering length density for the core). For randomly oriented particles:

$$F^2(q) = \mathbb{Z}\, F^2(q,a)\sin a\, da \qquad \text{(A.8)}$$

A.2.2 Power Law model

This model can be applied for a range of fractal materials, surfaces and sheets equation below.

$$I(q) = scale.q \qquad Power + background \qquad \text{(A.9)}$$

The exponent power is a positive number for the model fitting. The Q range of scatters shows that they are likely to be lamellae with sharp interfaces of particles (-2 < Q < -4 Å ^{1}) in this research.

A.3 NMR Calculation

The total number of PEGs in the system (including both grafted, and un-grafted) was calculated using ^{1}H NMR. The key peak of the PEG is the CH_2 group at *s* ± 3.6 ppm, which has four protons per ethylene oxide unit.

$$N^{sc}$$

$$Number of PEG per backbone (N_c) = \frac{N_{sc}}{N_{bb}} \quad \text{(A.10)}$$

where Nsc is the total number of PEG and N_{bb} the total number of the grafted points of (IB or Octa) backbones, by apply the below equation.

$$N_c = \frac{N_{sc}}{N_{bb}} = \frac{R\text{-}CH\text{-}R_2}{4N_{sc}\quad CH} \quad \text{(A.11)}$$

where N_{sc} is the number ethylene oxide unit per PEG, as the mass of each unit is 44 g.mol ^{1}, and the average Mn of the un-grafted PEG samples are [550, 2000, or 5000] g.mol ^{1}, so N_{sc} = 13, 45, or 113, respectively.

N_{bb} is the number of grafted points in the backbone, 39 for IB backbone and (106 or 177) for the Octa backbone. The ratio of the CH_2 integrals at 3.6 ppm and CH at 1.1 ppm can be obtained from ^{1}H NMR spectrum.

A.4 Prepare solutions by Mix PEG and Backbone

The required amount of (2 wt.%) as received of the PEG (Mn: 550, 2000, 5000), IB and Octa backbone and the solvent were weighted into a vial and dissolve in (10 ml of THF) using magnetically stirrer for 24 hours. Then in a new vail 2 ml of each of PEG and IB or Octa left magnetically stirrer for 2 hours. Values presented are the average of three measurements, carried out at three different positions on the new coating surfaces.

Glass microscope slides was used as substrates to investigate the hydrophilicity of the copolymer films. Copolymer films were spray-coated onto the substrate from

prepared suspension using an artist's spray gun and hydrocarbon airbrush propellant. Three layers of coating were sprayed onto the substrates to ensure all areas of the surface were covered. The unused suspension left to dry in air for 24 hours, the dry powder used for FTIR spectrum and TGA measurements.

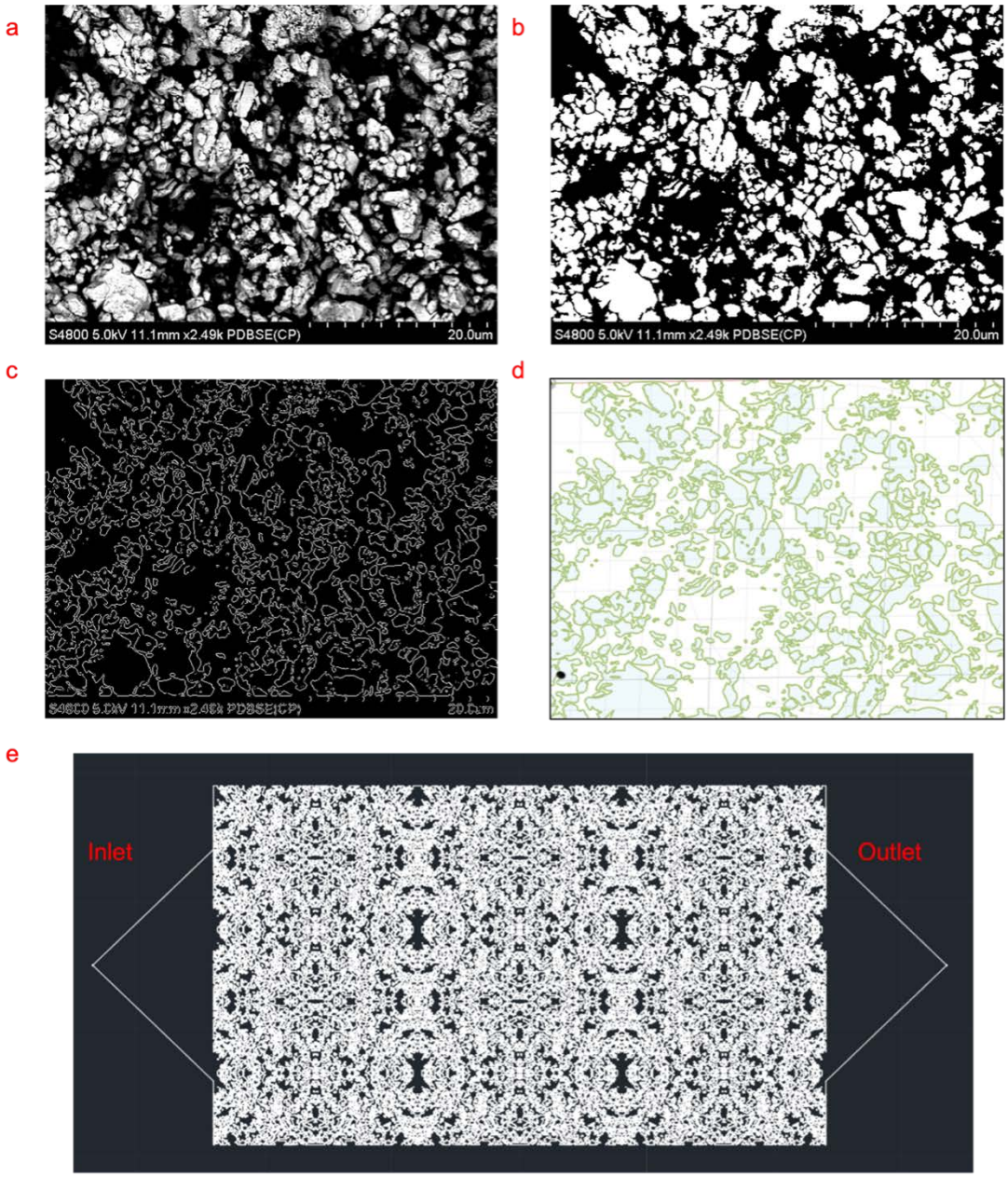

FIGURE A.2: Shows (a) the backscattering of SEM image from a piece of a sandstone reservoir rock, (b)100 contrast MATLAB image of edge of SEM image, (c) The micromodel creation by Autodesk fusion program, and (e) final micromodel mast pattern by Autodesk fusion program.

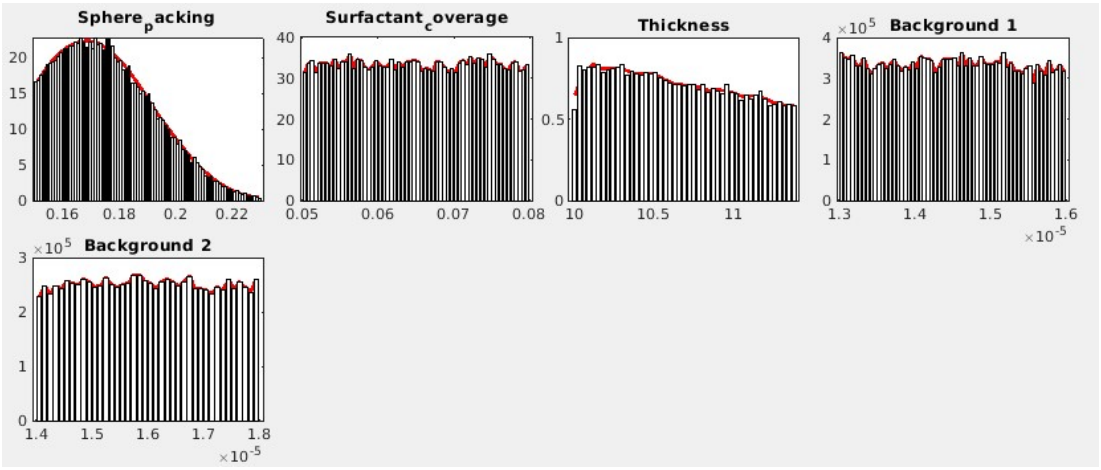

FIGURE A.3: Bayesian analysis-posteriors for MEEA-NP/SDS

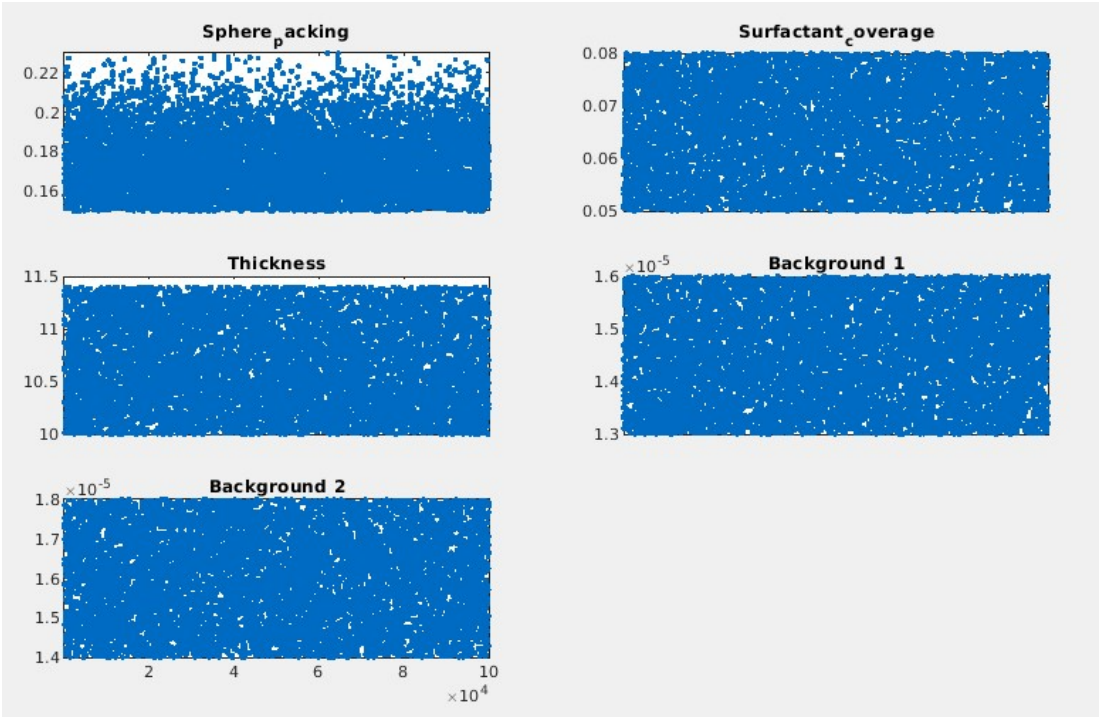

FIGURE A.4: Bayesian analysis-diagnostics for MEEA-NP/SDS

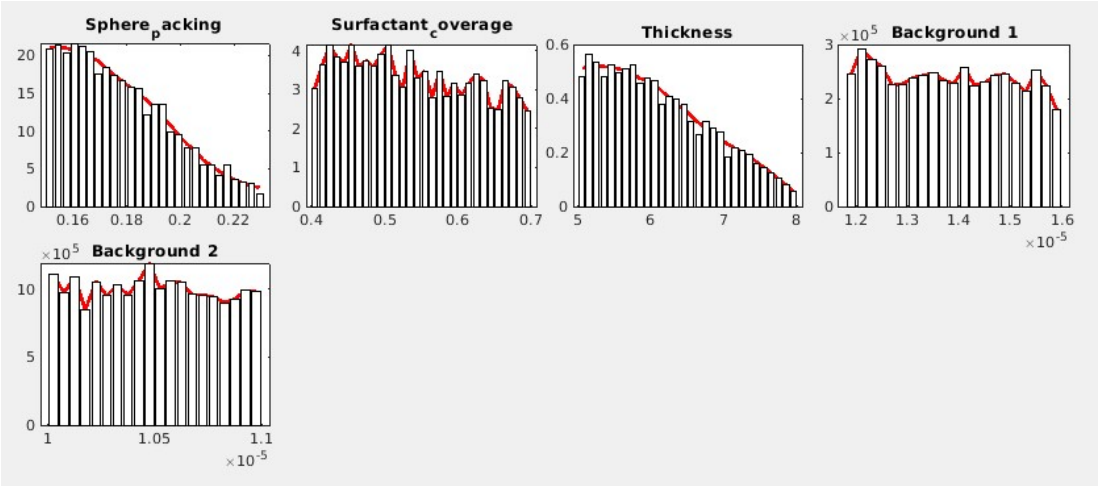

FIGURE A.5: Bayesian analysis-posteriors for OCT-NP/SDS

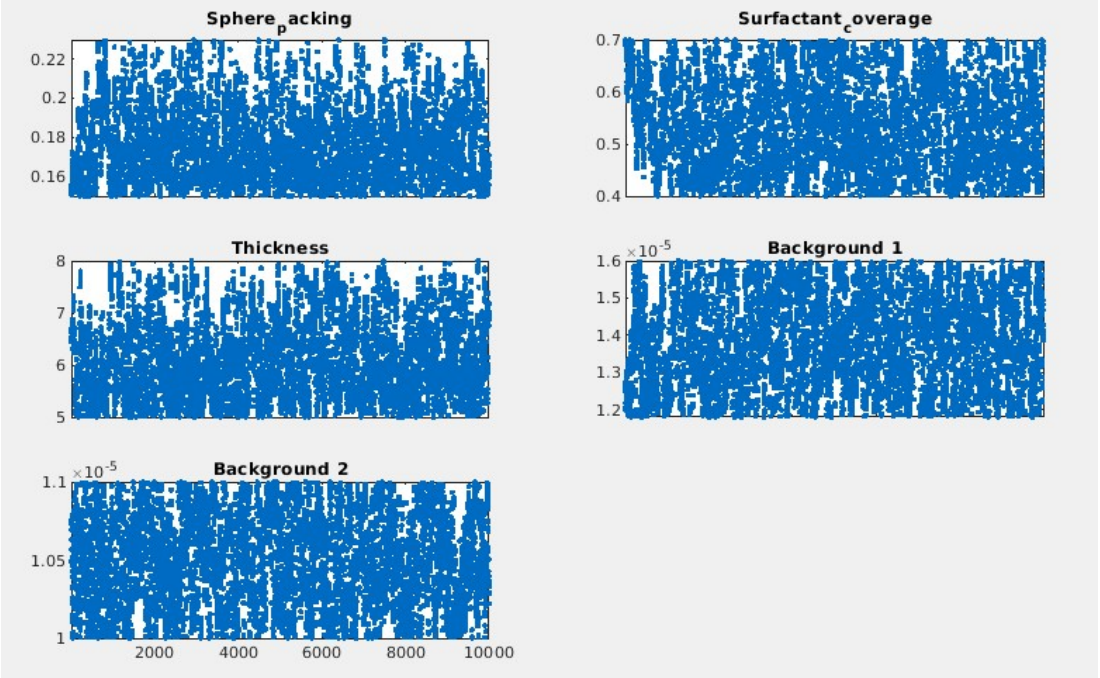

FIGURE A.6: Bayesian analysis-diagnostics for OCT-NP/SDS

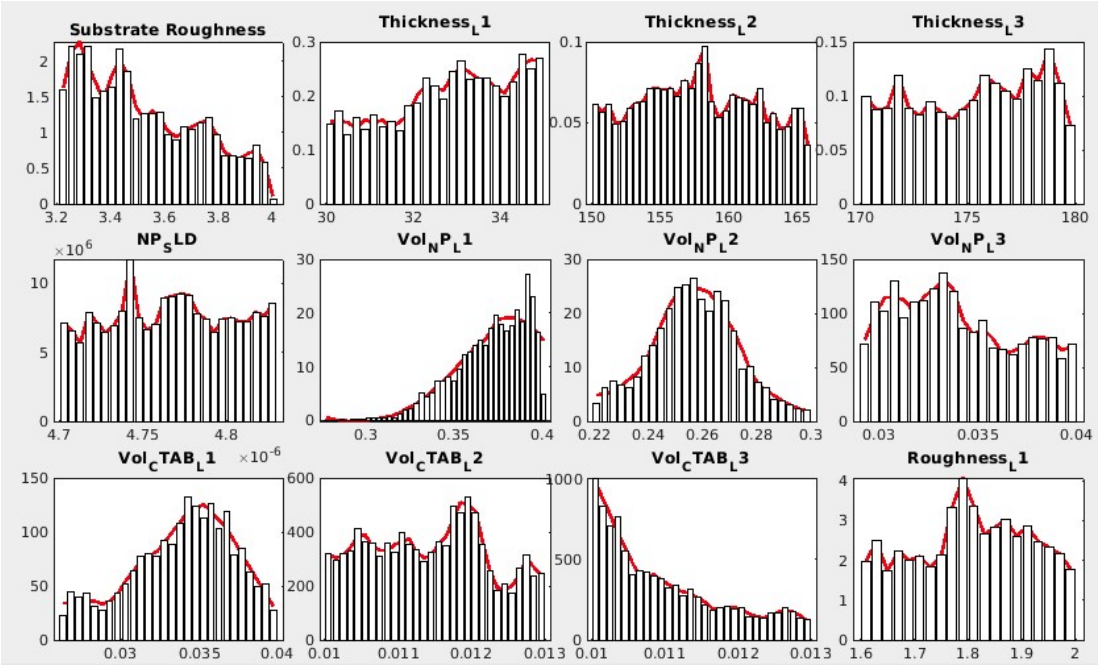

FIGURE A.7: Bayesian analysis-posteriors for MEEA-NP/CTAB

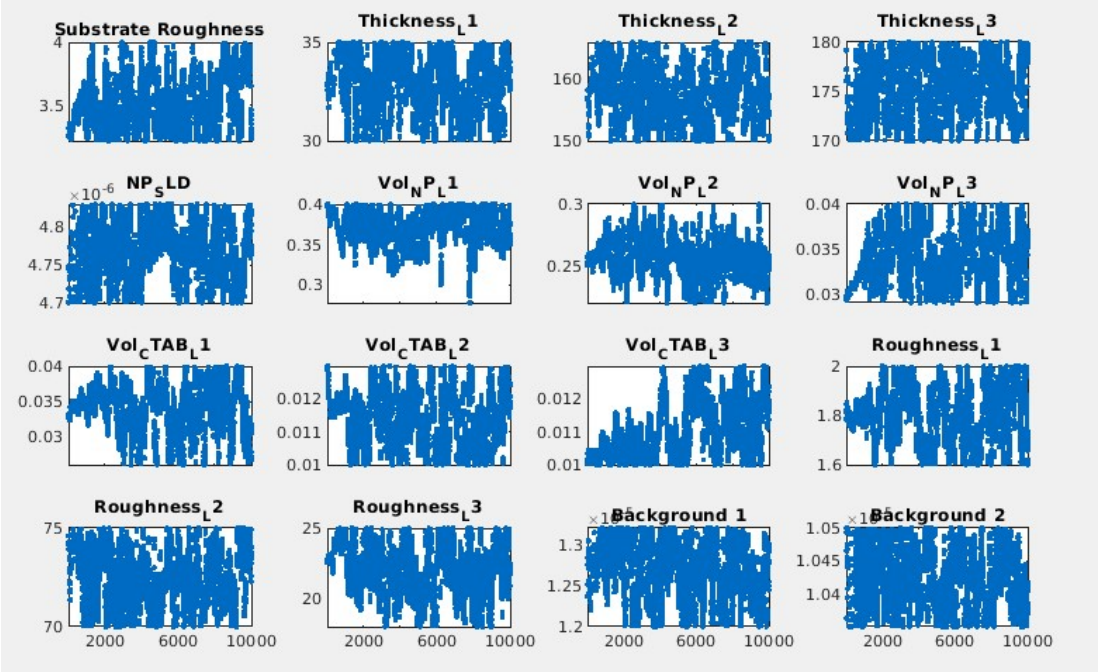

FIGURE A.8: Bayesian analysis-diagnostics for MEEA-NP/SDS

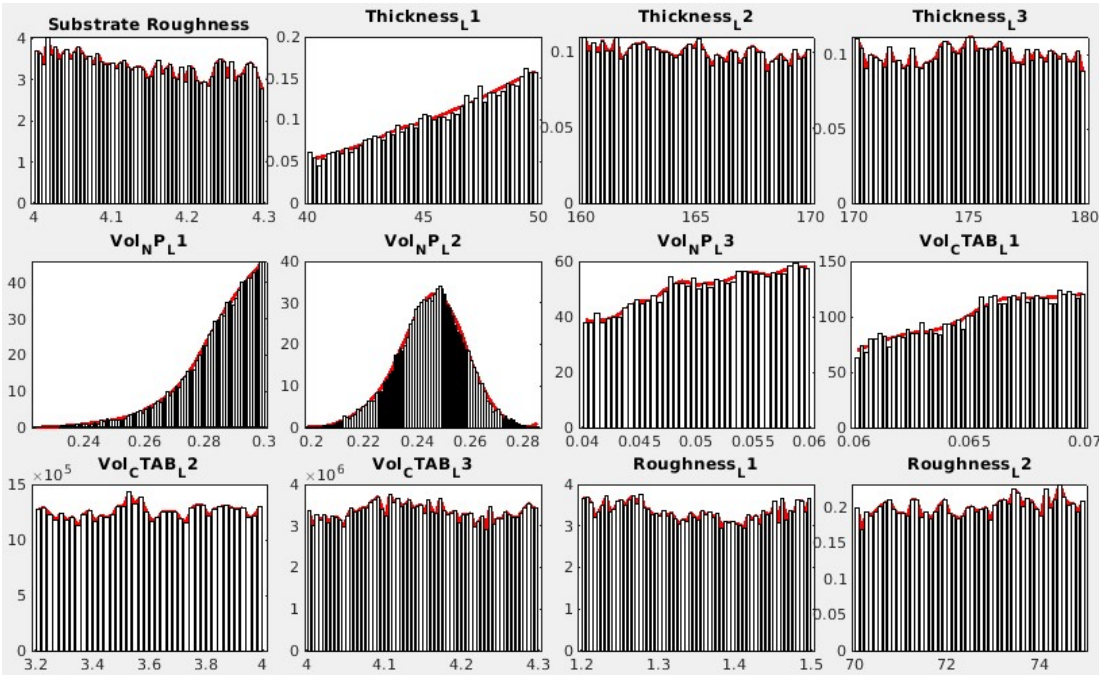

FIGURE A.9: Bayesian analysis-posteriors for OCT-NP/CTAB

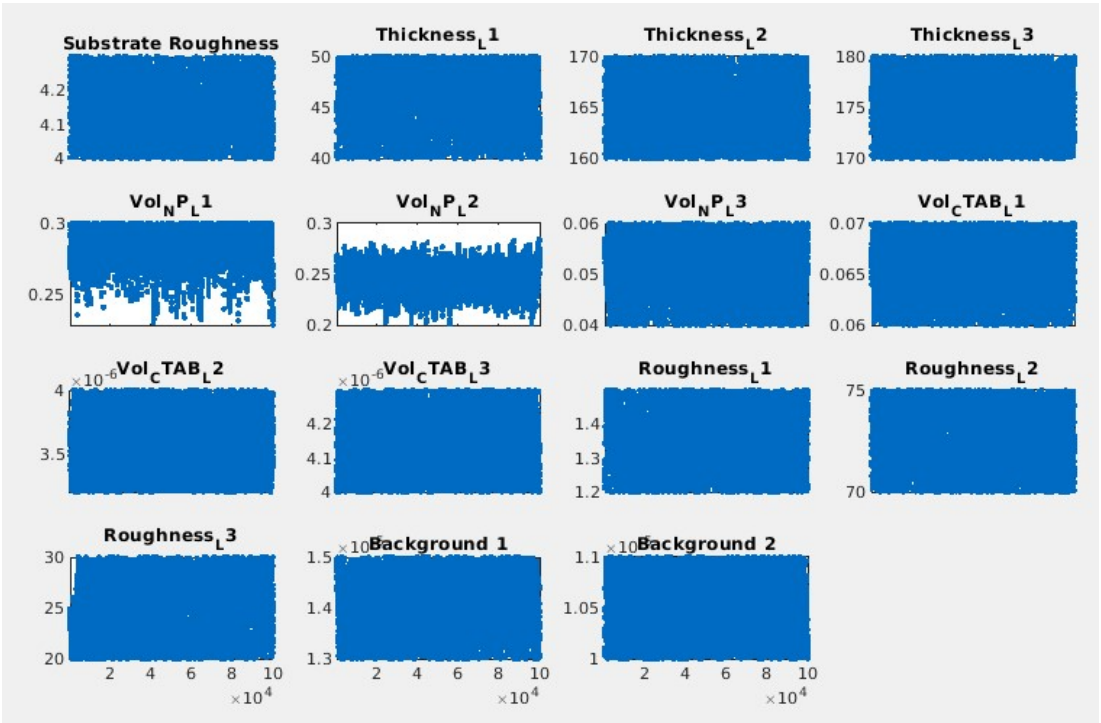

FIGURE A.10: Bayesian analysis-diagnostics for OCT-NP/SDS

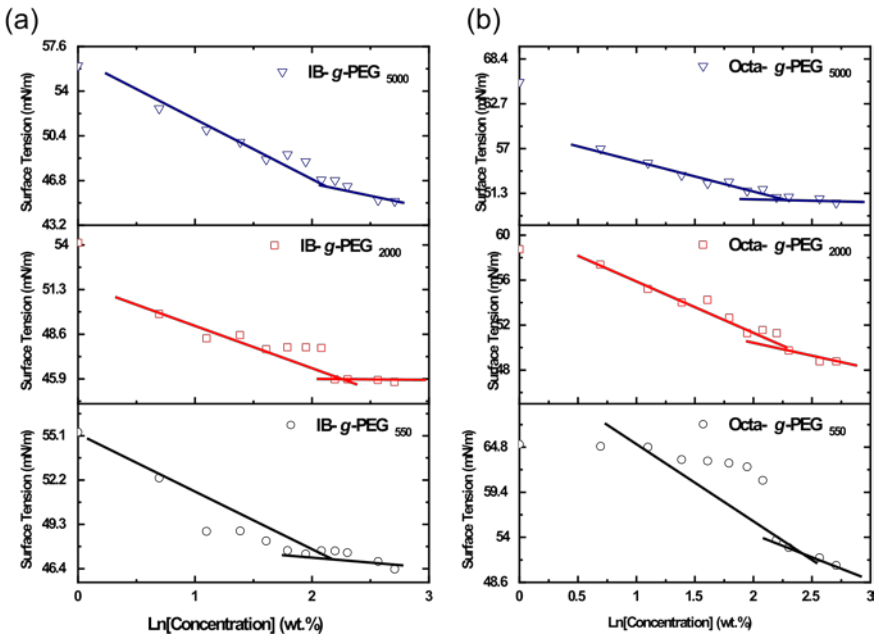

FIGURE A.11: Surface tension measurements of grafted polymer-brine (1 wt.% NaCl) droplet in air: (a) grafted PEG onto IB backbone, and (b) grafted PEG onto Octa backbone.

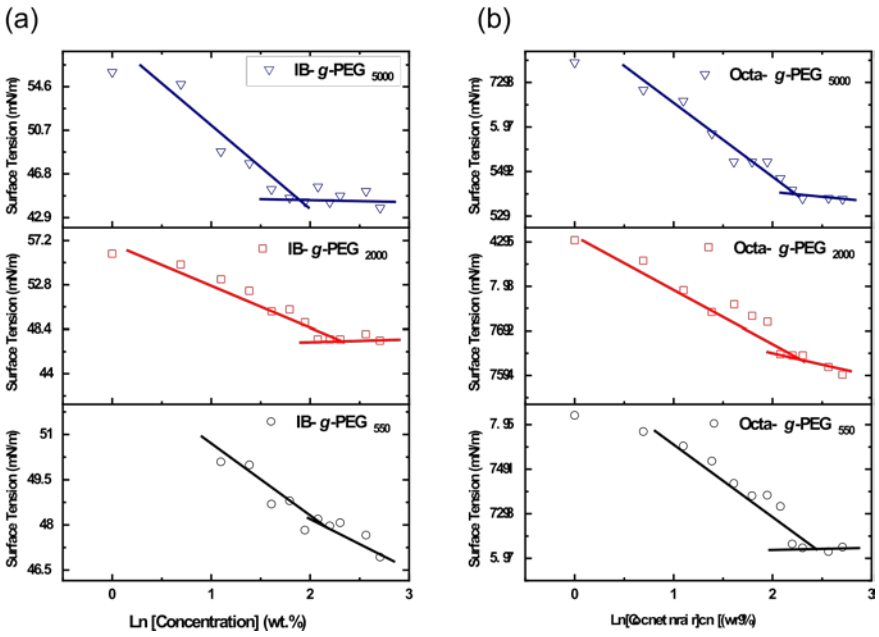

FIGURE A.12: Surface tension measurements of grafted polymer-brine (un dilute seawate) droplet in air: (a) grafted PEG onto IB backbone, and (b) grafted PEG onto Octa backbone.

TABLE A.1: DLS microemulsion size of grafted PEG onto IB and Octa backbone in decane with time.

		Size (nm) after Grafted		
		one hour	a day	a week
polymer Oil:water ratio				
(PEG-*g*-Octa)$_{550}$	50:50	303.1	66.55	16.14
(PEG-*g*-Octa)$_{550}$	25:75	149.6	91.18	68.51
(PEG-*g*-Octa)$_{550}$	10:90	63.67	69.48	Non
(PEG-*g*-Octa)$_{2000}$	50:50	53.73	68.32	81.31
(PEG-*g*-Octa)$_{2000}$	25:75	210.3	449.1	41.42
(PEG-*g*-Octa)$_{2000}$	10:90	110.1	179.7	Non
(PEG-*g*-Octa)$_{5000}$	50:50	22.13	207.8	241.4
(PEG-*g*-Octa)$_{5000}$	25:75	1052	124	116
(PEG-*g*-Octa)$_{5000}$	10:90	100.4	645.9	74.11
(PEG-*g*-IB)$_{550}$	50:50	1954	472.1	2415
(PEG-*g*-IB)$_{550}$	25:75	929	130.1	354.2
(PEG-*g*-IB)$_{550}$	10:90	83	93.24	184.7
(PEG-*g*-IB)$_{2000}$	50:50	293.6	1782	2395
(PEG-*g*-IB)$_{2000}$	25:75	199.2	71.99	444.1
(PEG-*g*-IB)$_{2000}$	10:90	125.2	122.1	561.6
(PEG-*g*-IB)$_{5000}$	50:50	436.9	242.9	2343
(PEG-*g*-IB)$_{5000}$	25:75	1013	160.9	214.9
(PEG-*g*-IB)$_{5000}$	10:90	997	604.2	1745
(PEG-*g*-Octa)$_{550}$NaCl	50:50	Non	Non	Non
(PEG-*g*-Octa)$_{550}$NaCl	25:75	2059	Non	62.83
(PEG-*g*-Octa)$_{550}$NaCl	10:90	704	469.5	2021

(PEG-*g*-Octa)$_{2000}$NaCl	50:50	106.2	54.82	Non

Table A.1 continued from previous page

		Size (nm) after		
		one hour	a day	a week
(PEG-*g*-Octa)$_{2000}$NaCl	25:75	254.3	74.99	279.8
(PEG-*g*-Octa)$_{2000}$NaCl	10:90	230.1	101.4	40.21
(PEG-*g*-Octa)$_{5000}$NaCl	50:50	Non	Non	Big
(PEG-*g*-Octa)$_{5000}$NaCl	25:75	2137	1140	2892
(PEG-*g*-Octa)$_{2000}$NaCl	10:90	155.7	261.9	845.1
(PEG-*g*-IB)$_{550}$ NaCl	50:50	Non	Non	Non
(PEG-*g*-IB)$_{550}$ NaCl	25:75	Non	Non	Non
(PEG-*g*-IB)$_{550}$ NaCl	10:90	Non	Non	Non
(PEG-*g*-IB)$_{2000}$ NaCl	50:50	Non	Non	1990
(PEG-*g*-IB)$_{2000}$ NaCl	25:75	Non	1124	1970
(PEG-*g*-IB)$_{2000}$ NaCl	10:90	2403	4642	2142
(PEG-*g*-IB)$_{5000}$NaCl	50:50	1521	Non	2811
(PEG-*g*-IB)$_{5000}$NaCl	25:75	1310	1649	2875
(PEG-*g*-IB)$_{5000}$NaCl	10:90	1673	861.2	2239

Grafted polymer Oil:water ratio

TABLE A.2: DLS microemulsion size of grafted PEG onto IB and Octa backbone in hexadecane with time.

		Size (nm) after Grafted		
		one hour	a day	a week
polymer Oil:water ratio				
(PEG-*g*-Octa)$_{550}$	50:50	112.7	85.9	26.08
(PEG-*g*-Octa)$_{550}$	25:75	19.91	42.5	42.5
(PEG-*g*-Octa)$_{550}$	10:90	27.81	18.79	32.38
(PEG-*g*-Octa)$_{2000}$	50:50	107.5	148.6	(404.1, 3829)

Table A.2 continued from previous page

		Size (nm) after Grafted		
		one hour	a day	a week
polymer Oil:water ratio				
(PEG-*g*-Octa)$_{2000}$	25:75	102.1	58.75	38.12
(PEG-*g*-Octa)$_{2000}$	10:90	47.25	42.32	24.65
(PEG-*g*-Octa)$_{5000}$	50:50	411.3	334.9	(555.1, 108.3)
(PEG-*g*-Octa)$_{5000}$	25:75	78.32	138.5	144.4
(PEG-*g*-Octa)$_{5000}$	10:90	62.71	51.57	26.52
(PEG-*g*-IB)$_{550}$	50:50	62.66	187.3	(766.66, 93.07)
(PEG-*g*-IB)$_{550}$	25:75	20.98	23.54	15.78
(PEG-*g*-IB)$_{550}$	10:90	23.79	20.08	45.66
(PEG-*g*-IB)$_{2000}$	50:50	20.21	87.5	(450, 55.27)
(PEG-*g*-IB)$_{2000}$	25:75	24.43	36.75	10.23
(PEG-*g*-IB)$_{2000}$	10:90	51.61	38.65	10.55
(PEG-*g*-IB)$_{5000}$	50:50	267.1	133.1	650
(PEG-*g*-IB)$_{2000}$	25:75	45.47	114.1	39.34

$(PEG\text{-}g\text{-}IB)_{2000}$	10:90	34.26	17.04	50.34
$(PEG\text{-}g\text{-}Octa)_{550}NaCl$	50:50	big	3522	2038
$(PEG\text{-}g\text{-}Octa)_{550}NaCl$	25:75	2683	4634	1887
$(PEG\text{-}g\text{-}Octa)_{550}NaCl$	10:90	949.1	733.4	718.7
$(PEG\text{-}g\text{-}Octa)_{2000}NaCl$	50:50	357.8	407.9	735.7
$(PEG\text{-}g\text{-}Octa)_{2000}NaCl$	25:75	47.18	68.51	112.5
$(PEG\text{-}g\text{-}Octa)_{2000}NaCl$	10:90	26.79	21.1	57.86
$(PEG\text{-}g\text{-}Octa)_{5000}NaCl$	50:50	464.9	3199	2186
$(PEG\text{-}g\text{-}Octa)_{5000}NaCl$	25:75	1782	Non	1835
$(PEG\text{-}g\text{-}Octa)_{5000}NaCl$	10:90	51.42	1717	693.7

Table A.2 continued from previous page

Size (nm) after Grafted polymer		Oil:water ratio		
		one hour	a day	a week
$(PEG\text{-}g\text{-}IB)_{550}NaCl$	50:50	Non	Non	Non
$(PEG\text{-}g\text{-}IB)_{550}NaCl$	25:75	Non	Non	Non
$(PEG\text{-}g\text{-}IB)_{550}NaCl$	10:90	Non	Non	Non
$(PEG\text{-}g\text{-}IB)_{2000}NaCl$	50:50	241	351.3	(188.9, 1015)
$(PEG\text{-}g\text{-}IB)_{2000}NaCl$	25:75	661	413.4	285.5
$(PEG\text{-}g\text{-}IB)_{2000}NaCl$	10:90	323.6	125.6	671
$(PEG\text{-}g\text{-}IB)_{5000}NaCl$	50:50	80.31	117	312.3
$(PEG\text{-}g\text{-}IB)_{5000}NaCl$	25:75	4360	1156	2444
$(PEG\text{-}g\text{-}IB)_{5000}NaCl$	10:90	293.3	1450	1564

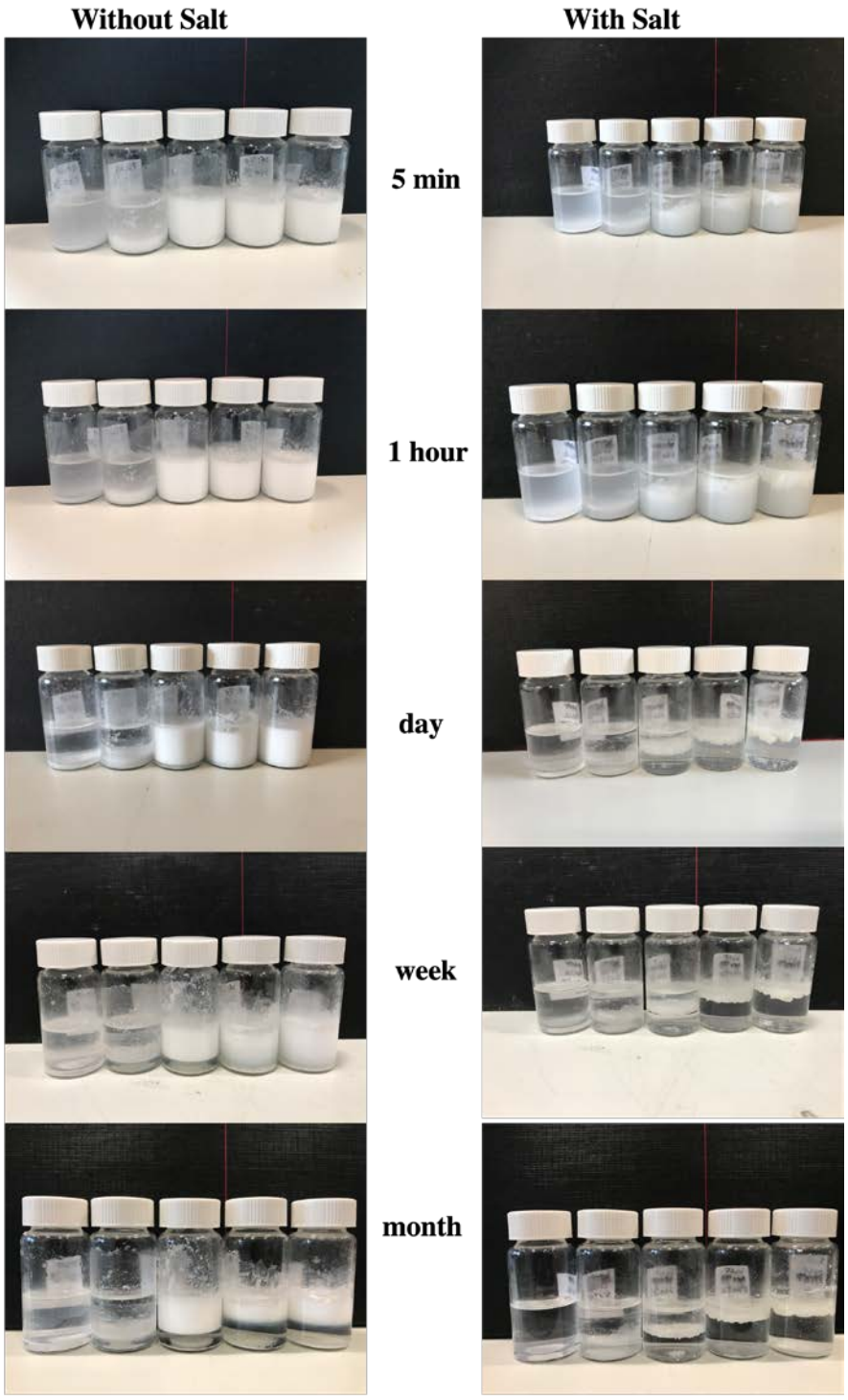

FIGURE A.13: A photo graphical images of emulsions made of 0.3 wt.% of grafted IB backbone onto PEG_{550} in hexadecane with and without salt, from left to right: 90:10, 75:25, 50:50, 25:75, and 10:90 water to oil ratios for different tested times at 25 C.

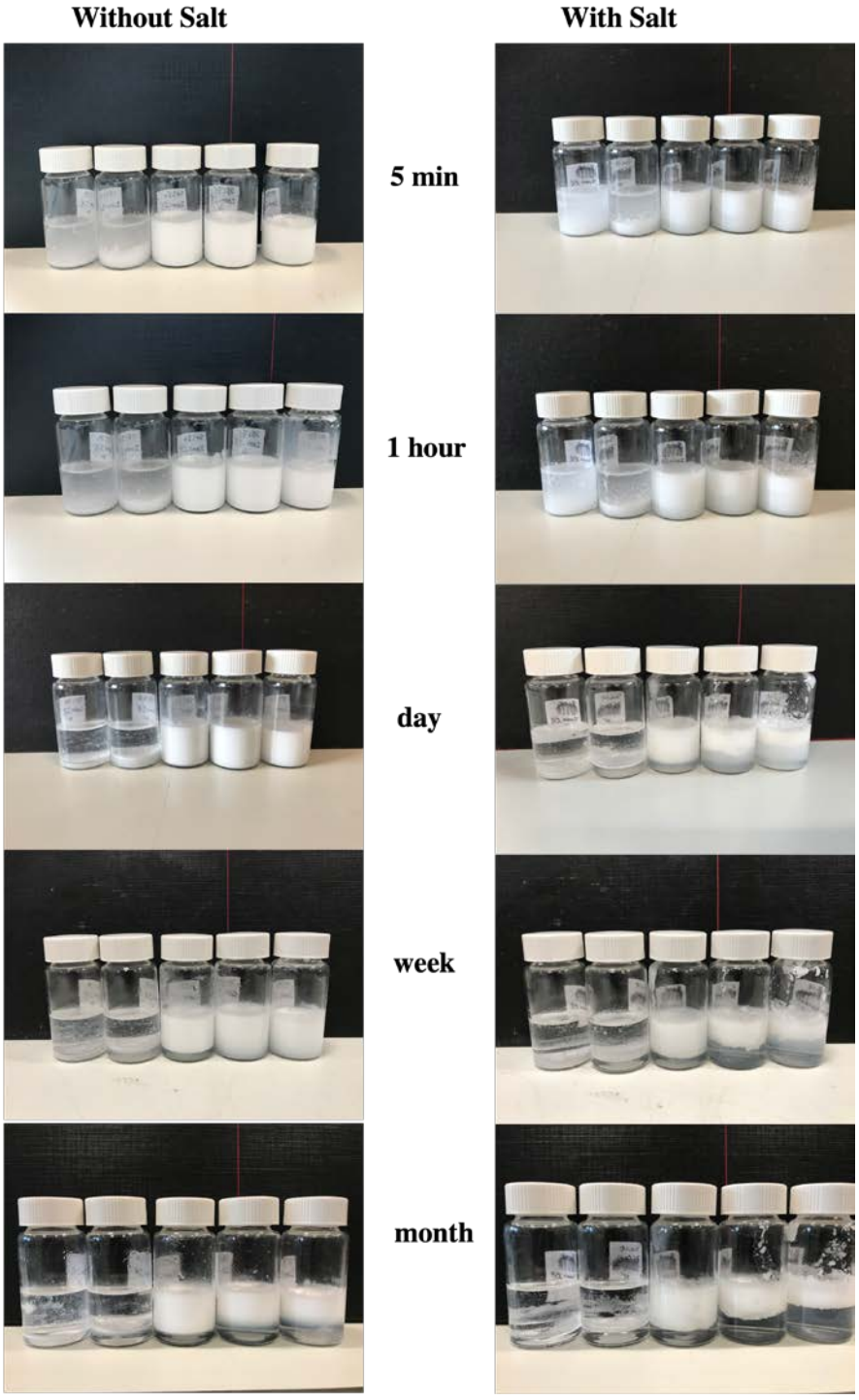

FIGURE A.14: A photo graphical images of emulsions made of 0.3 wt.% of grafted IB backbone onto PEG_{2000} in hexadecane with and without salt, from left to right: 90:10, 75:25, 50:50, 25:75, and 10:90 water to oil ratios for different tested times at 25 C.

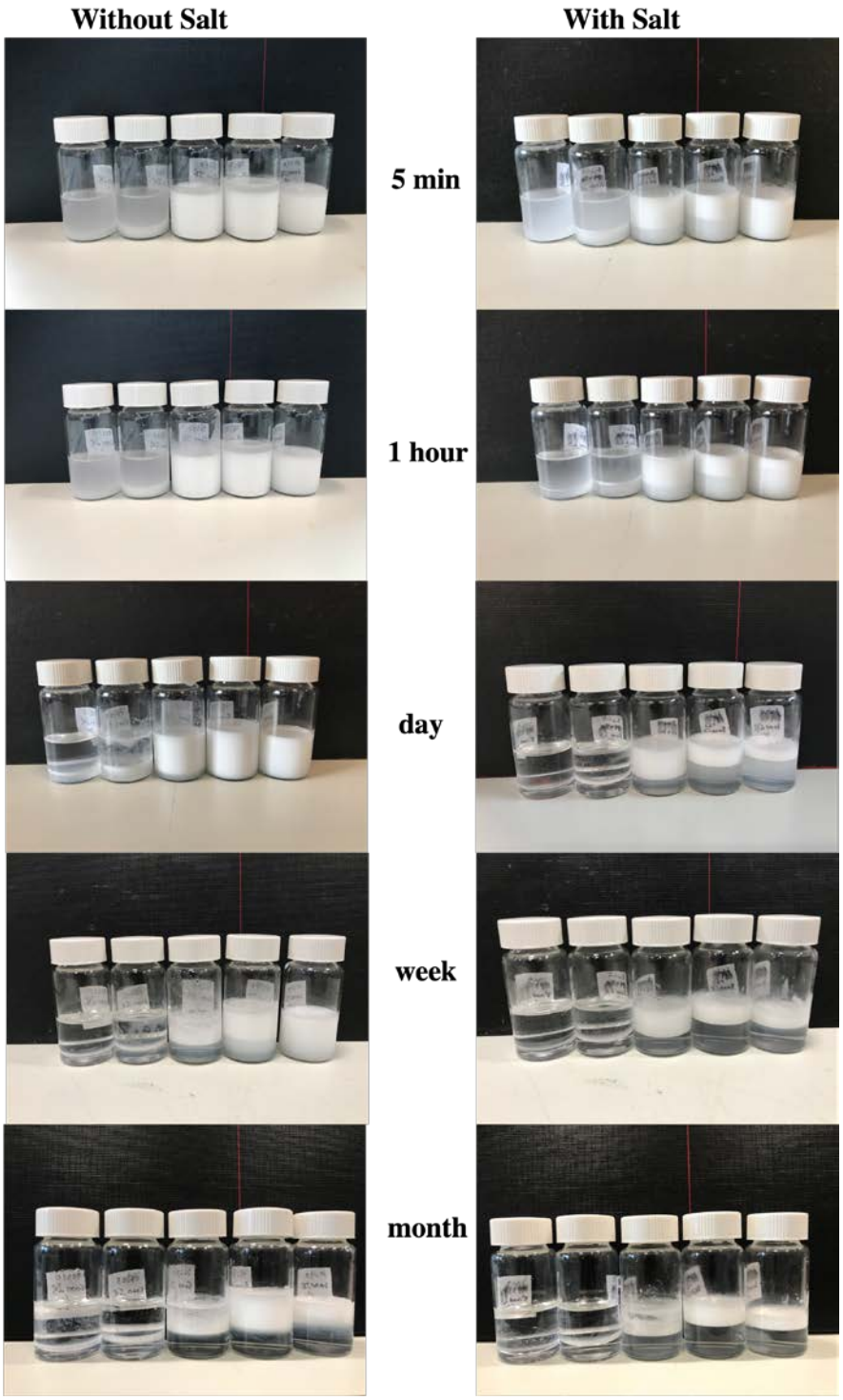

FIGURE A.15: A photo graphical images of emulsions made of 0.3 wt.% of grafted IB backbone onto PEG_{5000} in hexadecane with and without salt, from left to right: 90:10, 75:25, 50:50, 25:75, and 10:90 water to oil ratios for different tested times at 25 C.

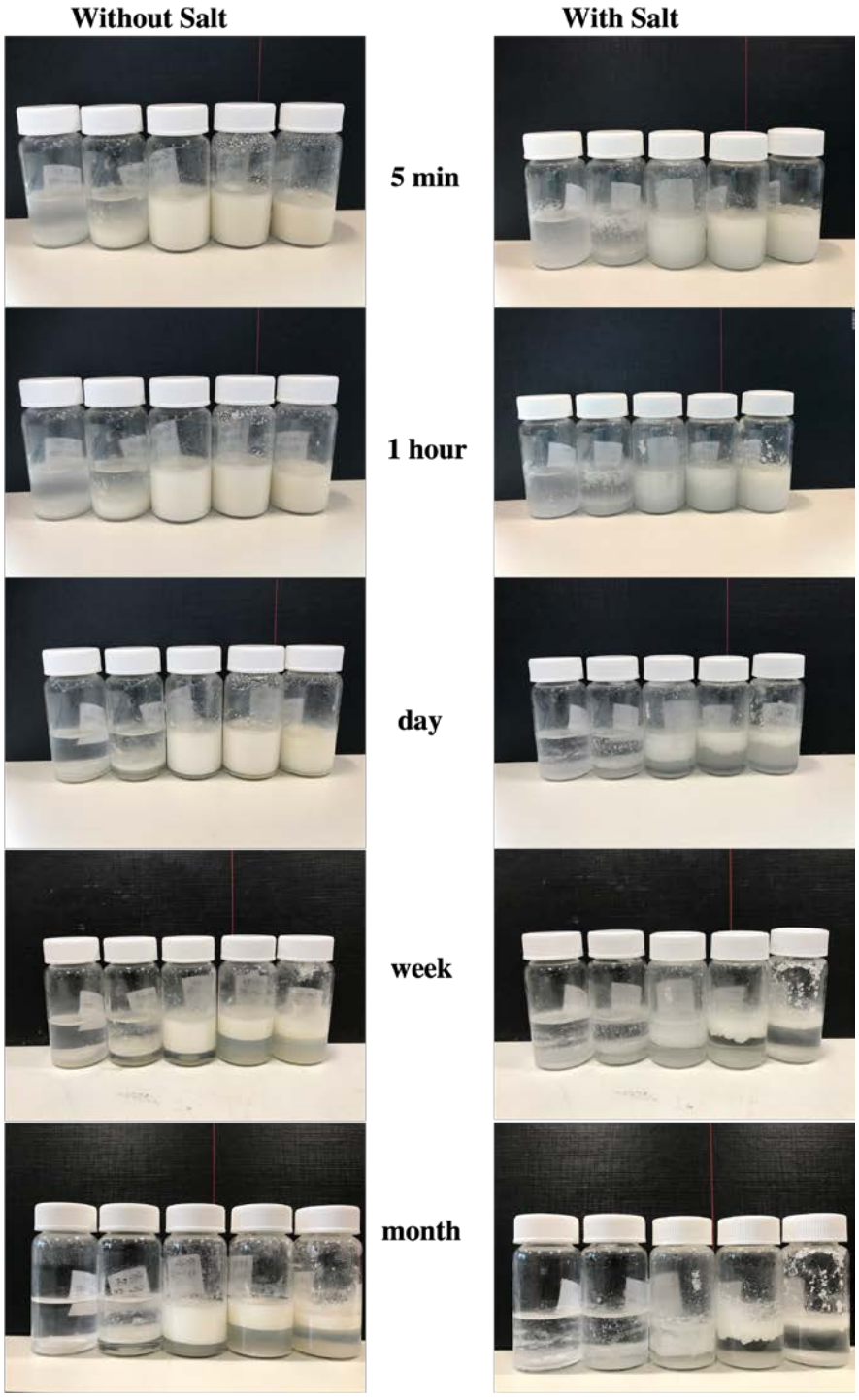

FIGURE A.16: A photo graphical images of emulsions made of 0.3 wt.% of grafted IB backbone onto PEG_{550} in decane with and without salt, from left to right: 90:10, 75:25, 50:50, 25:75, and 10:90 water to oil ratios for different tested times at 25 C.

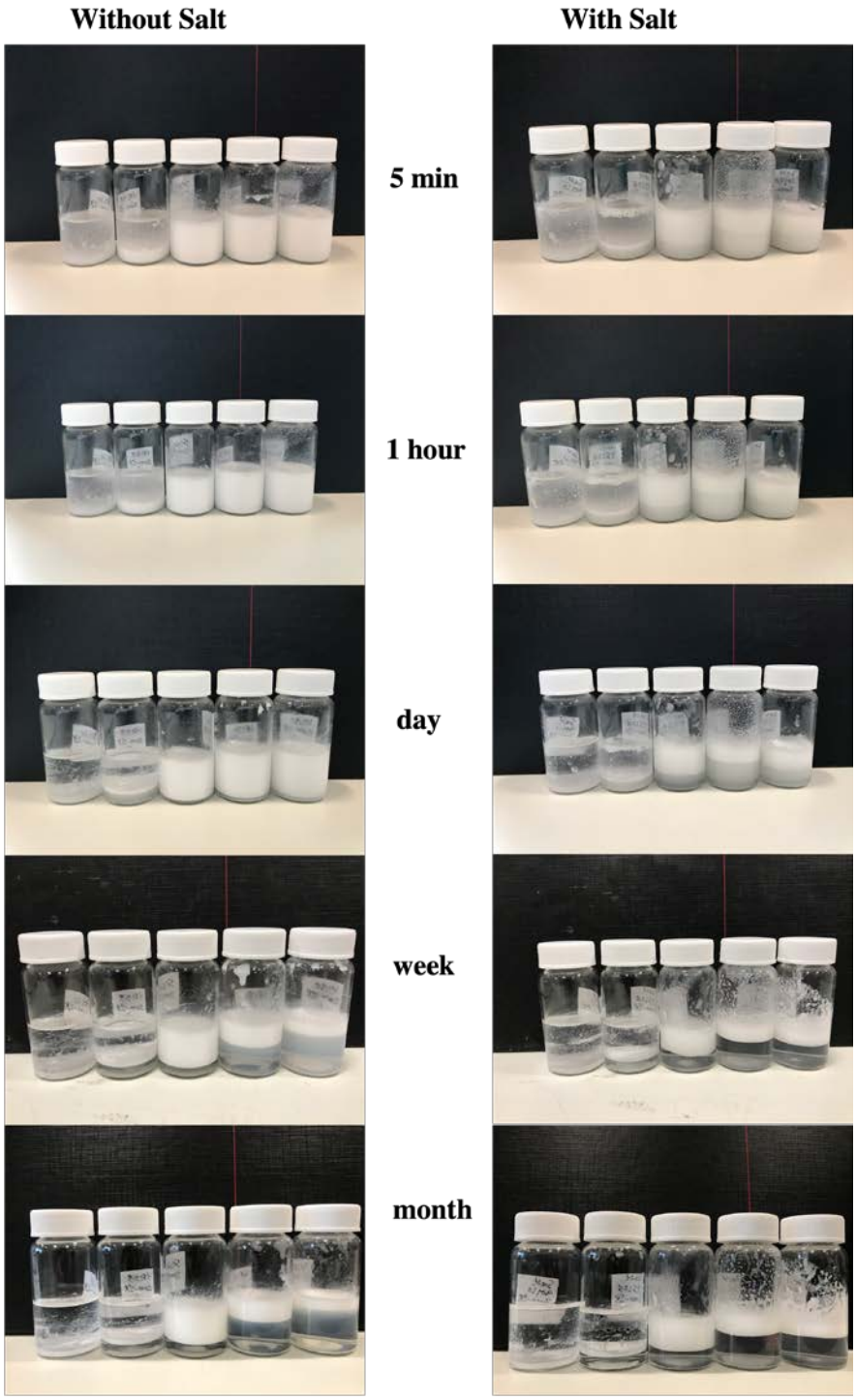

FIGURE A.17: A photo graphical images of emulsions made of 0.3 wt.% of grafted IB backbone onto PEG_{2000} in decane with and without salt, from left to right: 90:10, 75:25, 50:50, 25:75, and 10:90 water to oil ratios for different tested times at 25 C.

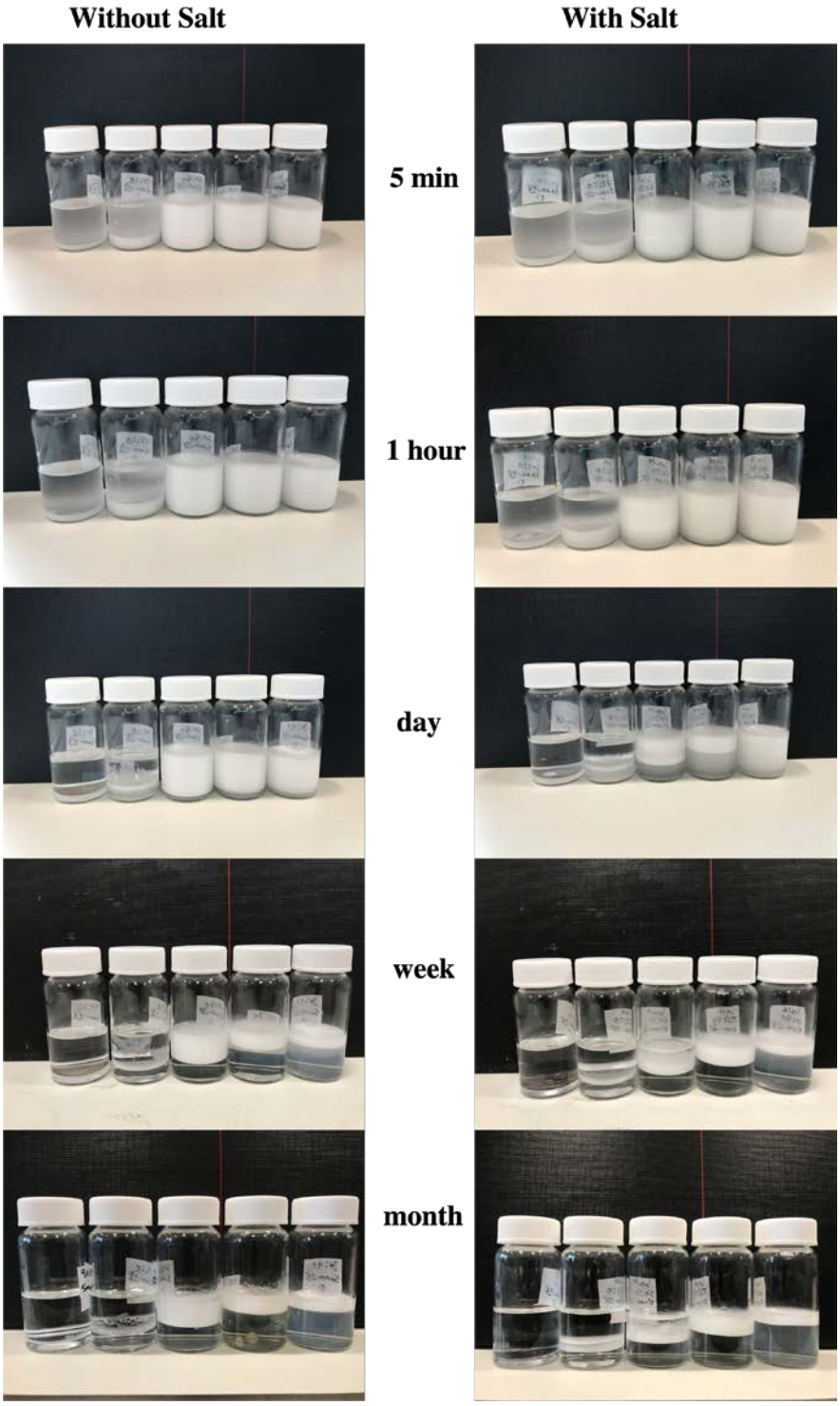

FIGURE A.18: A photo graphical images of emulsions made of 0.3 wt.% of grafted IB backbone onto PEG_{5000} in decane with and without salt, from left to right: 90:10, 75:25, 50:50, 25:75, and 10:90 water to oil ratios for different tested times at 25 C.

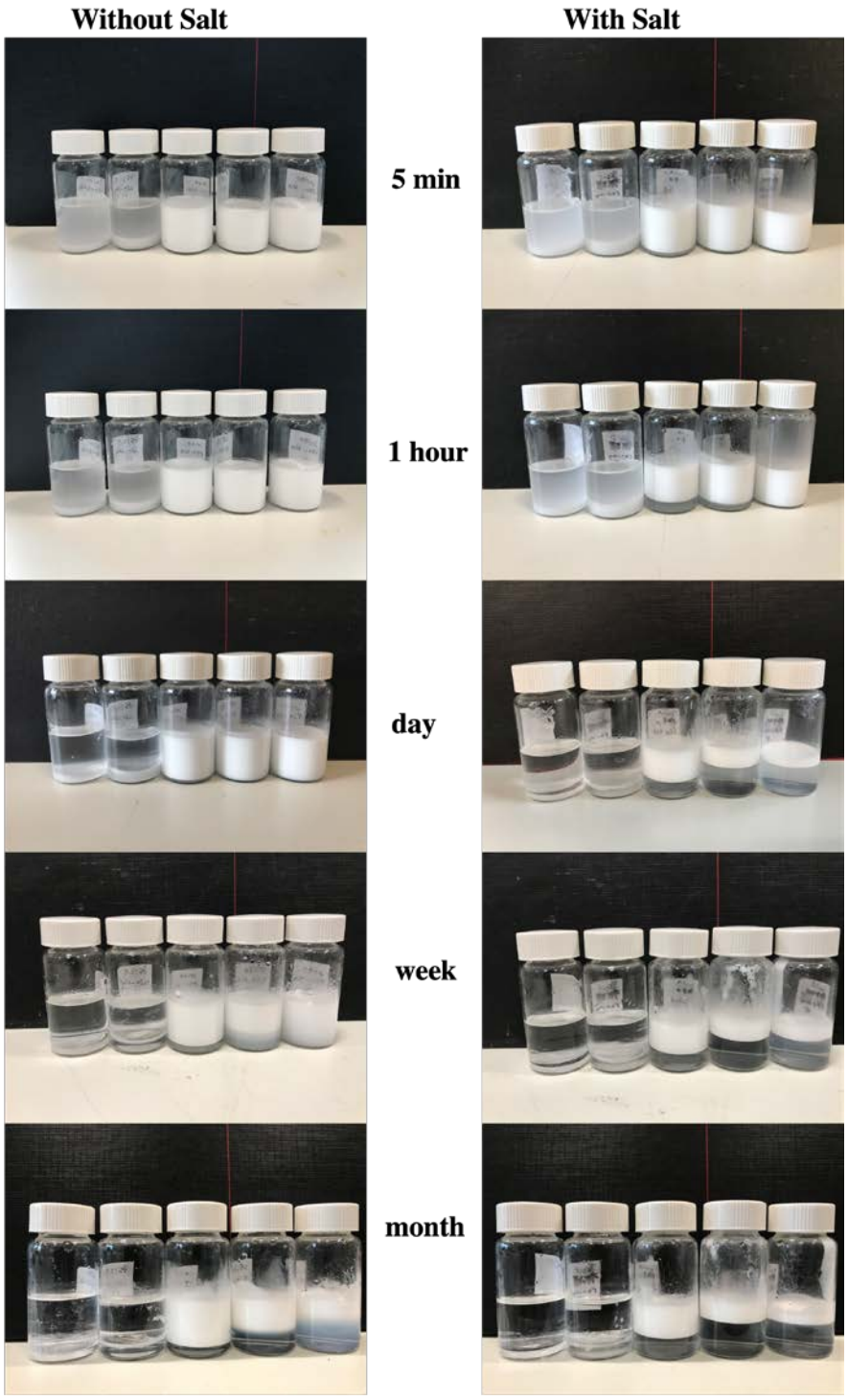

FIGURE A.19: A photo graphical images of emulsions made of 0.3 wt.% of grafted Octa backbone onto PEG_{550} in hexadecane with and without salt, from left to right: 90:10, 75:25, 50:50, 25:75, and 10:90 water to oil ratios for different tested times at 25 C.

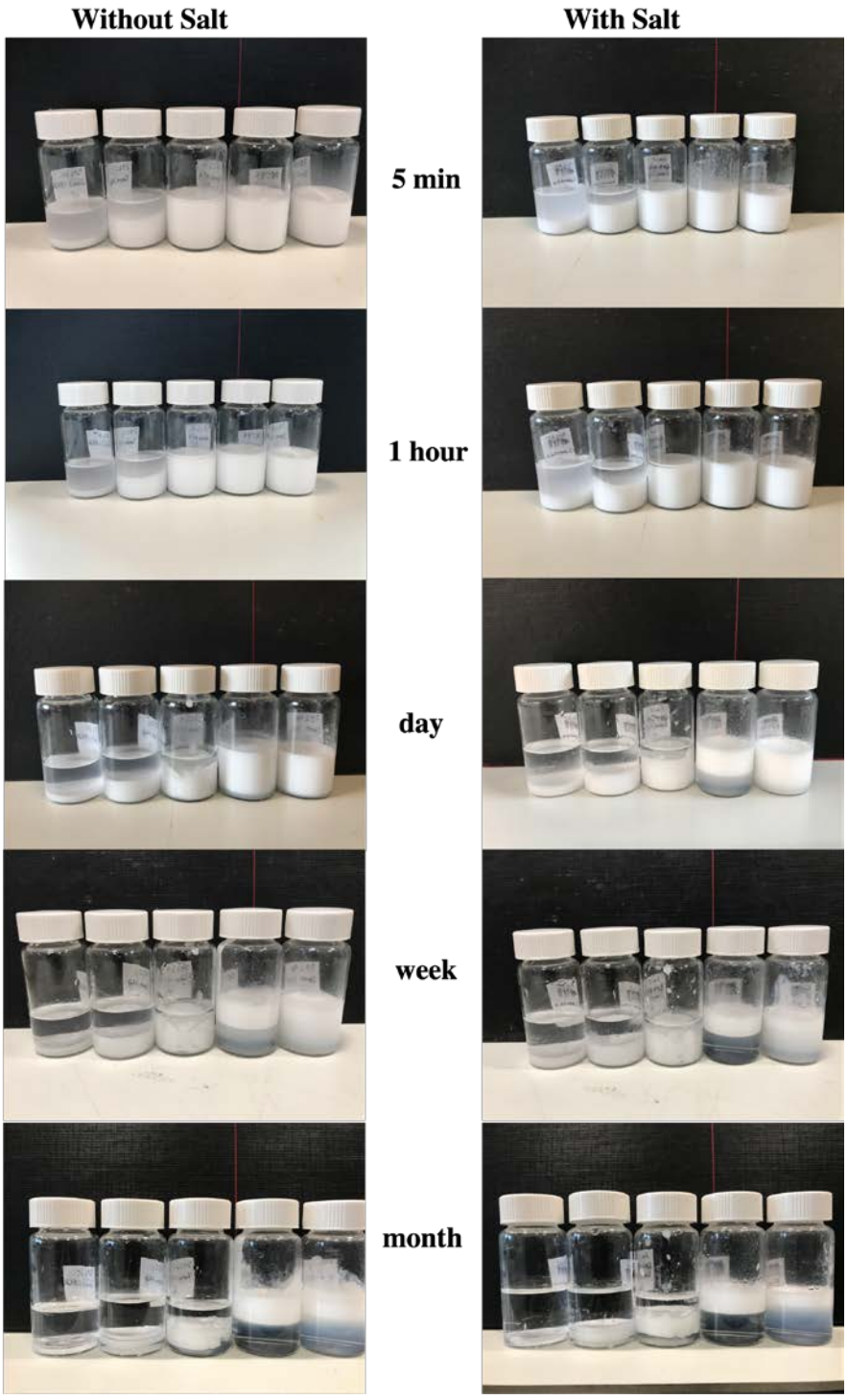

FIGURE A.20: A photo graphical images of emulsions made of 0.3 wt.% of grafted Octa backbone onto PEG_{2000} in hexadecane with and without salt, from left to right: 90:10, 75:25, 50:50, 25:75, and 10:90 water to oil ratios for different tested times at 25 C.

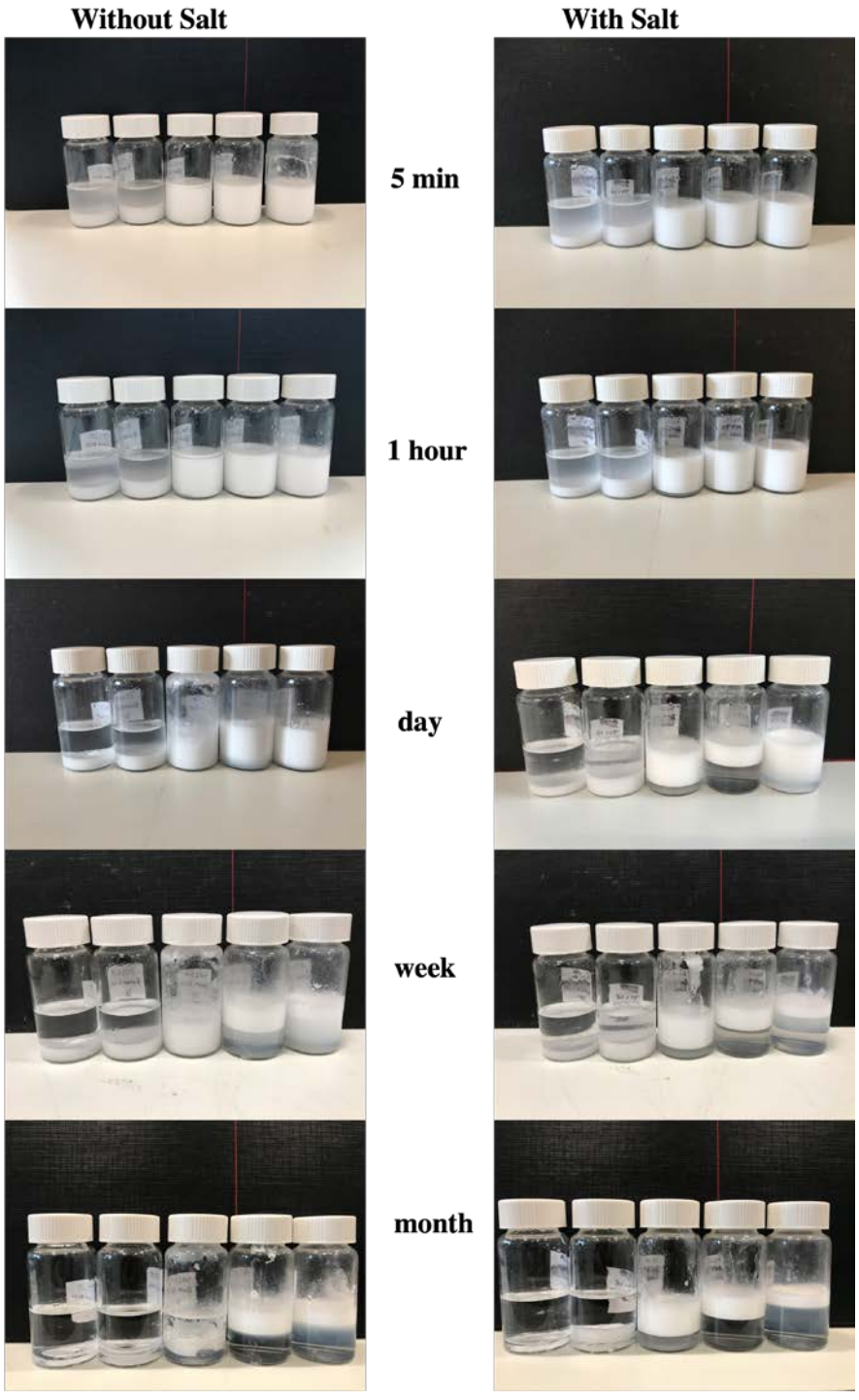

FIGURE A.21: A photo graphical images of emulsions made of 0.3 wt.% of grafted Octa backbone onto PEG_{5000} in hexadecane with and without salt, from left to right: 90:10, 75:25, 50:50, 25:75, and 10:90 water to oil ratios for different tested times at 25 C.

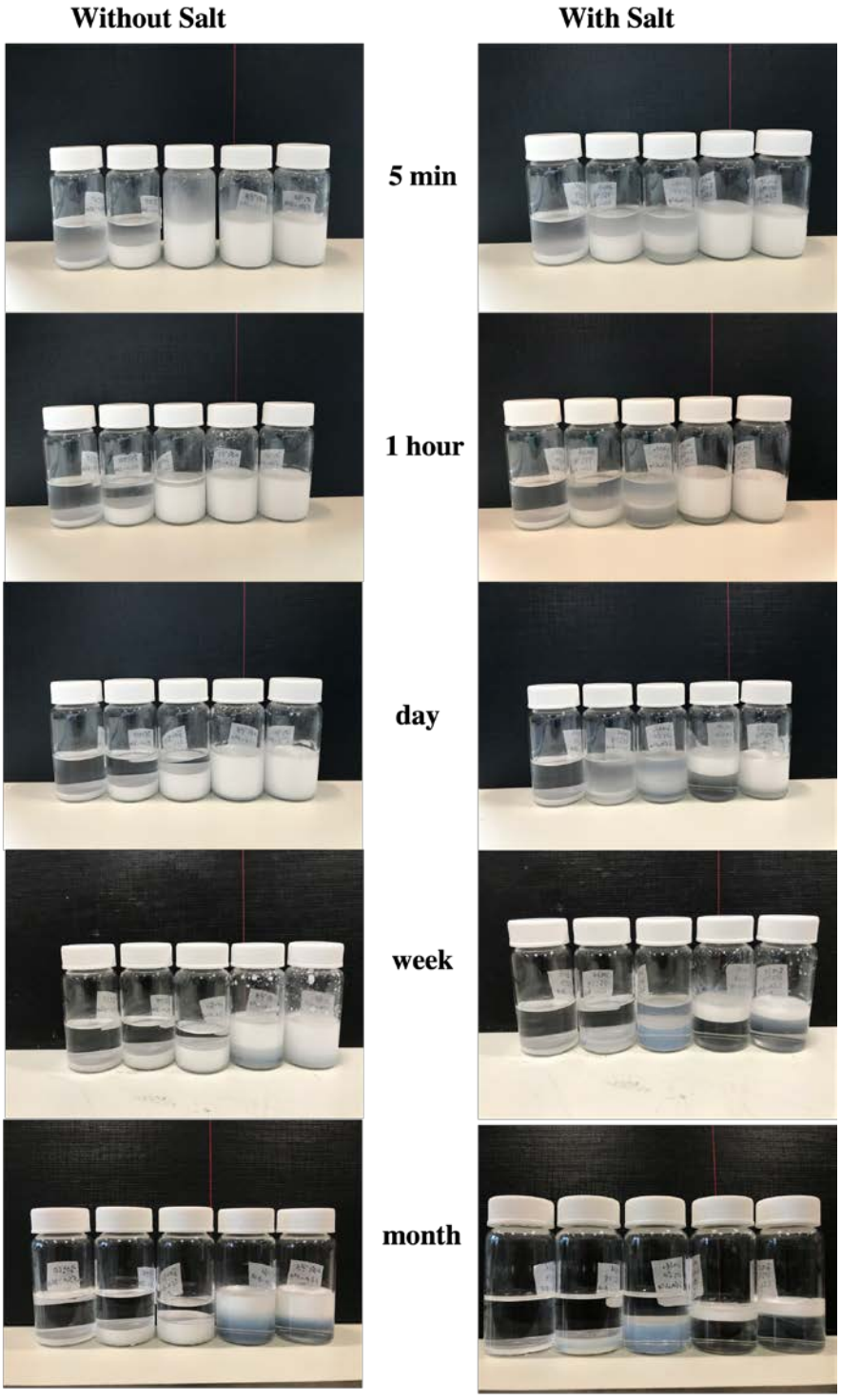

FIGURE A.22: A photo graphical images of emulsions made of 0.3 wt.% of grafted Octa backbone onto PEG_{550} in decane with and without salt, from left to right: 90:10, 75:25, 50:50, 25:75, and 10:90 water to oil ratios for different tested times at 25 C.

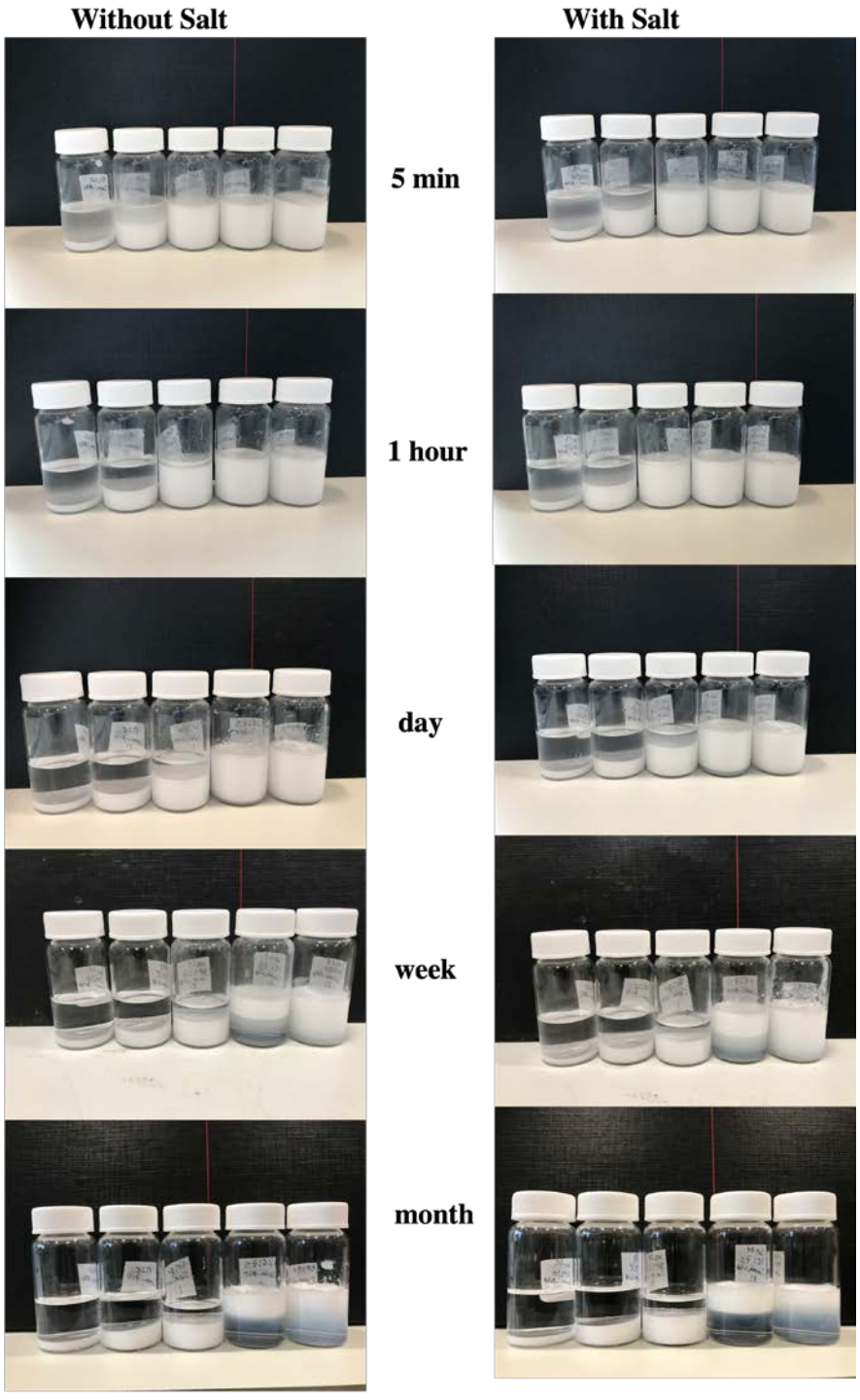

FIGURE A.23: A photo graphical images of emulsions made of 0.3 wt.% of grafted Octa backbone onto PEG_{2000} in decane with and without salt, from left to right: 90:10, 75:25, 50:50, 25:75, and 10:90 water to oil ratios for different tested times at 25 C.

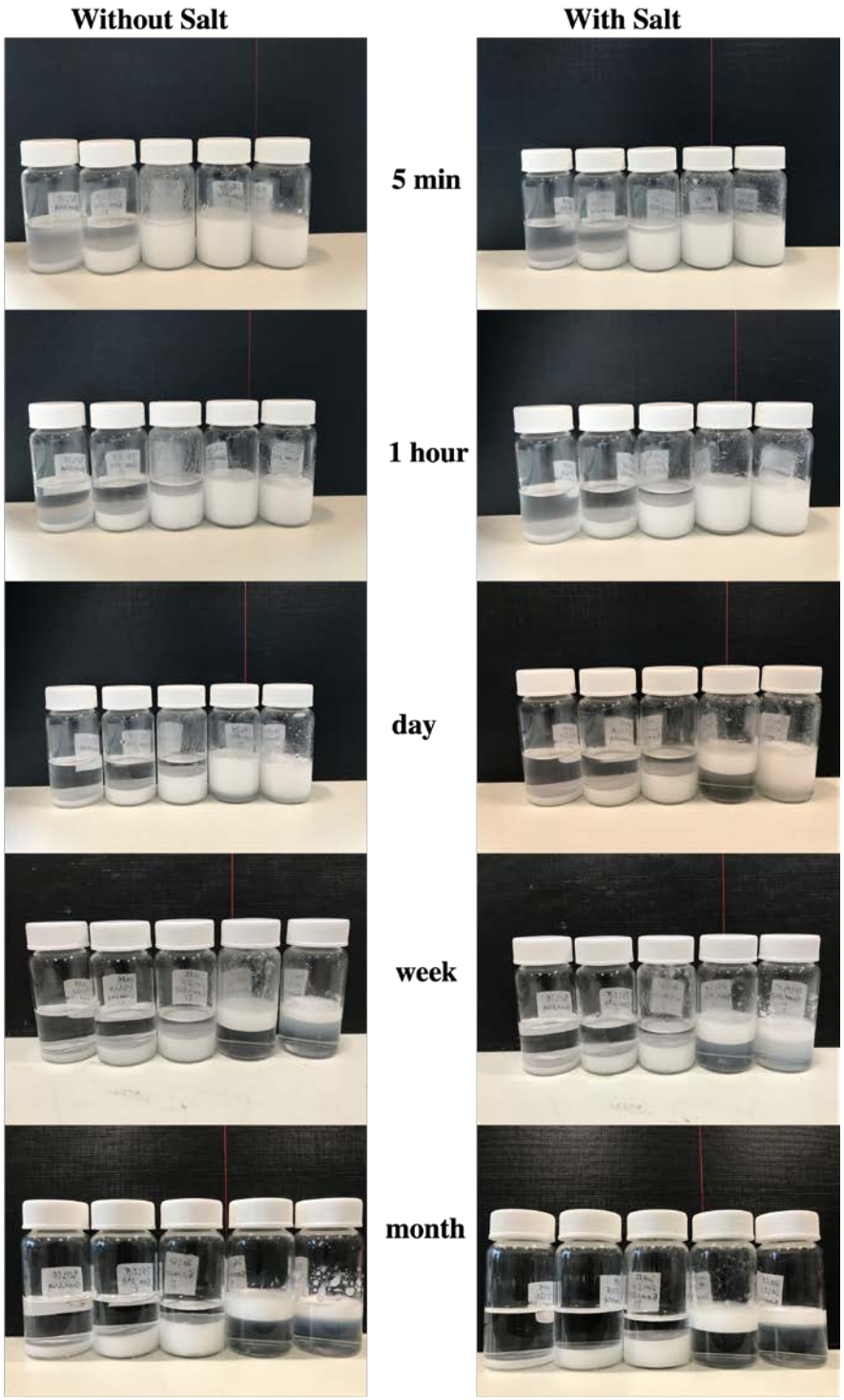

FIGURE A.24: A photo graphical images of emulsions made of 0.3 wt.% of grafted Octa backbone onto PEG_{5000} in decane with and without salt, from left to right: 90:10, 75:25, 50:50, 25:75, and 10:90 water to oil ratios for different tested times at 25 C.

References

Abhishek, Rockey, Aly A Hamouda, and Ivan Murzin (2018). “Adsorption of silica nanoparticles and its synergistic effect on fluid/rock interactions during low salinity flooding in sandstones”. In: *Colloids Surf , A* 555, pp. 397–406.

Ahmed, Tarek et al. (2018). *Reservoir engineering handbook*. Gulf professional publishing.

Al-Anssari, Sarmad et al. (2018). “Wettability of nanofluid-modified oil-wet calcite at reservoir conditions”. In: *Fuel* 211, pp. 405–414.

Al-Shatty, Wafaa, Shirin Alexander, and Andrew R Barron (2022). “Stability of carboxylic acid modified alumina nanoparticles for enhanced oil recovery applications”. In: *AIP Conference*, pp. 1–8.

Al-Shatty, Wafaa et al. (2017). “Tunable surface properties of aluminum oxide nanoparticles from highly hydrophobic to highly hydrophilic”. In: *Acs Omega* 2.6, pp. 2507–2514.

Alexander, Shirin et al. (2014). “Aggregation behavior of polyisoprene–pluronic graft copolymers in selective solvents”. In: *Langmuir* 30.20, pp. 5747–5754.

Almajid, Muhammad M and Anthony R Kovscek (2016). “Pore-level mechanics of foam generation and coalescence in the presence of oil”. In: *Adv. Colloid Interface Sci* 233, pp. 65–82.

Alnarabiji, Mohamad Sahban et al. (2018). “Nanofluid enhanced oil recovery using induced ZnO nanocrystals by electromagnetic energy: Viscosity increment”. In: *Fuel* 233, pp. 632–643.

Alomair, Osamah A, Khaled M Matar, and Yousef H Alsaeed (2014). “Nanofluids application for heavy oil recovery”. In: *SPE Asia Pacific oil & gas conference and exhibition*. OnePetro.

Alvarez-Berrios, Merlis P et al. (2018). “Effect of the surface charge of silica nanoparticles on oil recovery: wettability alteration of sandstone cores and imbibition experiments”. In: *Int. Nano Lett* 8.3, pp. 181–188.

Amirsadat, Seyyed Ahmadreza et al. (2017). “Investigating the effect of nano-silica on efficiency of the foam in enhanced oil recovery”. In: *Korean J Chem Eng* 34.12, pp. 3119–3124.

Anderson, William (1986). “Wettability literature survey-part 2: Wettability measurement”. In: *J. Pey. Technol.* 38.11, pp. 1246–1262.

Anghel, DF et al. (2007). “The aggregation of nonionic surfactants in the presence of poly (methacrylic acid)”. In: *Colloid Polym Sci* 285.7, pp. 771–779.

Archer, John S and Colin G Wall (2012). *Petroleum engineering: principles and practice*. Springer Science & Business Media.

Arnold, Owen et al. (2014). “Mantid—Data analysis and visualization package for neutron scattering and μ SR experiments”. In: *Nucl. Instrum. Methods Phys. Res.* 764, pp. 156–166.

Avraam, DG and AC Payatakes (1999). “Flow mechanisms, relative permeabilities, and coupling effects in steady-state two-phase flow through porous media. The case of strong wettability”. In: *Ind. Eng. Chem. Res* 38.3, pp. 778–786.

Bayat, Ali Esfandyari et al. (2014). “Impact of metal oxide nanoparticles on enhanced oil recovery from limestone media at several temperatures”. In: *Energy & fuels* 28.10, pp. 6255–6266.

Bettahar, Faiza et al. (2021). “Tough hydrogels based on maleic anhydride, bulk properties study and microfiber formation by electrospinning”. In: *Polymers* 13.6, p. 972.

Bhattacharya, Amitava et al. (1994). “Studies on the photodegradation of carbofuran”. In: *Chemosphere* 29.2, pp. 155–162.

Bielas, Rafał et al. (2020). “The potential of magnetic heating for fabricating Pickering-emulsion-based capsules”. In: *Colloids Surf , B* 192, p. 111070.

Binks, Bernard P et al. (2010). “Drop sizes and particle coverage in emulsions stabilised solely by silica nanoparticles of irregular shape”. In: *Phys Chem Chem Phys* 12.38, pp. 11967–11974.

Bjorlykke, Knut (2010). *Petroleum geoscience: From sedimentary environments to rock physics*. Springer Science & Business Media.

Bontempo, Debora and Heather D Maynard (2005). “Streptavidin as a macroinitiator for polymerization: in situ protein- polymer conjugate formation”. In: *J Am Chem Soc* 127.18, pp. 6508–6509.

Bornaee, Amir Hossein et al. (2014). “Oil-in-water Pickering emulsions stabilized with functionalized multi-walled carbon nanotube/silica nanohybrids in the presence of high concentrations of cations in water”. In: *J Ind Eng Chem* 20.4, pp. 1720–1726.

Braun, Larissa et al. (2017). “Polymers and surfactants at fluid interfaces studied with specular neutron reflectometry”. In: *Adv Colloid Interface Sci* 247, pp. 130–148.

Brown, Glenn O (2004). “Jules Dupuit’s Contributions in Water Resources”. In: *Water Res.* Pp. 104–110.

Buchgraber, M et al. (2012). “Creation of a dual-porosity micromodel for pore-level visualization of multiphase flow”. In: *J Petrol Sci Eng* 86, pp. 27–38.

Burcik, Emil J (1957). *Properties of petroleum reservoir fluids*. Springer.

Caldelas, Federico et al. (2011). “Factors governing distance of nanoparticle propagation in porous media”. In: *SPE production and operations symposium*. OnePetro.

Campana, Mario (2012). “Structural studies of surfactants at interfaces”. PhD thesis. QMUL.

Cantrell, Dave L and Royal M Hagerty (1999). “Microporosity in arab formation carbonates, Saudi Arabia”. In: *GeoArabia* 4.2, pp. 129–154.

Cao, Jie et al. (2019). “Studies on the rheological properties of amphiphilic nanosilica and a partially hydrolyzed polyacrylamide hybrid for enhanced oil recovery”. In: *Chem Eng Sci* 206, pp. 146–155.

Chatenever, Alfred and John C Calhoun (1952). “Visual examinations of fluid behavior in porous media-part i”. In: *J Petrol Technol* 4.06, pp. 149–156.

Chen, Cheng-Wei Aaron (2014). *Functional Maturation of Human Pluripotent Stem Cell Derived Cardiomyocytes using Engineered Multi-scale Biomimetic Structures*. University of California, Irvine.

Cheng, J-T et al. (2004). “Linking pressure and saturation through interfacial areas in porous media”. In: *Geophys Res Lett* 31.8.

Cheraghian, Goshtasp et al. (2014). “Adsorption polymer on reservoir rock and role of the nanoparticles, clay and SiO2”. In: *Int. Nano Lett* 4.3, pp. 1–8.

Cheraghian, Goshtasp et al. (2017). “Silica nanoparticle enhancement in the efficiency of surfactant flooding of heavy oil in a glass micromodel”. In: *Ind. Eng. Chem. Res* 56.30, pp. 8528–8534.

Chung, Dae-won and Jong Choo Lim (2009). “Study on the effect of structure of polydimethylsiloxane grafted with polyethyleneoxide on surface activities”. In: *Colloids Surf , A* 336.1-3, pp. 35–40.

Chung, Eunhyea et al. (2012). “Interaction of silica nanoparticles with a flat silica surface through neutron reflectometry”. In: *Environ. Sci. Technol.* 46.8, pp. 4532–4538.

Cosgrove, Terence et al. (2012). “Polymeric materials having reduced tack, methods of making the materials and chewing gum compositions containing such materials”. In: US Patent 8,211,980.

Cottin, Christophe, Hugues Bodiguel, and Annie Colin (2010). “Drainage in twodimensional porous media: From capillary fingering to viscous flow”. In: *Phys Rev E* 82.4, p. 046315.

Dai, Caili et al. (2018a). “Emulsion behavior control and stability study through decorating silica nano-particle with dimethyldodecylamine oxide at n-heptane/water interface”. In: *Chem Eng Sci* 179, pp. 73–82.

Dai, Lei et al. (2018b). “Characterization of Pickering emulsion gels stabilized by zein/gum arabic complex colloidal nanoparticles”. In: *Food Hydrocolloid* 74, pp. 239–248.

Dargahi-Zaboli, Maliheh, Eghbal Sahraei, and Behzad Pourabbas (2017). “Hydrophobic silica nanoparticle-stabilized invert emulsion as drilling fluid for deep drilling”. In: *Pet Sci* 14.1, pp. 105–115.

Dehghan Monfared, Abolfazl et al. (2018). “Wettability alteration modeling for oilwet calcite/silica nanoparticle system using surface forces analysis: contribution of DLVO versus non-DLVO interactions”. In: *Ind. Eng. Chem. Res* 57.43, pp. 14482–14492.

Delcea, Mihaela and Christiane A Helm (2019). “X-ray and neutron reflectometry of thin films at liquid interfaces”. In: *Langmuir* 35.26, pp. 8519–8530.

Dillan, KW (1984). “Factors affecting oil/water interfacial tension in detergent systems: nonionic surfactants and nonpolar oils”. In: *J Am Oil Chem Soc* 61.7, pp. 1278–1284.

Donaldson, Erle C, Rex D Thomas, and Philip B Lorenz (1969). “Wettability determination and its effect on recovery efficiency”. In: *Soc Petrol Eng J* 9.01, pp. 13– 20.

Du, Dai-jun et al. (2018). “Solution properties and displacement characteristics of core–shell hyperbranched associative polyacrylamide for enhanced oil recovery”. In: *Energy & fuels* 32.8, pp. 8154–8166.

Duque, Juan G et al. (2010). “Diameter-dependent solubility of single-walled carbon nanotubes”. In: *ACS nano* 4.6, pp. 3063–3072.

Ebeltoft, E et al. (1998). “A novel experimental apparatus for determination of threephase relative permeabilities at reservoir conditions”. In: *J Petrol Sci Eng* 19.1-2, pp. 119–132.

Ehrfeld, W (1987). “Fabrication of Microstructures using the LIGA Prosess”. In: *Micro Robots and Teleoperators Workshop. Hyannis, IEEE*, 87–TH.

Ehtesabi, Hamide, M Mahdi Ahadian, and Vahid Taghikhani (2015). “Enhanced heavy oil recovery using TiO2 nanoparticles: investigation of deposition during transport in core plug”. In: *Energy & Fuels* 29.1, pp. 1–8.

Ehtesabi, Hamide et al. (2014). “Enhanced heavy oil recovery in sandstone cores using TiO2 nanofluids”. In: *Energy & Fuels* 28.1, pp. 423–430.

El-Diasty, Abdelrahman Ibrahim and Ahmed M Aly (2015). “Understanding the mechanism of nanoparticles applications in enhanced oil recovery”. In: *SPE North Africa techn. conf. and exhib.* OnePetro.

El-Hoshoudy, AN et al. (2017). “Hydrophobically associated polymers for wettability alteration and enhanced oil recovery–Article review”. In: *Egypt J Pet* 26.3, pp. 757– 762.

Emadi, Samira et al. (2017). “Effect of nano silica particles on Interfacial Tension (IFT) and mobility control of natural surfactant (Cedr Extraction) solution in enhanced oil recovery process by nano-surfactant flooding”. In: *J Mol Liq* 248, pp. 163–167.

Emrani, Arezoo S and Hisham A Nasr-El-Din (2017). “An experimental study of nanoparticle-polymer-stabilized CO2 foam”. In: *Colloids Surf , A* 524, pp. 17–27.

Endo, Morinobu et al. (2008). “Extreme-Performance Rubber Nanocomposites for Probing and Excavating Deep Oil Resources Using Multi-Walled Carbon Nanotubes”. In: *Adv Funct Mater* 18.21, pp. 3403–3409.

Ershadi, Mahshid et al. (2015). “Carbonate and sandstone reservoirs wettability improvement without using surfactants for Chemical Enhanced Oil Recovery (CEOR)”. In: *Fuel* 153, pp. 408–415.

Esmaeilzadeh, Pouriya et al. (2015). “Wettability alteration of carbonate rocks from liquid-wetting to ultra gas-wetting using TiO2, SiO2 and CNT nanofluids containing fluorochemicals, for enhanced gas recovery”. In: *J. Nat. Gas Sci. Eng.* 26, pp. 1294–1305.

Fancher, GH, JA Lewis, and KB Barnes (1933). “Physical tests and properties of oil and gas sands.[Methods for measurement of permeability and porosity]”. In: *World Petroleum Congress*. World Petroleum Congress, Prepr. No. 8.

Farajzadeh, R, BL Wassing, and LW Lake (2019). “Insights into design of mobility control for chemical enhanced oil recovery”. In: *Energy Reports* 5, pp. 570–578.

Fard, Ahmad Kayvani et al. (2016). “Enhancing oil removal from water using ferric oxide nanoparticles doped carbon nanotubes adsorbents”. In: *Chem Eng J* 293, pp. 90–101.

Fatisson, Julien et al. (2009). “Deposition of TiO2 nanoparticles onto silica measured using a quartz crystal microbalance with dissipation monitoring”. In: *Langmuir* 25.11, pp. 6062–6069.

Feng, Xin et al. (2020). “Properties of Pickering emulsion stabilized by food-grade gelatin nanoparticles: Influence of the nanoparticles concentration”. In: *Colloids Surf , B* 196, p. 111294.

Freeze, R Allan (1994). “Henry Darcy and the fountains of Dijon”. In: *Groundwater* 32.1, pp. 23–30.

Frelichowska, Justyna et al. (2009). “Topical delivery of lipophilic drugs from o/w Pickering emulsions”. In: *Int. J. Pharm.* 371.1-2, pp. 56–63.

Fu, Lipei et al. (2016). “Study on organic alkali-surfactant-polymer flooding for enhanced ordinary heavy oil recovery”. In: *Colloids Surf , A* 508, pp. 230–239.

Fu, Zhisheng et al. (2010). “Stabilization of water-in-octane nano-emulsion. II Enhanced by amphiphilic graft copolymers based on poly (higher *α*-olefin)-graft-poly (ethylene glycol)”. In: *Fuel* 89.12, pp. 3860–3865.

Garcia, Danny Eugenio et al. (2018). “Condensed tannin-based polyurethane as functional modifier of PLA-composites”. In: *Polym -Plast Technol Eng* 57.8, pp. 709– 726.

Gbadamosi, Afeez O et al. (2019). “Effect of aluminium oxide nanoparticles on oilfield polyacrylamide: Rheology, interfacial tension, wettability and oil displacement studies”. In: *J Mol Liq* 296, p. 111863.

Geistlinger, Helmut, Iman Ataei-Dadavi, and Hans-Jörg Vogel (2016). “Impact of surface roughness on capillary trapping using 2D-micromodel visualization experiments”. In: *Transport Porous Med* 112.1, pp. 207–227.

Ghazanfari, Mohammad Hossein et al. (2007). “Capillary pressure estimation using statistical pore size functions”. In: *Chem. Eng. Technol.* 30.7, pp. 862–869.

Giraldo, Juliana et al. (2013). “Wettability alteration of sandstone cores by aluminabased nanofluids”. In: *Energy & Fuels* 27.7, pp. 3659–3665.

Gomez-Flores, Allan et al. (2020). “Shape and orientation of bare silica particles influence their deposition under intermediate ionic strength: A study with QCM–D and DLVO theory”. In: *Colloids Surf , A* 599, p. 124921.

Gong, Houjian et al. (2016). “Effect of wettability alteration on enhanced heavy oil recovery by alkaline flooding”. In: *Colloids Surf , A* 488, pp. 28–35.

Griffith, Christopher and Hugh Daigle (2018). “Manipulation of Pickering emulsion rheology using hydrophilically modified silica nanoparticles in brine”. In: *J. Colloid Interface Sci.* 509, pp. 132–139.

Guo, Xiaoming et al. (2021). “Edible CaCO3 nanoparticles stabilized Pickering emulsion as calcium-fortified formulation”. In: *J. Nanotech.* 19.1, pp. 1–16.

Gupta, Srishti et al. (2020). “Synthesis of PEG and quaternary ammonium grafted silicone copolymers as nanoemulsifiers”. In: *ACS Appl. Polym* 2.5, pp. 1856–1864.

Gutierrez, Leonardo et al. (2010). “Deposition and aggregation kinetics of rotavirus in divalent cation solutions”. In: *Environ. Sci. Technol.* 44.12, pp. 4552–4557.

Hammouda, Boualem (2013). “Temperature effect on the nanostructure of SDS micelles in water”. In: *J. Res. Natl. Inst. Stand. Technol* 118, p. 151.

Hassler, GL and E Brunner (1945). “Measurement of capillary pressures in small core samples”. In: *Transactions of the AIME* 160.01, pp. 114–123.

Heinemann, Zoltan and Georg Mittermeir (2013). *Fluid flow in porous media*. University of Leoben.

Hendraningrat, Luky, Shidong Li, and Ole Torsæter (2013a). "A coreflood investigation of nanofluid enhanced oil recovery". In: *J Petrol Sci Eng* 111, pp. 128–138.

Hendraningrat, Luky, Shidong Li, and Ole Torsæter (2013b). "Effect of some parameters influencing enhanced oil recovery process using silica nanoparticles: an experimental investigation". In: *SPE Res.Char. and Sim. Conf. and Exh.* OnePetro.

Hendraningrat, Luky and Ole Torsæter (2014). "Effects of the initial rock wettability on silica-based nanofluid-enhanced oil recovery processes at reservoir temperatures". In: *Energy & Fuels* 28.10, pp. 6228–6241.

Hendraningrat, Luky and Ole Torsæter (2015a). "A stabilizer that enhances the oil recovery process using silica-based nanofluids". In: *Transport Porous Med* 108.3, pp. 679–696.

Hendraningrat, Luky and Ole Torsæter (2015b). "Metal oxide-based nanoparticles: revealing their potential to enhance oil recovery in different wettability systems". In: *Appl Nanosci* 5.2, pp. 181–199.

Holmberg, Anna, Lennart Piculell, and Magnus Nydén (2002). "Effects of an amphiphilic graft copolymer on an oil-continuous microemulsion. Molecular selfdiffusion and viscosity". In: *J. Phys. Chem* 106.10, pp. 2533–2544.

Holmberg, Anna et al. (1999). "Effects of an Amphiphilic Graft Copolymer on an OilContinuous Microemulsion. Viscosity, Droplet Size, and Phase Behavior". In: *J. Phys. Chem* 103.49, pp. 10807–10815.

Hou, Tao et al. (2009). “Hydrogen production by low-temperature reforming of organic compounds in bio-oil over a CNT-promoting Ni catalyst”. In: *Int J Hydrogen Energ* 34.22, pp. 9095–9107.

Hu, Zhongliang et al. (2017). “Microemulsions stabilized by in-situ synthesized nanoparticles for enhanced oil recovery”. In: *Fuel* 210, pp. 272–281.

Huibers, Britta MJ et al. (2017). “Wettability alteration of sandstones by silica nanoparticle dispersions in light and heavy crude oil”. In: *J Nanopart Res* 19.9, pp. 1–18.

Hwang, Yujin et al. (2008). “Production and dispersion stability of nanoparticles in nanofluids”. In: *Powder Technol* 186.2, pp. 145–153.

INTER (2021). *Neutron Reflectometry*. Ed. by INTER. URL: DOI:10.5286/ISIS.E.RB2010541.

Ito, Masaei et al. (2011). “Carbon nanotube enables quantum leap in oil recovery”. In: *Mater Res Bull* 46.9, pp. 1480–1484.

Jang, Hochang, Wonsuk Lee, and Jeonghwan Lee (2018). “Nanoparticle dispersion with surface-modified silica nanoparticles and its effect on the wettability alteration of carbonate rocks”. In: *Colloids Surf , A* 554, pp. 261–271.

Jo, Kyoung-Il et al. (2020). “Enhanced Dynamics of Confined Polymers near the Immiscible Polymer–Polymer Interface: Neutron Reflectivity Studies”. In: *ACS Macro Lett* 9.2, pp. 210–215.

Joonaki, Edris and SJPS Ghanaatian (2014). “The application of nanofluids for enhanced oil recovery: effects on interfacial tension and coreflooding process”. In: *Pet Sci Technol* 32.21, pp. 2599–2607.

Ju, Binshan, Tailiang Fan, and Mingxue Ma (2006). “Enhanced oil recovery by flooding with hydrophilic nanoparticles”. In: *China Part* 4.1, pp. 41–46.

Kalonia, Cavan K et al. (2018). “Protein adsorption and layer formation at the stainless steel–solution interface mediates shear-induced particle formation for an IgG1 monoclonal antibody”. In: *Mol. Pharm.* 15.3, pp. 1319–1331.

Kamal, Muhammad Shahzad et al. (2015). “Review on polymer flooding: rheology, adsorption, stability, and field applications of various polymer systems”. In: *Polym Rev* 55.3, pp. 491–530.

Kao, Wen-Hsing et al. (2013). “Applying Boolean logic algorithm for photomask pattern design”. In: *J. Converg. Inf. Technol.* 4.3.

Kapusta, Sergio, Leandro Balzano, and Paul M Te Riele (2011). “Nanotechnology applications in oil and gas exploration and production”. In: *Int. Pet. Technol. Conf. 2011*. OnePetro.

Karadimitriou, NK and SM Hassanizadeh (2012). “A review of micromodels and their use in two-phase flow studies”. In: *Vadose Zone J* 11.3.

Karimi, Ali et al. (2012). “Wettability alteration in carbonates using zirconium oxide nanofluids: EOR implications”. In: *Energy & Fuels* 26.2, pp. 1028–1036.

Karimi, Mahvash et al. (2016). “Impact of sulfate ions on wettability alteration of oilwet calcite in the absence and presence of cationic surfactant”. In: *Energy & Fuels* 30.2, pp. 819–829.

Khalil, Munawar et al. (2017). “Advanced nanomaterials in oil and gas industry: Design, application and challenges”. In: *Applied energy* 191, pp. 287–310.

Kiani, Sajad, Shirin Alexander, and Andrew R Barron (2021). *Emerging platforms in fluid flow transport: surfactants, polymers, and nanoparticles*. PMiDAS Green Innovations.

Kiani, Sajad et al. (2019). “A new class of low surface energy anionic surfactant for enhanced oil recovery”. In: *Energy & Fuels* 33.4, pp. 3162–3175.

Kittithammavong, Virin, Ampira Charoensaeng, and Sutha Khaodhiar (2021). “Effect of ethylene oxide group in the anionic–nonionic mixed surfactant system on microemulsion phase behavior”. In: *J Surfactants Deterg* 24.4, pp. 631–648.

Ko, Saebom and Chun Huh (2019). “Use of nanoparticles for oil production applications”. In: *J Petrol Sci Eng* 172, pp. 97–114.

Koh, Heesong, Vincent B Lee, and Gary A Pope (2018). “Experimental investigation of the effect of polymers on residual oil saturation”. In: *SPE J* 23.01, pp. 1–17.

Kolari, Kai, Ville Saarela, and Sami Franssila (2008). “Deep plasma etching of glass for fluidic devices with different mask materials”. In: *J Micromech Microeng* 18, p. 064010.

Kripotou, Sotiria et al. (2016). “Structure and crystallization behavior of poly (ethylene oxide)(PEO) chains in core–shell brush copolymers with poly (propylene oxide)block-poly (ethylene oxide) side chains”. In: *Macromolecules* 49.16, pp. 5963– 5977.

Kumar, Rajesha et al. (2016). “Evaluation of hydrolyzed poly (isobutylene-alt-maleic anhydride) as a polyelectrolyte draw solution for forward osmosis desalination”. In: *Desalination* 394, pp. 148–154.

Kumari, Rashmi et al. (2018). “Synergistic effect of mixed anionic and cationic surfactant systems on the interfacial tension of crude oil-water and enhanced oil recovery”. In: *J Disper Sci Technol*.

Kwon, Jun-Mi et al. (2008). “Adsorptive desulfurization and denitrogenation of refinery fuels using mesoporous silica adsorbents”. In: *ChemSusChem* 1.4, pp. 307– 309.

Lakey, Jeremy H (2019). “Recent advances in neutron reflectivity studies of biological membranes”. In: *COCIS* 42, pp. 33–40.

LARMOR (2020). *Small Angle Neutron Scattering*. Ed. by LARMOR. URL: DOI: 10.5286/ISIS.E.RB2010526.

Latiff, Noor Rasyada Ahmad et al. (2011). "Novel enhanced oil recovery method using dielectric zinc oxide nanoparticles activated by electromagnetic waves". In: *2011 National Postgraduate Conference*. IEEE, pp. 1–7.

Laurent, Ch, Emmanuel Flahaut, and Alain Peigney (2010). "The weight and density of carbon nanotubes versus the number of walls and diameter". In: *Carbon* 48.10, pp. 2994–2996.

Law, Kock-Yee and Hong Zhao (2016). *Surface wetting: characterization, contact angle, and fundamentals*. Springer International Publishing Basel, Switzerland.

Lee, Seung Goo et al. (2016). "Site-selective in situ grown calcium carbonate micromodels with tunable geometry, porosity, and wettability". In: *Adv Funct Mater* 26.27, pp. 4896–4905.

Lenormand, Roland, Cesar Zarcone, and A Sarr (1983). "Mechanisms of the displacement of one fluid by another in a network of capillary ducts". In: *J Fluid Mech* 135, pp. 337–353.

Li, Shidong and Ole Torsæter (2014). "An experimental investigation of EOR mechanisms for nanoparticles fluid in glass micromodel". In: *Paper SCA2014-022 was prepared for presentation at the International Symposium of the Society of Core Analysts held in Avignon, France*, pp. 8–11.

Li, Xinxin et al. (2020). "Rheological behavior of a wormlike micelle and an amphiphilic polymer combination for enhanced oil recovery". In: *Phys Fluids* 32.7, p. 073105.

Li, Yuyang et al. (2017). "A novel nanofluid based on fluorescent carbon nanoparticles for enhanced oil recovery". In: *Ind. Eng. Chem. Res* 56.44, pp. 12464–12470.

Lim, JitKang et al. (2013). “Characterization of magnetic nanoparticle by dynamic light scattering”. In: *Nanoscale Res. Lett* 8.1, pp. 1–14.

Link (2020). *A photo image of Shall rock and a geographical map that represent the most countries with large oil shall resources*. Ed. by Link. URL: http://enefitutah.com/project/what-is-oil-shale/.

Lu, Taotao et al. (2021). “Recent progress in nanoclay-based Pickering emulsion and applications”. In: *J Environ Chem Eng* 9.5, p. 105941.

Luo, Chan et al. (2010). “Direct Three-Dimensional Imaging of the Buried Interfaces between Water and Superhydrophobic Surfaces”. In: *Angew Chem-ger Edit* 122.48, pp. 9331–9334.

Maghzi, Ali et al. (2012). “Monitoring wettability alteration by silica nanoparticles during water flooding to heavy oils in five-spot systems: A pore-level investigation”. In: *Exp Therm Fluid Sci* 40, pp. 168–176.

Maghzi, Ali et al. (2014). “The impact of silica nanoparticles on the performance of polymer solution in presence of salts in polymer flooding for heavy oil recovery”. In: *Fuel* 123, pp. 123–132.

Maguire-Boyle, Samuel J et al. (2012). “Alumoxane/ferroxane nanoparticles for the removal of viral pathogens: the importance of surface functionality to nanoparticle activity”. In: *Nanoscale* 4.18, pp. 5627–5632.

Mahmoud, Tahany et al. (2020). “Modification Wettability and Interfacial Tension of Heavy Crude Oil by Green Bio-surfactant Based on Bacillus licheniformis and Rhodococcus erythropolis Strains under Reservoir Conditions: Microbial Enhanced Oil Recovery”. In: *Energy & Fuels* 35.2, pp. 1648–1663.

Mamusa, Marianna et al. (2020). “Tuning the Encapsulation of Simple Fragrances with an Amphiphilic Graft Copolymer”. In: *ACS Appl. Mater. Interfaces* 12.25, pp. 28808–28818.

Manesh, Rasool Rasooli et al. (2017). “Synthesis and evaluation of nano *g*-Al2O3 with spherical, rod-shaped, and plate-like morphologies on enhanced heavy oil recovery”. In: *Mater Res Express* 4.9, p. 095025.

Martínez, Francisco, Eugenia Uribe, and Andrés F Olea (2005). “Copolymerization of Maleic Anhydride with Styrene and *a*-Olefins. Molecular and Thermal Characterization”. In: *J Macromol Sci , Part A: Pure Appl Chem* 42.8, pp. 1063–1072.

Mattax, C and J Kyte (1961). “Ever See Water”. In: *Oil and Gas* 59, pp. 115–128.

Maurya, Neetish Kumar, Prabhakar Kushwaha, and Ajay Mandal (2017). “Studies on interfacial and rheological properties of water soluble polymer grafted nanoparticle for application in enhanced oil recovery”. In: *J Taiwan Inst Chem Eng* 70, pp. 319– 330.

McElfresh, Paul, David Holcomb, and Daniel Ector (2012). “Application of nanofluid technology to improve recovery in oil and gas wells”. In: *SPE international oilfield nanotechnology conference and exhibition*. OnePetro.

Minsky, Marvin (1996). “Memoir on inventing the confocal scanning microscope”. In: *philpapers*.

Mitzel, Michael R et al. (2016). “Hydrophobicity of biofilm coatings influences the transport dynamics of polystyrene nanoparticles in biofilm-coated sand”. In: *Water research* 92, pp. 113–120.

Moeini, Farzaneh et al. (2014). “Toward mechanistic understanding of heavy crude oil/brine interfacial tension: The roles of salinity, temperature and pressure”. In: *Fluid phase equilibria* 375, pp. 191–200.

Mohd, Tengku Amran Tengku et al. (2016). “Effects of particle shape and size on nanofluid properties for potential Enhanced Oil Recovery (EOR)”. In: *MATEC Web of Conferences*. Vol. 69. EDP Sciences, p. 03006.

Monicard, Robert P (1980). *Properties of reservoir rocks: core analysis*. Editions Technip.

Montemagno, Carlo D and William G Gray (1995). “Photoluminescent volumetric imaging: A technique for the exploration of multiphase flow and transport in porous media”. In: *Geophys. Res. Lett.* 22.4, pp. 425–428.

Nazari Moghaddam, Rasoul et al. (2015). “Comparative study of using nanoparticles for enhanced oil recovery: wettability alteration of carbonate rocks”. In: *Energy & Fuels* 29.4, pp. 2111–2119.

Negin, Chegenizadeh, Saeedi Ali, and Quan Xie (2016). “Application of nanotechnology for enhancing oil recovery–A review”. In: *Petroleum* 2.4, pp. 324–333.

Neugebauer, Dorota et al. (2006). “Densely heterografted brush macromolecules with crystallizable grafts. Synthesis and bulk properties”. In: *Macromolecules* 39.2, pp. 584–593.

Niosi, Jorge and Susan E Reid (2007). “Biotechnology and nanotechnology: sciencebased enabling technologies as windows of opportunity for LDCs?” In: *World Dev* 35.3, pp. 426–438.

Nutting, PG (1925). “Chemical Problems in the Water Driving of Petroleum from Oil Sands.” In: *Ind. Eng. Chem. Res. .* 17.10, pp. 1035–1036.

Nwidee, Lezorgia N et al. (2017). “Wettability alteration of oil-wet limestone using surfactant-nanoparticle formulation”. In: *J. Colloid Interface Sci.* 504, pp. 334–345.

Oak, MJ (1988). “A new X-ray absorption method for measurement of three-phase relative permeability”. In: *SPE Reservoir Eng* 3.01, pp. 199–206.

Odrobinska, Justyna and Dorota Neugebauer (2020). “Micellar carriers based on am-´ phiphilic PEG/PCL graft copolymers for delivery of active substances”. In: *Polymers* 12.12, p. 2876.

Oliveira, Priscila F et al. (2019). “Hydrolysis and thermal stability of partially hydrolyzed polyacrylamide in high-salinity environments”. In: *J Appl Polym Sci* 136.29, p. 47793.

Olsson, Adam LJ et al. (2013). “Using the quartz crystal microbalance with dissipation monitoring to evaluate the size of nanoparticles deposited on surfaces”. In: *ACS nano* 7.9, pp. 7833–7843.

Onyekonwu, Mike O and Naomi A Ogolo (2010). “Investigating the use of nanoparticles in enhancing oil recovery”. In: *Nigeria Annual international conference and exhibition*. OnePetro.

Oostrom, Martinus et al. (2016). “Pore-scale and continuum simulations of solute transport micromodel benchmark experiments”. In: *Computat Geosci* 20.4, pp. 857–879.

Ouikhalfan, Mohammed et al. (2019). “Stability and thermal conductivity enhancement of aqueous nanofluid based on surfactant-modified TiO2”. In: *J Disper Sci Technol*.

Panchal, Himanshu et al. (2021). “A systematic review on nanotechnology in enhanced oil recovery”. In: *Petroleum Research* 6.3, pp. 204–212.

Parizad, Amirhossein, Khalil Shahbazi, and Abbas Ayatizadeh Tanha (2018). "Enhancement of polymeric water-based drilling fluid properties using nanoparticles". In: *J Petrol Sci Eng* 170, pp. 813–828.

Peillon, Samuel et al. (2019). "Adhesion of tungsten particles on rough tungsten surfaces using Atomic Force Microscopy". In: *J Aerosol Sci* 137, p. 105431.

Peng, Suping and Jincai Zhang (2007). *Engineering geology for underground rocks*. Springer Science & Business Media.

Petosa, Adamo R et al. (2010). "Aggregation and deposition of engineered nanomaterials in aquatic environments: role of physicochemical interactions". In: *Environ. Sci. Technol.* 44.17, pp. 6532–6549.

Pisárcik, Martin et al. (2018). "Silver nanoparticles stabilised with cationic single-ˇ chain surfactants. Structure-physical properties-biological activity relationship study". In: *J Mol Liq* 272, pp. 60–72.

Pourjavadi, Ali and Malihe Doulabi (2013). "Improvement in oil absorbency by using modified carbon nanotubes in preparation of oil sorbents". In: *Adv. Polym. Technol* 32.1.

Pouryousefy, Ehsan, Quan Xie, and Ali Saeedi (2016). "Effect of multi-component ions exchange on low salinity EOR: Coupled geochemical simulation study". In: *Petroleum* 2.3, pp. 215–224.

Qin, LC (1997). "CVD synthesis of carbon nanotubes". In: *J. Mater. Sci. Lett.* 16.6, pp. 457–459.

Raffa, Patrizio, Antonius A Broekhuis, and Francesco Picchioni (2016). "Amphiphilic copolymers based on PEG-acrylate as surface active water viscosifiers: Towards new potential systems for enhanced oil recovery". In: *J Appl Polym Sci* 133.42.

Raffa, Patrizio and Pablo Druetta (2019). *Chemical enhanced oil recovery: advances in polymer flooding and nanotechnology*. Walter de Gruyter GmbH & Co KG.

Raffa, Patrizio and Francesco Picchioni (2021). “Preliminary evaluation of amphiphilic block polyelectrolytes as potential flooding agents for low salinity chemical enhanced oil recovery”. In: *J Petrol Sci Eng* 198, p. 108181.

Raffa, Patrizio et al. (2015). “Polymeric surfactants: synthesis, properties, and links to applications”. In: *Chemical reviews* 115.16, pp. 8504–8563.

Ramezanpour, Milad and Majid Siavashi (2019). “Application of SiO2–water nanofluid to enhance oil recovery”. In: *J Therm Anal Calorim* 135.1, pp. 565–580.

Rana, Subinoy et al. (2012). “Control of surface tension at liquid–liquid interfaces using nanoparticles and nanoparticle–protein complexes”. In: *Langmuir* 28.4, pp. 2023–2027.

Ren, Zhao Hua (2015). “Mechanism of the salt effect on micellization of an aminosulfonate amphoteric surfactant”. In: *Ind. Eng. Chem. Res* 54.40, pp. 9683–9688.

Rezvani, Hosein et al. (2018). “Experimental investigation of interfacial properties in the EOR mechanisms by the novel synthesized Fe3O4@ Chitosan nanocomposites”. In: *Colloids Surf , A* 544, pp. 15–27.

Roman, Sophie et al. (2016). “Particle velocimetry analysis of immiscible two-phase flow in micromodels”. In: *Adv Water Resour* 95, pp. 199–211.

Rotko, Grzegorz et al. (2019). “Towards biocompatible NIR-II nanoprobes–transfer of hydrophobic Ag2S quantum dots to aqueous solutions using phase transfer catalysed hydrolysis of poly (maleic anhydride-alt-1-octadecene)”. In: *Colloids Surf , B* 181, pp. 119–124.

Russell, TP (1990). “X-ray and neutron reflectivity for the investigation of polymers”. In: *Mater. Sci. Rep.* 5.4, pp. 171–271.

Sagisaka, Masanobu et al. (2019). “Water-in-CO2 microemulsions stabilized by fluorinated Cation–anion surfactant pairs”. In: *Langmuir* 35.9, pp. 3445–3454.

Saha, Debasish et al. (2020). “Amphiphilic Comb Polymers as New Additives in Bicontinuous Microemulsions”. In: *Nanomaterials* 10.12, p. 2410.

Sakthivel, Sivabalan et al. (2017). “Interfacial tension of crude oil-water system with imidazolium and lactam-based ionic liquids and their evaluation for enhanced oil recovery under high saline environment”. In: *Fuel* 191, pp. 239–250.

Samanta, Abhijit et al. (2013). “Mobility control and enhanced oil recovery using partially hydrolysed polyacrylamide (PHPA)”. In: *Int. J. Oil Gas Coal Technol.* 6.3, pp. 245–258.

SASVIEW (2021). *SASVIEW program*. Ed. by SASVIEW. URL: http://www.sasview.org/.

Schaefer, DM et al. (1995). “Surface roughness and its influence on particle adhesion using atomic force techniques”. In: *J Adhes Sci Technol* . 9.8, pp. 1049–1062.

Schembre, JM, G-Q Tang, and AR Kovscek (2006). “Wettability alteration and oil recovery by water imbibition at elevated temperatures”. In: *J Petrol Sci Eng* 52.14, pp. 131–148.

Senn, T et al. (2010). “Replica molding for multilevel micro-/nanostructure replication”. In: *J. Micromech. Microeng* 20.11, p. 115012.

Shah, Bakht Ramin et al. (2016). “Preparation and optimization of Pickering emulsion stabilized by chitosan-tripolyphosphate nanoparticles for curcumin encapsulation”.

In: *Food Hydrocolloid* 52, pp. 369–377.

Shah, Dinesh Ochhavlal et al. (1981). *Surface phenomena in enhanced oil recovery*. Springer.

Sharma, Tushar and Jitendra S Sangwai (2017). “Silica nanofluids in polyacrylamide with and without surfactant: Viscosity, surface tension, and interfacial tension with liquid paraffin”. In: *J Petrol Sci Eng* 152, pp. 575–585.

Sharma, Tushar et al. (2015). “Thermal stability of oil-in-water Pickering emulsion in the presence of nanoparticle, surfactant, and polymer”. In: *J Ind Eng Chem* 22, pp. 324–334.

Sheng, James J (2010). *Modern chemical enhanced oil recovery: theory and practice*. Gulf Professional Publishing.

Shimokita, Keisuke et al. (2021). “Investigation of Interfacial Water Accumulation between Polypropylene Thin Film and Si Substrate by Neutron Reflectivity”. In: *Langmuir* 37.49, pp. 14550–14557.

Sigen, A et al. (2017). “Hyperbranched PEG-based multi-NHS polymer and bioconjugation with BSA”. In: *Polym Chem-uk* 8.8, pp. 1283–1287.

Slastanova, Anna et al. (2020). “Synergy, competition, and the “hanging” polymer layer: Interactions between a neutral amphiphilic ‘tardigrade’comb co-polymer with an anionic surfactant at the air-water interface”. In: *J Colloid Interface Sci* 561, pp. 181–194.

Sofla, Saeed Jafari Daghlian, Lesley Anne James, and Yahui Zhang (2018). “Insight into the stability of hydrophilic silica nanoparticles in seawater for Enhanced oil recovery implications”. In: *Fuel* 216, pp. 559–571.

Soll, WE, Michael Anthony Celia, and JLr Wilson (1993). “Micromodel studies of three-fluid porous media systems: Pore-scale processes relating to capillary pressure-saturation relationships”. In: *Water Resour. Res.* 29.9, pp. 2963–2974.

Songolzadeh, Reza and Jamshid Moghadasi (2017). “Stabilizing silica nanoparticles in high saline water by using ionic surfactants for wettability alteration application”. In: *Colloid Polym Sci* 295.1, pp. 145–155.

Stöhr, M, K Roth, and B Jähne (2003). “Measurement of 3D pore-scale flow in indexmatched porous media”. In: *Exp Fluids* 35.2, pp. 159–166.

Sugii, Yasuhiko, Shigeru Nishio, and Koji Okamoto (2002). “In vivo PIV measurement of red blood cell velocity field in microvessels considering mesentery motion”. In: *Physiol. Meas.* 23.2, p. 403.

Sugii, Yasuhiko and Koji Okamoto (2004). “Quantitative visualization of micro-tube flow using micro-PIV”. In: *Journal of visualization* 7.1, pp. 9–16.

Suleimanov, Baghir A, FS Ismailov, and EF Veliyev (2011). “Nanofluid for enhanced oil recovery”. In: *J. Pet. Sci. Eng.* 78.2, pp. 431–437.

Sun, Xiaofei et al. (2017). “Application of nanoparticles in enhanced oil recovery: a critical review of recent progress”. In: *Energies* 10.3, p. 345.

Sun, Xiaopeng, Fanghong Yang, and Zhanhai Yao (2020). “Influence of Ungrafted Monomers in Graft Copolymers on Electrical Insulating Properties of Polyethylene”. In: *Ind. Eng. Chem. Res* 59.37, pp. 16112–16121.

Szutkowski, Kosma et al. (2018). “Clear distinction between CAC and CMC revealed by high-resolution NMR diffusometry for a series of bis-imidazolium gemini surfactants in aqueous solutions”. In: *RSC advances* 8.67, pp. 38470–38482.

Taborda, Esteban A et al. (2016). “Effect of nanoparticles/nanofluids on the rheology of heavy crude oil and its mobility on porous media at reservoir conditions”. In: *Fuel* 184, pp. 222–232.

Tajik, Sanaz et al. (2018). “Application of functionalized silica-graphene nanohybrid for the enhanced oil recovery performance”. In: *Colloids Surf , A* 556, pp. 253–265.

Taylor, Kevin C and Hisham A Nasr-El-Din (1998). “Water-soluble hydrophobically associating polymers for improved oil recovery: A literature review”. In: *J Petrol Sci Eng* 19.3-4, pp. 265–280.

Tetteh, Joel, Nazirah Mohd Janjang, and Reza Barati (2018). “Wettability alteration and enhanced oil recovery using low salinity waterflooding in limestone rocks: a mechanistic study”. In: *SPE ATS&E*. OnePetro.

Teulère, Coralie et al. (2020). “Synthesis and self-assembly of amphiphilic heterografted molecular brushes prepared by telomerization”. In: *Eur Polym J* 141, p. 110080.

Torres, LG et al. (2007). “Preparation of o/w emulsions stabilized by solid particles and their characterization by oscillatory rheology”. In: *Colloids Surf , A* 302.1-3, pp. 439–448.

Torsæter, Ole and Manoochehr Abtahi (2003). “Experimental reservoir engineering laboratory workbook”. In: *NTNU*.

Treiber, LE and WW Owens (1972). “A laboratory evaluation of the wettability of fifty oil-producing reservoirs”. In: *Soc Petrol Eng J* 12.06, pp. 531–540.

Uren, Lester C and EH Fahmy (1927). “Factors influencing the recovery of petroleum from unconsolidated sands by waterflooding”. In: *Transactions of the AIME* 77.01, pp. 318–335.

Vanoyan, Nune et al. (2010). “Reduced bacterial deposition and attachment by quorum-sensing inhibitor 4-nitro-pyridine-N-oxide: the role of physicochemical effects”. In: *Langmuir* 26.14, pp. 12089–12094.

Venault, Antoine et al. (2020). “Simultaneous amphiphilic polymer synthesis and membrane functionalization for oil/water separation”. In: *J Membrane Sci* 604, p. 118069.

Voorn, DJ, W Ming, and AM Van Herk (2006). “Polymer- clay nanocomposite latex particles by inverse pickering emulsion polymerization stabilized with hydrophobic montmorillonite platelets”. In: *Macromolecules* 39.6, pp. 2137–2143.

Wang, J and M Dong (2009). “Optimum effective viscosity of polymer solution for improving heavy oil recovery”. In: *J Petrol Sci Eng* 67.3-4, pp. 155–158.

Webster, JRP et al. (2011). “Reflectometry techniques on the Second Target Station at ISIS: Methods and science”. In: *Eur Phys J Plus* 126.11, pp. 1–5.

Wereley, Steven T and Carl D Meinhart (2005). “Micron-resolution particle image velocimetry”. In: *Microscale diagnostic techniques*. Springer, pp. 51–112.

Whitby, Catherine P, Daniel Fornasiero, and John Ralston (2010). “Structure of oilin-water emulsions stabilised by silica and hydrophobised titania particles”. In: *J. Colloid Interface Sci.* 342.1, pp. 205–209.

Williams, Christopher T and David A Beattie (2002). “Probing buried interfaces with non-linear optical spectroscopy”. In: *Surf. Sci.* 500.1-3, pp. 545–576.

Williams, Peter A (2008). *Handbook of industrial water soluble polymers*. John Wiley & Sons.

Winston, Roland (1970). “Light collection within the framework of geometrical optics”. In: *Josa* 60.2, pp. 245–247.

Wnek, Gary E and Gary L Bowlin (2008). *Encyclopedia of biomaterials and biomedical engineering*. CRC Press.

Wu, Li-guang et al. (2020). “Fabrication of polyvinylidene fluoride blending membrane coupling with microemulsion polymerization and their anti-fouling performance”. In: *Polymer* 203, p. 122767.

Wu, Xiaogang et al. (2018). “Solution properties and aggregating structures for a fluorine-containing polymeric surfactant with a poly (ethylene oxide) macromonomer”. In: *R. Soc. Open Sci.* 5.8, p. 180610.

Wu, Yining et al. (2017). “Reducing surfactant adsorption on rock by silica nanoparticles for enhanced oil recovery”. In: *J Petrol Sci Eng* 153, pp. 283–287.

Wyckoff, RD et al. (1933). “The measurement of the permeability of porous media for homogeneous fluids”. In: *Rev Sci Instrum* 4.7, pp. 394–405.

Xie, Donghai et al. (2016). “Application of organic alkali for heavy-oil enhanced oil recovery (EOR), in comparison with inorganic alkali”. In: *Energy & Fuels* 30.6, pp. 4583–4595.

Xie, Guojun et al. (2017). “Heterografted molecular brushes as stabilizers for waterin-oil emulsions”. In: *Macromolecules* 50.7, pp. 2942–2950.

Xu, Ke et al. (2017). “A 2.5-D glass micromodel for investigation of multi-phase flow in porous media”. In: *Lab Chip* 17.4, pp. 640–646.

Yan, Qiang et al. (2009). “Cellulose-based dual graft molecular brushes as potential drug nanocarriers: stimulus-responsive micelles, self-assembled phase transition behavior, and tunable crystalline morphologies”. In: *Biomacromolecules* 10.8, pp. 2033–2042.

Yang, Shu-Di, Bao-Wei Cui, Jing-Cheng Song, et al. (2020). “The polymer micelles and application in tumor targeted therapy system”. In: *TMR Cancer* 3.6, pp. 257– 264.

Yang, Weipeng, Tengfei Wang, and Zexia Fan (2017). “Highly stable foam stabilized by alumina nanoparticles for EOR: effects of sodium cumenesulfonate and electrolyte concentrations”. In: *Energy & Fuels* 31.9, pp. 9016–9025.

Yekeen, Nurudeen et al. (2018). “A comprehensive review of experimental studies of nanoparticles-stabilized foam for enhanced oil recovery”. In: *J Petrol Sci Eng* 164, pp. 43–74.

Yousefvand, H and AJPMS Jafari (2015). “Enhanced oil recovery using polymer/nanosilica”. In: *Procedia Mater Sci* 11, pp. 565–570.

Yousefvand, Hojat Alah and Arezou Jafari (2018). “Stability and flooding analysis of nanosilica/NaCl/HPAM/SDS solution for enhanced heavy oil recovery”. In: *J Petrol Sci Eng* 162, pp. 283–291.

Yu, Kui, Lifeng Zhang, and Adi Eisenberg (1996). “Novel morphologies of “crew-cut” aggregates of amphiphilic diblock copolymers in dilute solution”. In: *Langmuir* 12.25, pp. 5980–5984.

Yun, W and AR Kovscek (2015). “Microvisual investigation of polymer retention on the homogeneous pore network of a micromodel”. In: *J Petrol Sci Eng* 128, pp. 115–127.

Yun, Wonjin et al. (2017). “Creation of a dual-porosity and dual-depth micromodel for the study of multiphase flow in complex porous media”. In: *Lab Chip* 17.8, pp. 1462–1474.

Zarbakhsh, A, J Bowers, and JRP Webster (1999). “A new approach for measuring neutron reflection from a liquid/liquid interface”. In: *Meas Sci Technol* 10.8, p. 738.

Zehm, Daniel et al. (2010). “Amphiphilic dual brush block copolymers as “giant surfactants” and their aqueous self-assembly”. In: *Langmuir* 26.5, pp. 3145–3155.

Zhang, Changyong et al. (2010). “Pore-scale study of transverse mixing induced CaCO3 precipitation and permeability reduction in a model subsurface sedimentary system”. In: *Environ. Sci. Technol* 44.20, pp. 7833–7838.

Zhang, Guoyin and RS Seright (2014). “Effect of concentration on HPAM retention in porous media”. In: *SPE J* 19.03, pp. 373–380.

Zhang, Hua, Alex Nikolov, and Darsh Wasan (2014). “Enhanced oil recovery (EOR) using nanoparticle dispersions: underlying mechanism and imbibition experiments”. In: *Energy & Fuels* 28.5, pp. 3002–3009.

Zhang, Shumin, Yinghao Zhou, and Cheng Yang (2015). “Pickering emulsions stabilized by the complex of polystyrene particles and chitosan”. In: *Colloids Surf , A* 482, pp. 338–344.

Zhang, Xiaoyong et al. (2012). “PEGylation and polyPEGylation of nanodiamond”. In: *Polymer* 53.15, pp. 3178–3184.

Zhang, Xiaoyong et al. (2013). “PEGylation of fluoridated hydroxyapatite (FAp): Ln 3+ nanorods for cell imaging”. In: *Polym Chem-uk* 4.15, pp. 4120–4125.

Zhao, Benzhong, Christopher W MacMinn, and Ruben Juanes (2016). “Wettability control on multiphase flow in patterned microfluidics”. In: *Proc Natl Acad Sci* 113.37, pp. 10251–10256.

Zhao, Xinyu et al. (2018). “Eco-friendly Pickering emulsion stabilized by silica nanoparticles dispersed with high-molecular-weight amphiphilic alginate derivatives”. In: *ACS Sustain. Chem. Eng.* 6.3, pp. 4105–4114.

Zhou, Xiao-Lin and Sow-Hsin Chen (1995). “Theoretical foundation of X-ray and neutron reflectometry”. In: *Phys Rep* 257.4-5, pp. 223–348.

Zou, Yuan et al. (2015). “Pickering emulsion gels prepared by hydrogen-bonded zein/tannic acid complex colloidal particles”. In: *J Agric Food Chem* 63.33, pp. 7405–7414.